



**This electronic thesis or dissertation has been  
downloaded from Explore Bristol Research,  
<http://research-information.bristol.ac.uk>**

*Author:*

**Ishak, M I**

*Title:*

**Developing antimicrobial polymeric nanostructured surfaces to combat biomaterial  
associated infections**

**General rights**

Access to the thesis is subject to the Creative Commons Attribution - NonCommercial-No Derivatives 4.0 International Public License. A copy of this may be found at <https://creativecommons.org/licenses/by-nc-nd/4.0/legalcode>. This license sets out your rights and the restrictions that apply to your access to the thesis so it is important you read this before proceeding.

**Take down policy**

Some pages of this thesis may have been removed for copyright restrictions prior to having it been deposited in Explore Bristol Research. However, if you have discovered material within the thesis that you consider to be unlawful e.g. breaches of copyright (either yours or that of a third party) or any other law, including but not limited to those relating to patent, trademark, confidentiality, data protection, obscenity, defamation, libel, then please contact [collections-metadata@bristol.ac.uk](mailto:collections-metadata@bristol.ac.uk) and include the following information in your message:

- Your contact details
- Bibliographic details for the item, including a URL
- An outline nature of the complaint

Your claim will be investigated and, where appropriate, the item in question will be removed from public view as soon as possible.



# Developing antimicrobial polymeric nanostructured surfaces to combat biomaterial associated infections

by

Mohd Irill Ishak

A dissertation submitted to the University of Bristol in accordance with the requirements for  
award of the degree of

**Doctor of Philosophy in the Faculty of Health Sciences**

Bristol Dental School

January 2020

Word count: 51,400



# Abstract

The demand for polymeric medical devices is expected to increase rapidly in the next few decades. However, the risk of bacterial infection of medical devices remains a major issue. Due to the problem of biomaterial-associated infections (BAIs) and growing numbers of antimicrobial resistant bacteria, it is crucial to develop novel materials that can combat BAIs. One such option is to develop a scalable nanofabrication technique that can exploit the antibacterial properties shown by nanostructured surfaces found in nature.

This research project focused on the development of a scalable nanofabrication protocol to synthesise tuneable nanotopography that is compatible with a wide range of polymer substrates. The correlation between physical properties of the resulting nanopillars and antibacterial properties of the nanostructured surfaces was then investigated. Nanopillars were characterised using a range of analytical techniques, including DSA, SEM, and AFM, to quantify the contact angle, surface energy, surface roughness, and nanotribological properties. Using three model bacterial species (*Escherichia coli*, *Klebsiella pneumoniae*, *Staphylococcus aureus*), the antibacterial performance of the nanostructured surfaces was quantified in terms of capacity to damage the bacterial cell wall and to reduce the number of metabolically active adherent cells. It was found that the tip diameter, interpillar distance, surface energy, adhesive energy, and frictional instabilities of the nanopillars had a direct correlation with the antibacterial properties of the nanostructured surfaces.

Previous theoretical work proposed that the susceptibility of particularly Gram-negative bacterial cells to nanotopography-mediated lysis is due to stretching of the bacterial cell wall and eventual rupture. To better understand the adhesive forces that may cause this cell wall rupture, this project also explored the role of bacterial surface proteins in mediating interactions with the nanostructured surfaces. Trypsinisation was found to reduce the hydrophobicity and negative charge of the bacterial cells and impaired the antibacterial action of the nanostructured surfaces. Thus, bacterial surface proteins may contribute to the antibacterial performance of nanostructured surfaces by mediating the strong adhesive forces with the nanopillars required for effective cell disruption.

Taken together, these data provide important information that could be exploited to inform the fabrication of antimicrobial surfaces for polymeric medical devices and provide an experimental basis from which a new theoretical model of bacterial attachment to nanostructured surfaces may be developed.



# Acknowledgements

First of all, I would like to express my sincere gratitude to my supervisors, Prof Bo Su and Dr Angela Nobbs for their support, intellect, wisdom and encouragement throughout my PhD journey. I am thankful for their knowledge and grateful to have inspirational researchers as my mentors.

I am also very grateful to have tremendous support from my third supervisor, Dr Wuge Briscoe in School of Chemistry, University of Bristol. I am especially thankful for the fruitful discussion we had during our meetings and for organising incentive AFM session in KTH, Stockholm, Sweden for training in colloidal probe AFM and friction measurement with the help of Dr Illia Dobryden.

I would like to thank other people from different department in University of Bristol; Dr Robert Harniman for his assistance in QNM-AFM, Dajana Gubala for her help in micromanipulator, Anna Slastanova for helping me with DLS measurements and Judith Mantell for training and guidance in SEM. I would also like to acknowledge to Dr Thomas Keller, Dr Satish Kumar and other members of DESY NanoLab in Hamburg, Germany for their help in XPS and FIB-SEM experiments and analysis.

Not to forget the wonderful members of BioMEG and Oral Microbiology group, especially Dr Terje Sjöström for his training in anodisation and hot embossing, Mark Ginty for his help in the lab, Dr Jane Brittan and Dr Lindsay Dutton for training me in microbiology assays, and other PhDs and post-docs members for their assists and advises. Special thanks to my officemates, colleagues and fellow scientists; Dr Josh Jenkins and Dr Marcus Eales for all their help, advice, and laughter. Hope we can get together for future collaborations, Subways and Key and Peele.

To my family, thank you for believing in me, and thank you for waiting 4 years to see me. Sorry Ibu, Ayah, that I was not home to celebrate Hari Raya with you. To my amazing wife, thank you for being part of me in this journey. Happy to share these wonderful memories with you, Iris and Iyad. Thank you for your patience, presence, and perseverance.

Finally, I would like to acknowledge thank my sponsors; Ministry of Education (MOE) in Malaysia and University Malaysia Perlis (UniMAP) for the funding of my PhD.

## Author's declaration

I declare that the work in this dissertation was carried out in accordance with the requirements of the University's *Regulations and Code of Practice for Research Degree Programmes* and that it has not been submitted for any other academic award. Except where indicated by specific reference in the text, the work is the candidate's own work. Work done in collaboration with, or with the assistance of, others, is indicated as such. Any views expressed in the dissertation are those of the author.

SIGNED: .....

DATE: .....

# List of publications

**The following chapters are the basis of a submitted manuscript**

Chapter 3 and 4

Mohd I. Ishak, Illia Dobryden, Per Martin Claesson, Wuge H. Briscoe and Bo Su, Friction at nanopillared polymer surfaces: Correlation between stick-slip amplitude coefficient (SSAC) and surface properties, *Langmuir*

# Table of Contents

<b>LIST OF FIGURES.....</b>	<b>viii</b>
<b>LIST OF TABLES .....</b>	<b>xii</b>
<b>LIST OF EQUATIONS .....</b>	<b>xiv</b>
<b>LIST OF ABBREVIATIONS.....</b>	<b>xvi</b>
<b>CHAPTER 1 INTRODUCTION.....</b>	<b>1</b>
1.1 Biomaterial-associated infections (BAIs) .....	1
1.1.1 Current preventive measures.....	3
1.1.2 Antimicrobial resistance and BAIs .....	6
1.2 Natural and biomimetic antibacterial surfaces.....	8
1.2.1 Antibiofouling surfaces.....	8
1.2.2 Contact killing surfaces.....	10
1.3 Structure and mechanical properties of the bacterial cell wall .....	12
1.3.1 Gram-negative vs. Gram-positive cell wall structure .....	12
1.3.2 Mechanical properties of the bacterial cell wall .....	14
1.4 Bacteria-substrata interactions.....	19
1.4.1 Surface sensing.....	19
1.4.2 Swimming dynamics of bacteria.....	20
1.4.3 Bacterial adhesion .....	20
1.5 Bacteria-nanostructure interactions .....	23
1.5.1 Stretching model .....	23
1.5.2 Thermodynamics model.....	25
1.5.3 Role of cell wall rigidity and viscoelasticity during bacteria-nanostructure interactions .....	26
1.6 Nanofabrication techniques for polymeric nanostructured surfaces.....	28
1.6.1 Nanolithography for protruded nanostructured surfaces.....	28
1.6.2 Current challenges with nanofabrication techniques .....	31
1.6.3 Anodisation .....	31
1.7 Aims and objectives .....	36
<b>CHAPTER 2 MATERIALS AND METHODS .....</b>	<b>37</b>
2.1 Nanofabrication of nanopillars on polymer substrates .....	37
2.1.1 Electrochemical setup .....	37
2.1.2 Electropolishing and two-step anodisation.....	38
2.1.3 Hot embossing .....	40
2.2 Microbiological studies .....	42
2.2.1 Bacterial strains.....	42
2.2.2 Quantifying the antibacterial performance of test surfaces .....	42
2.2.3 Adhesion assay of trypsinised E. coli .....	43
2.2.4 Hydrophobicity assay .....	44
2.3 Surface characterisation .....	44
2.3.1 Contact angle and surface wetting.....	44

2.3.2 X-ray photoelectron spectroscopy (XPS) .....	45
2.3.3 Surface charge by dynamic light scattering (DLS).....	45
<b>2.4 Imaging analysis .....</b>	<b>45</b>
2.4.1 Scanning electron microscopy (SEM) .....	45
2.4.2 Focused Ion Beam (FIB) – SEM .....	47
<b>2.5 Atomic force microscopy (AFM).....</b>	<b>48</b>
2.5.1 Colloidal probe AFM (CP-AFM).....	48
<b>2.6 Data analysis .....</b>	<b>57</b>
2.6.1 Statistical analysis .....	57
2.6.2 AFM imaging .....	57
2.6.3 Young's Modulus measurement .....	57
2.6.4 Imaging analysis .....	58
<b>CHAPTER 3 FABRICATION AND CHARACTERISATION OF BIOMIMETIC NANOSTRUCTURED SURFACES ON POLYMER SUBSTRATUM .....</b>	<b>59</b>
<b>3.1 Optimisation of master stamp fabrication protocol .....</b>	<b>59</b>
3.1.1 Electropolishing: the effect of electrolytes .....	59
3.1.2 Optimisation of anodisation.....	61
3.1.3 Two-step anodisation: the effect of first-step time .....	65
3.1.4 Considerations for scaling up .....	66
3.1.5 Tuning interpore distance by using phosphoric acid.....	68
3.1.6 Nanopillar design .....	69
<b>3.2 Optimisation of hot embossing.....</b>	<b>74</b>
3.2.1 Systematic assessment of hot embossing parameters.....	74
3.2.2 Polymer choice: PMMA, PET and PEEK .....	78
<b>3.3 Optimisation of silanisation protocol.....</b>	<b>83</b>
3.3.1 Difficulties with demoulding process .....	83
<b>3.4 Nanostructured surface characterisation .....</b>	<b>89</b>
3.4.1 Surface nanotopography.....	89
3.4.2 Contact angle and surface wetting.....	92
3.4.3 XPS analysis .....	97
<b>CHAPTER 4 NANOTRIBOLOGICAL AND NANOMECHANICAL PROPERTIES OF POLYMERIC NANOPILLARED SURFACES .....</b>	<b>100</b>
<b>4.1 Introduction .....</b>	<b>100</b>
<b>4.2 Results .....</b>	<b>102</b>
4.2.1 Friction force measurement.....	102
4.2.2 Normal force measurement.....	107
4.2.3 Stick-slip amplitude coefficient (SSAC) analysis .....	109
<b>4.3 Discussion.....</b>	<b>111</b>
4.3.1 Adhesion force of nanopillared surfaces.....	111
4.3.2 Young's modulus (YM) of the PET nanopillars.....	114
4.3.3 Frictional properties of PET nanopillared surfaces.....	123
4.3.4 Nanomechanical properties and SSAC .....	126

<b>CHAPTER 5 UNDERSTANDING THE BACTERIAL RESPONSE TO POLYMERIC NANOPILLARED SURFACES: A PHYSICOCHEMICAL AND NANOTRIBOLOGICAL PERSPECTIVE .....</b>	<b>128</b>
5.1 Introduction .....	128
5.2 Results .....	129
5.2.1 Bacterial membrane susceptibility on nanostructured surfaces .....	129
5.2.2 Metabolic activity of bacteria on different nanotopographies .....	133
5.2.3 Nanomechanical properties of the bacterial cell wall .....	135
5.2.4 Effects of trypsinisation on bacterial adhesion .....	136
5.2.5 Assessment of bacterial interactions with nanostructured surfaces using high resolution microscopy ..	142
5.3 Discussion.....	154
5.3.1 Bacterial response to the polymeric nanopillared surfaces .....	154
5.3.2 Potential bacterial evasion of nanopillars .....	162
5.3.3 Modulation of the bacterial cell wall.....	164
5.3.4 Effects of nanotopography, surface wetting and surface energy on bactericidal performance .....	165
5.3.5 Correlation between nanotribology and antibacterial activity of PET substrates .....	168
<b>CHAPTER 6 CONCLUSIONS AND FUTURE WORK .....</b>	<b>172</b>
6.1 Scalability of nanofabrication.....	172
6.2 Surface design .....	173
6.3 Nanotribological properties of PET nanopillared surfaces .....	174
6.4 Correlation between surface topography, wettability, nanotribology and bacterial response.....	175
<b>REFERENCES .....</b>	<b>179</b>
<b>APPENDICES .....</b>	<b>196</b>
Appendix A: Batch processing to count cells or particles (FIJI).....	196
Appendix B: Volume shrinkage calculation.....	197

# LIST OF FIGURES

Figure 1.1 Overview of current surface designs to combat BAIs. ....	4
Figure 1.2 SEM images of natural surfaces and their biomimetic counterparts. ....	10
Figure 1.3 Schematic of the (a) Gram-positive and (b) Gram-negative bacterial cell wall. ....	14
Figure 1.4 Creep deformation profile that shows the changes of force and deformation as a function of time for a viscoelastic material. ....	15
Figure 1.5 Viscoelastic deformation experiment. ....	18
Figure 1.6 Schematic to illustrate the differences between classical (DLVO) and extended DLVO (XDLVO) theory. ....	21
Figure 1.7 Schematic of the adsorbed bacterial outer layer with the two regions A and B. ....	24
Figure 1.8 Schematic of a bacterial cell that is completely adhered to the bottom of a nanopillared surface. ....	26
Figure 1.9 Results from the puncturing experiment on <i>S. typhimurium</i> using AFM. ....	28
Figure 1.10 Differences between laboratory and industrial protocol for anodisation. ....	33
Figure 1.11 Kinetics of porous oxide growth in a potentiostatic cell at 70 V in 0.3 M oxalic acid at 5°C. The ....	34
Figure 3.1 Electropolish profile for aluminium substrate. ....	60
Figure 3.2 Comparison between as received and electropolished aluminium sheet. ....	61
Figure 3.3 Applied potential and the resulting interpore distance for 0.3 M oxalic acid at 4.5°C in open cell setup. ....	62
Figure 3.4. Comparison between 0.3M oxalic acid and 0.4M phosphoric acid for anodisation	63
Figure 3.5 Effects of temperature on anodisation. ....	64
Figure 3.6 Effects of low stirring speed on anodisation. ....	65
Figure 3.7 SEM images of AAO produced using different first-step anodisation times ....	66
Figure 3.8 Humidity problem during long anodisation process in a beaker ....	67
Figure 3.9 Standard curve for 0.1 M phosphoric acid aluminium oxide etching at 100 rpm with 2 cm stirrer and temperature of 30°C. ....	69
Figure 3.10 Phase diagram proposed by Li. <i>et al</i> ....	71
Figure 3.11 Linear Venn diagram of the three test surfaces to show the comparison between each surface ....	72
Figure 3.12 SEM images of the master stamps used in this experiment. ....	73
Figure 3.13 Pressure and temperature profile for hot-embossing ....	74
Figure 3.14 Incomplete protrusion of PMMA during hot-emboss. ....	76

Figure 3.15 Molecular structures of (a) PMMA, (b) PET, and (c) PEEK .....	79
Figure 3.16 SEM image analysis .....	81
Figure 3.17 Storage modulus for semi-crystallised PEEK film and PET film .....	82
Figure 3.18 Contact angle of as received, cleaned and electropolished aluminium substrate, and of AAO substrate before (striped) and after (filled) silanisation step.....	85
Figure 3.19 Schematic of the silanisation process using DCDMS to coat the AAO stamp with an anti-stick coating.....	86
Figure 3.20 Top view SEM image of PET nanopillared surfaces fabricated using the same anodisation stamp.....	88
Figure 3.21 SEM images of the PET nanopillared surfaces used in this project .....	90
Figure 3.22 Representative AFM images of the nanopillared surfaces .....	91
Figure 3.23 Relationship between height, roughness and surface wetting .....	96
Figure 3.24 Correlation between surface topographies and surface energy .....	97
Figure 3.25 XPS analysis of as received and hot embossed PET substrate.....	98
Figure 4.1 Comparison between 0 V shear traces and 2 V shear traces.....	104
Figure 4.2 Fast Fourier transform (FFT) of the shear traces (from Figure 4.1) at a load force, $f_L$ , of 170 nN.....	105
Figure 4.3 Friction force, $f_f$ against load force, $f_L$ plots. ....	106
Figure 4.4 Representative force vs. distance curves for control and nanopillared surfaces. ...	108
Figure 4.5 Raw shear trace (grey line) and baseline corrected trace (black line) for SDN surface with sliding velocity, $v = 10 \mu\text{m s}^{-1}$ at load force 20 nN.....	110
Figure 4.6 The standard deviation of the shear signal plotted against applied load force for flat PET, SDN, BDN and BWN surfaces .....	110
Figure 4.7 Relationship between pull-off force ( $f_p$ ) of the nanostructured surfaces and surface properties.....	113
Figure 4.8 Interpreting the force vs. separation curves.....	117
Figure 4.9 Geometric assumption of the intrinsic contact between the colloidal particle and periodic nanopillars based on the pull-off force data.....	118
Figure 4.10 Probe interaction with the nanostructured surfaces.....	120
Figure 4.11 Young's modulus of a nanopillar as a function of the diameter, $DT$ .....	121
Figure 4.12 Nanoscale water bridges form on individual nanopillars. ....	122
Figure 4.13 Correlation between friction coefficient and vertical geometry of the surface. ...	125
Figure 4.14 Correlation between SSAC and surface properties of nanopillared surfaces.....	127



Figure 5.1 Potential mechanism of bacterial attachment to a nanopillared surface using its surface proteins. The driving force for adhesion is likely to be due to higher total interaction forces between the bacterial surface proteins and the nanopillared surface.....	129
Figure 5.2 Quantitation of viable and compromised bacteria on nanostructured surfaces. ...	131
Figure 5.3 Representative fluorescence micrographs of bacteria on the test surfaces. ....	132
Figure 5.4 Quantitation of bacterial vitality on nanostructured surfaces using Bactiter-Glo™. ....	134
Figure 5.5 Quantitation of <i>E. coli</i> adhesion following a time-course of trypsin treatment. ....	137
Figure 5.6 Hydrophobicity of non-treated (blue) and trypsinised <i>E. coli</i> (red) .....	138
Figure 5.7 Zeta potential distribution for untreated (red line) and trypsinised <i>E. coli</i> (green line) in PBS buffer at pH 7.4. ....	139
Figure 5.8 Effects of trypsinisation on <i>E. coli</i> attachment on flat control and SDN surfaces. ..	140
Figure 5.9 Representative SEM images of <i>E. coli</i> ± trypsinisation on flat or SDN surfaces.....	141
Figure 5.10 High tilted angle SEM images of <i>E. coli</i> bound to flat or SDN surfaces.....	143
Figure 5.11 SEM image of fully adsorbed <i>E. coli</i> cell on the SDN surface. <i>E. coli</i> cells were incubated for 3 hours on the SDN surface at 37°C. ....	144
Figure 5.12 Potential bacterial evasion of nanopillar contact. ....	145
Figure 5.13 FIB-SEM cross-section of an <i>E. coli</i> cell adhered to the SDN surface after a 3 hour incubation. ....	146
Figure 5.14 Underside cell wall deformation of adhered bacterial cells. ....	147
Figure 5.15 3D reconstruction of <i>E. coli</i> adhered to the SDN surface. ....	149
Figure 5.16 FIB-SEM analysis on an <i>E. coli</i> cell on the SDN surface. ....	150
Figure 5.17 FIB-SEM analysis on <i>S. aureus</i> cells bound to the SDN surface. ....	152
Figure 5.18 3D volume rendering of <i>S. aureus</i> cells bound to the SDN surface using Blender 2.8. ....	153
Figure 5.19 Comparison of bacterial attachment to a flat or nanostructured surface and its effects on the cell wall. ....	158
Figure 5.20 Deformation of the suspended cell wall of an adhered bacterium. ....	160
Figure 5.21 Predicted effects of trypsinisation on <i>E. coli</i> surface proteins.....	161
Figure 5.22 Vertical or polar attachment of bacterial cells to a surface.....	163
Figure 5.23 Volume shrinkage estimation. ....	164
Figure 5.24 Correlation between nanotopography tip diameter $D_T$ , interpillar distance $D_P$ , and roughness $R_q$ , and the antibacterial effects of the surface.....	166

Figure 5.25 Correlation between the surface energy $\gamma^{\text{TOT}}$ , work of adhesion $W_{\text{adh}}$ and pull-off force $f_p$ of a nanopillared surface and its antibacterial effects.....	167
Figure 5.26 Correlation between the friction coefficient $\mu$ , stick-slip amplitude coefficient SSAC, intrinsic pressure exerted on a nanopillar $\rho$ , and Young's modulus of a single pillar of a nanopillared surface, $E'$ and its antibacterial properties.....	170
Figure 5.27 Performance profile of the nanopillared surfaces. ....	171

# LIST OF TABLES

Table 1.1 Percentage of microorganisms isolated from BAIs .....	2
Table 1.2 Incidence of BAIs in the US and associated mortality .....	3
Table 1.3 Natural contact killing surfaces and their known effects.....	12
Table 1.4 List of Young's modulus values for Gram-negative and Gram-positive bacteria .....	17
Table 1.5 Viscoelastic parameters of different bacterial species determined using AFM-based creep deformation experiments .....	19
Table 1.6 Nanolithography techniques and their applications .....	29
Table 2.1 Information on the polymer substrate used in this study. ....	40
Table 2.2 Bacterial strains used in this study.....	42
Table 3.1 Electrolyte mixtures for electropolishing of aluminium that were tested during the optimisation phase.....	60
Table 3.2 Anodising conditions used to fabricate the master stamp in 0.3 M oxalic acid solution at 4.5°C.....	73
Table 3.3 List of sub-1000 nm polymeric nanostructured surfaces fabricated using imprinting technique .....	78
Table 3.4 Systematic study of temperature and pressure effects on nanopillar height for PET hot embossed on 70 V anodisation stamp.....	80
Table 3.5 Hot-embossing parameters for PET, PMMA and PEEK .....	81
Table 3.6 Rate of producing 15 PET nanopillared surfaces using two different processing technique .....	84
Table 3.7 Zeta potential of as received PET substrate and hot embossed PET substrate in PBS buffer (pH 7.4).....	86
Table 3.8 Measured base diameter $D_B$ , tip width $D_T$ , interpillar distance/pitch $D_P$ , height $h$ , aspect ratio $A_R$ and RMS ( $R_q$ ) of nanopillared PET substrates and the flat control.....	92
Table 3.9 Liquid surface tension ( $\gamma_L$ ), apolar component $\gamma_L$ , polar component $\gamma_{LAB}$ , electron acceptor $\gamma_L +$ , and electron donor $\gamma_L -$ of water, diiodomethane, and ethylene glycol.....	93
Table 3.10 Contact angle $\theta$ , surface energy components $\gamma_L$ , and work of adhesion $W_{adh}$ , of the flat, BWN, BDN and SDN surfaces.....	94
Table 3.11 Contact angle, Wenzel and Cassie-Baxter effective contact angle, solid fraction, and roughness factor for BWN, BDN and SDN.....	95
Table 4.1 Adhesion and friction properties of the flat and PET nanopillared surfaces. ....	107
Table 4.2 Calculated interactions between the colloidal probe and surfaces.....	120

Table 5.1 Young's modulus of the top side of <i>E. coli</i> cells when adhered to flat control or nanostructured surfaces. ....	136
Table 5.2 DLS data for untreated or trypsinised <i>E. coli</i> in PBS buffer (pH 7.4). ....	139

# LIST OF EQUATIONS

Equation 1.1: XDLVO equation.....	22
Equation 1.2: Pogodin’s bactericidal model .....	23
Equation 1.3: Effective interaction parameter of bacterial cell wall formula .....	23
Equation 1.4: Sum of stretching energy of the bacterial cell wall .....	25
Equation 2.1: Relative hydrophobicity value .....	44
Equation 2.2: Conversion of SEM greyscale value to metric unit .....	46
Equation 2.3: SEM unit rescaling conversion factor .....	46
Equation 2.4: AFM vertical signal relationship with the photodetector quadrants .....	51
Equation 2.5: Relationship between cantilever deflection, compliance region and piezo movement.....	51
Equation 2.6: AFM horizontal signal relationship with the photodetector quadrants.....	51
Equation 2.7: AFM stage tilt angle equation.....	52
Equation 2.8: AFM horizontal deflection sensitivity equation.....	52
Equation 2.9: Lorentzian function.....	53
Equation 2.10: Normal spring constant equation.....	53
Equation 2.11: Torsional spring constant equation using hybrid model .....	54
Equation 2.12: Converting cantilevers deflection signal to force value .....	54
Equation 2.13: Converting shear signal data to friction force .....	57
Equation 3.1: Interpore distance general formula.....	61
Equation 3.2: Best fit line of the standard curve for AAO etching in $H_3PO_4$ .....	69
Equation 3.3: Roughness factor formula .....	89
Equation 3.4: Young’s equation .....	92
Equation 3.5: Surface free energy equation .....	92
Equation 3.6: Debye-Keesom interaction equation.....	92
Equation 3.7: Total solid-liquid interfacial energy formula .....	93
Equation 3.8: Relationship between contact angle of pure liquid with known apolar and polar components .....	93
Equation 3.9: Wenzel contact angle equation .....	94
Equation 3.10: Cassie-Baxter contact angle equation .....	94
Equation 3.11: Solid fraction equation .....	94
Equation 4.1: Amonton’s Law .....	101
Equation 4.2: Relationship between friction force, finite friction force and load force.....	106

Equation 4.3: Hertzian model .....	114
Equation 4.4: Reduce modulus .....	114
Equation 4.5: JKR model .....	115
Equation 4.6: DMT model .....	115
Equation 4.7: JKR elastic deformation equation .....	115
Equation 4.8: Rearranging Equation 4.5 for $K$ .....	115
Equation 4.9: Rearranging Equation 4.7 for $K$ .....	116
Equation 4.10: $\alpha JKR$ in terms of $dJKR$ .....	116
Equation 4.11: Intrinsic contact radius $Ri$ equation .....	116
Equation 4.12: Total in contact nanopillars equation .....	117
Equation 4.13: Intrinsic force per pillars equation .....	117
Equation 4.14: Young's modulus of single nanopillar .....	117
Equation 5.1: General Young's modulus formula .....	135
Equation 5.2: Helmholtz-Smoluchowski equation .....	138
Equation 5.3: Pogodin's $\alpha B$ equation .....	159
Equation 5.4: Xue's $\alpha B$ equation .....	159
Equation 5.5: Li's $Sad$ equation .....	159
Equation A1: Volume of the cell .....	197

## LIST OF ABBREVIATIONS

Abbreviation	Explanation
AAO	Anodised aluminium oxide
AFM	Atomic force microscopy
ANOVA	Analysis of variance
AR	Aspect ratio
Arg	Arginine
BAIs	Biomaterial-associated infections
BDN	Blunt and dense nanopillars
BSE	Backscattered electrons
BTG	Bactiter-Glo
BWN	Blunt and wide nanopillars
CAGR	Compound annual growth rate
CFU	Colony forming units
CNTs	Carbon nanotubes
CP-AFM	Colloidal probe AFM
CVD	Chemical vapor deposition
DCDMS	Dimethyldichlorosilane
DHM	Digital holographic microscopy
DLS	Dynamic light scattering
DLVO	Derjaguin, Landau, Verwey, and Overbeek
DMT	Derjaguin, Muller, and Toporov
DSA	Drop shape analyser
EBL	Electron beam lithography
EHD	Electrohydrodynamic
EUVL	Extreme ultraviolet lithography
FE-SEM	Field emission SEM
FFT	Fast Fourier transform
FIB SEM	Focus ion beam SEM
GS	Grayscale
HR-AFM	High resolution AFM
JKR	Johnson, Kendall and Roberts
LPS	Lipopolysaccharide
Lys	Lysine
MEMS	Microelectromechanical system
MH	Mueller-Hinton
NAM	N-acetyl muramic acid
NIL	Nanoimprint lithography
OM	Outer membrane
PEEK	Polyether ether ketone
PEG	Polyethylene glycol
PET	Polyethylene terephthalate
PI	Propidium iodide

PMMA	Polymethyl methacrylate
PS	Polystyrene
PTFE	Polytetrafluoroethylene
PVC	Polyvinyl chloride
QNM	Quantitative nanomechanical mapping
RF	Relative humidity
RLU	Relative luminescence signal
SDN	Sharp and dense nanopillars
SDN TRY	Trypsinised cells on sharp and dense nanopillars
SDN WT	Wild type cells on sharp and dense nanopillars
SEM	Scanning electron microscopy
SPL	Scanning probe lithography
SPM	Scanning probe microscope
SSAC	Stick slip amplitude coefficient
TCH	Thiocarbohydrazide
TRY E. coli	Trypsinised E. Coli
TSB	Tryptic soy broth
UTIs	Urinary tract infections
WT E. coli	Wild type E. Coli
XDLVO	Extended DLVO
XPS	X-ray photoelectron spectroscopy
YM	Young's modulus



# CHAPTER 1 INTRODUCTION

## 1.1 Biomaterial-associated infections (BAIs)

Biomaterials and medical device industries have seen rapid development in the past decades and are expected to continue to grow in the future due to increasing clinical demands and advances in materials science and nanotechnology. The compound annual growth rate (CAGR) of biomaterials and medical devices is expected to rise to 15% in the late 21<sup>st</sup> century [1]. Global market sales for biomaterials and medical devices amounted to approximately USD 1.2 billion in 2015 and are expected to maintain a 10% annual growth for the next few decades. Global market sales are predicted to reach a staggering USD 400 billion in 2020 [1]. Of the biomaterials on the market, the most widely used are polymer-based biomaterials, with an estimated annual consumption of more than 8000 kilotons to fabricate syringes, catheters, drug and blood storage packaging, transfusion consumables and orthopaedic devices [2].

Medical devices are some of mankind's most important inventions that have greatly contributed to improving the quality of patient care. This includes their use for less-invasive patient monitoring and improvement of medicine administration and, in some applications, medical devices can be used to restore biological function [3]. However, the introduction of synthetic materials like catheters, orthopaedic implants, infusion lines, and sutures into the human body may trigger a foreign body response. Often, foreign body response mechanisms result in device fouling, which will limit the clinical lifetime of the implanted device. Another problem associated with medical devices is the risk of developing a biomaterials-associated infection (BAI) after implantation. Currently, the occurrence of a bacterial infection associated with growth of a biofilm on the implant depends on the type of devices which for example can be up to 50% for heart assist devices (Table 1.2) [4]. Once infection has been established, biofilm formation on the medical device will result in failure and the most effective way to remove the biofilm is by removing and replacing the device through often costly and invasive procedures, accompanied by the extensive use of antibiotics. Due to the importance of medical devices, novel approaches to combat BAIs require urgent attention [3].

A BAI is defined as an infection that occurs on a device that is synthesised from a biocompatible material [5]. Different microorganisms have been associated with BAIs, with *Staphylococcus epidermidis* being the most frequently isolated species overall and *Escherichia coli* being the most prevalent Gram-negative isolate (Table 1.1). There are approximately 1 million BAIs per

year in the USA alone and, since 2001, for every 2.6 million orthopaedic implants placed, 4.3% became infected [6]. BAIs result from interactions between microbial cells, the medical device and host factors. Of these, microbial cells have the most influence on the pathogenesis of the BAI, while device factors are the most versatile and offer the potential to be modified so as to prevent infections. Table 1.2 highlights the total number of first-time medical devices inserted per year in the US and illustrates the differences in the impact of infections according to type of medical device. Of note, the rate of infection after first-time insertion is often found to be higher upon subsequent reinsertion. For example, the rate of infection for first-time insertion of a penile implant is approximately 1-3% but can reach as high as 18% after reimplantation [7]. In addition to infection, microbial contamination of a medical device can also adversely affect its function. With increasing demand for polymer-based biocompatible devices, a growing ageing population and rising antimicrobial resistance that is hindering effective treatment of BAIs, the need for the development of novel antibacterial biomaterials is essential.

Table 1.1 Percentage of microorganisms isolated from BAIs

Microorganism	Percentage isolated from biomaterials*
<i>Staphylococcus epidermidis</i>	40-75%
<i>Staphylococcus aureus</i>	10-20%
Yeasts	5-10%
Enterococci/streptococci	2-5%
Gram-negative species	2-5%
Other	1-3%

\*Reproduced from [6].

Table 1.2 Incidence of BAIs in the US and associated mortality

Device	Estimated # inserted in the US per year	Rate of infection (%)	Attributable mortality
Bladder catheters	> 30,000,000	10-30	Low
Central venous catheters	5,000,000	3-8	Moderate
Fracture fixation devices	2,000,000	5-10	Low
Dental implants	1,000,000	5-10	Low
Joint prostheses	600,000	1-3	Low
Vascular grafts	450,000	1-5	Moderate
Cardiac pacemakers	300,000	1-7	Moderate
Mammary implants, in pairs	130,000	1-2	Low
Mechanical heart valves	85,000	1-3	High
Penile implants	15,000	1-3	Low
Heart assist devices	700	25-50	High

Reproduced from [4].

### 1.1.1 Current preventive measures

Strategies employed to prevent infection of medical devices originally relied upon use of aseptic techniques, control of environment sterility and perioperative antibiotic prophylaxis. More recently, several promising anti-infective biomaterials designed to combat BAIs have also been developed and introduced. These include nitric oxide-releasing surfaces, photoactive TiO<sub>2</sub> coatings, emerging biosurfactants, new antimicrobial biopharmaceutical agents and the use of novel polymer brushes to reduce bacterial adhesion [5]. The goal of all such current preventive measures is to inhibit bacterial biofilm formation on the surface of the medical device, thus prolonging its clinical lifetime.

#### 1.1.1.1 Surface treatments/coatings

The basic strategy when developing antimicrobial surfaces for medical devices is to exploit surface coatings or treatments that will reduce microbial adhesion (Figure 1.1). This comes from the hypothesis that no biofilm formation can occur if the bacteria cannot initially adhere to the surface. The first attempts based on this approach focused on manipulating surface wetting of the biomaterial, making it hydrophilic to increase hydration, reduce protein adsorption and limit deposition of a conditioning film that could otherwise promote bacterial colonisation [8]. This strategy came from the observation that hydrophobic materials such as most silicone-based

devices exhibited increased bacterial adhesion compared to hydrophilic materials. More sophisticated coating approaches were then utilised by altering the device surface physicochemical properties such as steric hindrance, hydration, conformation and topographies. This could be achieved through polymer coatings with surface chemistry alterations. Despite some successful evidence from in vitro microbial assays, these coating approaches often failed when tested in animal studies. These failures suggested that device coating alone is insufficient as the sole strategy to combat BAIs [5].

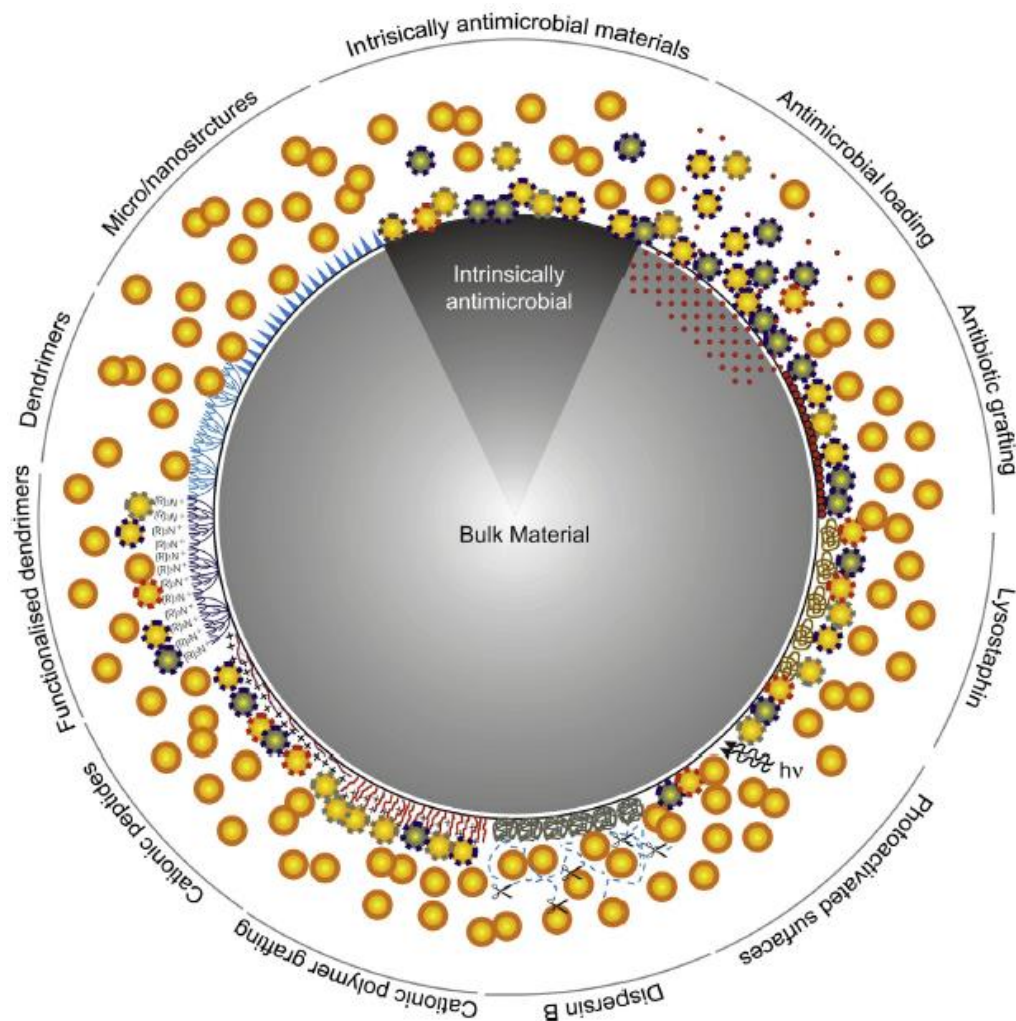


Figure 1.1 Overview of current surface designs to combat BAIs. The orange spheres with solid outline represents healthy bacteria while orange spheres with dashed outline represents susceptible bacteria. Taken from [8].

#### 1.1.1.2 Anti-infective silver release coatings

Silver has been one of the most commonly used antimicrobial agents in the past decades due to its promising antimicrobial activity. It has found use in a wide range of applications and has been given generally regarded as safe (GRAS) status at prescribed concentrations. One advantage of silver over most antibiotics is that silver exhibits broad spectrum antimicrobial activity, including against pathogens such as *Pseudomonas aeruginosa*, *E. coli*, *S. aureus*, and *S. epidermidis*, while many antibiotics show limited efficacy against certain strains [9]. The antibacterial properties of silver have been known for centuries and it has been incorporated into various medical devices such as catheters, endotracheal tubes, prosthetic heart valves and many other devices. The mechanics of silver's antimicrobial activity lies in the ionic form of silver,  $\text{Ag}^+$ , instead of the elemental metallic form [9].  $\text{Ag}^+$  is proposed to bind to DNA and key thiol groups in proteins, which then disturb bacterial cell membrane functions, blocking cell replication and disrupting some crucial metabolic proteins and enzymes, ultimately leading to cell lysis.  $\text{Ag}^+$  also displaces other metal ions like zinc and calcium, which are essential for cell survival [5].

Silver is usually employed as a coating agent in its metallic form on devices, being impregnated into the device matrix as particulates, silver salts, complexes or chelates, or as active ingredients for topical usage to control silver ion release. Nanosilver is another form of silver (other than metallic and ions) with unique physical properties due to its high surface area, surface oxidation state and ionic solubility. Nanosilver has been used to minimise BAIs on medical devices [10], and current applications include incorporation of nanosilver into microporous hydroxyapatites, calcium phosphate coating, silver oxide embedded in glasses, oxidised silver in polyamide coatings and many others [5].

#### 1.1.1.3 Drug release surfaces

Perhaps the most straightforward approach to control BAIs is to improve the efficacy of conventional antibiotics by carefully delivering the drugs in a controlled manner through coatings or impregnation. Indeed, current clinically approved methods for bioactive surfaces that utilise antibiotics are either drug impregnation or drug release coatings [5]. The advantages of delivering antibiotics in situ are that high dosage can be applied without the concern of toxicity of the drug. This, in theory, should improve antibiotic efficacy at the implant site and allow for tailored selection of antibiotics towards specific pathogens associated with the implant. Such design enables continuous antibiotic administration and potentially avoids promoting resistance [9]. However, the effectiveness of any antibiotic-releasing mechanism is

dependent on the rate of drug release, which is dependent on the matrix that the drug is being loaded or doped into. Antibiotics like vancomycin, tobramycin, cefamandole, amoxilin and gentamicin have been proposed to work in systems consisting of polyurethane, biodegradable polymers or carbonated hydroxyapatite.

Biocompatible polymer coatings like polyurethane, silicone rubber, and polyhydroxyalkanoates have been previously explored as active release matrix systems for local antibiotic delivery strategies. There is strong correlation between chemical similarity of the drug and the polymer matrix with the drug release rate and effectiveness. For example, when both polymer and antibiotics are lipophilic, drug distribution within the matrix is homogeneous. Such homogeneity is important to ensure effective antibiotic release. When a hydrophilic drug was coated with hydrophobic polymers, there was an initial spike of release followed by a lower level of release over extended periods. Conversely, there was no significant spike of release when both antibiotic and polymer were hydrophobic [9].

There is a system that has been shown to allow an initial burst of drugs followed by a period of sustained release. A gentamicin-PLGA combination was found to deliver a high initial dose that could protect against bacterial adhesion a few hours post implantation, and provided further protection at a lower dose that allowed integration between the device and the surrounding tissue [9]. A similar release profile has also been reported with a carbonated hydroxyapatite system using acidic (amoxicillin, cefamandole, carbenicillin, and cephalothin) and basic (vancomycin, gentamicin, and tobramycin) antibiotics [11,12]. However, issues with polymer-antibiotic chemical compatibility were found with this system, although the acidic antibiotics were found to be more effective due to the calcium-chelating properties of the carboxylate groups of carbonated hydroxyapatites.

In general, despite some promising advances with antibiotic-based polymer coatings, issues with antibiotic-host matrix compatibility has meant that this approach has been so far quite challenging. Moreover, a major limitation of this antibiotic-releasing approach is that it is transient, because leaching of antibiotics is subject to depletion over time. This is a major concern as a dwindling antibiotic concentration may inadvertently promote development and spread of antimicrobial resistance.

### *1.1.2 Antimicrobial resistance and BAI*

Antimicrobial resistance is defined as a natural process via which microbes develop resistance towards an antimicrobial agent(s), making it ineffective. Bacteria may develop resistance due to

selection pressure on the bacterial population arising from exposure to antimicrobials when used as therapeutics. This can particularly occur when the bacteria are part of a biofilm, which can afford protection to at least some of the constituent bacteria, allowing them to develop resistance, survive and proliferate. The genetic changes carried by these resistant bacteria will then be passed on to subsequent generations, meaning that the therapeutics will become less effective over time, if not completely useless [13].

Patient behaviour is believed to be the most common reason for allowing bacteria to encounter antimicrobials at a sub-therapeutic level. Most patients have reported stopping the use of antibiotics when they have recovered, rather than completing the prescribed course, which can allow pathogens to develop drug-resistant mutations [13]. Recently, poor quality medicines have emerged as another source of sub-optimal dose therapeutics for patients, especially in low- and middle-income countries. Such medicines are a form of counterfeit medical product that are deliberately mislabelled, and often do not have the correct amount of active ingredients, have degraded with time, or are poorly formulated so that the ingredients do not reach the blood stream [13].

Antimicrobial resistance is associated with medical devices in two ways. First, a recent report has suggested that an increasing number of microbial strains, particularly staphylococci, streptococci, and pseudomonads, that are associated with BAIs exhibit antimicrobial resistance. Currently, close to 60% of BAIs are caused by resistant microbes. This could be due to (a) excessive administration of the antimicrobial agent during the early days of implantation to combat bacterial infection and (b) the increasing volume of medical devices used each year [5]. Secondly, the regulations that allow medical devices containing antibiotics need urgent revision. The draft guidance document from the FDA in 2007 stated that they are aware of the emergence of antimicrobial resistance but believe that “the potential clinical benefit of the use of the antimicrobial agent, including its use on a medical device, should outweigh the associated risk” [14]. Currently, according to the guidance, any company that can demonstrate the benefit of using an antimicrobial may be able to get approval from the FDA. Clearly, with recent reports on the emergence of multiple superbugs - strains of bacteria that are resistant to more than one type of antibiotic - the FDA needs to update their industrial guidance to reduce the risk of generating more multidrug-resistant bacteria.

## 1.2 Natural and biomimetic antibacterial surfaces

Nature's mode of action for tackling bacterial infections is based on a rather simplistic yet effective approach. A thin layer of superhydrophobic material and some form of topography has proven to be a reliable strategy to combat bacterial colonisation, without any risk of promoting antimicrobial resistance. An antibacterial surface is defined as a surface that can repel or resist the adhesion of bacteria through a) inhibiting the attachment of bacteria, which is known as an antifouling surface, or (b) by killing the adhering bacteria, which is known as a bactericidal surface. In nature, different organisms have adopted different strategies to reduce bacterial attachment on their surface/skin. Aquatic organisms like shark, dolphin, phyla and lotus plant are known to have superhydrophobic surfaces that can repel bacteria. On the contrary, some insects have bactericidal surfaces, mostly on their wings, which consist of sharp nanospikes that kill incoming bacteria to keep their wings clean.

### 1.2.1 Antibiofouling surfaces

From an evolutionary perspective, it is important for aquatic organisms to develop antifouling properties as seen in gorgonian coral, shells and marine animals, since water is a universal solvent that could affect the properties of the material if exposed over a period of time. Most marine organisms are equipped with an antifouling surface that comprises some form of microtopography, secreted bioactive molecules, specialised mucus secretion or sloughing surface layers. Such adaptations are important for marine animals, where movement under water depends on the flowing of fluid over a solid surface. A fouling surface would inevitably increase drag (resistance), which would reduce the efficiency of marine animals while predating a food source or escaping predators [15].

Many marine mammals have evolved surface topographies on their skin to reduce liquid drag and to increase flow while navigating through the ocean. Elasmobranch fishes like sharks, skates and rays have a skin that is covered by placoid scales or dermal denticles, where each denticle is shaped like a diamond with a longitudinal rib pattern. Shark skin has been studied extensively and shown to exhibit antifouling properties against ectoparasites and settlement of *Ulva* spores, while reducing hydrodynamic drag by 44–50%. In 2006, Carman *et al.* presented the first Sharklet AF™ surface, which was inspired by the shark skin topography [16]. The Sharklet AF™ features microtopography of riblets of 2 µm in diameter, 3 µm in height and spacing of 2 µm, with the riblets organised in a diamond arrangement across the surface. This bioinspired surface has been shown to be effective at reducing the attachment of *Ulva*, *Chattonella marina*, diatoms



like *Navicula incerta* and *Seminavis robusta* and cyprids of *Balanus amphitrite*. Mathematical modelling of the Sharklet AF™ surface demonstrated that the surface energy of adhesion was a critical factor to reduce fouling [16].

In a study involving four different phyla species, it was found that the microtopography on the surface of the organisms showed significant antifouling properties (Figure 1.2). The surface of edible crab, *Cancer pagurus*, is covered with 200  $\mu\text{m}$  circular elevations with smaller 2-2.5  $\mu\text{m}$  microspikes in between the elevations. Blue mussel, *Mytilus edulis*, has 1-1.5  $\mu\text{m}$  wide ridges, while the egg case of a dogfish, *Scyliorhinus canicular*, has an anisotropic distribution of ridges that range from 5-115  $\mu\text{m}$ . Brittle star, *Ophiura texturata*, has a well-defined knobbed surface structure with a diameter of 10  $\mu\text{m}$  [17]. The topography of these surfaces was replicated on Devcon® epoxy and the antifouling properties were assessed extensively over a 3-4 week incubation period. All of the surfaces showed significant reductions in macro- and micro-fouling compared to a smooth control surface [18]. In another study, four different replicas of mytilid species with topography of repeating microridges were shown to exhibit reduced antifouling properties when the surface was treated so as to alter the surface chemistry. This study suggested that the antifouling properties found on some marine animals required a synergistic approach (i.e. topography combined with surface chemistry) to achieve the high anti-biofouling properties [18].

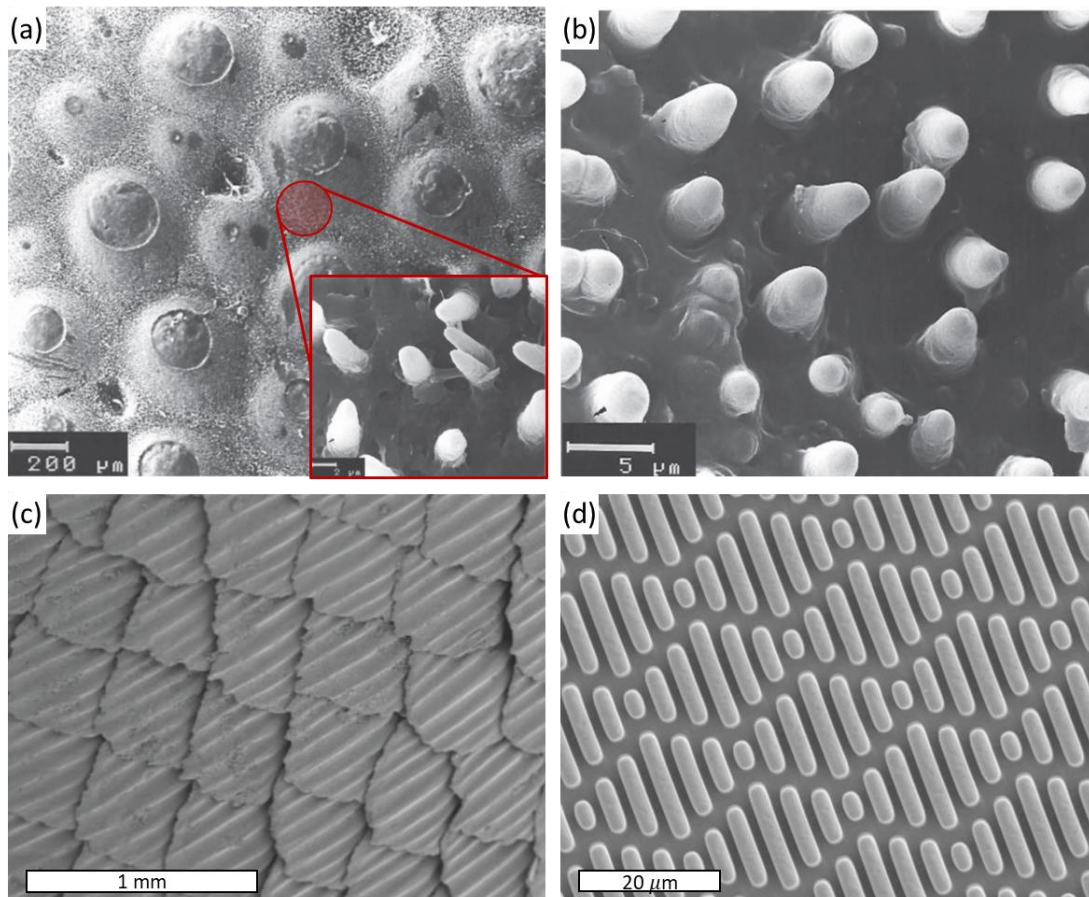


Figure 1.2 SEM images of natural surfaces and their biomimetic counterparts. *C. pagurus* topography, showing circular elevations and microspikes in between the elevations (inset)[18]; (b) replica of the *C. pagurus* topography on a Devcon® resin [18]; (c) topography found on spinner shark, *Carcharhinus brevipinna* sp. [16]; and (d) the Sharklet™ topography [16].

### 1.2.2 Contact killing surfaces

The first known protruded nanomaterial is the carbon nanotube (CNT), which was discovered by Japanese scientist Sumio Iijima in 1991 [19]. From then on, the development of nanoimprint technology [20] in 1996 has helped researchers to fabricate protruded nanostructured surfaces like nanopillars on thermoplastic materials, while advancement in novel lithographic processing has enabled the generation of structures like nanotubes, nanowires, nanospikes and nanoneedles on materials like titanium, aluminium, copper, silicon and others. Early applications for protruding nanostructured surfaces were mainly for self-cleaning surfaces due to their interesting wetting properties, as observed in the equivalent natural nanostructured surfaces. It was not until 2012 that the susceptibility of bacteria to the nanostructured surfaces was discovered, when Ivanova *et al.* reported that *P. aeruginosa* could be killed using nanopillars

found on the cicada wing surface via a purely physical means [21]. This discovery was important as it gave researchers another perspective on the study of bacterial interactions with substrata, especially with a nanostructured surface. Previous studies on bacterial interactions with a surface had predominantly focused on general adhesion mechanisms between bacteria and a flat surface with different materials or topography, and on how the bacteria responded to a surface with a polymer brush or nano-features. This new discovery with cicada wings indicated that the mechanics of adhesion between bacterial cells and the nanotopography were more complex, and offered the potential to be exploited for the development of novel antibacterial surfaces.

There are several surfaces found in nature that have since been tested as a bactericidal surface and have shown promising results. Most of these bactericidal surfaces have been found on insect wings, and the topographies are nanoscopic, with nanopillars or nanospikes ranging in diameter from 500 nm to less than 50 nm (Table 1.3). Cicada and dragonfly wings have been studied extensively compared to other insects, and have shown promising results against Gram-negative bacteria like *E. coli*, *P. aeruginosa*, *Branhamella catarrhalis*, and *Pseudomonas fluorescens*, as well as against Gram-positive bacteria like *Bacillus subtilis*, and *Staphylococcus aureus* (Table 1.3). Recently, it was found that the surface of a biomimetic moth eye, which consisted of 200 nm tall nanopillars (almost identical to cicada wings), had promising killing effects against *S. aureus* and *E. coli*. The presence of polyethylene glycol (PEG) derivatives found on the moth eye film were speculated to work synergistically with the nanotopography, helping to inactivate *S. aureus* which was otherwise known to be resistant to the effects of the same nanotopography on the cicada wing [22].

Table 1.3 Natural contact killing surfaces and their known effects

Type of insect	Species	Wettability	Bactericidal activity	Reference
Cicada	<i>Psaltoda claripennis</i>	Hydrophobic	<i>B. catarrhalis</i> , <i>E. coli</i> , <i>P. aeruginosa</i> , <i>P. fluorescens</i>	[21]
Cicada	<i>Megapomponia intermedia</i>	Hydrophobic	<i>P. fluorescens</i>	[23]
Cicada	<i>Cryptotympana aguilula</i>	Hydrophobic	<i>P. fluorescens</i>	[23]
Cicada	<i>Ayuthia spectabile</i>	Hydrophobic	<i>P. fluorescens</i>	[23]
Dragon fly	<i>Orthetrum villosovitatum</i>	Superhydrophobic	<i>E. coli</i>	[24]
Dragon fly	<i>Diplacodes bipunctata</i>	Superhydrophobic	<i>B. subtilis</i> , <i>P. aeruginosa</i> , <i>S. aureus</i>	[25]
Dragon fly	<i>Hemiana Papuensis</i>	Superhydrophobic	<i>B. subtilis</i> , <i>P. aeruginosa</i> , <i>S. aureus</i>	[25]
Dragon fly	<i>Austroaeschna Multipunctata</i>	Superhydrophobic	<i>B. subtilis</i> , <i>P. aeruginosa</i> , <i>S. aureus</i>	[25]

### 1.3 Structure and mechanical properties of the bacterial cell wall

The current hypothesis for the bactericidal mechanism of nanostructured surfaces involves the deformation and subsequent tearing of the bacterial cell wall following contact with the nanotopography. The bacterial cell wall is a multi-layered structure that protects the microbe from osmotic pressure and mechanical damage by providing strength, rigidity and shape to the cell. This protective layer can bear turgor pressure of up to 25 atmosphere (atm) and so shield bacteria from mechanical stress and osmotic pressure in the environment [26]. The cell wall was found to be hydrated yet stiff and viscoelastic [27,28], and is the essential structural element in both Gram-negative and Gram-positive bacteria.

#### 1.3.1 Gram-negative vs. Gram-positive cell wall structure

In general, the cell walls of bacteria have two different interfaces with which they constantly interact: (a) the inside of the cell, where the environment is highly regulated by homeostatic biochemical processes, and (b) outside of the cell, where the chemical and physical nature of the environment is highly variable. The protective barrier of the cell wall also plays an important

role in the structural formation of the bacterial cell, regulating selective movement of materials in and out of the cell, as well as alerting the cell about the external environment. Bacteria can be classified into two distinct group based on their cell wall structure, components and functions: Gram-positive and Gram-negative (Figure 1.3).

The Gram-negative bacterial cell wall is composed of an outer membrane, an inner membrane, and a periplasmic space containing a thin peptidoglycan layer [29,30]. The Gram-positive bacterial cell wall lacks an outer membrane and instead has a more rigid outer peptidoglycan layer [29–31]. The peptidoglycan layer in Gram-positive bacteria ranges between 30 to 100 nm in thickness, which is about four to five times thicker than that of Gram-negative bacteria [31]. Beneath this peptidoglycan layer is then an inner membrane that is comparable to that of Gram-negative bacteria. The outer membrane of Gram-negative bacteria is further decorated with porin proteins and lipopolysaccharide, while additional major components of the Gram-positive cell wall are teichoic and lipoteichoic acids.

Peptidoglycan has a crystalline lattice structure comprising disaccharides, short peptides and peptide bridges. The disaccharide unit is connected to alternating *N*-acetyl glucosamine (NAG) and *N*-acetyl muramic acid (NAM), which are linked by  $\beta$ -1,4 glycosidic bonds and serve as the peptidoglycan backbone. Four amino acids (L-alanine, D-glutamine, L-lysine, and D-alanine) constitute the short tetrapeptide tail that is linked to the NAM molecule [27,32]. The peptide bridge formed between the neighbouring tails is known as the peptaglycine cross-link and serves to make a high strength mesh structure, which gives support to the cell membrane [33]. The mesh structure has uniform nanopores of ~2 nm and a thickness of 3 – 6 nm.

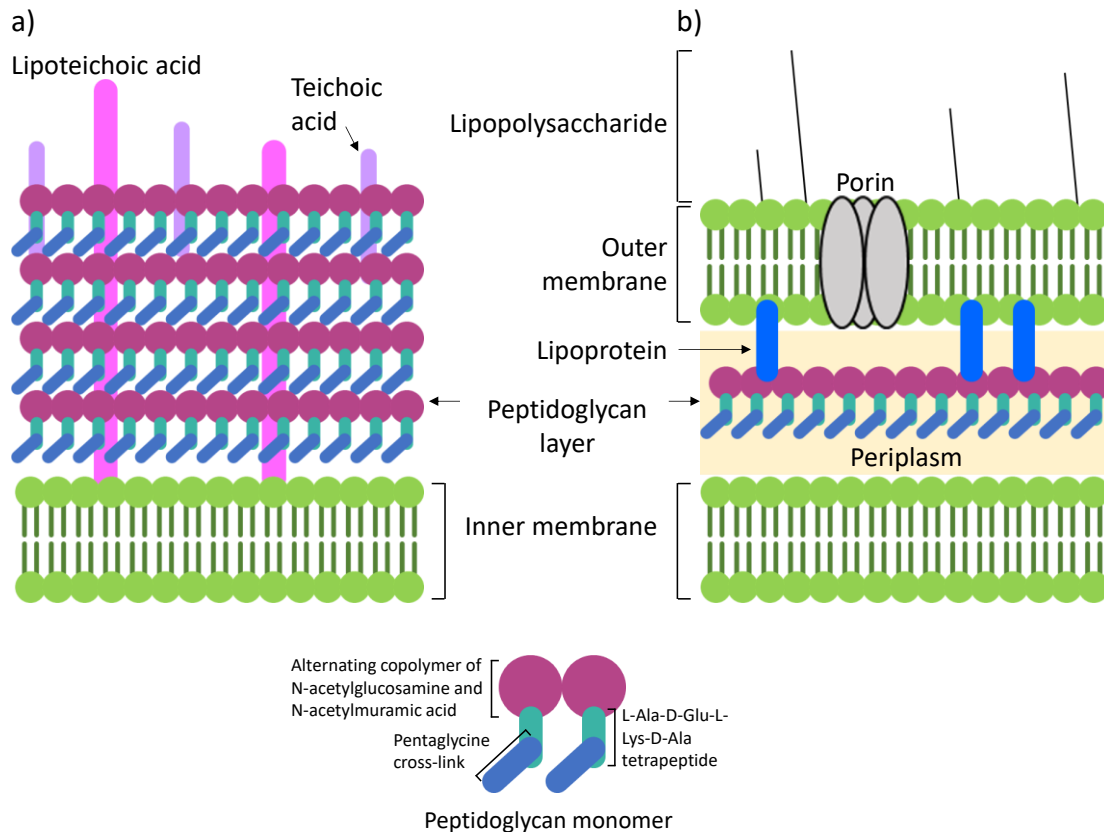


Figure 1.3 Schematic of the (a) Gram-positive and (b) Gram-negative bacterial cell wall. The major differences between the two cell walls are the thickness of the peptidoglycan layer, which is significantly thicker (30-100 nm) for Gram-positive compared to the Gram-negative (approximately 5 nm), and that the Gram-negative cell wall has an outer membrane. The pentaglycine cross-link only presents in Gram-positive bacteria.

### 1.3.2 Mechanical properties of the bacterial cell wall

A soft material like biological samples is made of both strong and relatively weak bonds, which allow the material to deform under external force that varies with time. Most biological material resists shear flow and strain linearly with time, while also stretching and deforming. This time-dependent response is known as viscoelasticity, and consists of instantaneous deformation due to the stretch of strong bonds and time-dependent deformation resulting from a flow of material (viscoelastic liquid) or deformation that approaches an asymptotic value (viscoelastic solid) [27]. Depending on the temperature and time, a viscoelastic material can behave as a viscous fluid, an elastic solid or a combination between these two properties. The time-dependent deformation of a viscoelastic solid material is referred to as creep (Figure 1.4). Creep deformation is often associated with changes in physical bonding interactions like van der Waals interactions, hydrogen bonding and entanglements.

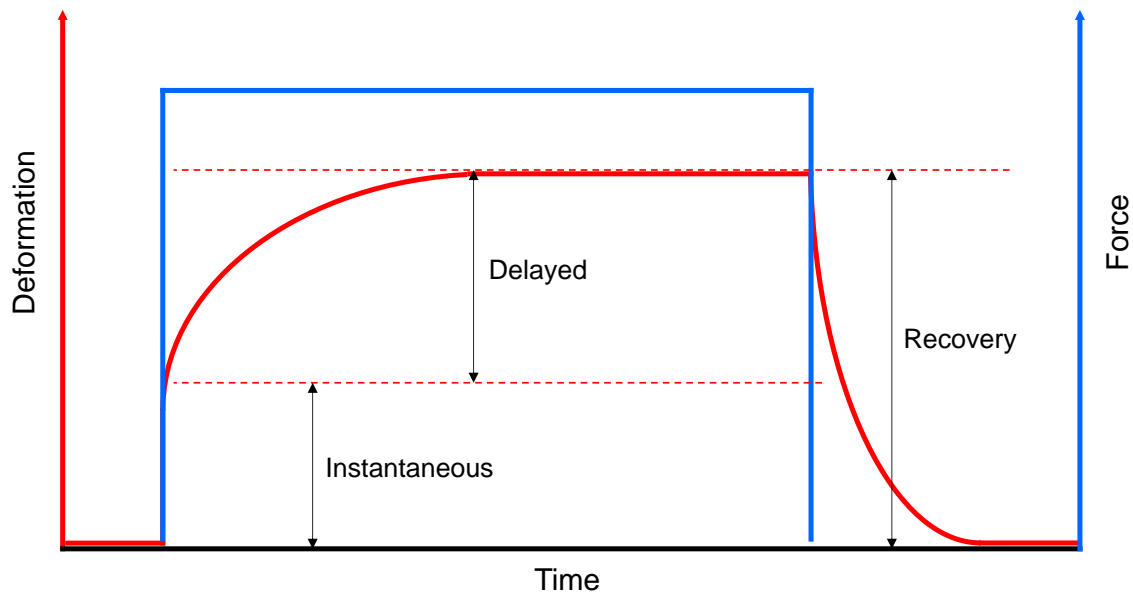


Figure 1.4 Creep deformation profile that shows the changes of force and deformation as a function of time for a viscoelastic material. The material experiences instantaneous elastic deformation when subjected to external force followed by time-dependent elastic deformation until it reaches the asymptote. When the applied force is removed, the material recovers to its original shape. Adapted from [27].

#### 1.3.2.1 Mechanical strength

The most important mechanical requirement of the bacterial cell wall is strength. This is essential to protect the cell membrane from the outside forces and to be able to withstand the turgor pressure inside the cell. Turgor pressure is a hydrostatic pressure that is maintained osmotically, which pushes the inner membrane against the cell wall. Turgor pressure is important to give and maintain the structure of the bacterial cell. The cell wall also has to endure the electrostatic repulsion generated between cell components during normal growth. There are no other cytoplasmic organelles that have similar mechanical strength and that could bear this turgor pressure or electrostatic repulsion [34].

#### 1.3.2.2 Young's modulus and turgor pressure

The cell wall was initially thought to be a rigid structure given that protocols to rupture the cells often require vigorous physical methods. Realisation of the flexibility of the cell wall started when it was found that many bacteria showed remarkable adaptability under various growth conditions including pH, ions and osmolarity. For example, Gram-positive *Bacillus megaterium* cells were found to contract by 26% in response to ionic and pH changes. Isolated cell walls of Gram-negative *E. coli* were found to be able to expand reversibly by up to 300% relative to their

relaxed state compared to an intact *E. coli* cell that could only decrease by 20% when the turgor pressure was removed [35,36].

The first indirect quantification of the mechanical properties of bacterial cells was proposed by Thwaites and Mendelson in 1985 [37]. They developed a novel approach to produce bacterial threads of *Bacillus subtilis* up to 1 m long and 100  $\mu\text{m}$  in diameter, the properties of which could then be measured using conventional textile techniques. Based on several assumptions, their model showed that as the salt concentration of the medium increased, the cell wall became more flexible, while changes in the pH did not show any significant alterations to the mechanical properties of the cell wall. At high relative humidity, the cell wall became weak and soft, resembling a rubber, while at low relative humidity, the cell wall behaved as a glassy polymer that is stiff, strong and brittle. Later, it was reported that the mechanical properties of the cell wall depend on the speed of the external force, which is a unique attribute of viscoelastic materials [35,36].

Measurement of the mechanical properties of a single cell was made possible by using the Atomic Force Microscope (AFM). Beveridge *et al.* pioneered a protocol to measure the mechanical properties of the bacterial surface using AFM imaging mode [35,36]. This was achieved by imaging the extracted bacterial membrane that was placed over a solid narrow groove. Multiple images of the membrane were taken at different imaging forces, which caused the membrane to creep into each groove. The elastic properties of the membrane were then determined by finding the correlation between the imaging force and the corresponding creeping distance. This initial study has encouraged other researchers to utilise sharp AFM tips as nanomechanical indenters to measure the mechanical properties of micron sized objects. To better fit the AFM data with other contact mechanics models like Hertz, JKR and DMT, a colloidal probe can be used as a suitable alternative to the sharp AFM tip [27].

Typically, when a sharp pyramidal AFM tip is indented onto the cell wall, the resulting force-indentation curve will have a non-linear and a linear regime (Figure 1.5). The non-linear regime is often fit to a contact mechanics model like Hertz, JKR DMT or some combination thereof [27]. These theories explain the interaction between a deformable elastic material (cell membrane) and non-deformable indenter (AFM tip), which can result in deformation that can be predicted by the model. The linear regime is correlated to the compression of the plasma membrane of the cell, and the best fit line of the curve corresponds to the effective spring constant of the cell. Then, the compression and the spring constant values can be used to calculate the turgor pressure of the cell. Table 1.4 shows a list of Young's modulus values for different bacteria. The



turgor pressure within bacterial cells can be enormous. For *E. coli*, it was estimated to be from 0.3 atm [38] to 3 atm [39] and significantly higher for Gram-positive *B. subtilis* [40] at 20 atm. For comparison purposes, the pressure inside a normal party balloon is 1 atm and the recommended tyre pressure for a sedan car is 2.2 atm [41].

Table 1.4 List of Young's modulus values for Gram-negative and Gram-positive bacteria

Species	Strain	$E$ (MPa)	Conditions
<i>E. coli</i>	AB264	25	Isolated sacculi
<i>E. coli</i>	JM109	12.8	Whole cells
<i>E. coli</i>	JM109	0.12	Whole cells
<i>E. coli</i>	JM109	0.05	Whole cells+EDTA
<i>E. coli</i>	DH5a	2-3	Whole cells (live)
<i>E. coli</i>	DH5a	6	Whole cells (dead)
<i>E. coli</i>	NCTC 9001	221	Whole cells
<i>E. coli</i>	NCTC 9001	182	Whole cells+COS
<i>E. coli</i>	BE100	32	Whole cells
<i>E. coli</i>	ATCC 9637	2.6	Whole cells
<i>S. paucimobilis</i>	-	0.05	Whole cells
<i>S. paucimobilis</i>	-	0.08	Whole cells
<i>S. paucimobilis</i>	CN32	0.21	pH 4 – AFM
<i>S. paucimobilis</i>	CN33	0.04	pH 10 - AFM
<i>S. paucimobilis</i>	CN34	69-98	Force volume mode
<i>S. aureus</i>	NCTC 8532	95	Whole cells
<i>S. aureus</i>	NCTC 8532	88	Whole cells
<i>S. aureus</i>	ATCC 25923	1.8	Whole cells
<i>S. aureus</i>	ATCC 25923	0.2	Post - lysostaphin
<i>S. aureus</i>	ATCC 25923	0.57	Whole cells
<i>B. subtilis</i>	FJ7	10-30	Bacterial filament
<i>B. casei</i>	-	769	Whole cells

Adapted from [42].

### 1.3.2.3 Viscoelastic properties

Rodriguez *et al.* showed that the viscoelasticity of a bacterial cell can be calculated by using a colloidal probe AFM [43]. In their study, a colloidal probe of 600 nm in diameter was used to apply and maintain a constant force to a fully hydrated individual bacterial cell. The applied force was varied, and it was found that the deformation on the cell was significant. A quick image of the bacteria was taken immediately after the force was removed and revealed that the cells had completely recovered from the deformation. Gram-positive *B. subtilis* 168 was found to be less deformable compared to the Gram-negative strains like *E. coli* and *P. aeruginosa* (Table 1.5).

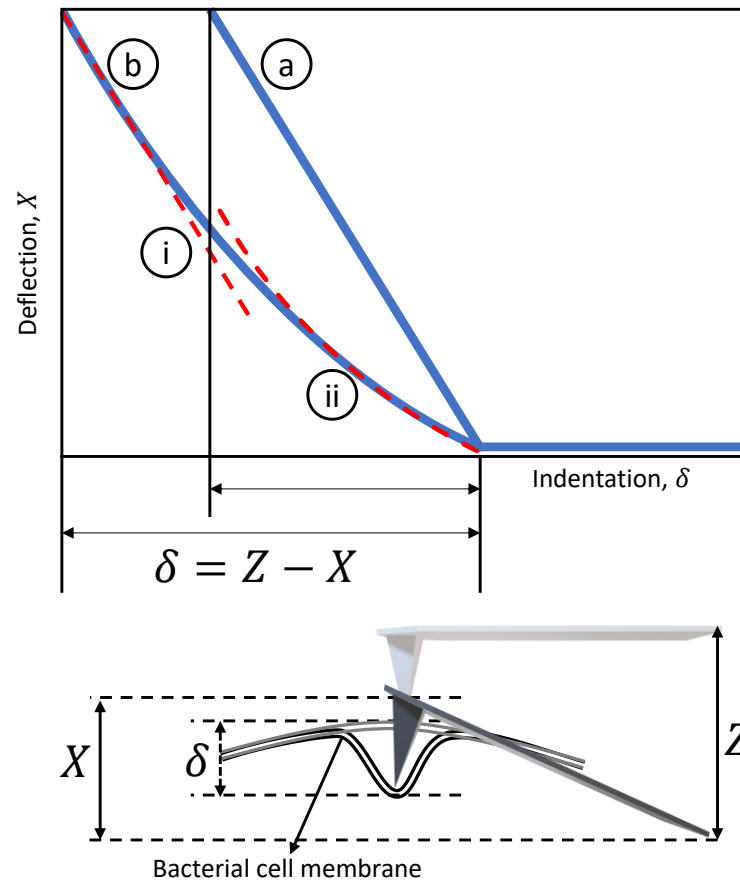


Figure 1.5 Viscoelastic deformation experiment. Indentation curve of (a) colloidal probe AFM cantilever and (b) pyramidal AFM cantilever, when indenting the surface of a bacterial cell. The indentation ( $\delta$ ) is determined by finding the difference between the piezo displacement ( $Z$ ) and the deflection of the cantilever ( $X$ ). Indentation of colloidal probe AFM is found to be linear on the force-indentation plot, which allows the estimation of the bacterial cell's spring constant by calculating the ratio between the loading force and the depth of indentation. Of note, a pyramidal AFM tip is found to have both (i) linear and (ii) nonlinear regimes. The linear regime will determine the spring constant while the nonlinear regime is often fitted to the Hertz model and gives the Young's modulus of the cell. Adapted from [27].

#### 1.3.2.4 The importance of viscoelasticity for bacterial cells

Viscoelasticity of the bacterial cell wall is important for a number of reasons. For instance, during cell growth, the bonds between the thin and highly ordered peptidoglycan network will be broken for the new peptidoglycan monomers to be incorporated. Autolysin molecules that are produced within the cell are used to break the bonds and transport new peptidoglycan through the cell wall. During the breaking and bonding activities, the mechanical integrity of the peptidoglycan layer is perturbed due to stress from the neighbouring bonds that are susceptible to break. If the cell wall is an elastic material, this condition will lead to a chain of events that will eventually tear the cell wall, leading to cell lysis. It is probable that the viscoelastic behaviour

of the cell wall could delay the accumulation of localised strain and allow neighbouring bonds to reform before a larger network of bonds are ruptured [27].

Table 1.5 Viscoelastic parameters of different bacterial species determined using AFM-based creep deformation experiments

	Viscoelastic parameters*			
	$k_1$ (N·m <sup>-1</sup> )	$k_2$ (N·m <sup>-1</sup> )	$\eta_2$ (Ns·m <sup>-1</sup> )	$\tau$ (s)
<i>Pseudomonas aeruginosa</i>	0.044±0.002	0.81±0.08	1.37±0.27	1.82±0.2
<i>P. aeruginosa</i> (GA-treated)	0.11±0.03	1.5±0.1	1.0±0.2	0.8±0.3
<i>Escherichia coli</i> K12	0.056±0.008	0.54±0.13	0.36±0.05	0.64±0.08
<i>Escherichia coli</i> (lpp+)	0.045±0.01	0.54±0.1	0.61±0.28	1.1±0.2
<i>Escherichia coli</i> (lpp)	0.026±0.006	0.33±0.06	0.3±0.07	0.91±0.3
<i>Bacillus subtilis</i> 168	0.1±0.02	1.2±0.3	3±0.6	2.6±1.1

\*  $k_1$  and  $k_2$ , elastic stiffness values;  $\eta$ , viscosity value;  $\tau$ , response time of the cells, which is defined as  $n_2/k_2$ . Adapted from [27].

## 1.4 Bacteria-substrata interactions

Although the general theory of bacterial adhesion to a solid surface has been proposed, no theory has yet been developed that encompasses the mechanistic complexity that underpins bacterial interactions with a flat surface. To understand the bacterium-substratum interaction, several aspects need to be considered, such as bacterial surface sensing mechanisms, which can enable bacteria to switch from swimming to swarming when it is close to a surface, and initial bacterial attachment to the solid substratum. The lack of understanding of the principles of bacterial adhesion could explain failure of animal studies testing the tuning of the physicochemical properties and wettability of a novel biomaterial surface.

### 1.4.1 Surface sensing

Almost all species of bacteria live in a community that is established on a surface, with successful interactions between different species allowing the bacteria to colonise different environments. Researchers have always wondered how bacteria know they are on a surface. Surface sensing has been postulated to be a set of different mechanisms that (1) allow bacteria to perceive the proximal distance to the solid surface, and that (2) enable physicochemical scanning of the surface for attachment [44]. A novel study on the swimming dynamics of *Vibrio parahaemolyticus* in 1988 showed that when the bacteria were in close proximity to a surface,

the flagellar motion was restricted and instead, the appendages started to “sense” the surface, triggering transduction pathways that switched on the swarming motility of the lateral flagella [44]. This finding was supported when a similar flagellar behaviour was observed for bacteria incubated in a highly viscous medium, where the swarming motility was switched on even when the cells were in a planktonic state [44].

#### 1.4.2 Swimming dynamics of bacteria

More studies on bacterial swimming dynamics and the role of flagella in surface sensing have been reported for *Proteus mirabilis* and *E. coli*. Belas *et al.* found that *P. mirabilis* swarmer cell gene transcription is switched on when flagellum rotation is restricted [45]. More recently, Qi *et al.* published the swimming dynamics of *E. coli*, using digital holographic microscopy (DHM) to track the precise movement of individual bacterial cells in 3D [46]. This technique gives important information like the change in swimming velocity and density distribution, collision probability with the surface, swimming propulsion force, and swimming orientation of the bacteria. Qi *et al.* used a lab made DHM to track the movement of *E. coli* cells in real time on four different surfaces with different surface wetting properties. It was reported that *E. coli* favoured adhesion to a more hydrophobic surface. On the most hydrophobic surface, *E. coli* cells showed a decrease in swimming velocity as they approached the surface due to the exertion of a surface attraction against the motility of the cell during collisions. Before *E. coli* cells adhered to the surface, the 3D trajectory suggested that the cells swam and accumulated close to the surface due to hydrodynamic attraction, which dragged the cells closer towards the surface. The hydrodynamic interaction also caused a change in swimming orientation of the cell from perpendicular to parallel to the surface. The change in direction, together with the rotation of the flagella and Brownian motion, caused the cell to collide with the surface. From 300 tracked cells, 70% were found to collide with the surface. In particular, at 1  $\mu\text{m}$  away from the surface, the collision of flagella and the surface was found to occur at a significantly higher rate than collision between the cell and the surface. These observations led to the conclusion that the landing of *E. coli* on a surface was dependent on flagella collision, which was affected by the hydrophobicity interaction between the cell and the surface [46].

#### 1.4.3 Bacterial adhesion

Understanding the swimming dynamics of the cell highlights the behaviour of bacteria to switch from a planktonic state to a sessile state upon “sensing” a surface. As the bacterial cell gets closer to a surface, at less than 50 nm, the surface forces start to act upon the cell. The current

theory to describe bacterial adhesion to a surface is a combination of the extended DLVO theory and thermodynamic approach. DLVO theory suggests that the total interaction energy between a surface and colloidal particle is the sum of their van der Waals and Coulomb interactions (Figure 1.6). DLVO has been used to describe bacterial adhesion to a surface, as the size of the average bacterial cell is similar to the size of colloidal particles (i.e. 0.5-2  $\mu\text{m}$ ) [47].

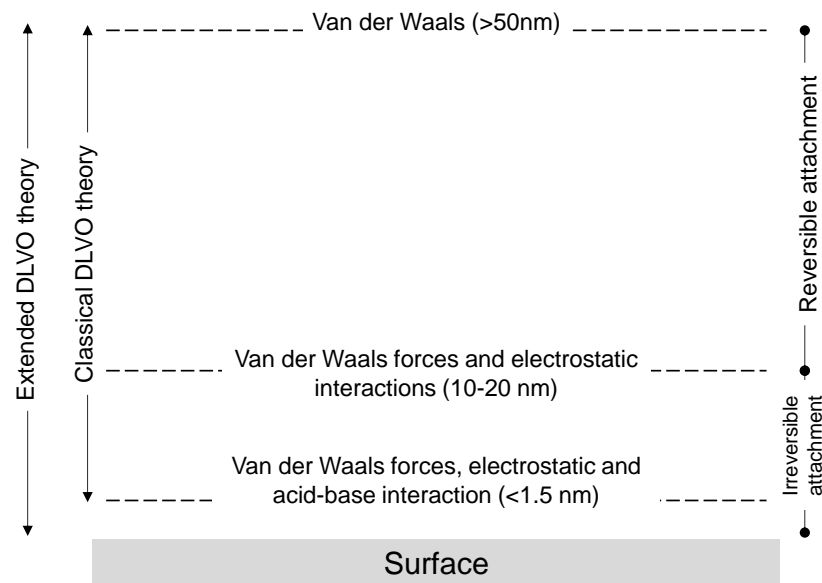


Figure 1.6 Schematic to illustrate the differences between classical (DLVO) and extended DLVO (XDLVO) theory.

#### 1.4.3.1 DLVO theory

According to the DLVO theory, as the van der Waals forces get stronger near the substratum, the bacterial cell will not be able to separate from the surface by Brownian motion. The counter ions present in an aqueous solution will form an electric double layer on the substratum and the bacterium. If the ionic strength in an aqueous solution is low, a strong repulsive force will form on the substratum due to the lack of shielding from the electric double layer. This energy barrier will hinder the bacterium from approaching the surface by swimming or Brownian motion.

DLVO theory describes bacterial adhesion as a two-phase process. In the first step of cell adhesion, a bacterial cell approaches the surface via its motility, Brownian motion and/or hydrodynamic attraction and adheres to the surface reversibly. Then, the bacterium uses surface appendages like pili or flagella, which can pierce the energy barrier due to their small radii to bridge the cell and surface irreversibly [47]. If the ionic strength in an aqueous solution

is low, the energy barrier becomes higher and farther from the substratum, which will make it difficult for the cells to adhere since the bacterial surface appendages are unable to reach the surface. In contrast, at high ionic strength, the energy barrier disperses, and the bacterium can easily attain irreversible adhesion. There have been several studies to test the energy barrier theory and these have found a correlation between increasing bacterial adhesion and increasing ionic strength, corroborating the DLVO theory [48–50].

#### 1.4.3.2 Thermodynamic approach

In contrast to the DLVO theory, the thermodynamic approach to bacterial adhesion assumes that the adhesion process is reversible, which is not always the case. By using the thermodynamic approach, the common observation shows that hydrophobic bacterial cells prefer hydrophobic substrata, while hydrophilic cells prefer hydrophilic substrata [47]. The hydrophobic interaction between two apolar moieties in water is the consequence of hydrogen bonding energy from cohesion of water molecules with the moieties. The hydrogen bonding that arises from the hydrophobic interaction can be viewed as an electron-donor and electron-acceptor interaction, which is also known as a Lewis acid-base interaction. In van Oss extended DLVO (XDLVO) theory, the hydrophobic/hydrophilic interactions and osmotic interaction are included, with the surface tension of water ( $\gamma$ ) consisting of Lifshitz-van der Waals component ( $\gamma^{vdW}$ ) and the Lewis acid-base component ( $\gamma^{AB}$ ). Since the osmotic interaction is negligibly small in bacterial adhesion, the total adhesion energy is expressed as:

Equation 1.1: XDLVO equation

$$\Delta G^{adh} = \Delta G^{vdW} + \Delta G^{dl} + \Delta G^{AB}$$

where  $\Delta G^{vdW}$  is the Lifshitz-van der Waals interaction,  $\Delta G^{dl}$  is the electric double layer interaction and  $\Delta G^{AB}$  is the acid-base interactions.  $\Delta G^{AB}$  describes the hydrophobic interactions and repulsive hydration effects, and their contribution to bacterial adhesion is enormous compared to  $\Delta G^{vdW}$  and  $\Delta G^{dl}$  interactions. It is important to note that the effective distance of acid-base interactions is relatively short-range, at around 5 nm.

#### 1.4.3.3 Complexity of bacterial adhesion

Although the models described above cover the general behaviour of a bacterial cell during adhesion, the actual mechanism of bacterial adhesion is often more complicated and frequently deviates from the models. Usually before bacteria adhere, various organic and inorganic matter adsorbs to the surface to form a conditioning film [47]. The physicochemical properties of this

film are then very different from the original bare surface, and so the interactions between the bacteria and the surface differ accordingly. It is necessary to consider the importance of the physicochemical properties of materials to prevent biofilm formation.

Another difference between simple colloidal particles and the bacterial cell surface is that the latter is structurally and chemically heterogeneous. Gram-negative bacteria have an outer membrane (OM) consisting of a lipid bilayer, with lipopolysaccharide (LPS) at the outermost layer of the OM that exhibits significant variation in the coverage density and local distribution. Various proteins are heterogeneously embedded within the OM, and many of them protrude away from the bacterial cell surface, forming cell appendages [51]. Cell appendages such as pili and flagella pierce the energy barrier described by the DLVO theory, but also cause deviation of cell adhesion behaviour from that predicted by the DLVO theory [47].

## 1.5 Bacteria-nanostructure interactions

### 1.5.1 Stretching model

The first paper that presented a biophysical model to explain the bactericidal mechanism of nanopillars was by Pogodin *et al.* The following expression helped them to make a general conclusion regarding the bactericidal mechanism of the surface [52]:

Equation 1.2: Pogodin's bactericidal model

$$1 + \alpha(r) = \begin{cases} 1 + \alpha_A = \sqrt{1 + 2(\lambda - \zeta)}, & \text{region A} \\ 1 + \alpha_B = \sqrt{1 + 2\lambda}, & \text{region B} \end{cases}$$

where  $\alpha_A$  and  $\alpha_B$  are local stretching region A and B, respectively,  $\zeta$  is the effective interaction parameter (which is defined as the ratio between the attraction and elasticity of the layer to the nanopillar), and  $\lambda$  is Lagrange multiplier. Lagrange multiplier is a mathematical optimisation tool that helps to find the local maxima and minima of a function that is subjected to equality constraints. The effective interaction parameter  $\zeta$  is given by

Equation 1.3: Effective interaction parameter of bacterial cell wall formula

$$\zeta \equiv -\frac{\varepsilon n_o}{k}$$

where  $\varepsilon$  is energy gain per adsorption site,  $n_o$  is the surface density of the attraction site on the relaxed layer, and  $k$  is the stretching modulus.

From Figure 1.7, in the case that  $\varepsilon$  is negative (which indicates the bacterium adsorbed to the nanopillars),  $\zeta$  will have a positive value. The stretching of the free membrane layer,  $\alpha_B$ , is higher than the stretching in the contact adhesion region,  $\alpha_A$ . This leads to the conclusion that the membrane is ruptured rather than pierced by the nanopillars.

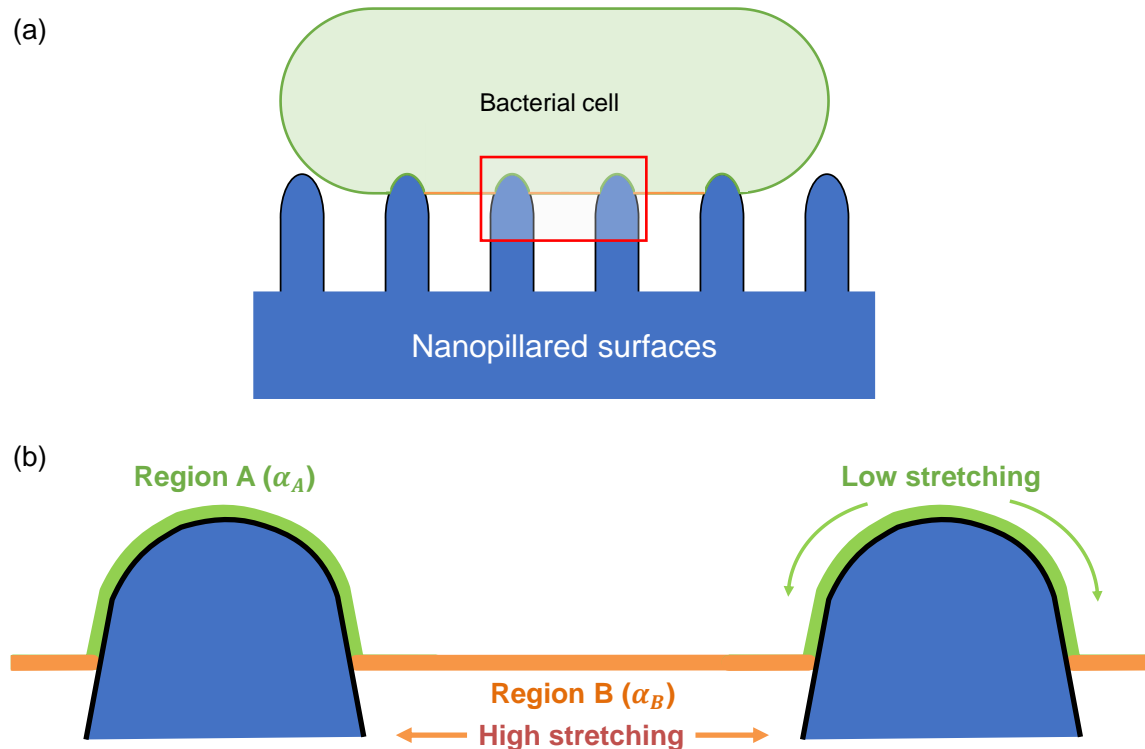


Figure 1.7 Schematic of the adsorbed bacterial outer layer with the two regions A and B. (a) Schematic of bacterial cell that is bound to nanopillared surfaces. (b) Enhanced image of the red box marked in (a). The adsorbed cell wall of region A ( $\alpha_a$ ) will have lower stretching compared to the suspended cell wall of region B ( $\alpha_b$ ). As the interaction force increases between the cell wall and the nanopillars, region B will be stretched and eventually ruptures. It is important to note that the specific interaction force between the cell wall and the nanopillars is currently unknown. Adapted from [52].

This paper also showed, using microwave irradiation experiments, that bacteria with low membrane rigidity were most susceptible to the nanopillar-mediated killing on cicada wings. This was proposed to explain why Gram-positive bacteria such as *B. subtilis* and *S. aureus*, which have greater cell rigidity, exhibited greater resistance to killing by cicada wings than Gram-negative bacteria [52].

Xue *et al.* further developed Pogodin's model by including specific and non-specific interactions like van der Waals forces and gravity, as well as other parameters such as bacterial density, the thickness of the cell wall and Young's modulus of the bacterial cell. This model predicted that sharper and low-density nanopillar structures would have optimal bactericidal properties. Xue



*et al.* also proposed that the optimal nanopillar structure to kill Gram-positive bacteria would have a radius of less than 58 nm and an inter-pillar distance larger than 176 nm. However, these findings do not agree with the experimental results shown by Kelleher [23] and Dickson [53], in which denser nanopillars were found to kill more bacteria [32].

### 1.5.2 Thermodynamics model

Li *et al.* developed a model by comparing the total free energy change of the system between cells adherent to a flat surface versus a nanopatterned surface. The proposed model offers a much simpler and elegant solution, is the closest model to the extended DLVO theory, and uses another established theoretical model based on membrane elasticity (Canham – Helfrich Hamiltonian model) [54]. In this model, the total free energy change of the system when a bacterium adheres to a flat surface ( $\Delta E$ ) is the sum of stretching free energy:

Equation 1.4: Sum of stretching energy of the bacterial cell wall

$$\Delta E = \frac{1}{2} \xi \frac{\Delta S^2}{S_0} + (E_{edge}^{Bend} - E_0^{Bend}) - \gamma S_{ad}$$

where  $\xi$  is the stretching modulus of the membrane,  $(\Delta S^2/S_0)$  is the stretching degree,  $E_{edge}^{Bend}$  is the deformed bending energy,  $E_0^{Bend}$  is the deformed bending energy of the initial cell membrane,  $\gamma$  is the contact adhesion energy density between the cell membrane and the flat surface, and  $S_{ad}$  is the contact adhesion area.

By using Equation 1.4, it is found that at equilibrium state of the system, the stretching degree of the cell is 29%. In other words, after the bacterium has comfortably adhered to the surface, its membrane is stretched by 29%.

The equation for the total free energy change of a bacterium adherent to a nanopatterned surface is slightly different to the flat surface in terms of the calculation for bending energy change. The total bending energy on a nanopatterned surface is  $(E_{edge}^{Bend} + E_{ad}^{Bend} - E_0^{Bend})$ , where  $E_{ad}^{Bend}$  is the deformed bending energy of the contact adhesion membrane on the patterned surface. For this approximation, it is assumed that the cell is completely adherent to the bottom of the surface (Figure 1.8).

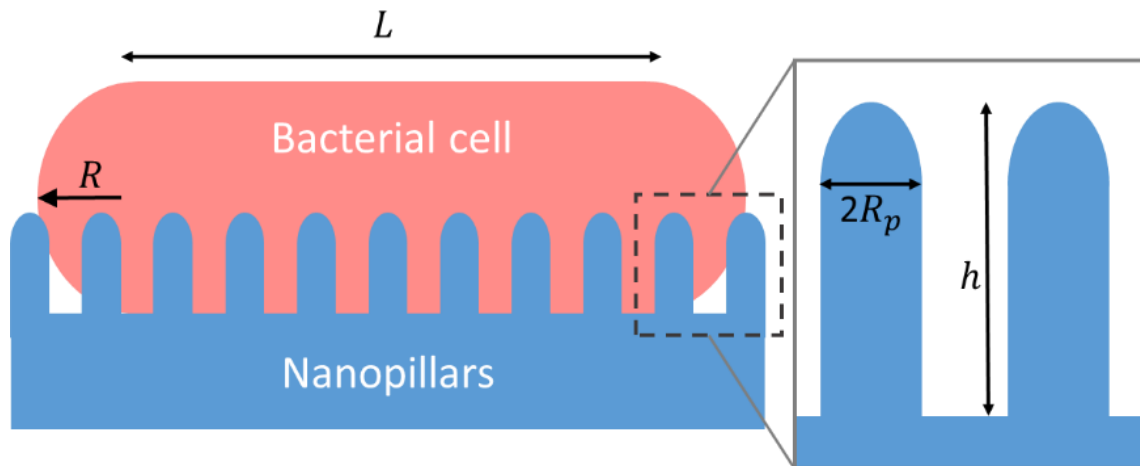


Figure 1.8 Schematic of a bacterial cell that is completely adhered to the bottom of a nanopillared surface.  $L$  is the length of the cell,  $R$  is the radius of the cell,  $R_p$  is the radius of the nanopillar and  $h$  is the height of the nanopillar.

It was found that the stretching degree of a bacterium that is adhered to a nanopatterned surface is 38%. The reason for this higher stretching degree is that the adhesion on nanopillars leads to a drastic increase of the contact adhesion area, which increases the stretching strain of the suspended membrane. The model also suggests that a smaller interpillar distance ( $D_p$ ), and thicker and taller pillars, will result in greater stretching degrees by increasing the contact adhesion area per unit horizontal area to the surface i.e. more nanopillars under one bacterium. A greater stretching degree means better bactericidal properties. This is in contrast with the finding modelled by Xue *et al.*, where sharper pillars and larger  $D_p$  had a better bactericidal effect [32].

When considered together, all three models described here present potential explanations for the bactericidal effects of nanopatterned surfaces, but without using any contact mechanics modelling (Hertz, JKR, DMT) or bacterial adhesion theory like the XDLVO model. All three models suggest that bacteria-nanotopography interactions cause the bacterial cell membrane to stretch beyond its critical point and rupture, inducing cell lysis. However, none of the models reported the main attraction force, potentially due to the complexity of bacteria-substrata interactions and difficulties with accurately assessing the cell-surface adhesion force in a controlled environment.

### 1.5.3 Role of cell wall rigidity and viscoelasticity during bacteria-nanostructure interactions

Biological responses of bacterial cells depend on the mechanical properties of the cell wall, such as rigidity and viscoelasticity, during bacterial interactions with nanostructured surfaces. For

instance, it is generally accepted that due to a weaker cell wall structure, Gram-negative bacteria are more susceptible to mechanical rupture during adsorption to a protruding nanostructured surface compared to a more rigid Gram-positive bacterium [52,55]. Although the specific conclusions from the theoretical models described above contradict one another, the general mode of action of the nanostructured surfaces is comparable i.e. the action is self-driven, in which the forces that cause the puncturing or rupturing of the cell wall are generated by the bacterium during cell-substratum adhesion [56]. Direct quantification of the rupturing forces by nanostructured surfaces has not yet been measured, despite numerous experimental and theoretical studies. Nevertheless, successful quantification of the force required to rupture a single bacterial cell has been successful using AFM.

Suo *et al.* reported that the force needed to rupture the cell wall of *Salmonella typhimurium* ranged between 1 to 2 nN [33]. This quantification was achieved by using a sharp AFM tip, which was lowered to the centre of a fixed cell and the load force increased until the tip ruptured the cell wall. Each bacterium was punctured multiple times (up to 20 times) and the viability of the cell was assessed afterwards. Of note, *S. typhimurium* was found to be viable and capable of replication even after multiple puncturing events (Figure 1.9). A similar puncturing experiment was also performed on dead cells and it was found that the force-penetration curves significantly differed from those generated using live cells. It was also found that the dead cell volume had reduced by 40% and had a low stiffness of 0.13 MPa compared to 0.5 MPa for live cells, which was likely due to the loss of turgor pressure. Suo *et al.* proposed that the ability of *S. typhimurium* to survive physical damage was due to the fact that the phospholipid membrane bilayer is highly dynamic and constructed with fluid-like membrane proteins.

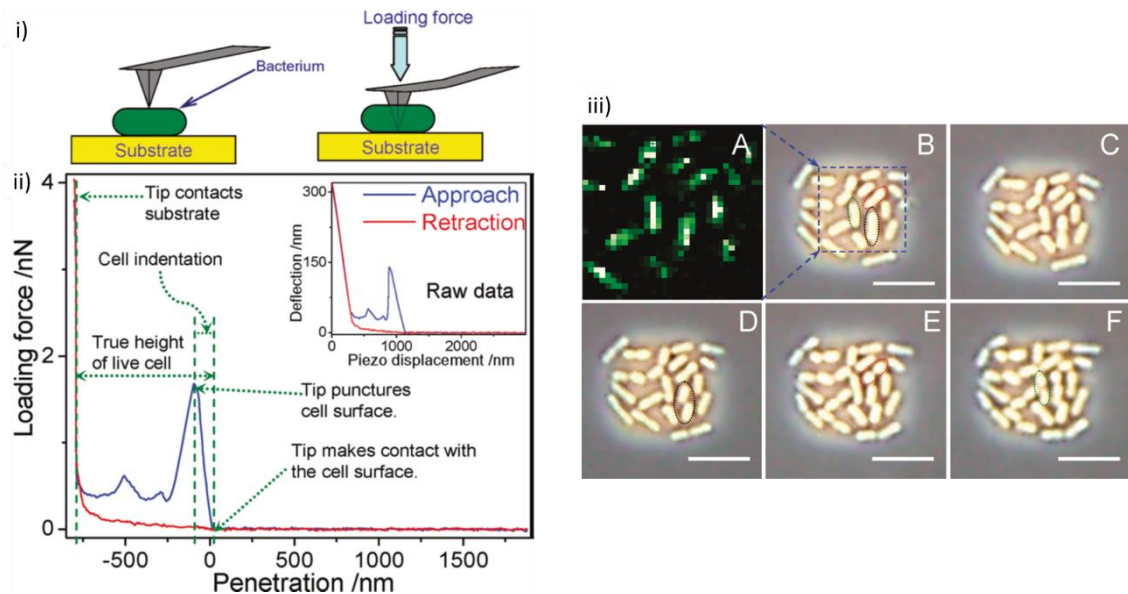


Figure 1.9 Results from the puncturing experiment on *S. typhimurium* using AFM. i) Schematic of AFM tip puncturing a fixed bacterial cell; ii) Representative force-penetration curve annotated with information as the cell was punctured by the sharp AFM tip; iii) Viability test showing that *S. typhimurium* cells divide after being punctured. (A) Force-volume image showing bright spots that indicate sites of cell puncturing and correlate with the group of bacteria shown within the blue dashed square; (B) B-F show time-lapse images of the same group of bacteria at 0, 25, 50, 75 and 100 min after being punctured [33].

Rodriguez *et al.* used a colloidal probe to apply high load force to a fixed *P. aeruginosa* cell multiple times in order to quantify the viscoelasticity of the cell (Figure 1.5) [43]. Similar to *S. typhimurium*, *P. aeruginosa* survived being “squashed” by the colloidal probe and the cell returned to its original shape without losing integrity. Both experiments from Suo *et al.* and Rodriguez *et al.* highlight the remarkable adaptability and strength of the bacterial cell wall to withstand physical force. Thus, the fact that nanostructured surfaces seemingly kill bacteria requires further understanding. To fully explain the bactericidal mechanisms, the DLVO or XDLVO adhesion theory and the flexibility and adaptability of the cell wall need to be considered.

## 1.6 Nanofabrication techniques for polymeric nanostructured surfaces

### 1.6.1 Nanolithography for protruded nanostructured surfaces

Nanolithography is a technology to generate patterns on a substrate in which one feature of the structure is measured to be equal to or less than 1000 nm. Lithography can be divided into two categories: (1) masked lithography and (2) maskless lithography [57].

Masked lithography uses a template or mould or mask or stamp to transfer patterns over a large area, enabling high-yield fabrication up to several wafers per hour. On the contrary, maskless lithography fabricates a nanopattern directly onto a substrate without a pre-patterned mask. As a result, this produces an ultrahigh resolution nanofeature but at the expense of time and resources (Table 1.6).

Table 1.6 Nanolithography techniques and their applications

Lithography Technique	Minimum Feature Size	Throughput	Applications
Photolithography	5 nm to few $\mu\text{m}$	Very high (60-80 wafers per hour)	Most common patterning techniques in laboratory and industry to produce various MEMS devices and advanced computer chips
Electron beam lithography	< 5 nm	very low (8 hrs to write a chip pattern)	Fabricate advance and high-resolution mask or template for research and development purposes
Scanning probe lithography	1 nm – 100 nm	very low	Bio-electronics, bio-sensors
Hot embossing, Nanoimprint lithography	10 – few $\mu\text{m}$	high (> 5 wafers per hour)	Bio-sensors, bio-electronics, nanowires, nanopillars, nanotubes

Adapted from [57]

Photolithography has been used for decades in the semiconductor and integrated chips industry for commercialised products like microchips, computer chips, and microelectromechanical system (MEMS) devices. However, the minimum feature size for photolithography is limited to the diffraction limit of the light source. For example, UV lights with wavelengths that range between 193 – 436 nm will have a minimum feature size of 2 – 3  $\mu\text{m}$ . In photolithography, a light sensitive polymer (photoresist) is exposed to the UV light to make a desired pattern based on the photomask, which consists of an opaque pattern on a transparent substrate. The UV light will break down the polymer chains of the exposed photoresist to form the desired topography [57].

Due to the wavelength limitations found in conventional photolithography, advanced photolithography techniques like extreme ultraviolet lithography (EUVL) have been developed, which uses 13.5 nm photons radiated from a plasma source that can fabricate structures with a

minimum feature size of 7 nm or smaller. Another similar masked lithography technique, electron beam lithography (EBL), uses an electron beam on an electron-sensitive resist to fabricate the nanostructured surfaces. An electron beam has a much lower diffraction limit than light, meaning that electron wavelengths of 1 Å can be achieved to attain a nanostructure with 10 nm as one of its dimensions.

Scanning probe lithography (SPL) uses a sharp scanning probe microscope (SPM) cantilever to make a nanopattern with high precision and has been shown previously to manipulate a single atom [58,59]. Electrons from the SPM tip can be used on a photoresist the same way as with EBL. This is done by moving the tip over the surface while applying high bias voltage, which produces electrons from the tip. The emitted electrons cause local chemical changes to the resist and can form highly accurate nanopatterns. For example, high aspect ratio nanopatterns with 20 nm in thickness and an aspect ratio of 10 have been reported. However, while the precision is very high, the writing speed is very low, which makes this technology unsuitable for commercial application at the moment.

Compared to other lithography techniques, hot embossing is seen as a candidate to be the next generation manufacturing method to fabricate MEMS devices, since this technology does not require the expensive optical lenses and light sources used in photolithography [60]. With a comparable resolution to photolithography and high throughput, hot embossing is an ideal candidate as a potential manufacturing protocol for applications like biosensors, nanofluidic devices, antifouling and antibacterial surfaces.

Hot embossing or nanoimprint lithography was first demonstrated in 1995 [61]. The process uses a prepatterned stamp on a thermoplastic polymer substrate under certain temperatures and pressures. The thermoplastic substrate is heated above its glass transition temperature,  $T_g$ , and pressed against the master stamp. The heated viscous polymer flows and fills the stamp when high pressure is applied. After a few minutes, the pressure is relieved, and the thermoplastic is cooled to reveal the pattern from the stamp [62].

Hot embossing offers several advantages over other fabrication techniques. For instance, hot embossing is a mechanical process that is not limited by the diffraction limit of light or the photoresist chemistry, as is the case for optical photolithography. Instead, the resolution limitation of hot embossing depends on the minimum feature size that can be fabricated on the master stamp. Since hot embossing does not require complex optics or light source, the overall cost is typically less expensive than optical based systems. Hot embossing also has the potential

to fabricate functional materials and 3D structures. Unlike most other nanofabrication techniques, which are limited to 2D patterning, hot embossing can generate a 3D pattern with a single embossing step [63].

### *1.6.2 Current challenges with nanofabrication techniques*

The translation from laboratory research findings to commercialised products is often difficult and many attempts end in failure [64]. One of the main issues with commercialising scientific research, especially for material sciences, is that the fabrication processes are often very niche and specific, which then usually limits the availability of equivalent processes in industry. An example of this scenario is seen with carbon nanotubes (CNTs). CNTs were discovered by a Russian scientist in 1952 and since then have been purported as the material of the future due to their incredible mechanical properties. CNTs are known for their high elastic modulus and tensile strength at 1 TPa and 100 GPa, respectively, which are 10-fold higher than any known industrial fibre. The thermal conductivity of CNTs is also higher than diamond at  $3500 \text{ Wm}^{-1}\text{K}^{-1}$  (whereas diamond ranges from  $895 - 1350 \text{ Wm}^{-1}\text{K}^{-1}$ ) [65]. Unfortunately, due to current limitations in manufacturing, the longest CNT that has been successfully grown is just 550 mm long, and there are yet to be any commercialised products that use the full potential of CNT mechanical properties [66].

Due to the high susceptibility of current medical devices to bacterial infection, and concerns regarding antibiotic resistance, overcoming challenges with nanofabrication is a priority. The choice of nanofabrication method was therefore a crucial aspect of this project, as the selected technique needed to be versatile enough to tailor different designs with some degree of control over the nanotopography i.e. spacing, diameter and height, and the fabrication technique needed to be up-scalable for practical applications. Anodisation was considered, as this is a versatile technique that has been used to design nanopore stamps, and can be used in conjunction with cheap and scalable hot embossing to fabricate nanopillars on medically relevant thermoplastic polymer materials like polymethyl methacrylate (PMMA), polyethylene terephthalate (PET) or high performance polymer like polyether ether ketone (PEEK).

### *1.6.3 Anodisation*

Anodisation is a known and reliable technique to generate uniform nanopores on metal surfaces (i.e. aluminium and titanium) and has been used extensively in industry for many applications. One of the applications of anodisation is its use as a template or stamp to make metal nanowires,

CNTs, polymeric nanopillars or other protruded nanostructures [67]. Due to its simplicity and versatility in producing highly ordered nanopore patterns, anodisation has been the preferred method to make the master stamp for hot embossing techniques [68–71].

Typically, in a laboratory setting, anodisation is performed in an anodisation cell, because the cell gives better control of the anodisation process, leading to the formation of more regular and highly reproducible nanopores. The anodisation cell is usually made from PTFE (Teflon), comes with a lid and its contents are often stirred by a mechanical stirrer to help control the dissolution of the nanopores (Figure 1.10A).

Anodisation has been used in industry since 1923, primarily as a coating technology [67]. For this industrial anodisation process, the anodising metal (e.g. aluminium) is dipped into big open containers, aligned in series (Figure 1.10B). The dipping process of the anodising metal is controlled by a robot that starts the process by washing the metal sheet in a cleaning solution, followed by drying the sheet in the next empty container equipped with a dryer. The process then continues with electropolishing, washing, anodising, and the final washing and drying step, with each step happening in a separate container [72]. This processing technique allows the manufacturer to work efficiently, maximising productivity and maintaining the quality of the product.

As far as industrial chemistry is considered, application of advancements in anodisation like nanophotonics, sensing devices, functional electrodes, magnetic recording media and antifouling surfaces, are yet to be translated successfully [67]. These new applications of anodisation require complicated material treatments and processing, and the techniques used are not optimised for large scale production.



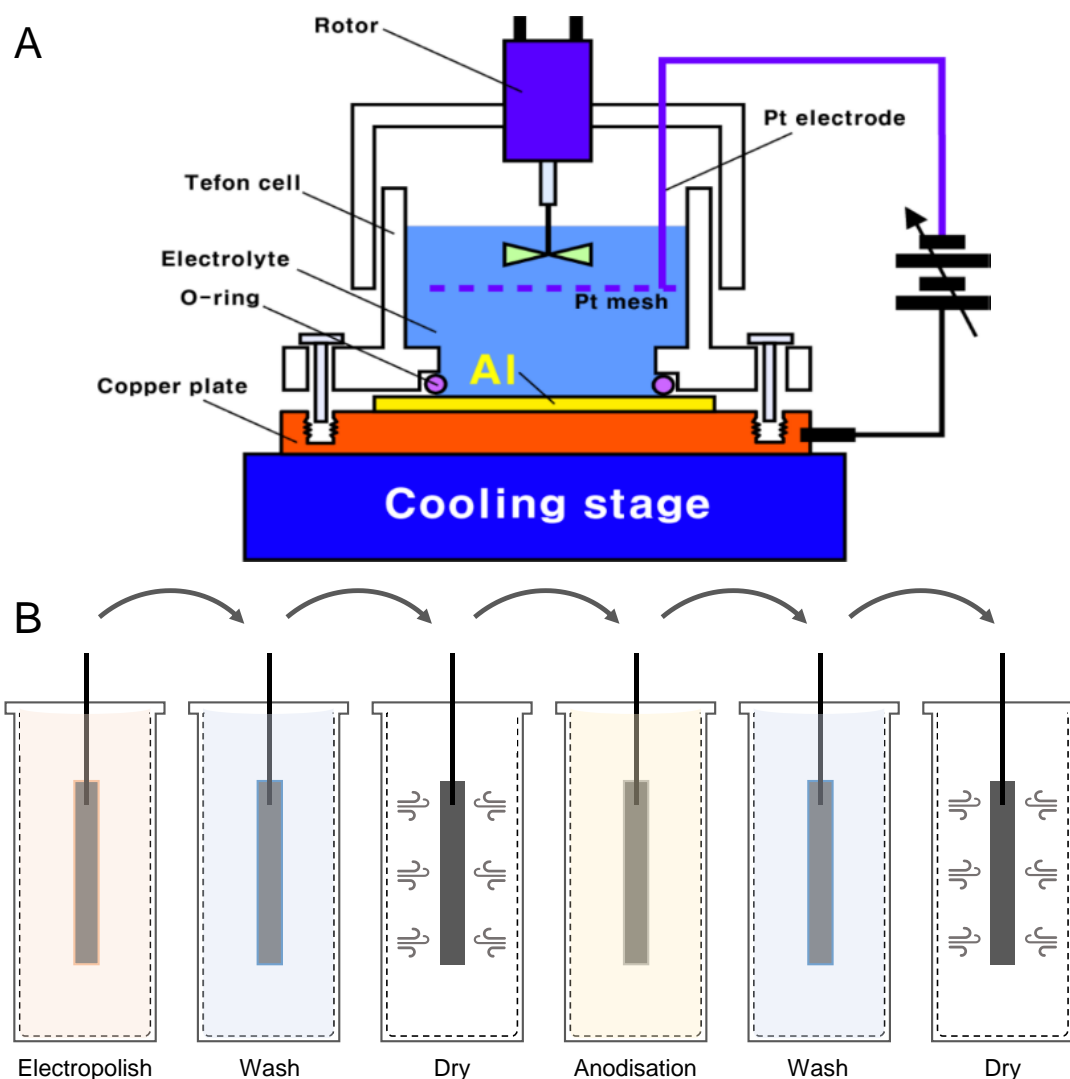


Figure 1.10 Differences between laboratory and industrial protocol for anodisation. (A) Schematic of typical anodisation cell used in the laboratory made from PTFE and placed on a mechanical stirrer to control the dissolution of aluminium (from [73]); (B) Schematic of aluminium anodising process in industry, which is performed in big and open containers that are aligned in series.

The two-step anodisation process was first introduced by Masuda *et al.* and allowed the formation of self-ordered nanopores [74]. The process involves a very long first anodisation process ranging between 12-16 hours, followed by removal of the oxide layer before the final anodisation step, which is usually shorter than the first step; depending on the desired depth of the nanopores. The driving factor for the self-assembly of the self-ordered porous alumina has been attributed to the mechanical stress from the repulsive forces between neighbouring pores during anodisation [74,75].

It is generally accepted that during the anodisation step, the initial pore arrangement created on the surface is very irregular. Due to the long anodisation step, the repulsive forces between

neighbouring pores cause self-organisation to occur. Consequently, hexagonally close-packed arrays are formed at the interface between the porous aluminium oxide layer and the aluminium substrate. After the removal of the alumina layer by chromic acid solution, patterns of the hexagonal arrays are preserved on the aluminium surface. The prepatterned aluminium surface will serve as a starting position for the pore formation with high regularity during the second anodisation step under the same conditions as the first step [67,75].

The potentiostatic current density profile shows the formation of porous type alumina (Figure 1.11). During pore formation in potentiostatic regime, the current density will reach the maximum set current before decreasing rapidly (a) until it reaches the minimum values in (b). At the beginning of pore formation, the current density starts to develop on the oxide layer, increases to the maximum value allowed for the setup, and subsequently decreases again. This local fluctuation may lead to electric field enhanced or temperature enhanced dissolution of the formed oxide layer, which initiates pore formation on the substrate (c). Finally, a steady current density remains to initiate stable pore formation on the substrate (16).

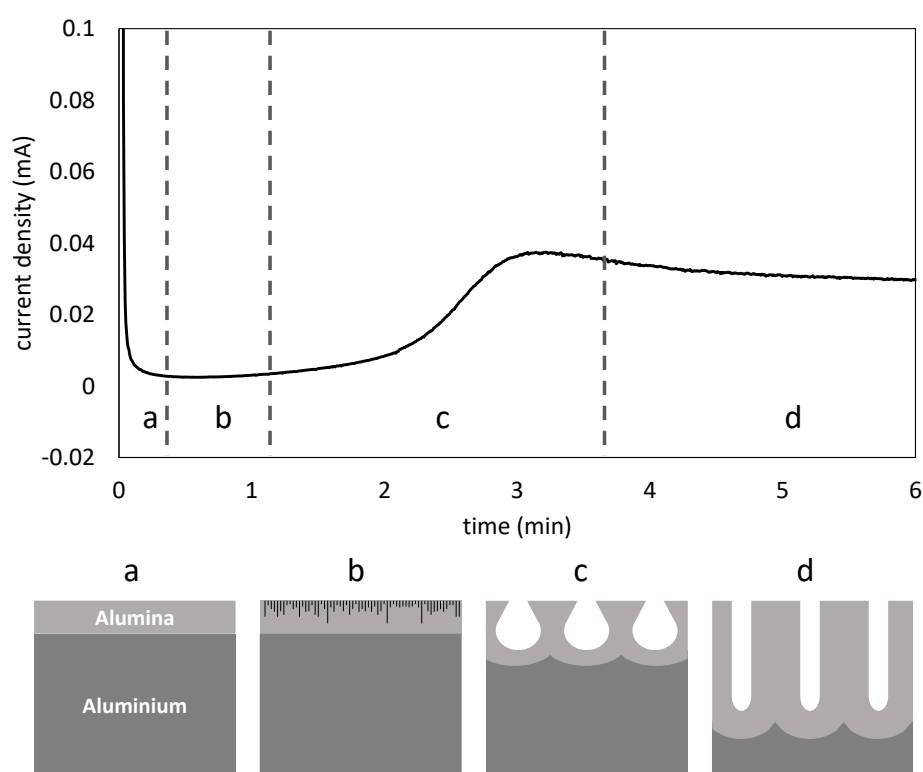


Figure 1.11 Kinetics of porous oxide growth in a potentiostatic cell at 70 V in 0.3 M oxalic acid at 5°C. The progressing stages of anodic porous oxide development are highlighted from the regions labelled on the plot. Region (a) shows maximum current density before it reaches the minimum value at (b). Region (c) indicates local fluctuation during the initiation of the pore formation before a stable current density is established in region (d) [76].

## 1.7 State of the art

Results from the literatures suggested promising effects of nanostructured surfaces in reducing bacterial colonisation on polymer substrates. Dickson *et al.* has showed 23% of cell death against *E. coli* on biomimetic PMMA surface [53] while Hazell *et al.* has showed up to 30% of cell death on PET nanocones against *E. coli* and *K. pneumoniae* [77]. PMMA bearing biomimetic moth eyes nanopillars was reported to be able to kill 55% of adhered *S. aureus* cells, 45% *E. coli* cells, and 30% *P. aeruginosa* cells [78]. Recently, Wu *et al.* reported high percentage of cell death of *S. aureus* which is around 98% on commercial polymer substrate Ormostamp that comprises of high density nanostructured surfaces [79]. Other example include the ability of polystyrene micro-lamella structures in reducing *S. aureus* adhesion [80]. In other study, nanolamella structures have showed effective prevention against *E. coli* and biofilm formation on polystyrene substrate [81]. PMMA nanopores has also showed restricted attachment of both bacterial and mammalian cell [82].

Results from these nanotextured surfaces are encouraging but none of them can be classified as bactericidal as the reduction of the total number of CFU/ml is less than 99.9% ( $\geq 3 \log 10$ ) [83]. Thus, the real challenge is to understand the fundamental mechanism of how bacteria interact with the nanostructured surfaces so that this technology can be optimized to enhance its bactericidal efficiency. Apart from the physical parameters like sharpness, density and height of the nanopillars, other factors like physicochemical and nanotribological properties of the surface need to be considered in order to fully understand the complex interaction between bacteria and the nanostructured surfaces.

Nanotribology is a growing field that involves experimental and theoretical studies of adhesion, wearing, friction and lubrication at molecular level [84]. Most of the researches in this field are focusing in the interactions between organic and inorganic molecules on metallic and graphitic nanotextured surfaces while there are less attention to interactions between biomolecules and cells with the nanotextured surfaces [84]. The susceptibility of bacterial cell wall against the nanostructured surfaces provide direct evidences that the surface nanotribology could have influence in the overall surface adhesive, wearing and tearing properties. Finding the correlations between surface nanotribology and bactericidal activity could provide valuable information in fabricating effective antibacterial surfaces to combat biomaterial associated infections.

## 1.8 Aims and objectives

There is a tremendous interest in developing a novel biomaterial for healthcare applications that are able to kill bacteria physically rather than chemically. This new approach has been inspired by nature, with several insects having been found to possess wings that comprise sharp nanostructured topographies that are able to kill bacteria upon attachment (e.g. cicada wings). Due to the urgent need to develop novel approaches to combat antimicrobial resistance, translation of this nanostructure technology needs to be actively pursued. However, much of our current understanding of the mechanistic basis for the bactericidal effects of these nanostructured topographies lacks clarity. The bacterial cell wall has a high mechanical strength and as such, bacteria have been shown to survive multiple puncturing by sharp AFM tips and compression by colloidal particles at high pressure. Moreover, in both cases, the bacteria not only survived but were reportedly still able to replicate. Thus, the fact that the broader nanopikes and multiple nanopillars found on cicada wings are able to kill bacteria is very interesting from the contact mechanics perspective. To better understand the dynamics of bacteria interactions with nanostructured surfaces and thus the mechanics of the bactericidal activity of cicada wing-mimicking surfaces, the aim of this project was to fabricate highly ordered periodic nanopillars on thermoplastic materials using anodisation/hot embossing, and to characterise their material and antibacterial properties. This was to be achieved via the following specific objectives:

- 1) Fabricate a range of cicada wing biomimetic nanopillars that have interrelated nanotopography on thermoplastic substrates such as PET, PMMA and PEEK.
- 2) Characterise the nanotopography and surface nanotribological properties of the nanopillars.
- 3) Determine the antibacterial performance of the nanostructured surfaces using motile and non-motile, Gram-negative and Gram-positive bacteria.
- 4) Assess current theoretical models of the potential bactericidal mechanisms of nanostructured surfaces.
- 5) Investigate the role of cell surface proteins in mediating bacterial attachment to nanostructured surfaces.

## CHAPTER 2 MATERIALS AND METHODS

### 2.1 Nanofabrication of nanopillars on polymer substrates

#### 2.1.1 Electrochemical setup

Anodisation and electropolish used the same electrochemical setup, which consisted of a power supply (Agilent technologies, N5752A, 600V/1.3A, 780W DC power supply) that was connected to a computer and controlled by LabView software (V2.1), a multimeter (Keithley, 2000 Multimeter), an anode, a cathode, and a water bath. The LabView program was used to control the current during the electrochemical reaction. It was first developed by Dr Sjöström and was modified to include parameters to control the time of anodisation in this work. The vertical position of the anode and cathode was controlled by a retort stand and the horizontal separation between the two electrodes was fixed at 28 mm, which was the size of the vortex generated by the magnetic stirrer. It is important to note that the size of vortex is dependent on the size of beaker and stirrer, the volume of electrolyte and the speed of stirrer. In this setup, a 1 L beaker (Pyrex, width 85 mm) with 1 L of electrolyte was used and vigorously stirred with a 24.5 mm magnetic stirrer at 700 rpm to control the dissolution of aluminium oxide during anodisation. The temperature of the polystyrene water bath was regulated by a temperature controller (Grant T120) and a cold finger (Julabo FT200 GB). The aluminium sheet and the counter electrode were held by copper alligator clips. The setup is depicted schematically in Figure 2.1.

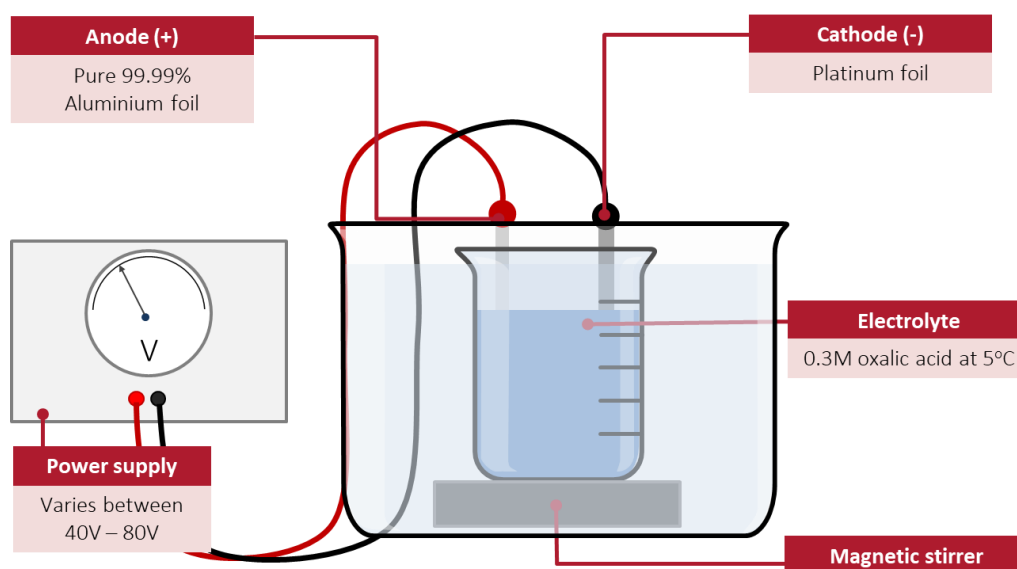


Figure 2.1 Schematic of the electrochemical setup used for electropolish and anodisation.

### 2.1.2 Electropolishing and two-step anodisation

The aluminium sheet with a thickness of 5 mm (99.9999% purity, Goodfellow) was first washed vigorously inside an ultrasonic bath (Grant Scientific XUB) with plenty of deionised (DI) water, ethanol (99.6%, Sigma Aldrich) and acetone (Analytical reagent grade (99.99%), Fisher Scientific) for 10 min in each washing solvent. The aluminium sheet was polished using an electropolishing method in a perchloric acid mixture (25% perchloric acid, 75% ethanol). The aluminium sheet was then cleaned with acetone and ethanol vigorously twice before being washed with plenty of DI water. The aluminium sheet was then cleaned using a plasma cleaner for 10 min with 50% power. Finally, the aluminium sheet was cleaned with acetone, ethanol and DI water for 10 min at each step. Electropolishing was chosen as the preferred polishing protocol as this technique is faster than other polishing techniques (i.e. mechanical polishing) at producing mirror-polish finish, which is one of the main pre-requisites for the formation of uniform porous alumina.

The first anodisation was performed at 40 V in 0.3 M oxalic acid solution at a temperature of 4.5°C for approximately 4 h. During the first process, the pore arrangement was not regular, and this layer was removed by dissolving the anodised aluminium sheet in a chromic acid solution (1.8% Cr<sub>2</sub>O<sub>3</sub>, 6% H<sub>3</sub>PO<sub>4</sub>) at 40°C for 2 h. The hexagonal pore arrays were still preserved on the aluminium surface, which allowed for high uniformity with the second anodisation, which was performed under the same temperature and potential conditions but for a shorter time. The anodisation time in the second step corresponded to the thickness of the oxide layer, which affected the depth of the nanopores.

#### 2.1.2.1 Phosphoric acid etching

Common etching solutions used to widen the pore diameter of anodised aluminium oxide (AAO) are 0.1 M sulphuric acid, 0.1 M phosphoric acid and 0.3 M oxalic acid. For this study, phosphoric acid was chosen as the preferred etching solution since it gave the most consistent results with our set-up (Figure 2.2A). A standard curve for phosphoric acid etching was developed in order to find the aluminium oxide etching rate with the set-up used in this project (Figure 2.2B). The standard curve was made by immersing the AAO nanopores in 30°C phosphoric acid for 10 min, 20 min, 30 min, 40 min or 50 min. The AAO nanopores were then immediately immersed in DI water and rinsed thoroughly with plenty of DI water and ethanol. The resulting AAO nanopores were imaged by SEM at 50 000× magnification on 3 different areas per sample. The diameter of the nanopores was quantified using the FIJI particle analysis plugin.

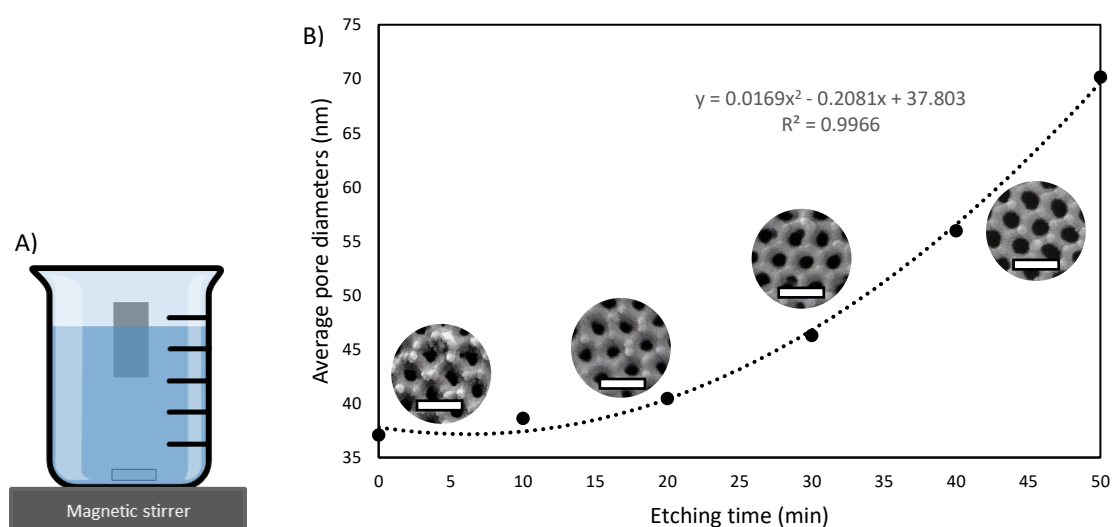


Figure 2.2. Schematic of the etching process for AAO with 0.1 M phosphoric acid. A) Set-up for etching the oxide layer on aluminium substrate; B) standard curve for phosphoric acid etching at 0.1 M, 100 rpm, 2 cm stirrer, 30°C. Scale bar, 100 nm.

#### 2.1.2.2 Post treatment of nanopores with silanisation solution

The AAO substrate was cleaned with water, ethanol and plasma cleaner to remove any impurities and to activate the surface with oxygen. A desiccator (Duran, D150) was put under vacuum (Edwards, RV8) without any sample to remove the impurities within the desiccator for 10 min. Dimethyldichlorosilane (DCDMS; 1.6 ml, 5%) in heptane (Sigma), known as silanisation solution 1, was transferred into a 2 ml glass vial. After 10 min, the vacuum inside the desiccator was released, and the AAO stamp and the silanisation solution 1 were placed into the desiccator immediately. The sample was vacuumed again for 10 min without sealing the valve and for an additional 12.5 min with the valve sealed. After the vacuum was released, the samples were immediately placed in a beaker filled with methanol for washing. This was crucial to avoid any polymerisation of the silanol on the surface of the sample.

The silanised samples were washed vigorously by sonication (Grant, XUB5) at 60% power and 20°C for 10 min in methanol, isopropanol, toluene, and ethanol. The samples were washed with plenty of DI water and air dried before being used for hot embossing. Silanisation was introduced for easy demoulding to allow reusability of the AAO stamp.

### 2.1.3 Hot embossing

In this study, three clinically relevant polymers were used; polymethyl methacrylate (PMMA), polyethylene terephthalate (PET), and polyetherether ketone (PEEK) (Table 2.1). In general, a polymer substrate with 1 mm thickness was cut into  $10 \times 10$  mm and cleaned thoroughly with water, ethanol and isopropanol in an ultrasonic bath (90% power) for 10 min at each step. The polymer substrate was embossed with a dual-plate hydraulic heat press (CYJ-600C, Zhengzhou CY Scientific Instrument Co. Ltd). The polymer substrate was placed on top of the AAO stamp and heated above the  $T_g$  of the polymer by increasing the temperature of the bottom heat plate. Due to low thermal conductivity of the polymer substrate, only the substrate surface that was in contact with the AAO stamp was in thermal equilibrium. Pressure (1.2 MPa) was applied for 10 – 20 min before the stamp-substrate sandwich was cooled to below the polymer substrate  $T_g$  and the pressure was released. The sample was cooled to room temperature and the nanopillars were released from the AAO stamp by carefully peeling off the polymer substrate using a scalpel while maintaining the angle between the polymer substrate and the AAO stamp at less than  $10^\circ$  (Figure 2.3).

After hot-embossing, the master stamp was immersed in 100% toluene for a minimum of 16 h to remove any contamination from the previous hot-embossing step. The master stamp was washed vigorously in water and ethanol inside an ultrasonic bath for 10 min at 60% power for each step. The stamp was air dried before being reused for another hot-embossing. The master stamp was reused for a maximum of 5 times, after which, the quality of the imprinting was significantly reduced.

Table 2.1 Information on the polymer substrate used in this study.

Material	PMMA	PET	PEEK
Source	Goodfellow	Goodfellow	Goodfellow
Thickness (mm)	1	1	1
Glass transition temperature, $T_g$ ( $^\circ\text{C}$ )	105	69	143
Melting point, $T_m$ ( $^\circ\text{C}$ )	160	255	343
Young's modulus (GPa)	3.2	3.1	3.6
Poisson's ratio	0.4	0.4	0.4

These information are available from Goodfellow website [85].



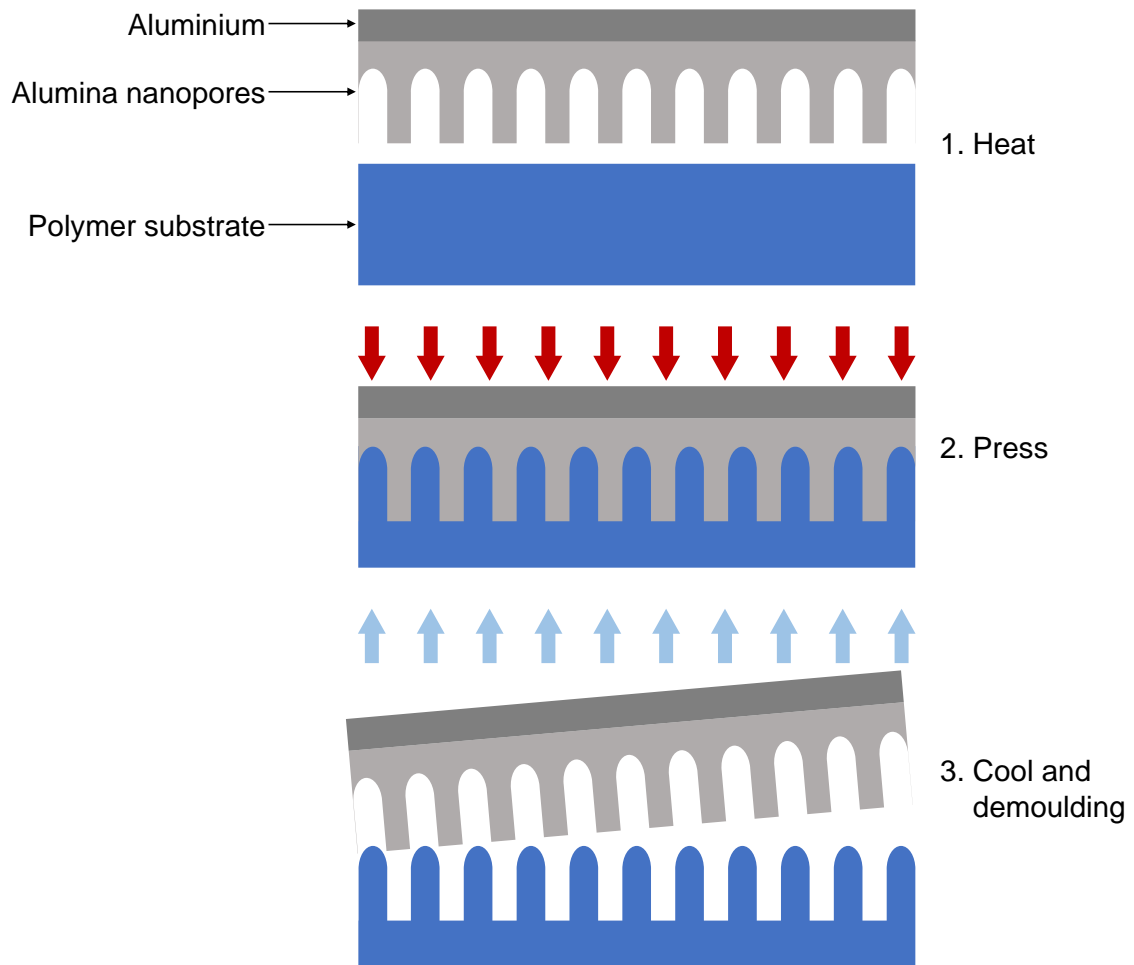


Figure 2.3 Schematic of the hot embossing process. (1) The temperature of the polymer substrate and the master stamp is increased above the polymer's  $T_g$ ; (2) force is applied, and pressure is maintained for a period of time to allow the polymer to diffuse into the cavities of the master stamp; (3) the stamp and the polymer substrate are cooled to below the  $T_g$  and separated.

## 2.2 Microbiological studies

### 2.2.1 Bacterial strains

Three different bacterial strains were used in this study to quantify the antibacterial performance of the test surfaces. The strains were selected to represent a range of bacteria with different properties: Gram-type, cell morphology and motility (Table 2.2). Bacteria were routinely cultured aerobically in tryptic soy broth (TSB, *Escherichia coli*) or Mueller Hinton (MH, *Klebsiella pneumoniae* and *Staphylococcus aureus*) for 16 h at 37°C with agitation (220 rpm).

Table 2.2 Bacterial strains used in this study

Strain	Morphology	Gram identity	Growth conditions*	Motility
<i>Escherichia coli</i> K12	Bacillus	Gram-negative	TSB 37°C	Motile
<i>Klebsiella pneumoniae</i> IS-2662A	Bacillus	Gram-negative	MH 37°C	Non-motile
<i>Staphylococcus aureus</i> Newman	Coccus	Gram-positive	MH 37°C	Non-motile

\* TSB, tryptic soy broth; MH, Mueller Hinton

### 2.2.2 Quantifying the antibacterial performance of test surfaces

Two different assays were used to quantify the antibacterial properties of the nanopillared PET surfaces. The BacLight™ Live/Dead assay was used to assess effects of the nanostructured surfaces on the bacterial cell membrane, while the BacTiter-Glo™ assay (Promega) was used to determine bacterial viability following exposure to the test surfaces.

Flat and nanopillared PET surfaces were sterilised in absolute ethanol for 10 min before being washed thoroughly with 0.01 M Tris-HCl (pH 7.0) and air dried in 24-well plates. Bacterial broth cultures (16 h) were sub-cultured into 20 ml of pre-warmed broth to OD<sub>600</sub> 0.1 and incubated at 37°C, 220 rpm to mid-exponential phase (incubation time for *E. coli* K12, 1.5 h; *K. pneumoniae*; 2 h; *S. aureus*, 2.5 h). Bacterial cells were then harvested by centrifugation (5000 rpm, 5 min) and washed twice in Tris-HCl buffer (pH 7.0). Bacterial suspensions were adjusted in Tris-HCl buffer (pH 7.0) to OD<sub>600</sub> 0.5 and aliquots (500 µL; equivalent to 5×10<sup>5</sup> CFU) transferred into 24-well plates containing the sterilised samples. Plates were incubated at 37°C for 3 h under static conditions.

#### 2.2.2.1 Live/Dead assay

After 3 h, the bacterial suspension from each well was discarded and the test surfaces washed gently by submerging in Tris-HCl buffer (pH 7.0) three times. LIVE/DEAD stain (3  $\mu\text{L}$  in 1 ml of Tris-HCl) was added to each test surface and incubated for 15 min in the dark at room temperature. The samples were washed gently twice with Tris-HCl buffer to remove excess stain, and then placed onto a glass slide, covered with a cover slip and visualised using an epifluorescence microscope at wavelengths of 450 – 490 nm (SYTO9) and 515 – 560 nm (propidium iodide, PI). A minimum of 5 images using the 20 $\times$  objective lens were taken randomly per surface. Green fluorescent bacteria indicated cells with an intact membrane, while red fluorescent bacteria indicated cells with a compromised membrane. The adherent bacteria were quantified using FIJI software (NIH) and the cell counter batch processing macro (APPENDIX A).

#### 2.2.2.2 BacTiter-Glo™ assay

After 3 h, 480  $\mu\text{L}$  of the bacterial suspension on each surface was transferred to a new opaque 24-well plate and 20  $\mu\text{L}$  from the suspension was mixed with 20  $\mu\text{L}$  of BacTiter-Glo™ assay reagent (Promega) to allow quantification of viable cells in the suspension. The test surfaces were washed gently with Tris-HCl buffer (pH 7.0), transferred to an opaque 24-well plate, and 20  $\mu\text{L}$  of BacTiter-Glo™ reagent was applied to each surface to allow quantification of adherent viable cells. Surfaces and suspensions were then incubated for 5 min before being transferred to a Tecan Infinite F200 PRO microplate reader to record the luminescence intensity (mode: luminescence; attenuation: automatic; integration time: 1000 ms; settle time: 0 ms). Standard curves were used to correlate the relative luminescence signal (RLU) to viable colony forming units (CFU) of the bacteria.

#### 2.2.3 Adhesion assay of trypsinised *E. coli*

Trypsin is a serine protease that is commonly used to remove proteinaceous moieties from the surface of mammalian cells. In this project, trypsin was used to study the importance of *E. coli* surface proteins in facilitating adhesion to the nanopillared surfaces. Bacterial broth cultures (16 h) were sub-cultured into 20 ml of pre-warmed TSB to OD<sub>600</sub> 0.1 and incubated at 37°C, 220 rpm to OD<sub>600</sub> 0.8. Aliquots (100  $\mu\text{L}$ ) of bacterial suspension were then mixed with 100  $\mu\text{L}$  of 0.5% trypsin in EDTA and incubated for 0 min (control), 5 min, 10 min or 15 min at room temperature. Bacterial cells were then washed three times in PBS buffer to remove excess trypsin and resuspended in PBS buffer to OD<sub>600</sub> 0.5. Aliquots (100  $\mu\text{L}$ ) of the cell suspension were added to

appropriate wells in 96-well plates and incubated for 3 hours at 37°C. Unbound cells were then removed, and the wells washed twice with 200  $\mu\text{L}$  PBS. Adherent bacteria were stained with 100  $\mu\text{L}$  of safranin for 15 min at room temperature and washed thoroughly with PBS. Stain was then released by the addition of 200  $\mu\text{L}$  of 10% acetic acid and biomass quantified by measurement of the optical density in a microtitre plate reader (BIORAD, iMARK) at OD<sub>490</sub>.

#### 2.2.4 Hydrophobicity assay

Bacterial broth cultures (16 h) were sub-cultured into 20 ml of pre-warmed TSB to OD<sub>600</sub> 0.1 and incubated at 37°C, 220 rpm to OD<sub>600</sub> 0.8. Cells were then harvested, washed twice in PBS buffer and resuspended to OD<sub>600</sub> 1.6 in either PBS, pH 7.0 (control) or 0.5%, pH 7.1 trypsin in EDTA (Gibco). After incubation at room temperature for 15 minutes, cells were washed three times with PBS buffer to remove excess trypsin, and resuspended in PBS to OD<sub>600</sub> 0.5. The relative hydrophobicities of *E. coli*  $\pm$  trypsinisation were then determined using the adhesion to hydrocarbon method. Cells (5 ml) were mixed with 500  $\mu\text{L}$  of hexadecane (or PBS for control) and incubated for 15 min at room temperature. The optical density (OD<sub>600</sub>) of the suspensions was then calculated and used to report the percentage of cells that did not adhere to the hydrocarbon. The relative hydrophobicity ( $R_{HP}$ ) was calculated using the following equation:

Equation 2.1: Relative hydrophobicity value

$$R_{HP} = \frac{OD_{600F}}{OD_{600i}}$$

where  $OD_{600F}$  is the final optical density of the suspension after 15 min incubation and  $OD_{600i}$  is the initial optical density before adding the hydrocarbon. These values represent the percentage of cells that did not adhere to the hydrocarbon and remained in the aqueous phase. The cells are considered relatively hydrophilic when the value is closer to 1 and relatively hydrophobic when the value is closer to 0.

## 2.3 Surface characterisation

### 2.3.1 Contact angle and surface wetting

A drop shape analyser (DSA100, KRÜSS) was used to measure the contact angle and surface energy of the surfaces. The measurement was performed at 25°C and relative humidity of 45%. The system was first calibrated, and the surface tension of water was recorded. A 2  $\mu\text{L}$  droplet of DI water, diiodomethane and glycerol was deposited onto the surface, and the resulting contact angles were recorded. The value of the contact angles was measured using a tangent

fitting method and a minimum of 30 measurements were automatically recorded by the KRÜSS ADVANCE 1.9.0.8 software. The resulting surface energy was calculated using an acid base Fowkes method, which is one of the most widely used models to calculate the surface energy of a surface from contact angles with more than one liquid.

### *2.3.2 X-ray photoelectron spectroscopy (XPS)*

The XPS experiment was performed at DESY, Hamburg, Germany, using monochromatic Aluminium K  $\alpha$  X-ray gun (photon energy 1486.6 eV, anode at 15 kV) as the incident radiation in an ultrahigh vacuum system with a pressure of  $1 \times 10^{-10}$  mbar. The sampling depth for XPS was approximately 10 nm with a dwell time of 0.1 s. The survey scans were collected from 0 to 1200 eV with a pass energy of 80 eV, or of 30 eV for high resolution scans. The charging effects were compensated using a flood gun. The elemental quantification was performed using CASAXPS software (V2.3.22).

### *2.3.3 Surface charge by dynamic light scattering (DLS)*

The zeta potential for bacteria and PET substrate was measured using Malvern Zetasizer Nano-ZS (Malvern Panalytical). For PET substrate, a very thin film (<1 mm) of the side of the polymer substrate comprising the nanopillars was carved using a scalpel and suspended in Milli-Q water. *E. coli* K12 cells were trypsinised, as described in section 2.2.3, and adjusted in PBS to OD<sub>600</sub> 1.0. Cells were then diluted 1:1000 before being vortexed and transferred onto a folded capillary zeta cell (DTS1070). The zeta potential was measured using Malvern Zetasizer software (Malvern V7.11) and collected using “general purpose” mode. Measurements were taken in triplicate from three independent experiments for both bacterial cells and the PET substrate.

## 2.4 Imaging analysis

### *2.4.1 Scanning electron microscopy (SEM)*

Samples with bacteria (prepared as per section 2.2.2) were fixed in 2.5% glutaraldehyde for 15 min at 4°C. Alcohol dehydration was performed using a serial dilution of 20%, 40%, 60%, 80% and 100% ethanol for 10 min each, before samples were dried using a critical point dryer. The samples were mounted onto 0.5' stubs (Agar Scientific) and sputter-coated with gold and palladium for SEM characterisation. The samples were imaged with FEI Quanta 200 with accelerating voltage between 10 kV to 20 kV at different angles and magnifications.

#### 2.4.1.1 SEM height analysis

SEM images (8-bit monochrome) with a grayscale (GS) unit were scaled linearly from 0 (black pixels) – 255 (white pixels) in FIJI software package. The line profile tool in FIJI uses the GS value as the y-axis, which can represent the height data. To estimate the height scale of the SEM image in a metric unit (i.e. nm), the arbitrary GS unit was converted to a metric unit using the information from the height data gathered from AFM or tilted SEM images (Figure 2.4). Multiplying the height GS unit ( $h_G$ ) with the conversion factor ( $C_F$ ) gave the height data in a metric unit ( $h_M$ ) as per the following equation:

Equation 2.2: Conversion of SEM greyscale value to metric unit

$$h_M = h_G \times C_F$$

where  $C_F$  is the ratio between the maximum GS value ( $G_{max}$ ) and maximum height value in nm ( $h_{max}$ ).

Equation 2.3: SEM unit rescaling conversion factor

$$C_F = \frac{h_{max}}{G_{max}}$$

This approach is only suitable on an image that contains structures made from the same materials, where the electron scattering and absorption are the same. It will give some approximation for the height of the nanostructures, but is not particularly accurate and may lead to false interpretation when using it on an image with more than two materials i.e. bacteria on the nanopillars or composite materials, due to differences in electron scattering and adsorption between different elements. Due to these limitations, this analysis was only used in this project to show relative differences in nanotopography where no complimentary AFM measurement was performed on the same samples.

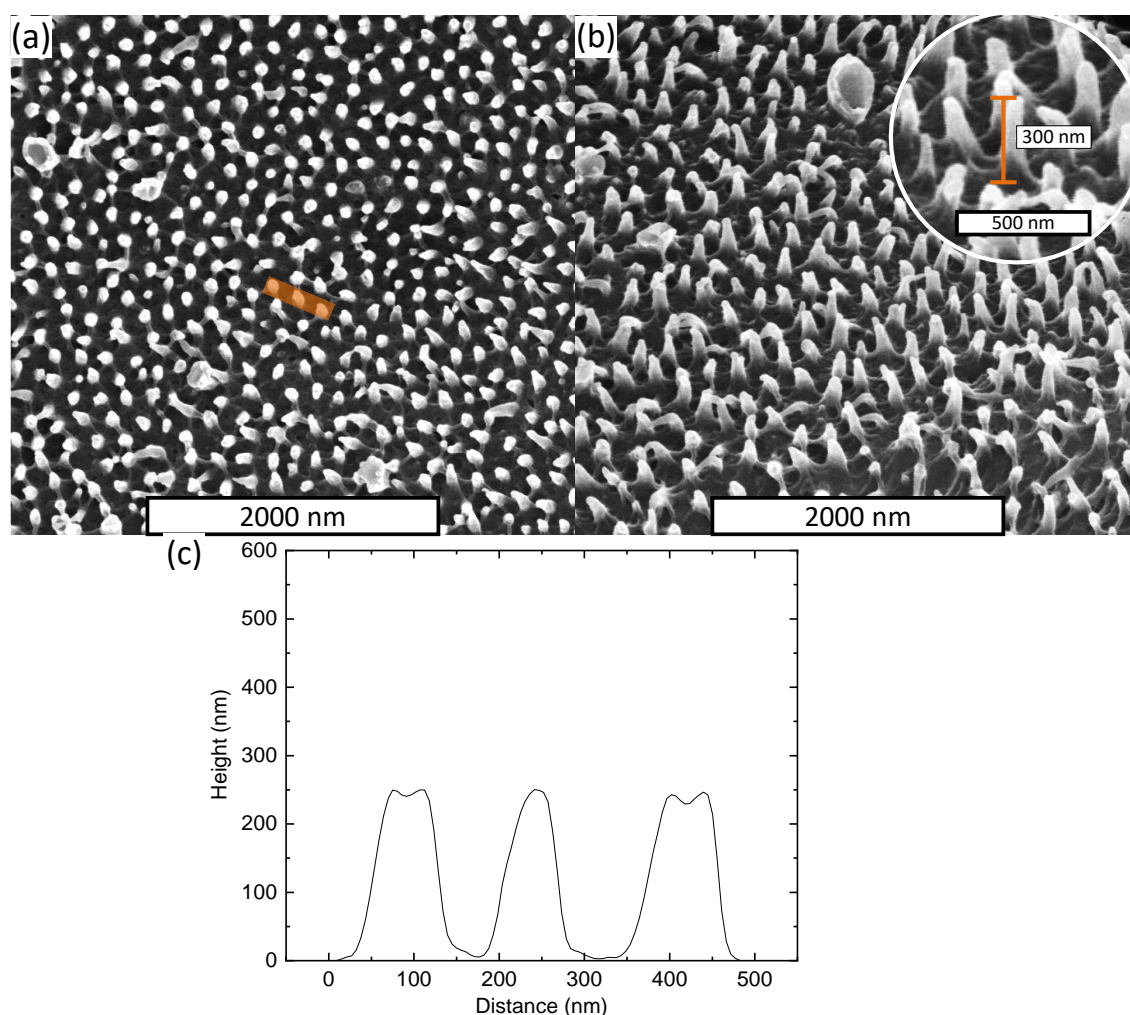


Figure 2.4 SEM height analysis. (a) Top view of hot embossed PET nanopillar surface; (b) 60° tilted SEM image of surface shown in (a). The inset is the magnified image to show the maximum height estimation from the tilted SEM image; (c) line profile of the nanopillars marked with a yellow line in (a), after converting the GS unit to nanometres.

#### 2.4.2 Focused Ion Beam (FIB) – SEM

Samples were prepared, as described in 2.4.1. After fixation, samples were washed in 0.1 M sodium cacodylate buffer ( $(\text{CH}_3)_2\text{AsO}_2\text{Na}$ ) and stained with 2% reduced osmium ( $\text{OsO}_4$ ) for 60 minutes on ice before being washed with DI water. The samples were also stained with thiocarbohydrazide (TCH), 2%  $\text{OsO}_4$  (aq), uranyl acetate and lead aspartate, with the samples washed thoroughly with DI water after each step. Finally, the samples were dehydrated using ethanol and critically point dried before imaging.

The samples were loaded into Scios DualBeam (FEI) chamber and the sample was aligned to be perpendicular to the gallium ion beam. The stage was tilted to 52°, and bacteria of interest were located using the electron beam with accelerating voltage of 5 kV and current of 50 pA. Once

found, the bacterium was first covered in 500 nm of protective platinum before a rough cut of trenches was milled around the bacterium with depths of 250 nm using an accelerating voltage of 30 kV and current of 1 nA. The bacterium was sliced sequentially with 30 nm thickness with an accelerating voltage of 5 kV and current of 47.5 pA, and images were acquired using the electron beam with an accelerating voltage of 5 kV and current of 98 pA. 3D models of each milled bacterium were reconstructed using Avizo modelling software (version 9.0.1).

## 2.5 Atomic force microscopy (AFM)

### 2.5.1 Colloidal probe AFM (CP-AFM)

To obtain accurate results for force measurement using AFM, four different calibration procedures were performed: (a) normal photodetector calibration, (b) lateral photodetector calibration, (c) normal spring constant calibration, and (d) torsional spring constant calibration. Information from these calibrations gave specific constant values i.e. deflection sensitivity ( $\delta_z$ ), horizontal deflection sensitivity ( $\delta_t$ ), normal spring constant ( $k_z$ ), and torsional spring constant, ( $k_t$ ), which were used to convert the raw AFM data. The raw AFM data were recorded in the unit of volt (V) and were converted to standard unit of force in Newton (N) using the measured constants.

A tipless cantilever (CSC36/tipless/AlBs, MicroMasch®) was first calibrated using thermal tuning method on Bruker Multi-mode 8. The calibration was a crucial step to determine the normal and torsional constant. The resonance frequencies and Q-values obtained from the cantilever tuning function in AFM software were used together with the dimension of the cantilever and radius of the colloidal probe to determine the normal and torsional spring constant. Normal force and shear force measurements were performed in air using Bruker Multi-mode 8. One silica colloidal particle with a diameter of 15  $\mu\text{m}$  was attached to a pre-calibrated tipless cantilever (CSC 36, MicroMasch HQ/tipless/AlBs, 65-130 kHz, 0.6-2.0 N/m) using a UV cured adhesive (Norland Optical Adhesive 68).

#### 2.5.1.1 Particle attachment

To prepare the colloidal probe, an aqueous dispersion of monodisperse spherical nonporous silica particles (SiO<sub>2</sub>-R-22.5, GmBH) was diluted with MilliQ water to 5% v/v, and 10  $\mu\text{L}$  of the diluted suspension was spread onto a glass slide and left to dry. A streak of UV curable glue (Norland Optical Adhesive 68) was placed onto the same glass slide, and an etched tungsten wire (tip diameter < 2  $\mu\text{m}$ ) was dipped into the glue and the glue was then transferred onto the calibrated tipless cantilever, which was also placed on the glass slide. A single silica particle was



selected under the microscope and picked up by a second clean tungsten wire. The particle was then placed carefully on top of the glue on the AFM cantilever. These steps were performed using a motorised micromanipulator (MicroStar Micromanipulator, Scientifica) (Figure 2.5). The glue was cured and the cantilever with the colloidal probe was cleaned in a UV-ozone chamber (42-220 UVO-Cleaner®, Jetlight Company, Inc) for 30 minutes. The colloidal probe was inspected to ensure it was free from excess glue before use with the light microscope and SEM (Figure 2.6).

The tungsten wire (diameter of 5 mm, Agar Scientific Limited, Essex, UK) was etched in 2 M KOH using the same set-up as the anodisation experiment (Figure 2.1). The applied potential was set at 30 V, the speed of mixing at 600 RPM, and time was varied to achieve different tip diameters (Figure 2.7).

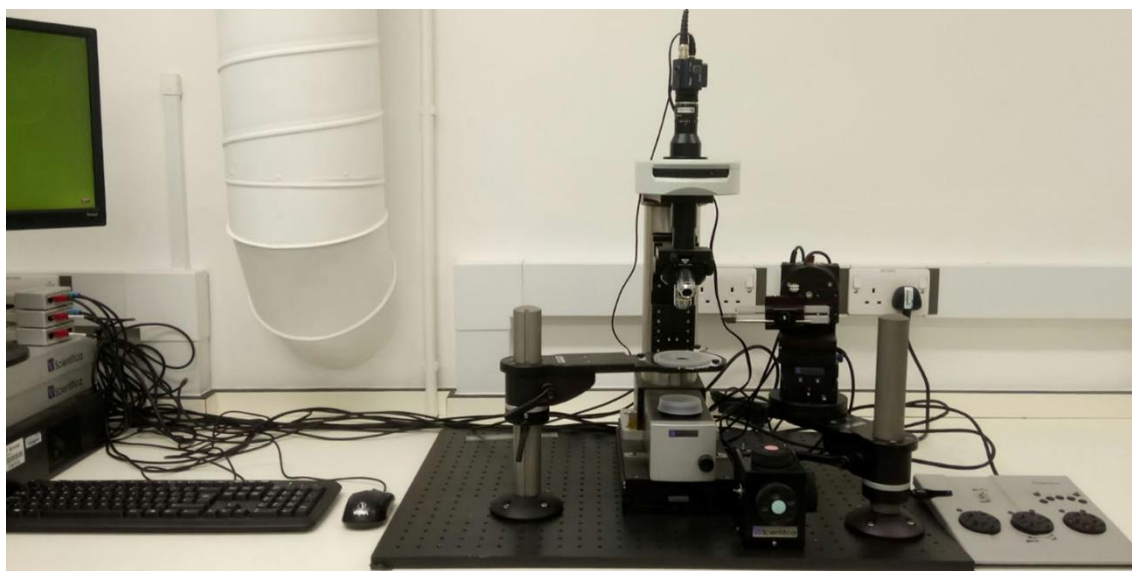


Figure 2.5 Image of motorised micromanipulator (MicroStar, Scientifica).

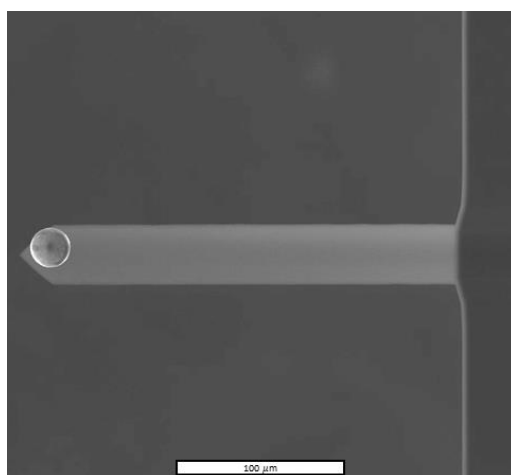


Figure 2.6 SEM image of 15  $\mu\text{m}$  silica probe attached to the tipless cantilever.

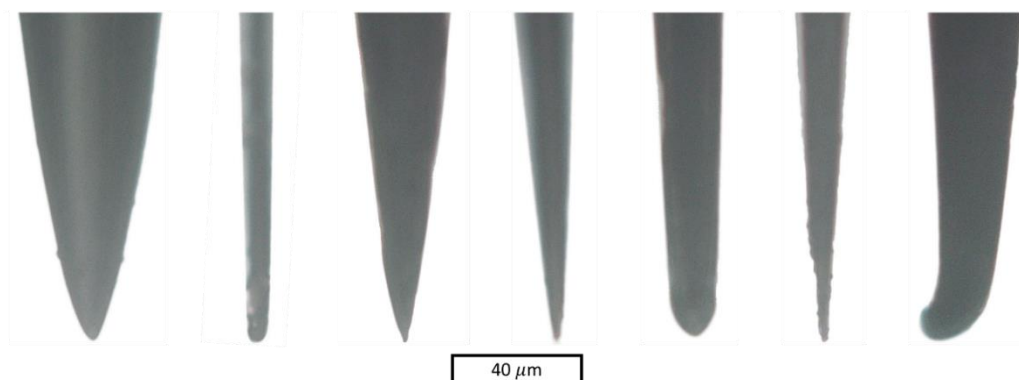


Figure 2.7 Etched tungsten wire with different tip diameters. Images were taken using the light microscope at 20x magnification.

#### 2.5.1.1 Photodetector calibration

The photodetector calibration was performed on a cleaned silicon wafer, since soft samples with comparable stiffness to the  $k_z$  of a cantilever will induce large errors due to sample deformation. Figure 2.8 shows a schematic of the laser positional movement on the photodetector. The photodetector had four quadrants, as shown as A, B, C, and D in Figure 2.8.

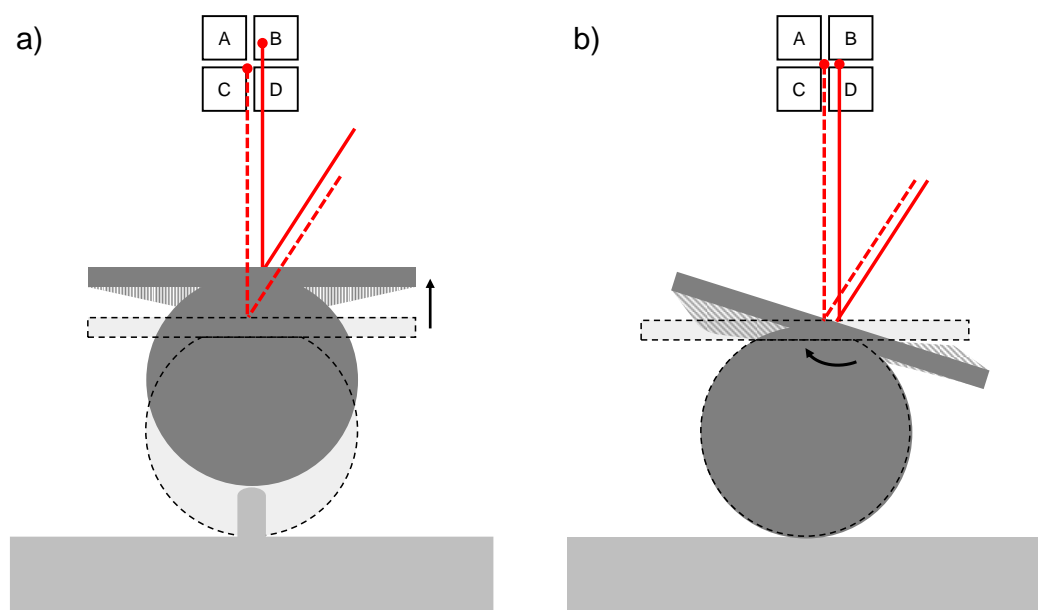


Figure 2.8 Schematic of the AFM photodetector. Hypothetical laser movement due to (a) normal and (b) torsional deflection of the cantilever is shown. The initial position of the laser is the dashed line and new position due to normal or torsional deflection is the solid line.

#### 2.5.1.1.1 Vertical/normal calibration

The normal direction was evaluated and normalised to the total signal by measuring the signal difference between top (A and B) and bottom (C and D) quadrants of the photodetector (Figure 2.8). The vertical signal,  $V$ , is expressed as:

Equation 2.4: AFM vertical signal relationship with the photodetector quadrants

$$V = \frac{(A + D) - (B + C)}{A + B + C + D}$$

This response was correlated to the sensitivity of the normal displacement experienced by the cantilever by assuming that the piezo movement and cantilever torsional bending were linear. The relationship was obtained by taking compliance region,  $S$ , vs. Z piezo movement, which gave the deflection  $d$ :

Equation 2.5: Relationship between cantilever deflection, compliance region and piezo movement

$$d = \frac{V}{S}$$

#### 2.5.1.1.2 Horizontal/lateral calibration

Horizontal photodetector sensitivity is less straightforward than the vertical calibration. Similar to evaluating vertical signal on the photodetector (Figure 2.8), the horizontal signal,  $H$ , was evaluated and normalised by measuring the difference between the left and right quadrants, which is given as:

Equation 2.6: AFM horizontal signal relationship with the photodetector quadrants

$$H = \frac{(A + C) - (B + D)}{A + B + C + D}$$

This response was then correlated to the torsional angles experienced by the cantilever. To accurately measure the torsional angles, the horizontal deflection sensitivity was first determined using Bogdanovic's method. This method was chosen to calibrate the horizontal deflection sensitivity due to its relatively fast and simple procedure.

First, the laser was aligned with the cantilever. Then, the cantilever was removed from the AFM head assembly and replaced with a mirror, which was tilted to 12° mounting angle to replicate the mounting angle of the AFM cantilever. The AFM head was remounted onto the AFM stage. One of the three AFM legs has a built-in motor and was controlled to change the angle of the AFM head. The AFM head was tilted by increments of 10 μm. The tilting of the AFM head

changed the horizontal signal on the photodetector and the corresponding values were recorded (Figure 2.9).

The relationship between the motor displacement  $l$ , leg displacement  $D$ , and the tilt angle  $\theta$  is given by the following equation:

Equation 2.7: AFM stage tilt angle equation

$$\theta = \tan^{-1}\left(\frac{l}{D}\right)$$

The tilt angle and the corresponding horizontal values were plotted, and the reciprocal slope was equal to the horizontal deflection sensitivity  $\delta_t$ . The relationship is expressed as:

Equation 2.8: AFM horizontal deflection sensitivity equation

$$\delta_t = \frac{\theta}{H}$$

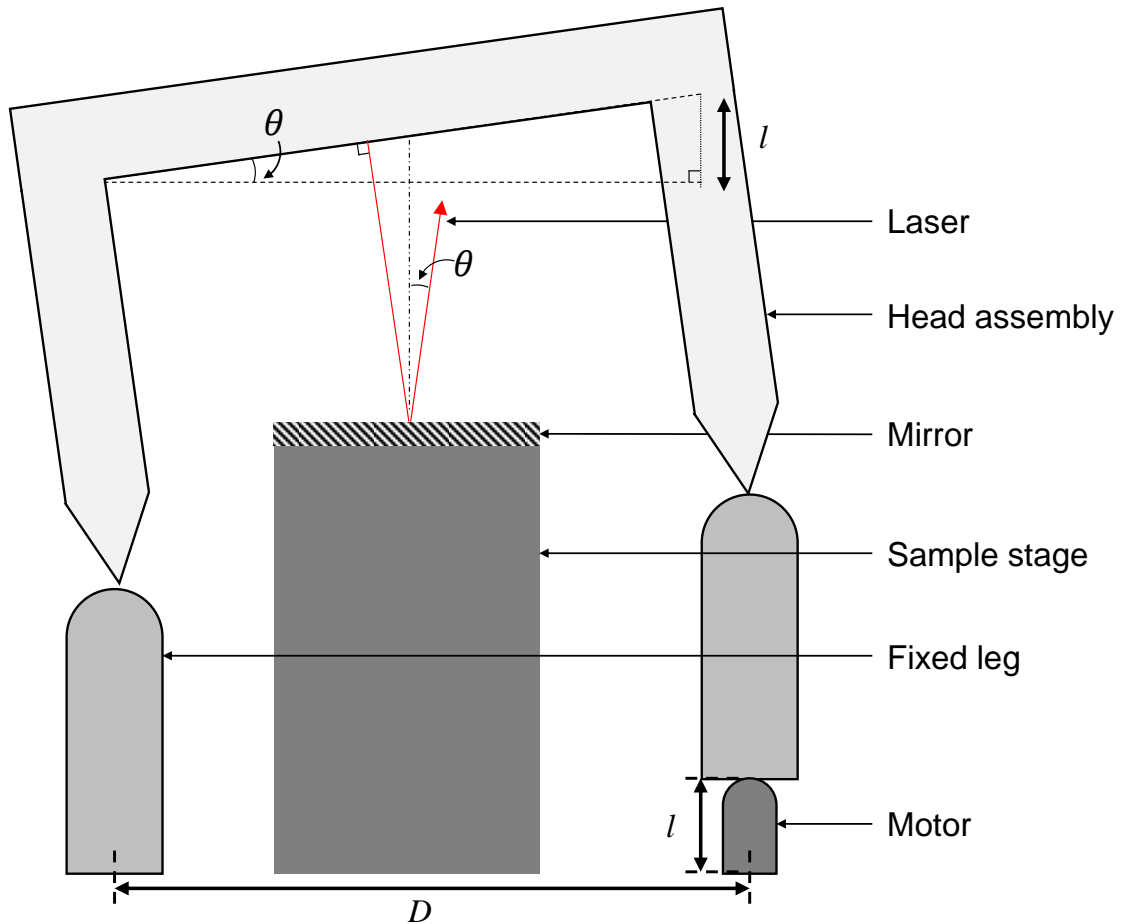


Figure 2.9 Schematic of Bogdanovic's method. This technique uses the relationship between the motor displacement  $l$ , leg displacement  $D$ , and the tilt angle  $\theta$  in calibrating lateral deflection signal to obtain the machine's horizontal sensitivity constant. The mirror was used instead of a cantilever for the reflection of the laser.

### 2.5.1.2 Spring constant calibration

#### 2.5.1.2.1 Normal spring constant

The normal spring constant was determined by using the thermal tune method, for which normal spring constant is determined from the unloaded resonance frequency. The normal resonance frequency was determined prior to particle attachment onto the AFM cantilever. First, the thermal noise of the detector was obtained by recording the normal detector signal variations. Then, fast Fourier transform was performed on the thermal noise data to obtain the resonance frequency of the spectrum. Signals due to high frequency noise (both ends of the spectrum) were removed by adjusting the bin width of the Fourier transform, and the resonance frequency was fitted by using Lorentzian function according to the following equation:

Equation 2.9: Lorentzian function

$$A(w) = A_{white} + \frac{A_o w^4}{(w^2 - w_r^2) + \left(\frac{w^2 w_r^2}{Q^2}\right)}$$

Then, the normal spring constant  $k_z$  was determined by using the dynamic approach, proposed by Sader *et al.*, which requires information on the physical dimensions of the cantilever, resonance frequency from the thermal tuning data, and surrounding fluid density, viscosity and quality factor during the calibration. Then  $k_z$  was determined using the following equation:

Equation 2.10: Normal spring constant equation

$$k_z = 0.1906 \cdot \rho_f b^2 L Q_f \omega_f^2 \cdot \Gamma_i(\omega_f)$$

where  $\rho_f$  is the density of the fluid,  $Q_f$  is the quality factor in fluid,  $\Gamma_i(\omega_f)$  is the imaginary component of the hydrodynamic function as a function of the resonance frequency in fluid,  $\omega_f^2$  is the mode resonant frequency of the cantilever,  $b$  and  $L$  are the width and length of the cantilever, respectively. To get an accurate result, the process to measure the spring constant was repeated three times. There are several other methods that measure the  $k_z$ . This method was chosen since it is fast, simple, non-destructive, and accurate.

#### 2.5.1.2.2 Lateral spring constant

For friction force measurement, torsional spring constant and normal spring constant are needed to calculate the friction forces from the raw data. A Hybrid model was used to calculate the torsional spring constant, which was developed recently by a group from KTH in 2013 [86].

The Hybrid model allowed much easier calculation, and combined the normal spring constant and the plate/beam theory to calculate the torsional spring constant. The Hybrid model used physical dimensions and mechanical properties of the cantilever such as length ( $L$ ), width ( $w$ ), Young's modulus ( $E$ ), and shear modulus ( $G$ ). The equation to calculate the torsional spring constant,  $k_t$ , according to the Hybrid model is:

Equation 2.11: Torsional spring constant equation using hybrid model

$$k_t = \frac{k_z 4L^2 G}{3E} \left\{ 1 - \left( \frac{w \cdot \tanh\left(\frac{L}{w} \sqrt{3\left(4 - \frac{E}{G}\right)}\right)}{L \sqrt{3\left(4 - \frac{E}{G}\right)}} \right) \right\}^{-1}$$

#### 2.5.1.3 Normal force measurement

Both pull-off force and friction force measurements were performed by using Nanoscope Multi-mode III AFM equipped with Picoforce scanner (Veeco Instruments, Ltd) to enable closed-loop operation in the normal direction. The force vs. distance curves were recorded over an area of  $4 \times 4 \mu\text{m}$ , and repeated at different areas of the sample. Typically, 20 curves were collected in each area. During normal force measurement, the AFM probe was moved vertically onto the surface by applying a voltage to the piezoelectric scanner, while the deflection of the laser from the cantilever was recorded by the software. Thus, the cantilever's deflection  $Z_c$  could be plotted against the relative displacement  $Z_p$ . The deflection of the cantilever could then be converted to the force experienced on the sample using Hooke's law, which is given below:

Equation 2.12: Converting cantilevers deflection signal to force value

$$F = -k_z Z_c$$

Force vs. separation curves were obtained by processing the raw data (Figure 2.10). Important data points and regions are highlighted in Figure 2.11. The equations used for the analysis are as follows:

Compliance region,  $\alpha = \Delta D / \Delta X$

Deflection,  $x = (X - Z) \times \alpha$

Separation,  $d = (D - C) - x$

Force,  $f_p = kx$

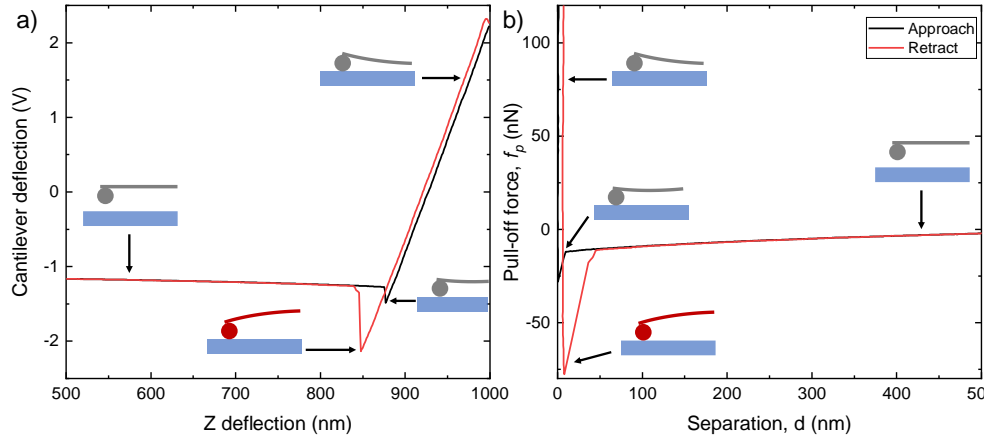


Figure 2.10 Interaction between the silica colloidal probe upon approaching and retracting from the flat PET surface. (a) Typical raw pull-off force data for PET flat surface with silica probe; (b) force vs. separation curve obtained after analysis of (a).

It is very difficult to establish the real contact region from the force-distance curve and assumptions need to be made carefully. In this analysis, three important assumptions were made which are: (1)  $\alpha$  is the hard wall region while (2)  $C$  is the assumed contact position, and (3)  $Z$  is the minimum deflection of the cantilever observed where  $\tan \theta = 0$ .

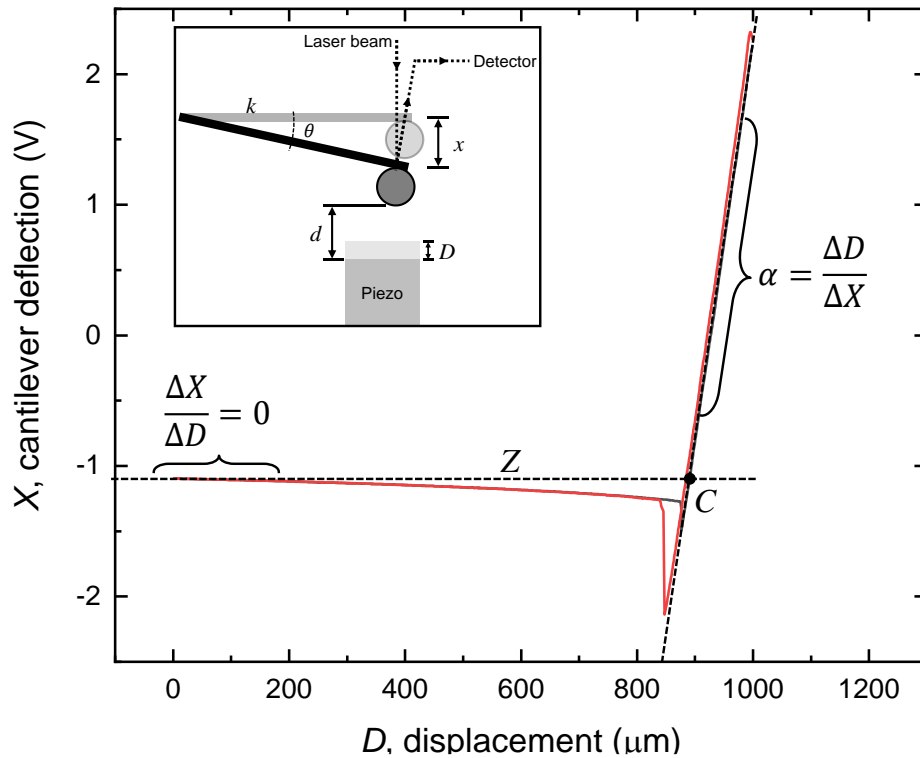


Figure 2.11 Important points and regions of the raw data for force vs. distance that were used for data analysis.  $\theta$  is the deflection angle of the cantilever,  $\alpha$  is the hard wall region,  $C$  is the assumed contact position,  $d$  is the distance between the piezo and the tip of the cantilever,  $D$  is displacement of the piezo,  $k$  is the spring constant of the cantilever,  $x$  is the deflection of the cantilever, and  $Z$  is the minimum deflection of the cantilever when  $\tan \theta = 0$ .

## 2.5.1.4 Friction force spectroscopy

AFM is capable of measuring lateral or friction forces between the tip of an AFM probe and the sample. When measuring the friction forces, the sample is sheared along the direction perpendicular to the cantilever long axis. As the probe is scanned across the sample, the cantilever experiences torsion, which causes the laser to deflect horizontally on the photodetector and the data is recorded by the AFM software (Figure 2.12).

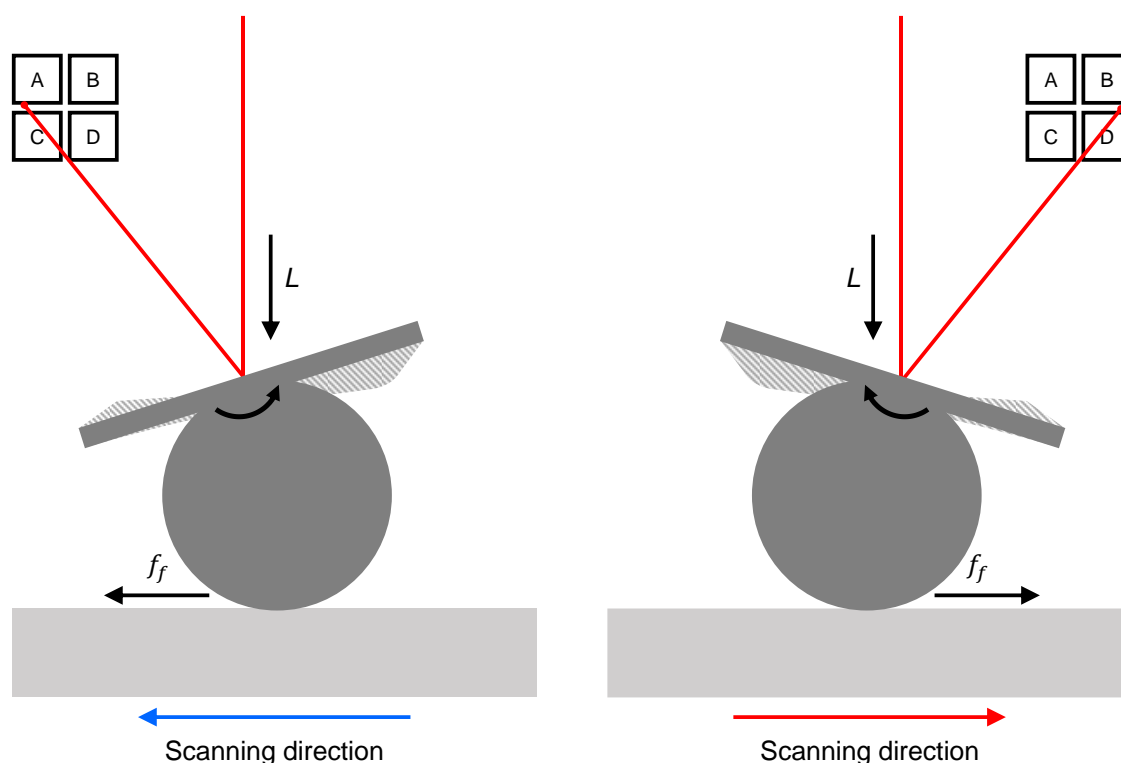


Figure 2.12 Schematic of friction force microscopy. The load force,  $L$ , is first applied and influences the friction force  $f_f$ , which causes the cantilever to twist on the long axis.

The laser is deflected from a distance  $\Delta V$  on the horizontal quadrant of the photodetector (left or right).

The deflection setpoint with respect to the normal force was first set to 0 V and kept constant by using the feedback loop control. Then, the trace and retrace data were collected by monitoring the lateral deflection of the cantilever at a scan speed of  $10 \mu\text{m} \cdot \text{s}^{-1}$ , while obtaining a rectangular scan area of  $1 \times 10 \mu\text{m}$  (512 points per line of 16 lines) with the scanning direction set to be perpendicular to the long axis of the cantilever. The deflection set point was increased up to 2.0 V with a 0.2 V step (loading) and decreased to 0.0 V with the same step (unloading). Each measurement was performed at two or more different locations per sample and each scan was repeated three times on different samples for each surface type. All measurements were



conducted in air at room temperature and relative humidity conditions of  $40\pm 10\%$ . The data obtained were analysed using OriginPro 2018b. For each frame, the mean and standard deviation of each shear trace were calculated by excluding the first and last 20 points of each trace. This was to eliminate instabilities introduced when the scanning direction was changed. The friction force was calculated using the following equation:

Equation 2.13: Converting shear signal data to friction force

$$f_f = \frac{\Delta V_{lat} k_t}{2\delta_t D_{tip}}$$

where  $\Delta V_{lat}$  is the lateral deflection of the cantilever that is half of the difference between the trace and retrace signal,  $k_t$  is the torsional spring constant,  $\delta_t$  is the torsional sensitivity, and  $D_{tip}$  is the diameter of the colloidal probe.

## 2.6 Data analysis

### 2.6.1 Statistical analysis

All statistical analyses were performed using Microsoft Excel (Microsoft 365). Viability data were analysed by ANOVA with a Tukey HSD post-hoc test and  $p$ -values of  $< 0.05$  were considered to be significant. Unless otherwise stated, bacterial viability data are representative of three experimental replicates ( $n=3$ ), performed in duplicate.

### 2.6.2 AFM imaging

Samples for AFM imaging did not require any specific sample preparation. Bruker Multi-mode III and VIII AFM coupled with a Nanoscope VII controller were used to take the AFM images. The samples were examined in tapping mode with ScanAsyst fluid cantilevers from Bruker bearing a silicon nitride tip of 40 nm diameter. The resonance frequency of the cantilever was measured at  $150\pm 50$  kHz and a spring constant of 0.7 N/m with back coating of titanium.

### 2.6.3 Young's Modulus measurement

*E. coli* K12 suspension ( $1\times 10^5$  CFU; 500  $\mu$ L) was incubated for 3 h on the nanopillared surfaces. The surfaces were then prepared as described in Section 2.4.1 for SEM imaging analysis. Following critical point drying, the samples were fixed onto magnetic stubs using sticky tape. A Multi-mode VIII AFM with Nanoscope V controller and PeakForce control mechanism were used. Nusense SCOUT cantilevers (tip radius of 5 nm, spring constant 21 – 42  $\text{N}\cdot\text{m}^{-1}$ ) were used to

measure the force-distance curve using the PeakForce system and data were analysed in real time by the Nanoscope V9.1 software to provide quantitative nanomechanical mapping (QNM) of the samples. The relative method was used to measure the Young's modulus,  $E_B$  of the bacterial cell wall. The system was calibrated to fit the known YM (*E. coli* cell wall is 2 – 3 MPa) using the Derjaguin, Muller, and Toporov (DMT) model. The  $E_B$  of a single bacterium was quantified by taking the average from scanning 3 small area of  $50 \times 50 \text{ nm}^2$ . Three repeats were performed per sample on three bacteria per surface type.

#### 2.6.4 Imaging analysis

The fluorescence images from LIVE/DEAD assay were processed to improve the contrast and saturation using image processing software before being imported into FIJI for quantification of the cells found per image. The quantification in FIJI was done through batch processing that involved finding the maximum threshold in an image per colour channel (red and green) (Appendix A: Batch processing to count cells or particles (FIJI)). The macro for batch processing in FIJI was developed by using the tutorial and guidance provided in the FIJI online community forum. The macro processing involved converting the .tiff to black and white data before adjusting the threshold to reveal individual particles (in this application, the particle was the bacterial cell). Watershading was applied to separate any attached bacteria. Finally, the counting was performed by locating the maximum threshold found in the image and the data was exported in .txt format. Batch processing eliminated user bias, especially for yellow/orange fluorescent bacteria, thereby enabling a more consistent and faster counting method compared to manual counting.

## CHAPTER 3 FABRICATION AND CHARACTERISATION OF BIOMIMETIC NANOSTRUCTURED SURFACES ON POLYMER SUBSTRATUM

This chapter will highlight the challenges faced and solutions devised to some of the problems encountered when making a reusable stamp and using this to fabricate nanostructured surfaces on different polymer substrates. Anodisation was chosen as the main technique to fabricate the nanopore stamp due to its versatility, cost effectiveness and its ability to produce a nanopattern that is similar to the one found on cicada wings. Hot embossing is a simple nanolithography technique and was used to make a nanopattern by moulding a soft polymer substrate with a hard stamp. Amongst other nanolithography techniques, hot embossing remains one of the cheapest and most highly scalable technique to fabricate nanostructured surfaces.

### 3.1 Optimisation of master stamp fabrication protocol

#### *3.1.1 Electropolishing: the effect of electrolytes*

Electropolishing is the preferred technique to polish a surface with minimal surface disturbance. The standard setup for electropolishing consists of an electrolyte, a cathode and a targeted sample at the anode. The electrodes are connected to an external power supply, which is controlled by a computer through a multimeter. Direct current is applied to the cell, where anodic dissolutions will result in levelling and brightening the anode surface [67,87]. The polishing behaviour is related to the formation of a viscous layer, which is also known as the anolyte layer, on the surface of the anode. The formation of the anolyte layer is due to the reaction between the metal and the electrolyte during the electropolishing process, and the layer becomes thinner at the peaks compared to at the valleys. This condition (thin at the peak, thick at the valley) means that the peaks have less resistance, with concentrated positive charge on their surface, resulting in higher current density than at the valleys. Due to the differences in local current density, the peaks will dissolve faster than the valleys, thus levelling the surface. The brightening and the mirror finished surface is due to formation of a thin film that follows the curve of the surface [67,88,89].

Three commonly used electropolish electrolytes were tested to find the best electrolyte for the setup used in this project (Table 3.1). Perchloric acid mixture is the most commonly used electrolyte to smooth an aluminium surface but was considered as the last option in this project due to safety concerns. Perchloric acid is a highly corrosive substance and can explode easily

when reacting with an organic material [90,91]. Thus, using the perchloric acid in an open cell setup may be dangerous if no safety precautions are made prior to use of the chemical. To comply with safety regulations, the electropolishing step with perchloric acid was performed in a closed fume hood and the electrolyte was covered with aluminium sheet to avoid any contamination.

Table 3.1 Electrolyte mixtures for electropolishing of aluminium that were tested during the optimisation phase.

Electrolyte	Temperature (°C)	Current density or potential	Time (min)	References
Perchloric acid + ethanol (1:4 v/v)	7	20 V	1-4	(10)
	30	160 mA/cm <sup>2</sup>	3.5	(11)
Phosphoric + ethanol + water (40:38:25 v/v)	60-75	5 mA/cm <sup>2</sup>	2	(12)
Sulphuric + water (4:1 v/v)	60	300 mA/cm <sup>2</sup>	10	(13)

The polishing results when using phosphoric acid and sulphuric acid mixtures were inconsistent between repeats. This inconsistency could be seen by the finishing appearance of the substrate and also from the current density vs. time plot, which showed fluctuation in the current profile (Figure 3.1(B-C)). Electropolishing using the perchloric acid mixture produced a better polishing finish and highly consistent results when compared to phosphoric and sulphuric acid mixtures. Figure 3.2 shows images of the as received aluminium sheet and the resultant electropolished aluminium sheet using the perchloric acid mixture.

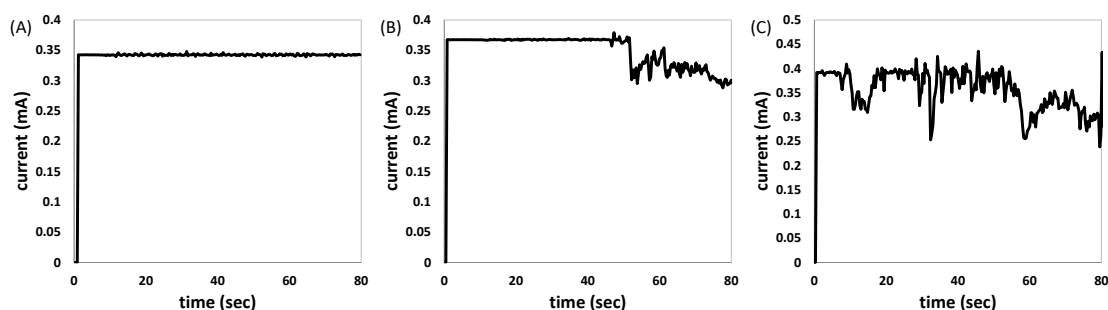


Figure 3.1 Electropolish profile for aluminium substrate. (A) perchloric acid mixture (7.0°C for 80 sec), (B) phosphoric acid mixture (70°C for 80 sec) and (C) sulphuric acid mixture (60°C for 80 sec). (A) shows the smooth and successful electropolish profile while (B) and (C) show inconsistency of the electrolyte, which is indicated by the fluctuation on the current profile.

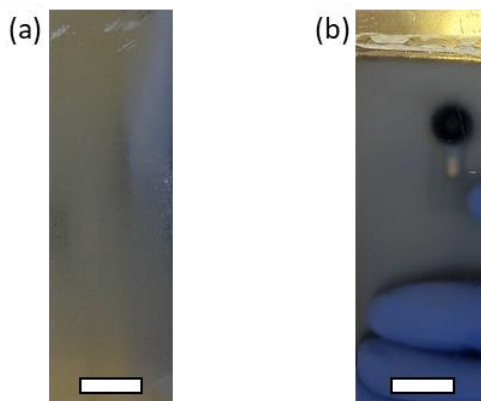


Figure 3.2 Comparison between as received and electropolished aluminium sheet. Optical images of aluminium sheet (a) before and (b) after electropolish in 1:4 v/v perchloric and ethanol mixture at 7.5°C at current density of 100 mA/cm<sup>2</sup> for 100 sec. (b) showed mirror polished reflection which is not present on (a). Error bar is 5 mm.

### 3.1.2 Optimisation of anodisation

There are at least four important anodisation parameters that influence the self-ordering of pore formation, which are the applied potential, types and concentration of electrolyte, anodisation temperature and agitation of the electrolyte. Each of these parameters were carefully studied in order to design a fabrication protocol that was efficient and cost effective.

#### 3.1.2.1 Potential

The applied potential,  $U$ , is one of the most important factors to control during anodisation. Previous studies have found that the interpore distance,  $D_{int}$ , has a linear relationship with  $U$  and can be expressed as:

Equation 3.1: Interpore distance general formula

$$D_{int} = kU$$

where  $k$  ( $nm \cdot V^{-1}$ ) is the proportionality constant ( $2.5 \leq k \leq 2.8$ ) [67]. To find the proportionality constant of 0.3 M oxalic acid at 4.5°C used in this project, 5 different applied potential were used and the resulting nanopores were imaged using field emission scanning electron microscope (FE-SEM) and analysed using FIJI software. The measured proportionality constant,  $k$  for 0.3 M oxalic acid used in this project was determine from the slope of  $U$  vs  $D_{int}$  (Figure 3.3) where  $k = 2.55 \text{ nm} \cdot V^{-1}$ . This value is in line with the range of proportionality constant reported in the literature [67].

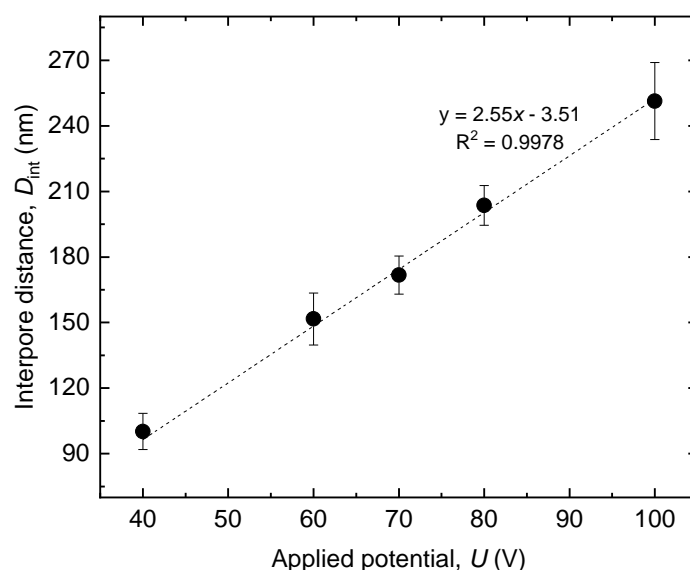


Figure 3.3 Applied potential and the resulting interpore distance for 0.3 M oxalic acid at 4.5°C in open cell setup. For each sample at different applied potential, 5 SEM images (size of  $10 \times 10 \mu\text{m}^2$ ) from 2 different batch of nanopores were used to quantify the interpore distance using the particle distribution plugin from BioVoxxel on FIJI software (V1.52p). Data indicate mean values  $\pm$  standard deviation.

### 3.1.2.2 Electrolyte

The concentration and the type of electrolyte are important parameters to obtain self-ordered pore growth where the formation of the nanopores will be highly consistent within the self-ordered regime for a specific concentration of the electrolyte. Generally, the self-ordered regime for sulphuric acid (0.3 – 6 M) is at the low potential anodisation (5 – 40 V), while oxalic acid (0.3 – 0.5 M) is at medium potential anodisation (30 – 120 V), and phosphoric acid (0.2 – 0.3 M) is at high potential applications (80 – 200 V) [67]. This restriction is due to the pH and conductivity of the electrolyte. For example, a low pH value has a low potential threshold to assist field enhanced dissolution during pore formation, which makes pH one of the parameters that can influence the diameter of the pore. Thus, for an application that requires large pore diameters, it is recommended to use a high concentration of phosphoric acid due to its high conductivity. To form a small pore diameter, oxalic acid or sulfuric acid at a low concentration should be considered [67,92]. In this project, two acid solutions were tested as the electrolyte for anodisation which were the 0.3 M oxalic acid and 0.4 M phosphoric acid for potentially generating very dense or widely sparse nanopores. It was found that oxalic acid solution gives the most consistent results within the self-ordered regime while the phosphoric acid showed non homogenous pattern across the aluminium sheet (Figure 3.4).

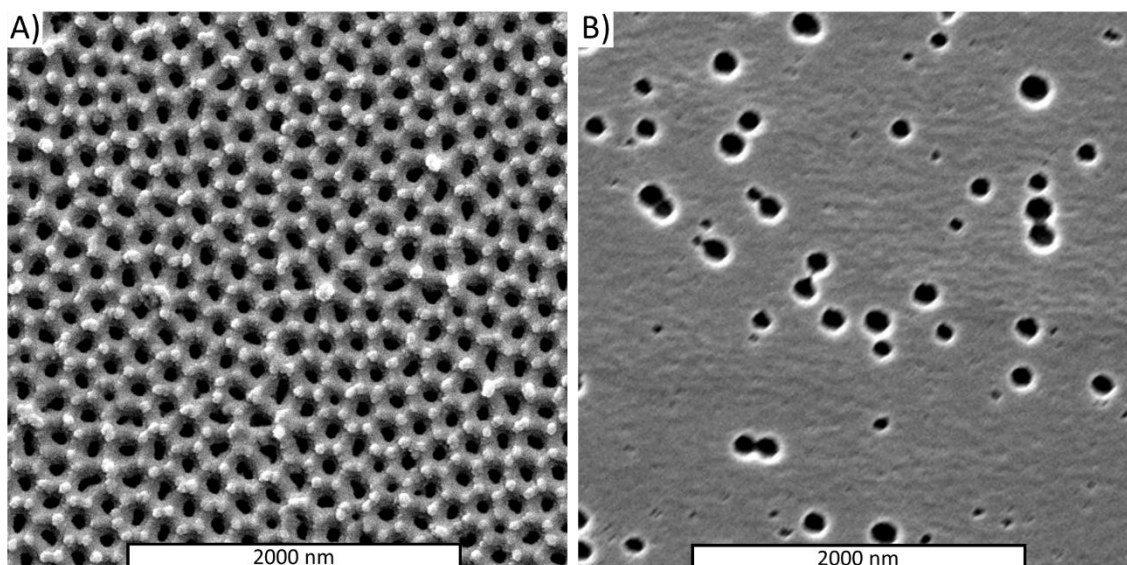


Figure 3.4. Comparison between 0.3M oxalic acid and 0.4M phosphoric acid for anodisation (A) Highly ordered nanopores formation when anodising with 0.3 M oxalic acid at 4.5°C and applied potential of 40V for 2 h. (B) Non-homogenous pattern of nanopores when anodising using 0.4 M phosphoric acid at 30°C and applied potential of 90V for 2 h.

### 3.1.2.3 Temperature

The temperature during anodisation should be maintained at below room temperature to prevent complete dissolution of the formed oxide layer. The temperature of anodisation is often kept at a very low temperature (0 – 10 °C) to avoid local heating at the bottom of the pores during anodisation. If the local heating is not well controlled, it could lead to excessive dissolution of the pores and may cause electrical breakdown of the oxide due to inhomogeneous electric field distribution (Figure 3.5). However, it is important to note that if the temperature is too low, some of the low concentration electrolyte may freeze and the growth rate of the oxide layer will be slower [67].

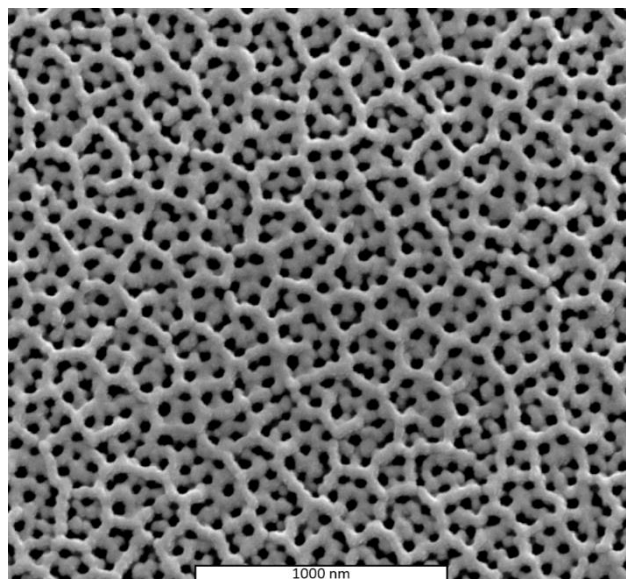


Figure 3.5 Effects of temperature on anodisation. Anodisation of aluminium sheet at 7.5°C in 0.3 M oxalic acid with potential of 40V showing retarded dissolution of the oxide layer. Typical temperature for anodisation in oxalic acid at 40V is 4.5°C (Figure 3.4A).

#### 3.1.2.4 Agitation

Under a constant current density regime, dissolution of the pore cell walls of alumina is influenced by temperature. Previous studies on the effect of stirring [67] showed that low stirring speed will increase local field assisted temperature, which will increase the rate of oxide dissolution and formation [67]. Figure 3.6 shows example of excessive dissolution on the oxide layer due to low stirring speed. With this in mind, the agitation method of choice that is compatible with the use of glass beaker is by using the magnetic stirrer. Few considerations were given when choosing the right speed of the magnetic stirrer. Firstly, the resulting nanopores of anodisation is dependent on the size of the vortex of the electrolyte where the aluminium sheet and the counter electrode were placed on the edge of the vortex where the stirring speed is the strongest and the most consistent. The size of the vortex is dependent on the size of the stirrer and the beaker, the volume of the electrolyte and the speed of the stirrer. It was found that the optimal parameters that will give a good agitation to control the dissolution of the electrolyte is by using a 1 L beaker with opening diameter of 85.4 mm, 1 L of electrolyte, 24.5 mm magnetic stirrer and 700 RPM of magnetic stirrer speed.



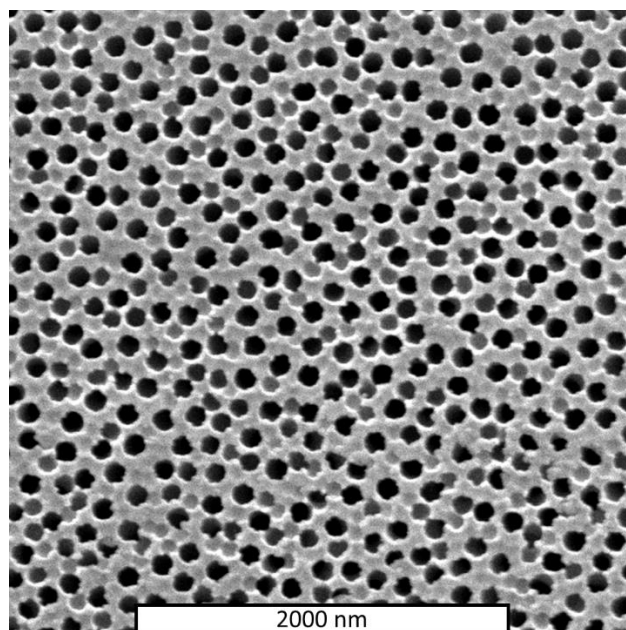


Figure 3.6 Effects of low stirring speed on anodisation. Anodisation of aluminium sheet at 4.5°C in oxalic acid with potential of 40V at 100 RPM stirring speed with 20mm stirrer showing excessive dissolution of the oxide layer. The optimal stirring speed used in this project is 700 RPPM with 24.5 mm magnetic stirrer.

### 3.1.3 Two-step anodisation: the effect of first-step time

A typical two-step anodisation technique has a very long first-step anodisation time to achieve high order and uniformity of the nanopores. However, to improve the efficiency of the processing, a shorter anodisation procedure should be adopted. Anodisation over 16 hours will require a longer chromic acid oxide layer etching time (around 4 hours), before the aluminium substrate can be used for the second-step anodisation. To completely fabricate one piece of  $1 \times 3 \text{ cm}^2$  AAO will require approximately 22 hours to yield only 3 stamps for subsequent nanopillar fabrication.

A systematic study was conducted to find out if any significant difference in nanopore structure would occur using long vs. short first-step anodisation times. The time for the first-step anodisation was varied while other parameters including conditions during chromic acid etching and second-step anodisation were kept constant for this study. The SEM images of AAO produced at two different first-step anodisation times are shown in Figure 3.7. It can be seen that there was no significant difference in terms of pore size and regularity between the 16 h anodised and much shorter 4 h anodised AAO. The 4 h anodised AAO still exhibited the uniform hexagonal unit pattern across the whole surface without any significant variation. Similar observations were reported by Zaraska *et al.*, following quantification of the regularity of the

nanopores by performing a 2D fast Fourier transform (FFT) analysis on the FE-SEM images. No significant differences were found between anodising times of 16 h, 12 h, 8 h and 4 h [93].

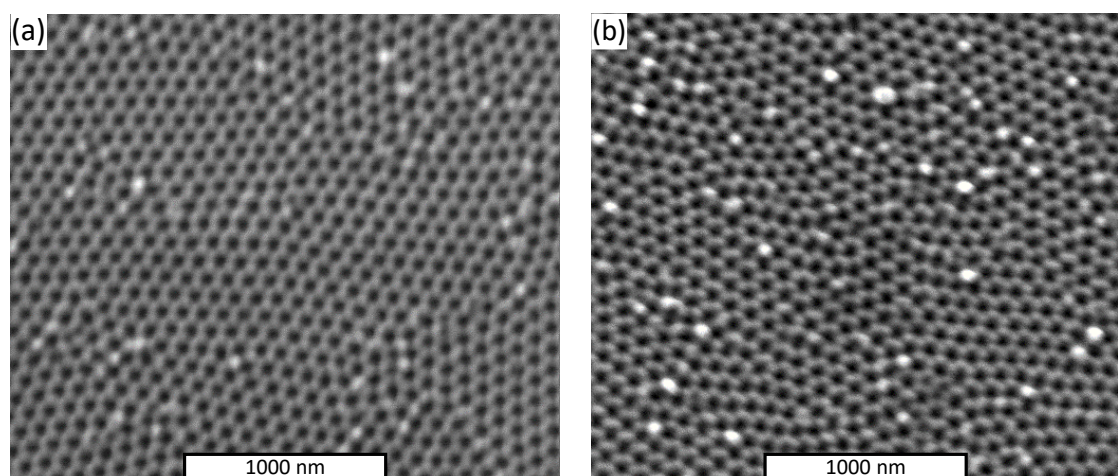


Figure 3.7 SEM images of AAO produced using different first-step anodisation times. (a) 16 h and (b) 4 h. Note that there are no significant differences in terms of size and regularity of the resultant nanopores.

#### 3.1.4 Considerations for scaling up

There are many advantages when using an anodisation/electrochemical cell for any electrochemical process because (1) humidity and temperature are well controlled within the container and (2) since the sample is placed at the bottom of the cell (Figure 1.10), these conditions allow the dissolution of the aluminium to be well controlled, which reduces the chance of forming unwanted defects on the aluminium surface [76]; and (3) anodisation can be performed confidently over several hours (> 4h) without worrying about changes in temperature [67]. Development of water droplets on the aluminium substrates over long hours of anodisation is inevitable when using an open cell setup due to condensation of water molecules from the surrounding area due to the presence of a large water bath (Figure 3.8a,b). The formation can be explain using the standard water vapour diagram (Figure 3.8c). For example, if the air temperature of 20°C and 50% relative humidity (RH) (point A) is touching a solid surface with a temperature of 9°C or less (point B), condensation will likely to occur [94].

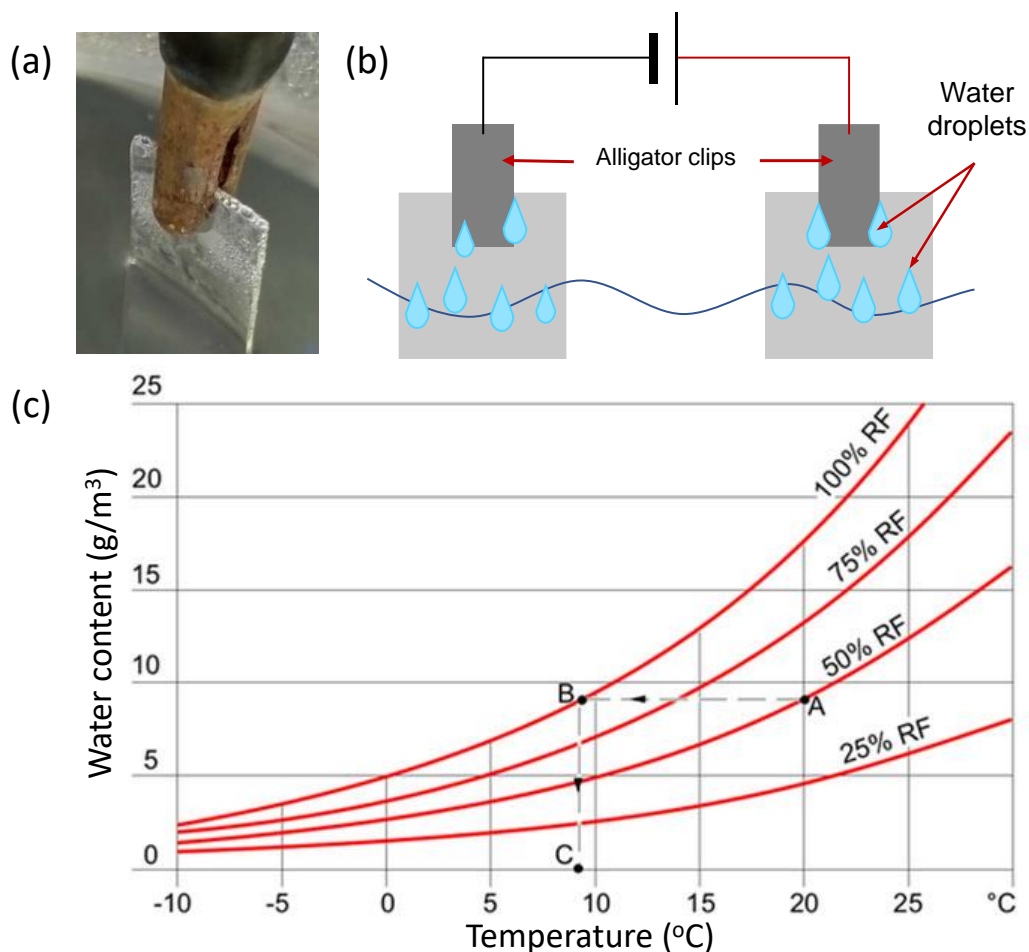


Figure 3.8 Humidity problem during long anodisation process in a beaker. (a) Water droplets were observed after 40 minutes of anodisation at 4.5°C when the relative humidity was above 40%. (b) Schematic to show a possible secondary reaction where the water droplet could serve as a weak secondary electrolyte. (c) Water vapour diagram (from ref (4)) that shows possible condensation of water at 25%, 50%, 75% and 100% relative humidity (RF) with respect to ambient temperature and water content, from [94]. For example, consider a room with a water content of 9 g/m<sup>3</sup>, air temperature of 20°C and air humidity of 50% RF (point A). If the air is cooled down to 9°C or below, and the water content remain constant at 9 g/m<sup>3</sup>, the humidity will reach 100% RF (point B). At this point, condensation on a solid surface with a surface temperature of 9°C (point C) is likely to occur.

There are a few limitations to using the anodisation cell to prepare a high volume of samples:

- (1) The sample size that can be used is very small, usually restricted to 10×10 mm<sup>2</sup>, resulting in a longer production time in comparison to the open electrochemical setup;
- (2) Changing a different aluminium substrate and electrolytes is also troublesome and time consuming, which will add further hours to the formation of a stamp, making the whole fabrication process less efficient.

All the limitations associated with using an anodisation cell can be addressed when anodising the aluminium substrate in an open cell setup, utilising a glass beaker instead of PTFE container. In this project, various sample sizes were tested and the largest sample that was successfully anodised was a  $30 \times 60 \text{ mm}^2$  aluminium sheet in a 1 litre glass beaker. For open cell setup, the limitation for the sample size depends on the size of the container. For this reason, this method is preferred in industry where large sheets of metal can be processed in a very large container (3). Another advantage with open cell setup is that the changing of the sample is straight forward and does not involve constantly handling the electrolyte, which can introduce contaminants to the electrolyte. For example, electrolytes for anodisation can be prepared in a separate beaker while waiting for the electropolishing step. Then, the electrolyte can be changed by simply removing the beaker containing the electropolishing electrolyte from the water bath and replacing it with a beaker containing the anodisation electrolyte.

As discussed earlier, since the temperature of the electrolyte is not well controlled in an open cell setup, there is a chance of unstable dissolution of the oxide layer occurred during anodisation, especially at the top of the beaker where the local temperature can be affected by the humidity and room temperature. To reduce these undesired effects, anodisation was only run for a maximum of 4 hours instead of 16 hours in this work. The effects of the first-step anodisation time have been discussed in section 3.1.3. Therefore, apart from the reduced anodisation time, an aluminium lid was also placed at the top of the beaker to minimise the effects of condensation, while the exposed area at the top of the aluminium was removed before hot embossing.

### *3.1.5 Tuning interpore distance by using phosphoric acid*

Common etching solutions used to widen the pore diameter of AAO are 0.1 M phosphoric acid, 0.1 M phosphoric acid and 0.3 M oxalic acid. For this experiment, phosphoric acid was chosen as the preferred etching solution since it gave the most consistent results with our setup.

A standard curve for phosphoric acid etching was developed in order to find the aluminium oxide etching rate. The standard curve did not have a linear relationship between etching time and the pore diameter as previously reported in the literature but rather a quadratic relationship between the pore diameter and etching time (Figure 3.9). This is potentially due to differences in terms of the size of the aluminium substrate, stirring condition and volume of the acid used. Once the standard curve was established, the time needed to widen the pore from 40 nm to 80 nm could be calculated by using the best fit line equation:

Equation 3.2: Best fit line of the standard curve for AAO etching in  $\text{H}_3\text{PO}_4$

$$y = 0.0169x^2 - 0.2081x + 37.8$$

where  $y$  is the final diameter of the intended nanopores and  $x$  is the etching time.

The etching rate in this study was 1.2 nm/min at 30°C while the electrolyte was stirred compared to 0.6 nm/min at 30°C reported by Kim *et al.* [71]. This discrepancy may have been due to better heat distribution at the surface of the AAO with the agitated electrolyte, which helped with the distribution of heat.

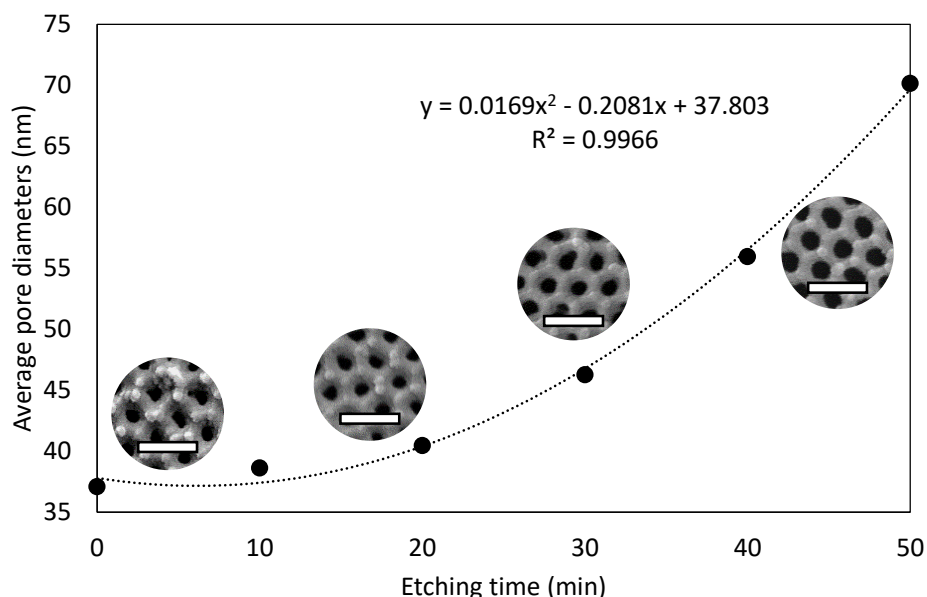


Figure 3.9 Standard curve for 0.1 M phosphoric acid aluminium oxide etching at 100 rpm with 2 cm stirrer and temperature of 30°C. Scale bar is 100 nm.

### 3.1.6 Nanopillar design

#### 3.1.6.1 Guidance from the theoretical models

One of the aims of this project is to answer the fundamental question regarding parameters that are the most important when designing contact killing antimicrobial surfaces. Common arguments in the literatures on the most prominent features to consider when aiming for higher anti-microbial activities are the sharpness and density (or interpillar distance) of the nanopillars [21,32,52–54,95,96]. Ivanova *et al.* [21], Kelleher *et al.* [95], and Dickson *et al.* [53], have experimentally found that denser nanopillars will have higher killing efficiency. While other

study have proposed a different bactericidal mechanism that is not based on the stretching theory [24]. Instead, Bandara *et al.* proposed a mechanism that considers the bending of the nanopillars upon adhesion which then inducing shear stress to the cell and makes the cell wall to wrinkle that lead to cell lysis [24].

The theoretical models from Xue *et al.* [32] and Li *et al.* [54] showed that both models are consistent with the results from literatures for nanostructured surfaces found on cicada wing or the biomimetic surfaces where the diameter of the nanotopography is between 75 nm – 200 nm, and pitch is 175 nm – 250 nm. However, Xue *et al.* have found that by assuming the curvature of a deform bacterial membrane to be parabolic and considering the effects of gravity and van der Waals forces, their model suggested that sharp and widely sparse nanopillars will have enhanced bactericidal performance if the diameter less than 10 nm and pitch of the nanopillars is more than 800 nm. On the contrary, Li *et al.*, suggested that surfaces with diameter between 40 – 80 nm and pitch of 100 nm will have the highest degree of membrane stretching compared to nanostructured surfaces found on cicada wing. Thus, similar to the experimental studies, there are discrepancies between different theoretical models on the potential mechanisms involved during bacterial cell death on nanostructured surfaces.

This project is also aimed to get a better understanding on the effects not only from the nanotopography but also the surface wetting, surface energy, as well as nanotribology and mechanical properties of the nanopillared surfaces. Li *et al.* have proposed a phase diagram which show interrelated effects of nanopillar radius and density on the bactericidal performance of the surface (Figure 3.10) [54]. The phase diagram helps to narrow the design direction when fabricating a contact killing surface. The different colours on the phase diagram indicates the theoretical stretching degree of the bacterial cell wall where blue region is the suppression phase where there is no stretching on the cell wall of the bacteria while the red region is the enhancement phase which has high degree of the cell wall stretching. From the phase diagram, 3 different surface designs were chosen to (1) show the interrelated effects of the nanopillar diameter and spacing and (2) to test the validity of the theoretical model against experimental results.



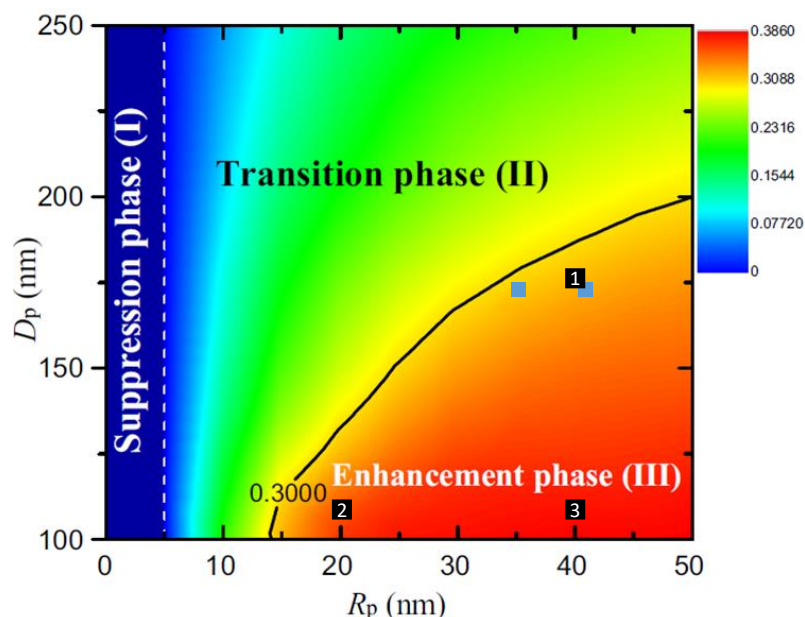


Figure 3.10 Phase diagram proposed by Li. *et al.* Graph shows the differences in the stretching of a bacterial membrane that is influenced by the radius and spacing of the nanopillars. The colour bar indicates the level of stretching for the membrane, with red indicating the highest values in the enhancement phase and blue the lowest values in the suppression phase, from [54]. The blue squares represent results from Ivanova *et al.* and Dickson *et al.*. Black square 1 represent blunt and wide nanopillars (BWN), square 2 represent sharp and dense nanopillars (SDN) and square 3 represent blunt and dense nanopillars (BDN).

In this project, 3 different surfaces were carefully designed to have sharp and dense nanopillars, blunt and dense nanopillars, and blunt and sparse nanopillars. Justification for the design choice of these nanopillared surfaces is as follows:

#### 3.1.6.2 Blunt and sparse

Blunt and wide nanopillared surface (BWN) was designed to mimic the nanopillars found on the cicada wing (*P. claripennis*) with a diameter of 80 nm and spacing of 170 nm. Recent studies in mimicking cicada wing surfaces had shown that a polymer surface copied from the cicada wing had relatively low bactericidal properties, killing only around 30% of the adhered bacteria [53]. This BWN surface therefore provided direct comparison to the cicada wing surfaces that had been reported in the literature.

#### 3.1.6.3 Sharp and dense

Sharp and dense nanopillared surface (SDN) was designed to have the sharpest (diameter = 40 nm) tip width of the nanopillared surfaces tested and the surface with the greatest number of pillars per unit area. According to theoretical phase diagram from Li *et al.*, this surface would be

expected to have significantly higher bactericidal efficiency when compared to the flat surface and the BWN surface [54].

#### 3.1.6.4 Blunt and dense

Blunt and dense surface nanopillared (BDN) was theoretically predicted to have the best bactericidal performance according to the phase diagram with a density of 100 pillars per  $\mu m^2$  and tip width diameter of 80 nm. However, according to Xue *et al.*, sharper nanopillars with the same density will perform better because the bacterial surface tension will increase, which can cause the rupturing of the cell wall. Comparison of the SDN surface with the BDN surface would therefore shows any relationship between sharp and dense surface with blunt and wide surface that can be better explored (Figure 3.11). In general, this surface shared the same density with SDN and the same diameter with BWN [32].

Another parameter that is considered as a potential key feature affecting the bactericidal properties of nanopatterned surfaces was height. However, the aspect ratio (AR) of the nanopillars had been found to be more relevant compared to height due to possible changes in the material's mechanical properties i.e. Young's modulus  $E$ , which is influenced by the AR of the material rather than the height [97].

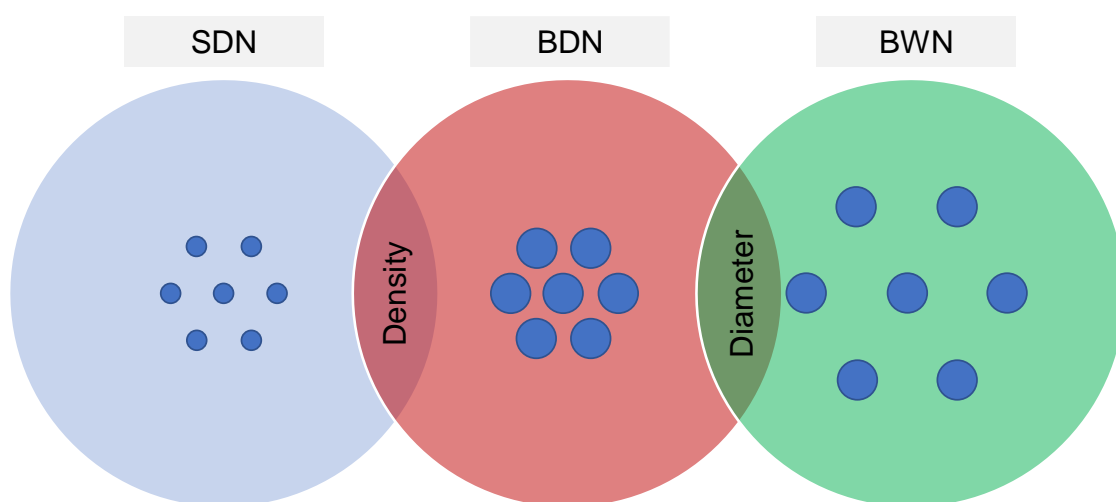


Figure 3.11 Linear Venn diagram of the three test surfaces to show the comparison between each surface. The small blue circles show the relative differences in diameter and density of the nanopillars between each surfaces. Dimensions drawn to scale.



## 3.1.6.5 The making of master stamp

After the design was finalised, the master stamps were fabricated using the two step anodisation. The SDN and BDN stamps were anodised at 40 V in 0.3 M oxalic acid for 4 h while BWN stamps were anodised at 70 V for 4 h. Then, the oxide layer from the first anodisation were removed using chromic acid solution for 2 h at 40°C. SDN and BDN were anodised at 40 V for the second anodisation step for 150 sec and 250 sec, respectively while BWN was anodised at 70 V for 100 sec. The nanopores on BDN was widen by etching in 0.1 M phosphoric acid at 30°C for 55 min. Table 3.2 summarise the anodisation step and Figure 3.12 showed the difference between each master stamp.

Table 3.2 Anodising conditions used to fabricate the master stamp in 0.3 M oxalic acid solution at 4.5°C

	Anodising step		
	First anodisation	Second anodisation	H <sub>3</sub> PO <sub>4</sub> etching
SDN	40V, 4h	40V, 150sec	N/A
BDN	40V, 4h	40V, 250sec	55 min
BWN	70V, 4h	70V, 100sec	N/A

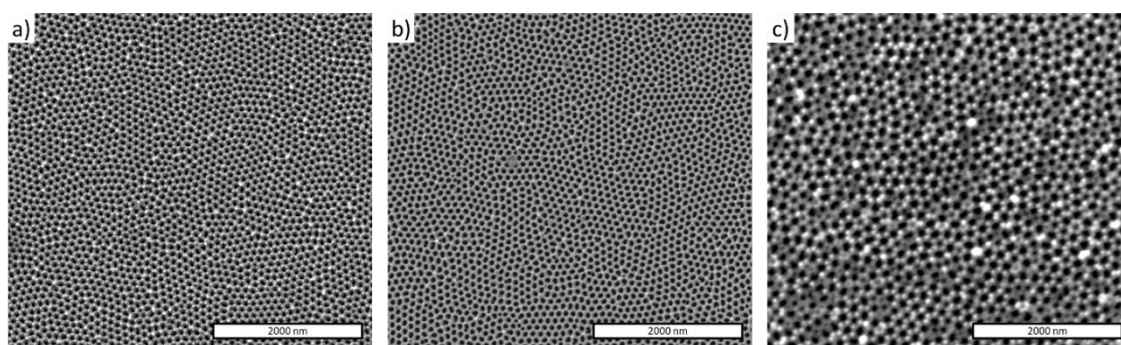


Figure 3.12 SEM images of the master stamps used in this experiment. (a) sharp dense nanopillars (SDN), (b) blunt dense nanopillars (BDN) and (c) blunt wide nanopillars (BWN)

## 3.2 Optimisation of hot embossing

### 3.2.1 Systematic assessment of hot embossing parameters

Hot embossing or nanoimprint lithography is a technique that works through mechanical deformation of a thermoplastic by heating the sample above its glass transition temperature ( $T_g$ ), with the nanostructure formed by applying a certain pressure. Embossing requires three components to work: (1) a patterned stamp, (2) a thermoplastic or printable material, and (3) equipment to control the pressure and temperature. The template/mould/stamp that is used in this project was an anodised aluminium oxide (AAO) nanoporous substrate that has been discussed earlier.

Hot embossing has four basic steps (Figure 3.13). First, the stamp and the polymer substrate are heated above the  $T_g$  of the polymer substrate, meaning that the polymer will behave as a purely viscoelastic material, which will help it to deform inside the stamp (region a). Then, the AAO stamp is pressed against the polymer substrate at a desired pressure, causing the substrate to respond with a squeeze flow and the reverse pattern from the stamp to be formed on the polymer substrate (region b). Finally, the system is cooled down below the substrate  $T_g$  while maintaining the pressure to relax any stress and to prevent the polymer from flowing back (region c). The polymer substrate is then removed from the AAO stamp (region d) (26).

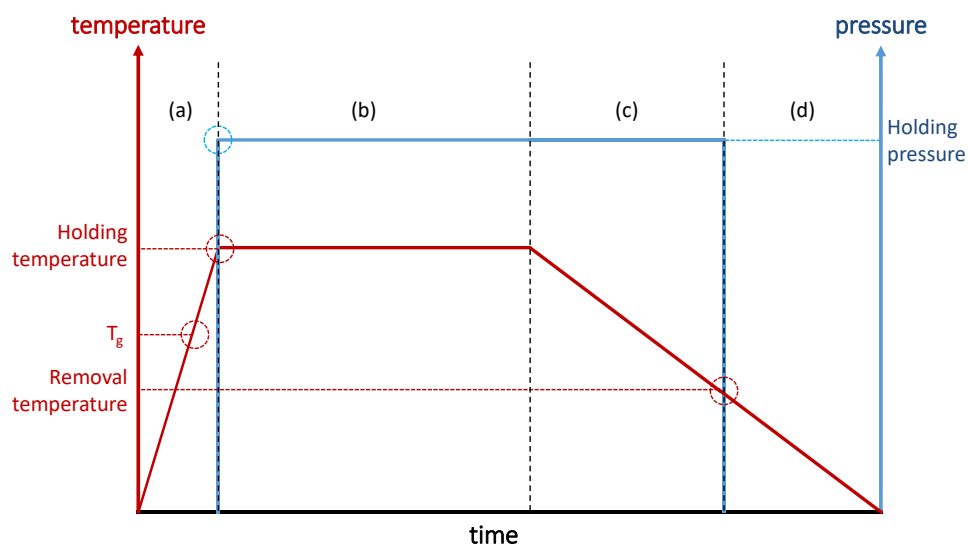


Figure 3.13 Pressure and temperature profile for hot-embossing. The process can be divided into four different working regions: region (a), the temperature is set to be above the polymer glass transition temperature ( $T_g$ ); region (b), pressure is applied and held for several minutes; region (c), the system is cooled down until it reaches a few degrees below  $T_g$ ; region (d), the substrate is peeled off the stamp. Adapted from [62].

Hot embossing is also known as nanoimprint lithography (NIL) with one key difference between the two techniques. Hot embossing employs a thick thermoplastic substrate, so the thickness of the stamp protrusions is much smaller, while NIL uses a thin layer of polymer film, the thickness of which is almost the same height as the stamp protrusion. This difference causes different squeeze flow responses from the thick and thin polymer substrates during the stamping process [98]. For hot embossing, the polymer substrate responds according to the Navier-Stokes equation, while the thin polymer substrate in NIL follows nano-rheology. Navier-Stokes equations describe the motion of viscous fluid into small cavities, which is also known as creeping [99].

In general, any equipment that could control the temperature and pressure can perform hot embossing over any deformable material. For example, a heat press machine like a simple fabric imprinter can be used to make nanostructured surfaces if the heat and pressure can be controlled precisely. Recently, a research group from Spain managed to fabricate a nanoimprinter by using a 3D printer. The 3D printed nanoimprinter can fabricate sub 100 nm features on a PDMS membrane and can be customised to have designated features like the UV lights and plasma source [100].

The simplest embossing setup that has been tested in this project involved utilisation of a lab benchtop hot press to control the temperature and a calibrated weight (INSTRON, F1) to apply the pressure. This approach was straightforward, with the temperature controlled by the hot plate and the weight being used to apply a constant pressure towards the polymer substrate. However, it was difficult to balance a significant amount of weight upright to achieve the targeted pressure without the chance of the weight falling off, leading to health and safety issues. Another issue associated with this method was that the rate of the applied force was not controlled, which could affect the diffusion rate of the polymer into the nanopores. This could cause incomplete protrusion of the polymer into the nanopores, resulting in short and stubby nanodots instead of nanopillars (Figure 3.14). Height analysis was carried out by using an estimation method that converts the grey scale (GS) unit into a metric unit (i.e. nm) from the height data measured using AFM or tilted SEM images (Figure 3.14b). It was found that the short and stubby nanostructures had an indentation in the middle of the pillars, with an outer and inner diameter around 200 nm and 120 nm, respectively, and an estimated pillar height of 30 – 40 nm. The depth of the indentation was 15 – 20 nm.

The polymer behaviour during hot embossing can be explained by understanding the dynamics of polymer flow into the stamp cavities. When a pressure is applied, the viscous polymer is

squeezed into the stamp cavities and flows up the walls of the stamp, before compression of the polymer in the centre of the cavity. Due to lateral compressions, the surface fluctuations are intensified thus causing a buckling of the polymer substrate. The charges found on the stamp and substrate cause electrohydrodynamic (EHD) instability, which will favour the formation of periodic capillary waves in the thermoplastic with boundaries at the stamp's cavity wall [101]. As the pressure is maintained, the local instabilities cause the capillary wave to grow smaller peaks continuously from the wall until it is touching the topside of the cavity and one central peak is formed. If the substrate did not reach the ideal elevated temperature, the polymer will remain in its glassy state rather than the rubbery state, which has limited viscoelastic flow, thus reducing the diffusion of the polymer into the cavities. If the pressure applied is insufficient to provide enough pressure to the polymer, the lateral compressions inside the cavities will be halted and there will not be enough capillary wave to push the peaks from the cavity wall to form one central peak [101]. The characteristics of the PMMA seen in Figure 3.14 indicate that the hot embossing process reached the ideal temperature to allow the polymer to diffuse into the nanopores but lacked sufficient pressure to form the central peak.

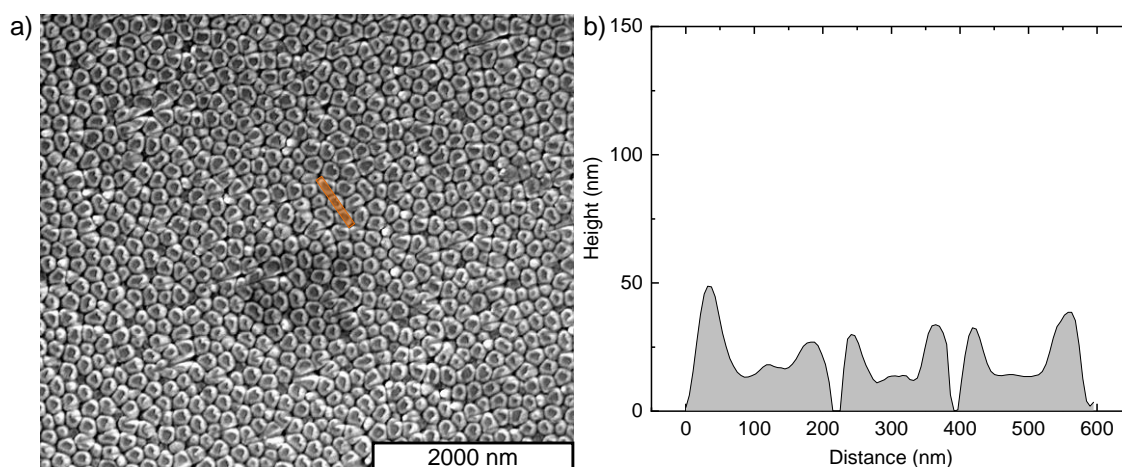


Figure 3.14 Incomplete protrusion of PMMA during hot-emboss. (a) SEM image shows the incomplete protrusion of PMMA substrate during hot-embossing using a benchtop hot plate and 100 N of calibrated weights. The nanostructures were short, and an indentation was found in the middle of the nanopillars with a typical characteristic for incomplete protrusion during hot embossing. (b) Line profile from the orange line marked in (a) shows the “nanovolcano” structures with outer and inner diameter of 200 and 100 nm, respectively. The indentation was estimated at around 15 – 20 nm in depth, and the height at 30 – 40 nm.

Ultimately, as reported in the literature, the most common method to fabricate nanostructured surfaces via hot-embossing involves an investment in sophisticated and expensive equipment dedicated for such a process. To the author's knowledge, there are no studies that report successful fabrication of sub 1000 nm nanostructured surfaces without using a dedicated commercialised hot-embossing machine like X300H from SCIVAX Corp and HEX03 from Jenoptik or homemade hot embossing machine (Table 3.3). The commercialised nanoimprinter allows precise control of the applied pressure (and rate), is equipped with a vacuum chamber to remove all the air bubbles and comes with UV functionality for potential UV assisted photolithography to cure UV curable resin. However, the maximum temperature of the dedicated machine is often relatively low, thus limiting the applications on high performance polymers, which have very high  $T_g$ . The working area is often very small and limited to only one sample at a time with dimension of  $10 \times 10 \text{ mm}^2$ .

In this project, a dual plate hydraulic heat press machine was used to fabricate all the samples. The machine from CYSI has a dual chromium heating plate with a maximum operating temperature of up to  $450^\circ\text{C}$ , heating at a rate of  $5\text{-}10^\circ\text{C min}^{-1}$  and a heating accuracy of  $\pm 0.1^\circ\text{C}$ , and is equipped with a water cooling system and a large working area of  $100 \text{ cm}^2$ . The supplied pressure gauge (0-340 bar) was replaced with a more sensitive pressure gauge (0-5 bar) to have better control of the applied pressure. The dual heating plate with a high maximum temperature allowed the possibility of performing hot embossing on high performance polymers that have a very high  $T_g$  e.g., polyetherether ketone (PEEK) with a  $T_g$  of  $205^\circ\text{C}$ . The large working area allowed the fabrication of multiple samples ( $\leq 20$  pieces of  $10 \times 10 \text{ mm}^2$ ) at one time.

Table 3.3 List of sub-1000 nm polymeric nanostructured surfaces fabricated using imprinting technique.  $D$ ,  $D_p$ , and  $h$  is the diameter, pitch and height of the nanotopographies, respectively.

Material	$D$ (nm)	$D_p$ (nm)	$h$ (nm)	Pre-treatment	Embossing method	Ref(s)
Cycloolefin	70	152	152	Anti-stick agent	X-300H (SCIVAX Corp)	[102]
	40	117	117			
PMMA	215	595	300	Anti-stick agent	HEX03, Jenoptik	[53]
	190	320	300			
	70	170	210			
	60	170	210			
PMMA	100	450	400	N/A	Homemade hot - embossing machine	[71]
	200	450	500			
	200	450	1000			
	350	450	1000			
PET	60-500	1000	80	N/A	Nanoimprint 24, Obducat	[103]
PMMA	70	170	210	Anti-stick agent	HEX03, Jenoptik	[104]
	120	320	300			
	100	500	700			
	215	595	300			

### 3.2.2 Polymer choice: PMMA, PET and PEEK

Three polymers (PMMA, PET and PEEK) have been studied in this project. Both PMMA and PET are clinically relevant materials that have been used to make medical devices since the 1960s [105]. PET is a semi crystalline polymer that is widely used in industry as synthetic fibres (usually known as polyester fabric) and food packaging. PET has found its application to medical devices in the form of artificial corneas, drug delivery systems, prosthetic vascular grafts, sutures, and wound dressings. PET is relatively stable in vivo due to high crystallinity and hydrophobicity (Figure 3.15). PMMA has been used for contact lenses, bone cements, chest drainage units, breathing apparatus accessories, IV accessories, medical cassettes, blood handling components and catheter accessories [105]. In general, the mechanical properties of PET tend to be slightly higher than PMMA, despite PET having a much lower glass transition temperature at 69 °C [103] compared to PMMA at 105 °C [104]. These attributes are the reason for choosing PET as the polymer of choice in this study, for which the overall processing time to make the nanostructured surface by hot embossing will be shorter when compared to PMMA, and yet the surfaces will have comparable mechanical properties.

High performance polymer is a type of thermoplastics that is known to have better mechanical properties compared to other type of polymers. PEEK in particular is known for its stability at high temperatures (melting point at 343°C) due to the presence of polyaromatic ketones in the chemical structure. PEEK also resistance to chemical and radiation damages, compatible with many reinforcing agents like glass and carbon fibers, and have higher tensile strength than most metals. PEEK has a Young's modulus,  $E$  of 3.6 GPa while reinforced PEEK can achieve  $E$  of 18 – 150 GPa which is higher than pure titanium (100 GPa) [106,107]. Due to its promising mechanical properties and biocompatibility, PEEK has been used as an alternative to metals for orthopaedics, trauma, spinal, and dental implants.

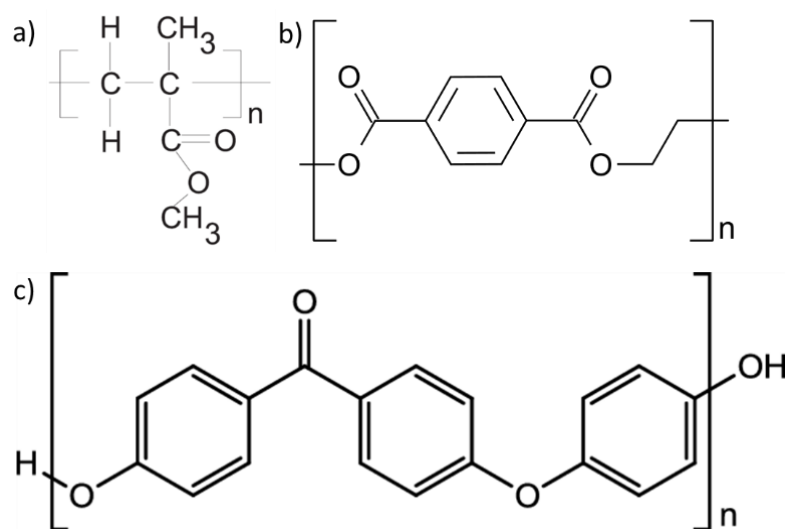


Figure 3.15 Molecular structures of (a) PMMA, (b) PET, and (c) PEEK. The presence of a pendant methyl group in PMMA molecules gives this polymer its characteristic as a tough and rigid plastic by preventing the molecules from packing closely and rotating freely around the carbon-carbon bonds. The aromatic rings in PET and PEEK molecules are responsible for the high stiffness and strength of these polymers.

A systematic study on hot-embossing parameters was carried out to find the optimal parameters to make nanopillars on PET and PMMA from the AAO stamp. The pressure and temperature were varied to find the best combination to fabricate the nanopillars with minimal defects (Table 3.4). It was found that the heating and holding temperature for both PET and PMMA was about 25°C above their  $T_g$  of 95°C and 130°C, respectively. The applied pressure for both polymer substrates was found to be the same, potentially due to their almost identical mechanical properties.

To test the versatility of the CYSI hot press, PEEK was hot-embossed using a BWN stamp alongside PMMA and PET (Figure 3.16). The embossing parameters for each polymer are presented in Table 3.5, with dimensions for all polymer substrates being 10×10 mm<sup>2</sup> with a thickness of 1 mm. The holding temperature for all the polymer substrates was dependent on the polymer  $T_g$ , with the holding temperature being about 20 – 30 °C above the  $T_g$  except for PEEK, where the holding temperature was at 250 °C (50 °C above the  $T_g$ ) due to its high melting point (343 °C) [106]. The applied and holding pressure was the same for PET and PMMA at 1.2 MPa while this was slightly higher for PEEK at 1.8 MPa. Both PMMA and PET obtained well-defined nanopillars with a periodic distribution with a diameter of 75 nm, spacing of 150 nm and height of 250 nm. However, the parameters used to hot-emboss the PEEK substrate obtained a nanopattern without fully erected nanopillars. SEM height analysis showed that the incomplete protrusion of embossed PEEK substrate had a diameter of 85 nm, spacing of 150 nm and an estimated height of only 20 nm. The PEEK line profile shared similar characteristics with the impaired PMMA for which the nanopillars were not fully erected and which had an indentation in the middle of the pillars (Figure 3.16). However, the PEEK nanopillars were significantly shorter ( $h = 20$  nm) than the impaired PMMA nanopillars ( $h = 60$  nm). This could be due to the high melting point of PEEK and rigid molecular structure resulting in a different cavity filling mechanism. The cavity filling mechanism is governed by several factors like squeeze flow, electrostatic interactions between the stamp and the polymer, viscous fingering and surface energy minimization [62]. Schulz *et al.* have studied the importance of polymer flow by looking at the resulting patterns from a stamp containing negative and positive patterns [108]. They have found that unsuccessful and inhomogeneous patterns were the result of a reduced degree of polymer flow and lack of material transfer into the cavity.

Table 3.4 Systematic study of temperature and pressure effects on nanopillar height for PET hot embossed on 70 V anodisation stamp

Temperature (°C)	80	85	90	100	110	80	125
Pressure (MPa)	1.0	1.0	1.0	1.0	1.2	1.4	1.0
Height <sup>§</sup> (nm)	26.61 ±3.28	44.04 ±15.64	38.01 ±9.51	35.52 ±5.04	38.63 ±5.53	55.67 ±6.13	101.28 ±16.99

§ Data indicate mean values ± standard deviation; N=5.



Table 3.5 Hot-embossing parameters for PET, PMMA and PEEK

Polymers	PET	PMMA	PEEK
Glass transition temperature, $T_g$ (°C)	65	108	205
Heating/holding temperature, (°C)	90	130	250
Released temperature, (°C)	60	100	150
Applied/holding pressure (MPa)	1.2	1.2	1.8
Embossing time (min)	10	15	30
Heating time (min)	10	15	25
Cooling time (min)	5	10	20

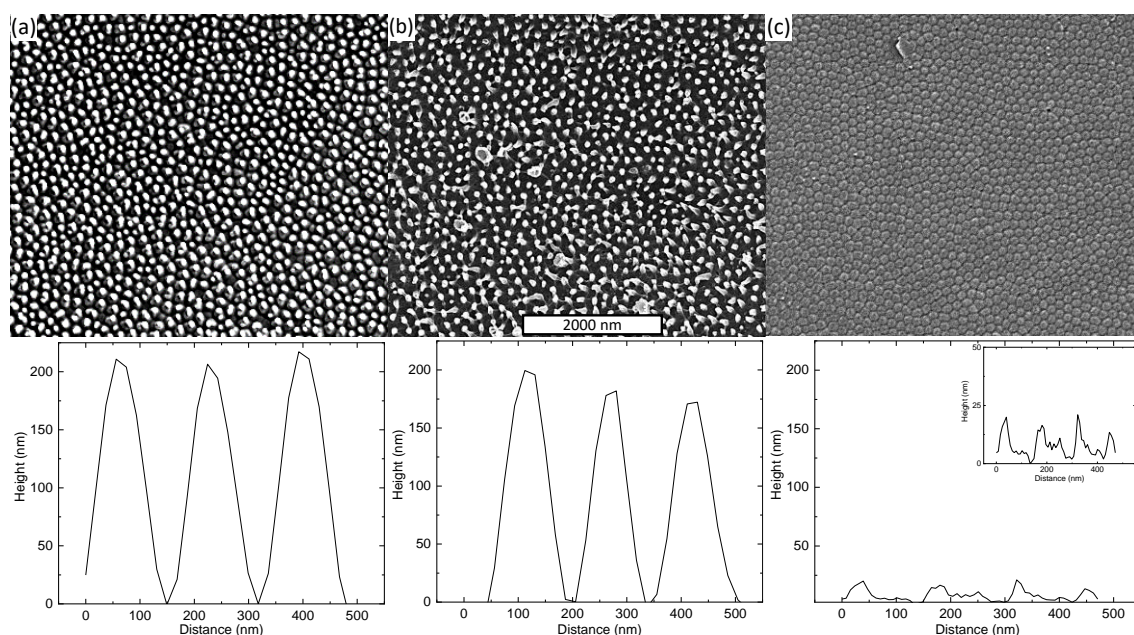


Figure 3.16 SEM image analysis. Top view of (a) PMMA, (b) PET, (c) PEEK hot embossed on a BWN stamp and the line profile of the SEM images at the bottom row. The inset in line profile for the PEEK is the same profile with a different scale on the y-axis to show the features of the PEEK nanostructures.

Highly dense nanopillared surfaces were successfully fabricated with a high degree of reproducibility and throughput. The simple hot embossing setup could produce up to 20 nanopillared samples of  $10 \times 10 \text{ mm}^2$  size in 30 min. The technique used in this project was also shown to be versatile, being used with the different thermoplastic substrates PMMA, PET and PEEK. The fabricated nanopillars on the PMMA and PET substrates resembled the nanopillar pattern on the cicada wing when using the BWN master stamp, which had an aspect ratio of 2.5,

and was confined in a hexagonal unit pattern with 120 nm in spacing and 60 nm in tip diameter. Results from hot embossing on the PEEK substrate at high temperature showed evidence of incomplete protrusion of PEEK. This could have been due to high rigidity of the PEEK polymer even at a temperature above its  $T_g$ , where the storage modulus was still too high compared to that of PMMA and PET. Storage modulus is the ability of a material to store deformation energy in elastic manner. A high storage modulus and low molecular mobility limited the diffusion of PEEK into the cavities, which resulted in short nanostructures with a height of only 20 nm. Figure 3.17 shows the dynamic storage modulus,  $E_D$  of PEEK and PET, respectively, when heated above their  $T_g$ . The  $E'$  of PET drops from 800 MPa to less than 100 MPa when the temperature is above its  $T_g$ , while the  $E'$  of PEEK only drops to a minimum of 250 MPa when the temperature is above its  $T_g$ .

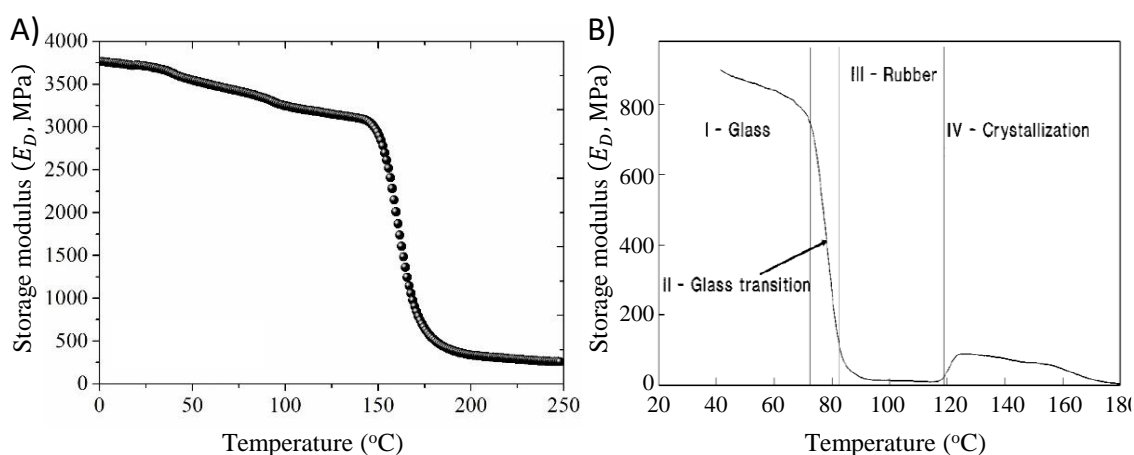


Figure 3.17 Storage modulus for semi-crystallised PEEK film and PET film. (A) Storage modulus for PEEK taken from [109] and (B) storage modulus for PET taken from [110]. Amorphous polymer like PET will be in their glassy state (region I) before reaching the glass transition temperature upon heating. In region II, the material will turn into a soft material (not melted) and will be in rubbery state in region III which leads to a significant drop in  $E$ . The last transition region is the crystallisation of initially amorphous PET which leads to a significant increase in  $E$  (not  $E_D$ ). It is important to note that it is not common for polymers to have the crystallisation transition.

### 3.3 Optimisation of silanisation protocol

#### 3.3.1 *Difficulties with demoulding process*

The demoulding process has been deemed to be the most challenging aspect of making the nanopillars using any template method. Three different demoulding techniques were tested in this project and analysed in order to find the most efficient and cost-effective fabrication process.

##### 3.3.1.1 Demoulding without pre-treatment

Some studies had reported successful fabrication of polymeric nanopillars without prior anti-stick treatment of the aluminium stamp [111,112]. However, here it was observed that without any anti-stick coating, the demoulding process was often challenging, with chances to deform both the aluminium stamp and the PET substrate. PMMA was found to be slightly easier to peel off compared to PET, potentially due to the higher surface energy found on PET substrate [113]. PET substrate with higher density nanopores was also more difficult to separate from the AAO stamp without causing any deformation and distortion to both the AAO stamp and the polymer substrate.

##### 3.3.1.2 AAO stamp etching

The nanopillars could be revealed by serially etching the AAO stamp in different solutions [114,115]. First, the aluminium substrate was dissolved by etching in 0.02 M CuCl<sub>2</sub>·HCl solution in an ice bath for 30 min before removing the oxide layer in 10 wt% phosphoric acid at 45°C for 1 h. While testing this method, two issues were identified: (1) the reaction of Al and CuCl<sub>2</sub> is an exothermic reaction that produces enough heat to deform the nanopillars if the temperature of the solution is not controlled properly. Although the temperature of the CuCl<sub>2</sub> solution was controlled using an ice bath, the local temperature between the sandwich of the stamp and the polymer may have varied significantly; (2) the method was time consuming and costly, taking around 2 h to reveal the nanopillars compared to just a few seconds by peeling, and the AAO stamp was completely dissolved after the process. There was also a concern that the heat from the process could deform the nanopillars. The nanopillared PET also needed to be cleaned very carefully after the etching process to avoid any contamination from the CuCl<sub>2</sub> and the resulting debris from the dissolution of the AAO stamp. Thus, this method was costly and time consuming. For example, it took 40 hours to make 15 nanopillared PET substrates using the etching process, while the peeling method took about 12.6 hours (Table 3.6).

Table 3.6 Rate of producing 15 PET nanopillared surfaces using two different processing technique. CuCl etching requires longer processing time to make 15 PET nanopillared surfaces compared to the peeling method.

Step	Processing technique	CuCl etching	Peeling
1	Anodisation	6 h	6 h
2	Silanisation	0 h	1.5 h
3	Hot emboss	0.5 h	0.5 h
4	CuCl etching	1.5 h	N/A
5	Peeled off	N/A	0.01 h
6	Post washing	N/A	0.5 h
7	Time to make 3 PET	8 h	8.51 h
	Time to make 15 PET	40 h*	12.6 h

\*CuCl etching will require the fabrication of new AAO stamp for every 3 new nanopillared PET substrate while the peeling method can reuse the same stamp of up to 5 times.

### 3.3.1.3 Stamp silanisation

Two approaches for depositing silanes onto a surface were tested, i.e. liquid and gas phase deposition. Liquid phase deposition to coat a surface with silane is achieved by simply dipping or submerging the sample into a silane solution. However, this approach was not compatible with the AAO stamp used in this project due to the small nanopore diameter and high density of the nanopores. Since the nanopore diameter was too small, the chance of over-coating the surface was substantial, and this would have potentially blocked the pores. An over-coated AAO stamp cannot be used because the polymer substrate would not be able to fill in the blocked nanopores. To ensure the AAO stamp had a thin layer of silane to serve as an effective anti-stick agent, the deposition of the silanol onto the surface had to be controlled.

Chemical vapor deposition (CVD) was found to be a much better technique to deposit a thin layer of silane onto a surface. CVD is a simple technique that deposits a material onto the surface of a substrate from a gaseous phase under vacuum. Two slightly different approaches were tested before the final protocol for silanisation was adopted. The first approach was to place a 1.6 ml DCDMS mixture into a glass petri dish before the air was purged. This approach almost instantly vaporised all of the silane solution, which should then be immediately adsorbed onto the surface of the stamps. The second approach was to add 1.6 ml of DCDMS mixture into a 2 ml vial with an opening diameter of about 4.7 mm. By having a smaller exposed surface area to

be vaporised (compared to the larger area of the petri dish with a diameter of 89.3 mm), this allowed slower adsorption of the silane onto the surface of the stamps, which should give more control over the final adsorption thickness of the silane. The thickness of the silane was not directly quantified.

The success of the silanisation process was confirmed by measuring the contact angle of the AAO stamps before and after silanisation. The contact angle of the aluminium substrate decreased after the cleaning procedure and further decreased after the electropolish. The contact angle of the pre-silanised AAO stamps with different nanopore has configurations had different contact angles. The BWN stamp, with large and sparse nanopores, had the highest contact angle at  $93.1^\circ$ , followed by the BDN stamp ( $74.4^\circ$ ) and the SDN stamp ( $58.7^\circ$ ) ( Figure 3.18).

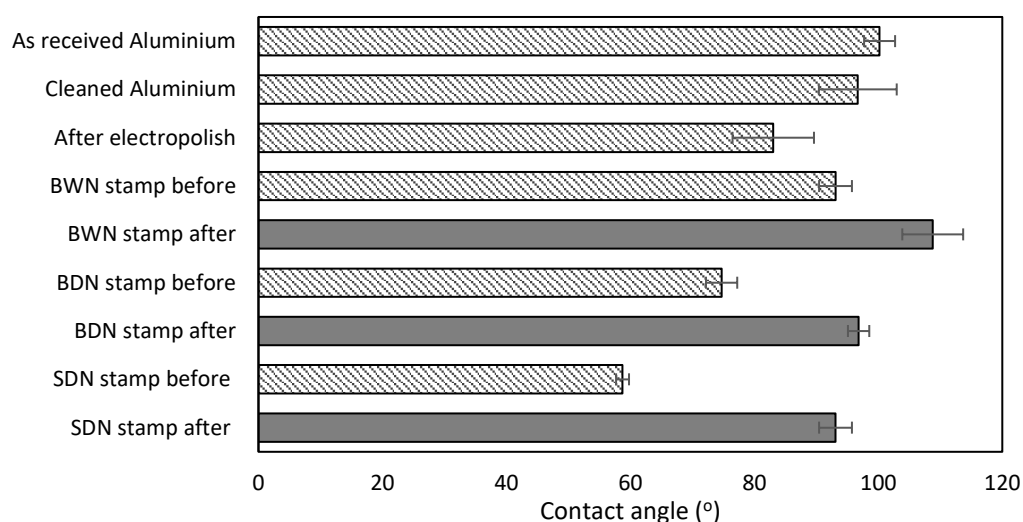


Figure 3.18 Contact angle of as received, cleaned and electropolished aluminium substrate, and of AAO substrate before (striped) and after (filled) silanisation step. Data indicate mean values  $\pm$  standard deviation; N=3

Ideally, an AAO stamp with good silanol coverage should have a contact angle between  $90^\circ$  to  $110^\circ$ . This range was confirmed by the feasibility studies into the peeling off process after hot embossing. A stamp with a contact angle less than  $90^\circ$  was very difficult to peel off, while a stamp with a contact angle above  $110^\circ$  would cover the nanopores completely with the silanol, impairing their capacity to make nanopillars. The silanised SDN stamp was found to have a higher increase in contact angle compared to the BDN stamp using the same silanisation process. This could have been due to the larger pore size of the BDN stamp, which would mean that a longer time was needed to have similar coverage of silanol on the surface of the stamp compared to the SDN stamp (Figure 3.19).

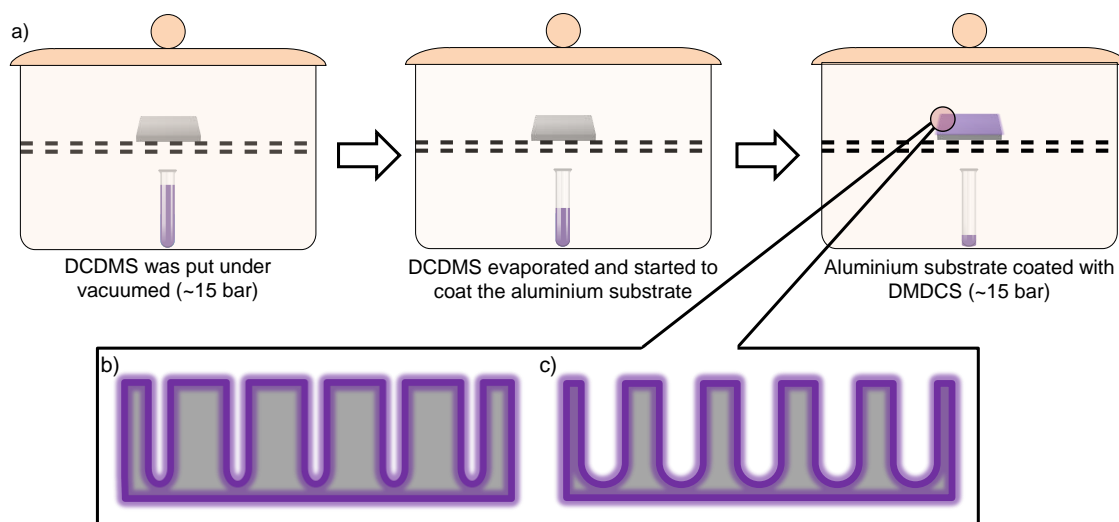


Figure 3.19 Schematic of the silanisation process using DCDMS to coat the AAO stamp with an anti-stick coating. (a) The process involved turning the silane solution into vapor and allowing the silane to slowly adsorb onto the surface under vacuum. The thickness of the silane could be controlled by varying the silanisation time. (b) and (c) show the effects of silanisation on AAO stamps with different nanopores. AAO stamps with small nanopores (radius,  $r = a$ ) (b) will be almost completely covered with polymerised silane while this will not occur using the same thickness of silane on stamps with larger nanopores ( $r = 2a$ ).

The surface charge of PET substrate and hot embossed PET substrate were also measured using DLS to check any contamination of the silanol on the PET substrate after the hot emboss. Table 3.7 shows that hot-embossed PET substrate was more negatively charged ( $-32.4 \pm 2.9$  mV) compared to the flat control ( $-25.2 \pm 6.8$  mV). This value was comparable to that reported in a previous study ( $-53$  mV) [116]. The hot-embossed PET substrate was more negatively charge potentially due to the contamination left from the silanisation layer on the master stamp. However, this difference is small and not anticipated to be substantial at influencing the antibacterial properties of the nanostructured surfaces.

Table 3.7 Zeta potential of as received PET substrate and hot embossed PET substrate in PBS buffer (pH 7.4).

	PET control (mV)	PET HE (mV)
AVG <sup>§</sup>	-25.2	-32.4
STDEV	6.8	2.9

<sup>§</sup> N = 3

The reusability of the stamp was studied systematically with PET substrate on BWN stamp. The same master stamp was reused 10 times and the resulting hot embossed substrates were assessed by SEM at 10 000 $\times$  magnification. The master stamp was washed thoroughly with ethanol and water using an ultrasonic bath (90% power, 15 min) to remove any excess contaminants from the previous hot embossing process. The hot embossed PET substrates showed no significant defects on the surface after reusing the same master stamp up to four times (Figure 3.20A-C), but small defects were observed when the master stamp was reused for the fifth time onwards (Figure 3.20D-F). The defects were found in a form of cracks, non-filled defects and particle debris. The non-filled defects and particle debris were also observed when hot embossing with a fresh master stamp but at a very small scale. The fact that the defects became more pronounced with use of the stamp could be due to degradation of the anti-stick layer on the master stamp. This would make the demoulding process more difficult after each use, and the shear forces generated between the stamp and the polymer substrate during demoulding could destroy the nanopillars (43). With this in mind, it is recommended to only reuse the stamp no more than 5 times to maintain the quality of the hot-embossed nanopillars.



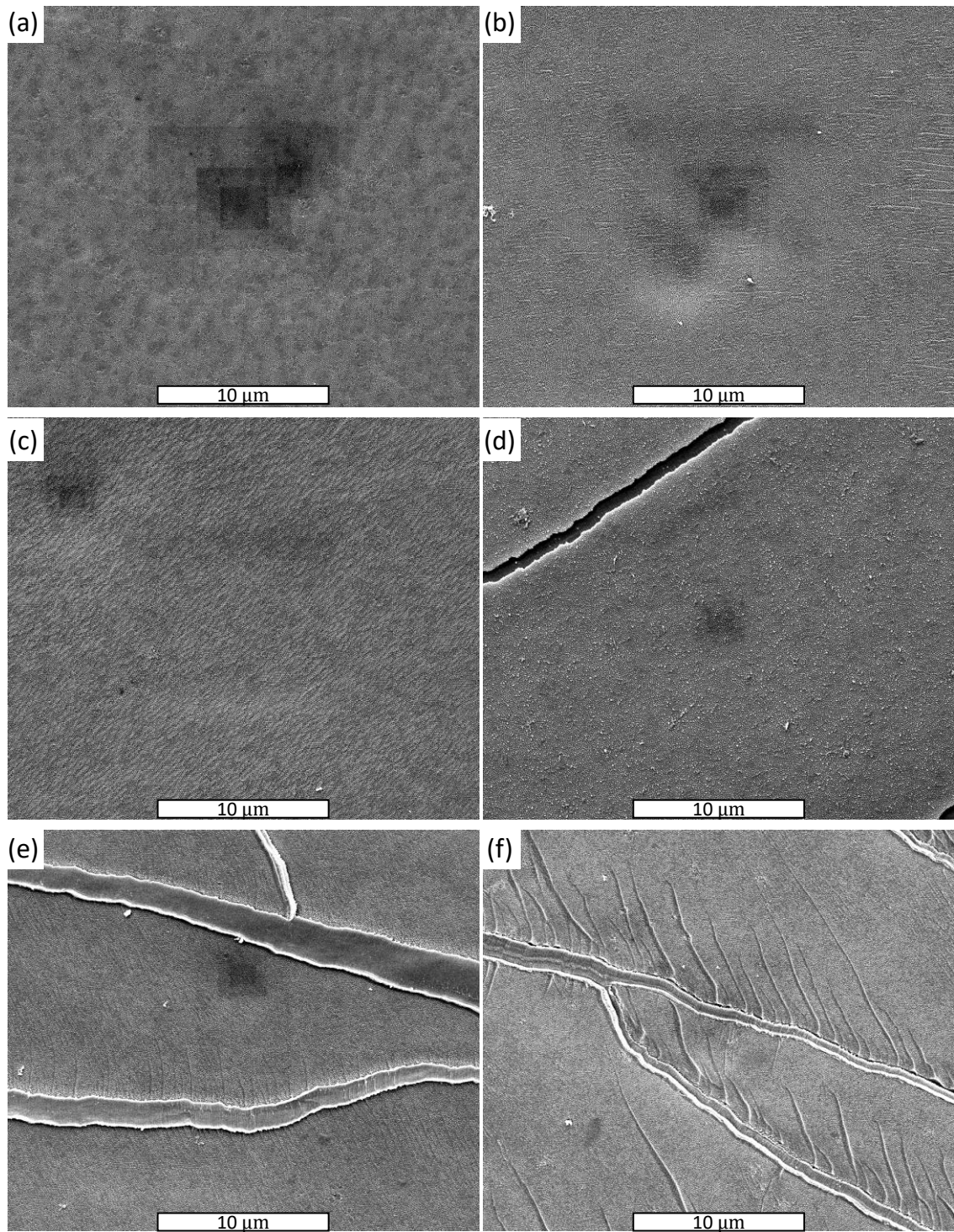


Figure 3.20 Top view SEM image of PET nanopillared surfaces fabricated using the same anodisation stamp. (a) First time, (b) second time (c) fourth time (d) sixth time (e) seventh time and (f) tenth time.



### 3.4 Nanostructured surface characterisation

#### 3.4.1 Surface nanotopography

The flat and the three nanopillared PET surfaces were characterised using AFM and SEM, in which the base diameter ( $D_B$ ), tip width ( $D_T$ ), interpillar distance/pitch ( $D_P$ ), height ( $h$ ) and RMS ( $R_q$ ) were quantified (Table 3.8).  $D_B$ ,  $D_T$ , and  $D_P$  were quantified using SEM images and analysed using FIJI, while  $h$  and  $R_q$  were quantified using AFM and analysed using Nanoscope analysis V8.2. Height data from tilted images of SEM were compared with AFM measurements, with no significant differences found between the two techniques. However, there was a small discrepancy in terms of the lateral measurement of the nanotopography between FIJI analysis and particle analysis from AFM data. This could have been due to a limitation of AFM in measuring lateral dimensions because of the tip-sample convolution. This is one of the widely known limitations of AFM when measuring lateral dimensions [117].

The resulting nanopillars were packed in a hexagonal unit pattern and were relatively isotropic in height. The SDN had a diameter of around 50 nm at the base and 39 nm at the tip, with an interpillar spacing around 85 nm. The BDN had approximately the same base and tip diameter of around 80 nm, with a spacing of 95 nm, while BWN had a tip width and spacing of 80 nm and 120 nm, respectively (Figure 3.21). The tip of the nanopillars was conical, except for BDN, which had a flattened tip rather than conical. The aspect ratio between different samples was almost identical except for BDN. The discrepancy of the BDN sample compared to other samples (in terms of tip shape and aspect ratio) may have been due to the lower squeeze flow protrusion into the cavities of the AAO stamp caused by the smaller spacing between the nanopores [62].

The surface roughness was measured using AFM on a  $1 \times 1 \mu\text{m}^2$  scan area on three different areas per surface type (Figure 3.22). Roughness factor was also calculated to compare the results between SEM analysis and AFM analysis, which is defined as:

Equation 3.3: Roughness factor formula

$$R_f = \frac{(D_p + D_c)^2 + 4D_c h}{(D_p + D_c)^2}$$

where  $D_p$ ,  $D_c$  and  $h$  is the diameter, interpillar spacing and height of the nanostructured surface, respectively (45).

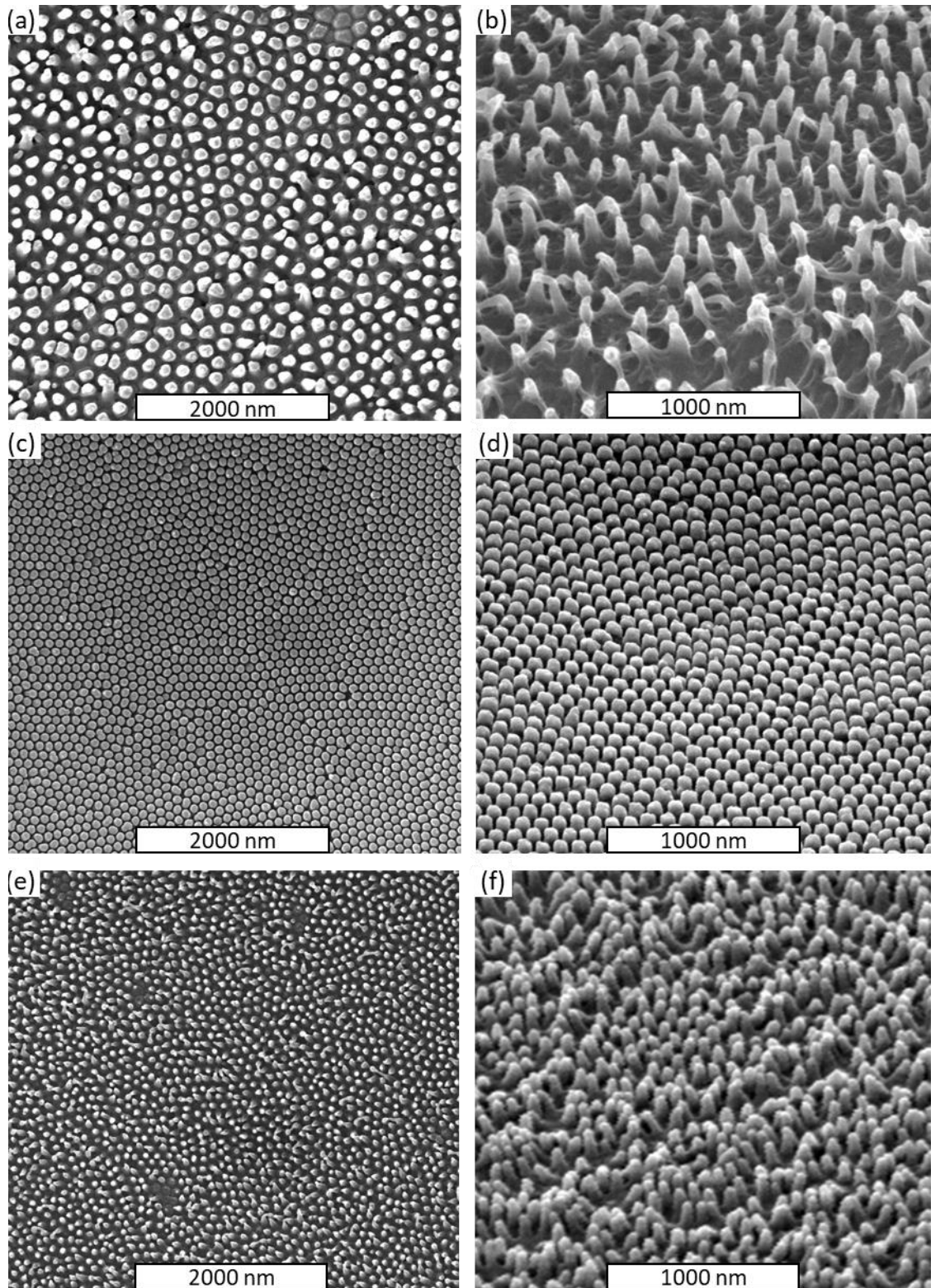


Figure 3.21 SEM images of the PET nanopillared surfaces used in this project. Top view SEM images of (a) BWN, (c) BDN and (e) SDN and 30° tilted images of (b) BWN, (d) BDN and (f) SDN nanopillar surfaces.

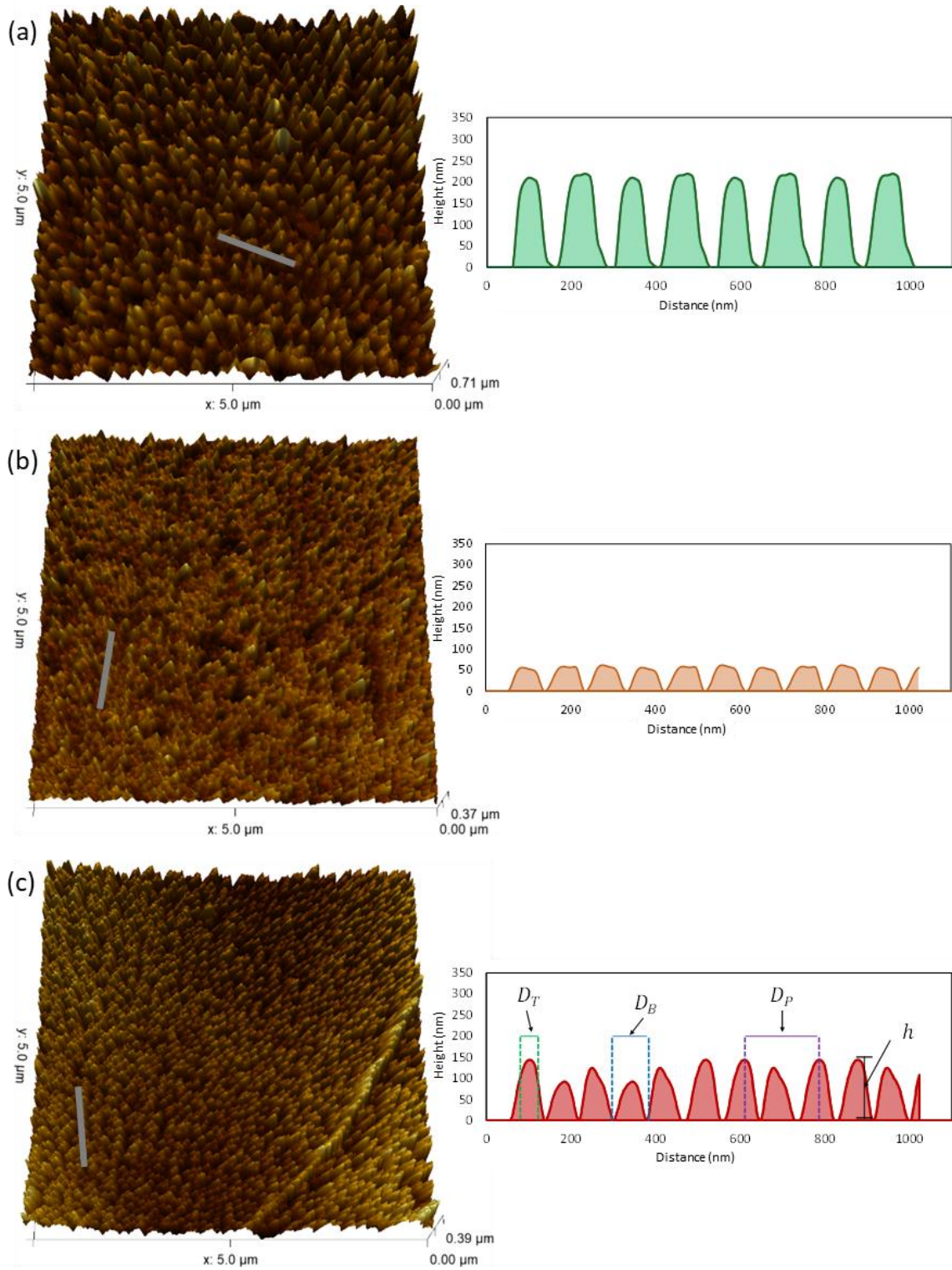


Figure 3.22 Representative AFM images of the nanopillared surfaces. 3D AFM images of (a) BWN, (b) BDN, and (c) SDN. The corresponding line profiles are shown to the side of the AFM image. Annotations on the AFM line profile for SDN correspond to the characterisation for tip width  $D_T$ , base diameter  $D_B$ , interpillar distance  $D_P$ , and  $h$ .

Table 3.8 Measured base diameter ( $D_B$ ), tip width ( $D_T$ ), interpillar distance/pitch ( $D_p$ ), height ( $h$ ), aspect ratio ( $AR$ ) and RMS ( $R_q$ ) of nanopillared PET substrates and the flat control

Sample	$D_B$ (nm)	$D_T$ (nm)	$D_p$ (nm)	$h$ (nm)	$AR$	$R_q$
Control	0.00	0.00	0.00	$7.12 \pm 3.44$	0.00	$2.33 \pm 0.65$
BWN	$136.23 \pm 5.38$	$79.39 \pm 6.66$	$121.77 \pm 3.95$	$256.33 \pm 15.57$	3.23	$98.54 \pm 4.12$
BDN	$85.32 \pm 1.09$	$76.44 \pm 2.71$	$90.43 \pm 0.90$	$153.68 \pm 1.22$	1.80	$39.28 \pm 0.04$
SDN	$51.75 \pm 1.83$	$39.07 \pm 0.43$	$85.40 \pm 1.97$	$176.76 \pm 45.89$	3.41	$57.72 \pm 15.47$

For each measured parameters, at least 3 corresponding SEM and/or AFM images were used to get the data. A minimum of 300 nanopillars were quantified using FIJI V1.52p for SEM images and Gwyddion V2.55 for AFM images. Data indicate mean values  $\pm$  standard deviation.

### 3.4.2 Contact angle and surface wetting

#### 3.4.2.1 Surface energy measurement and calculation

Wettability and surface energy of a solid surface is often quantified by measuring the contact angle formed by a given drop of liquid resting on a flat surface. The Young's equation has been used to explain wettability of pure liquids on a solid surface, which is given as:

Equation 3.4: Young's equation

$$\gamma_L \cos \theta = \gamma_S - \gamma_{SL}$$

where  $\gamma_L$  is the known surface tension of the liquid,  $\theta$  is the contact angle,  $\gamma_S$  is the surface energy of the solid and  $\gamma_{SL}$  is the solid/liquid interfacial energy. The work of adhesion  $W_{adh}$  can be defined as  $W_{adh} = \gamma_L \cos \theta$ , which is the left-hand side of Equation 3.4 [118,119]. To solve the problem with polar interactions, van Oss and Good considered the surface free energy ( $\gamma_i$ ) as a sum of the apolar Lifshitz-van der Waals component ( $\gamma_i^{AB}$ ) and Lewis - acid-base polar interaction, ( $\gamma_i^{LW}$ ).

Equation 3.5: Surface free energy equation

$$\gamma_i = \gamma_i^{LW} + \gamma_i^{AB}$$

The apolar interactions are mainly due to London dispersion interaction with possible Debye and Keesom interaction in some cases, while the polar interactions are due to hydrogen bonding, which has an electron donor ( $\gamma_i^-$ ) and electron acceptor subcomponent ( $\gamma_i^+$ ):

Equation 3.6: Debye-Keesom interaction equation

$$\gamma_i^{AB} = 2\sqrt{\gamma_i^+ \cdot \gamma_i^-}$$

Then, the total interfacial energy between the solid and liquid can be expressed as:

Equation 3.7: Total solid-liquid interfacial energy formula

$$\gamma_{SL} = \gamma_S + \gamma_L - 2 \left( \sqrt{\gamma_S^{LW} \cdot \gamma_L^{LW}} + \sqrt{\gamma_S^+ \cdot \gamma_L^-} + \sqrt{\gamma_S^- \cdot \gamma_L^+} \right)$$

By using Young's equation and Equation 3.7, the relationship between measured contact angle of pure liquid with known apolar and polar components and a solid substrate can be expressed as:

Equation 3.8: Relationship between contact angle of pure liquid with known apolar and polar components

$$\gamma_L \cdot (1 + \cos \theta) = 2 \left( \sqrt{\gamma_S^{LW} \cdot \gamma_L^{LW}} + \sqrt{\gamma_S^+ \cdot \gamma_L^-} + \sqrt{\gamma_S^- \cdot \gamma_L^+} \right)$$

The contact angles of the test liquids, i.e. Milli-Q water, ethylene glycol and diiodomethane, on the flat and nanopillared PET surfaces are given in Table 3.10. By using the test liquid contact angle values, the surface energies of the samples and their respective apolar and polar components were calculated using the Fowkes acid-base approach (Table 3.9). It was found that the presence of nanopillars increased the apparent surface energy of the PET substrate when compared to the flat PET substrate. Densely compacted nanopillared surfaces (BDN and SDN) exhibited higher surface energies compared to the surface with low density nanopillars (BWN). The surface bearing sharper nanopillars (SDN) appeared to exhibit higher surface energy compared to the surfaces with blunt nanopillars (BDN and BWN). Figure 3.24 shows the correlation between the nanotopography features i.e. tip diameter, pitch, height and roughness with the surface energy. Only  $D_p$  showed a linear relationship with the surface energy where smaller  $D_p$  will have higher  $\gamma^{TOT}$ . However, these differences in the surface energy between the different nanopillared surfaces were not significant.

Table 3.9 Liquid surface tension ( $\gamma_L$ ), apolar component  $\gamma_L$ , polar component  $\gamma_L^{AB}$ , electron acceptor  $\gamma_L^+$ , and electron donor  $\gamma_L^-$  of water, diiodomethane, and ethylene glycol

Surface tension data (mJ/m <sup>2</sup> )		$\gamma_L$	$\gamma_L^{LW}$	$\gamma_L^{AB}$	$\gamma_L^+$	$\gamma_L^-$
Water,	H <sub>2</sub> O	72.8	21.8	51	25.5	25.5
Diiodomethane,	CH <sub>2</sub> I <sub>2</sub>	50.8	50.8	0	0	0
Ethylene glycol,	C <sub>2</sub> H <sub>6</sub> O <sub>2</sub>	48	29	19	1.92	47

Table 3.10 Contact angle ( $\theta$ ), surface energy components ( $\gamma_L$ ), and work of adhesion ( $W_{adh}$ ), of the flat, BWN, BDN and SDN surfaces

	Contact angle, $\theta(^{\circ})$			Surface energy components, $\gamma_L$ (mN/m <sup>2</sup> )					mJ/m <sup>2</sup>
	$\theta^W$	$\theta^{Di}$	$\theta^{EG}$	$\gamma^{LW}$	$\gamma^+$	$\gamma^-$	$\gamma^{AB}$	$\gamma^{TOT}$	
Flat	76.90	29.29	56.90	44.51	0.21	9.83	2.90	47.41	89.30
BWN	92.60	17.12	49.65	48.57	0.07	0.03	0.09	48.67	69.50
BDN	84.91	18.30	39.16	48.26	0.35	0.70	0.98	49.25	79.26
SDN	73.60	20.58	37.49	47.61	0.12	6.32	1.76	49.37	93.35

## 3.4.2.2 Cassie-Baxter vs Wenzel model

Two models to describe surface wettability with micro/nano roughness are the Wenzel model and Cassie-Baxter model. The Wenzel model describes a wetting state that displaces the gas phase entirely between substrate asperities so that no air remains trapped within the nano/micro structures. In this model, the effective contact angle is directly proportional to the surface roughness and could be defined as:

Equation 3.9: Wenzel contact angle equation

$$\cos \theta_W = R_f \cdot \cos \theta_Y$$

where  $\theta_Y$  is the Young's contact angle, which is the equilibrium contact angle on a flat surface, and  $\theta_W$  is the contact angle on a rough surface, while  $R_f$  is the roughness factor (Equation 3.9). The Cassie-Baxter model suggests that the wetting of a sessile droplet is influenced by the presence of air pockets formed between the surface asperities. The apparent contact angle is given by:

Equation 3.10: Cassie-Baxter contact angle equation

$$\cos \theta_{CB} = \varphi(1 + \cos \theta_Y) - 1$$

where  $\varphi$  is the solid fraction in contact with the liquid and defined as:

Equation 3.11: Solid fraction equation

$$\varphi = \frac{D_c^2}{(D_c + D_p)^2}$$

The comparison between contact angle from the Wenzel and Cassie-Baxter models is presented in Table 3.11. According to the Wenzel model, dense nanopillared surfaces are more hydrophilic compared to less dense nanopillars, and sharp nanopillars are significantly more hydrophilic

compared to the blunt nanopillars. This significant difference between BDN and SDN could have been due to the non-homogeneous height distribution found on SDN that facilitated the wetting process to partially or completely wet the surface under the water droplet. From the experimental data and the comparison between the effective contact angle from the Wenzel and Cassie-Baxter models found in Table 3.11, the Wenzel model best describes the wetting behaviour of the PET nanopillared surfaces. The model essentially predicts that for a hydrophobic surface ( $\theta_Y > 90^\circ$ ), the surface will become more hydrophobic with a decrease in  $r$ , and for a hydrophilic surface ( $\theta_Y < 90^\circ$ ), the surface will become more hydrophilic, with a decrease in  $R_f$ . There was a small discrepancy between the theoretical contact angle and the measured contact angle. This was expected since the experimental data did not show any correlation between contact angle and overall surface roughness.

Table 3.11 Contact angle, Wenzel and Cassie-Baxter effective contact angle, solid fraction, and roughness factor for BWN, BDN and SDN

	$\phi$	$R_f$	$\theta_Y$	$\theta_W$	$\theta_{CB}$
BWN	0.16	3.01	92.6	97.9	148.4
BDN	0.24	2.70	84.9	76.2	138.0
SDN	0.14	2.95	73.6	33.5	144.7

There was a clear trend showing that the surface roughness ( $R_q$  and  $R_f$ ) increased as the height ( $h$ ) increased. Both  $R_f$  and  $R_q$  showed a similar trend with  $h$ ; as  $h$  increased, the  $R_f$  and  $R_q$  increased (Figure 3.23A-B). The  $R_q$  showed a linear relationship with  $h$ , while  $R_f$  did not. Dependency of height and roughness has been reported in several studies involving nanostructures with different materials, shape and mechanical properties [112,120,121].

Contact angles of the PET nanopillared surfaces were found to be much lower than the nanopillared surfaces on different polymer substrates reported in the literature. There was also no correlation found between the  $R_q$  and the  $\theta$  or the  $\gamma^{TOT}$ , which is contrary to what has been reported previously (Figure 3.23C-D) [116]. When comparing the diameter between two surfaces with the same interpillar distance (BDN vs. SDN), the SDN were found to have higher surface energy compared to the blunt surface. However, there was no direct correlation between the vertical dimension of the nanotopographies ( $h, R_q, AR$ ) and the surface energy.



Instead, the surface energy was found to be dependent on the density of the nanopillars, with higher density nanopillars having a higher surface energy (Figure 3.24).

The discrepancies in wetting behaviour of the PET nanopillared surfaces when compared to previous studies can be explained by using the Wenzel model, which states that a hydrophilic substrate will be more hydrophilic with the presence of nanostructures. Since the flat PET substrate was hydrophilic, the presence of nanopillars further reduced the contact angle and increased the surface energy. The nanopillars increased the total surface area, which will have increased the polar interactions between the surface components and the water droplet and so decreased the water contact angle. Zhao *et al.* reported that surfaces with a high  $R_q$  will have enhanced hydrophobicity [121]. When studying gold micro/nanopillared surfaces, they found that increasing surface roughness with nanopillars may trapped air between the cavities on the rough surfaces, resulting in a composite solid-air-liquid interface instead of a homogeneous solid-liquid interface [121]. Hazell *et al.* reported similar wetting behaviour on PET nanocones that were fabricated using colloidal particle mask lithography, and found that more densely compacted nanofeatures had a higher surface energy [77].

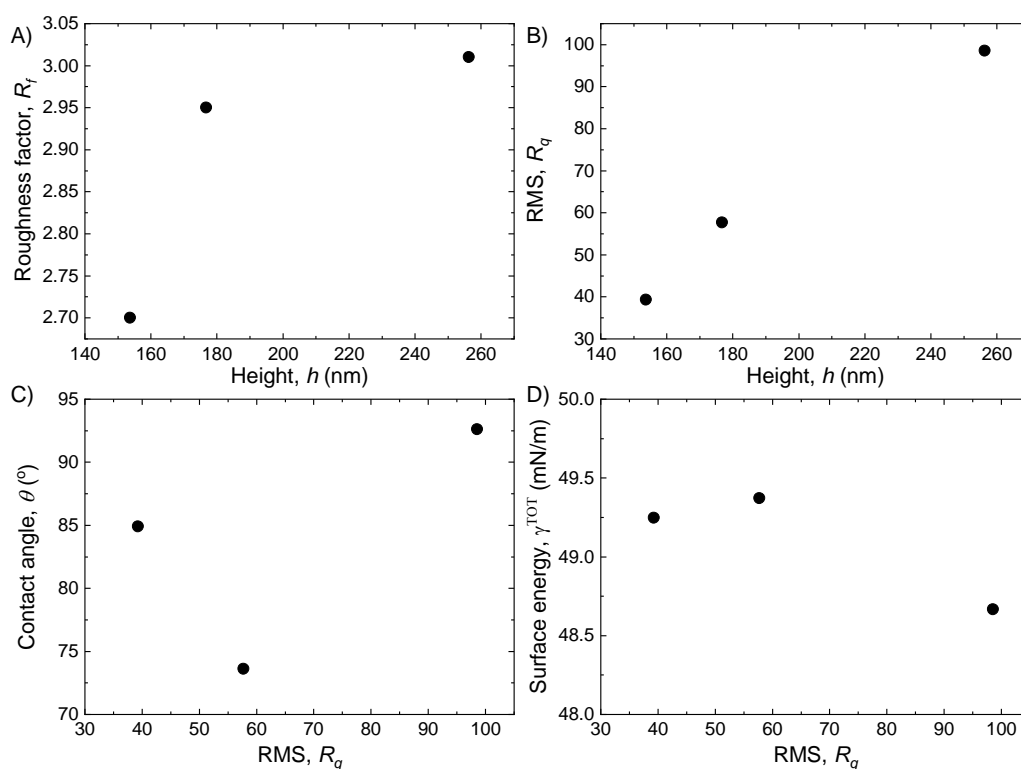


Figure 3.23 Relationship between height, roughness and surface wetting. (A) Calculated roughness factor,  $R_f$ ; (B) experimental RMS data,  $R_q$ ; (C) contact angle,  $\theta$ ; (D) surface energy,  $\gamma^{TOT}$ .



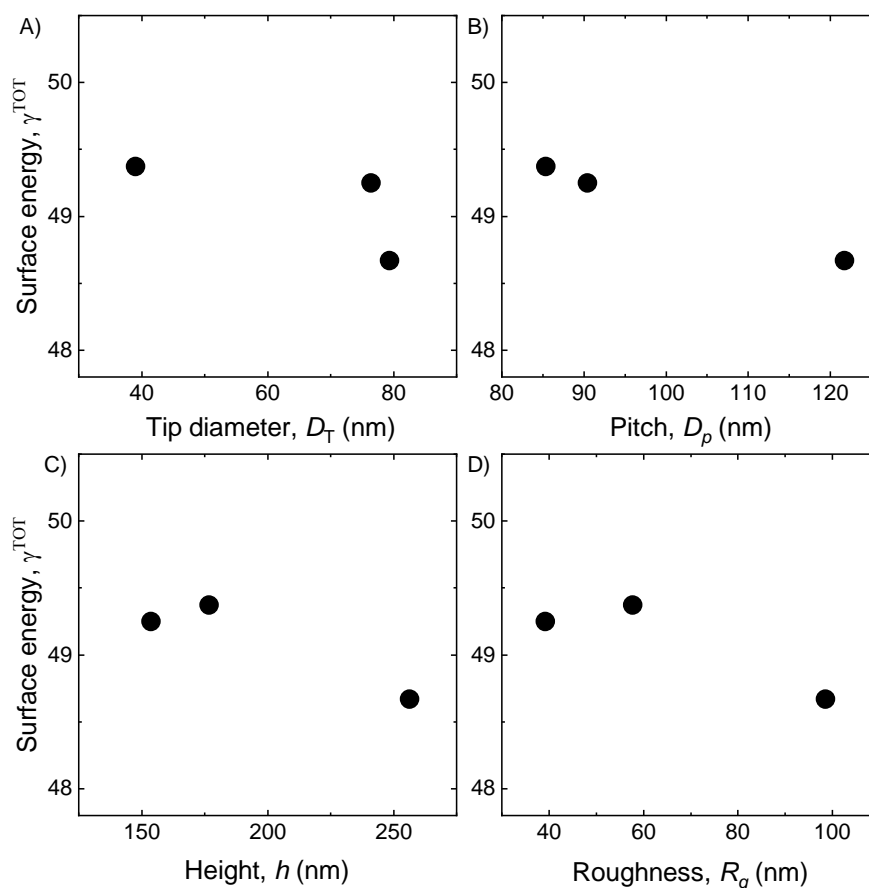


Figure 3.24 Correlation between surface topographies and surface energy. (A) Tip diameter,  $D_T$ ; (B) pitch,  $D_p$ ; (C) height,  $h$ ; (D)  $R_q$ . Only  $D_p$  showed a linear relationship to the  $\gamma^{TOT}$ . It is important to note, however, that the differences in surface energy between each nanopillared surface are not significant.

### 3.4.3 XPS analysis

Figure 3.25A shows the typical survey scan for a PET substrate, with the characteristic C 1s and O 1s peaks found at binding energies of 284 eV and 533 eV, respectively. XPS analysis revealed that contamination with silane on the PET substrate from the silanised AAO stamp was minimal, since the atomic percentage of Si 2s and Si 2p were increased by only 0.23% and 0.96%, respectively. This finding suggests that the wetting behaviour of the PET nanopillared surfaces was not influenced by contamination with silane but rather the contribution of the nanotopography. A high resolution scan on the C 1s (Figure 3.25B) showed no significant difference between the hot-embossed nanopillars with the control, which confirms that the hot embossing process did not physically alter the chemical structure of the original PET substrate.

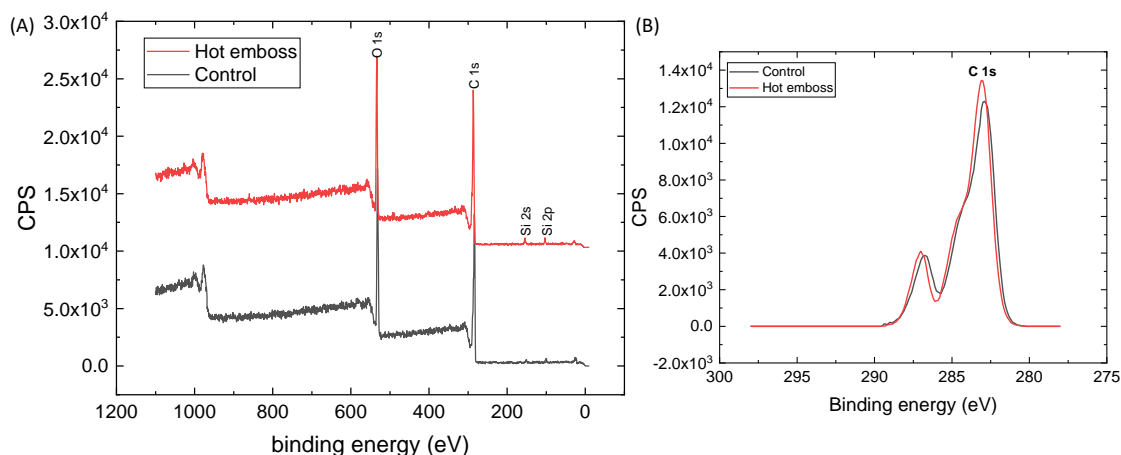


Figure 3.25 XPS analysis of as received and hot embossed PET substrate. (A) Survey scan of the flat control and hot-embossed PET substrate and (B) normalised high resolution scan of the C 1s for both control and hot-embossed PET substrate.

### 3.5 Summary

Due to increasing demand in polymeric medical devices and the risk of bacterial infections on biomaterial are still a major concern, it is essential to develop novel approach that can provide potential solution to the problem. In this chapter, anodisation and hot embossing techniques were optimised to allow development of scalable nanofabrication technique. By using current experimental and theoretical results of bacterial adhesion to nanostructured surfaces, three interrelated nanostructured surfaces were designed and fabricated on a PET substrate. The surface properties like contact angle, surface wetting, and surface roughness were quantified to understand the influence of the nanopillars diameter and interpillar distance in relation to these parameters.

Two industrial protocol adaptations have been systematically studied in this project which are the use of simple heat press machine as opposed to expensive and miniature NIL instruments and the optimisation of the up-scalable 2 step-anodisation process. These adaptation will help to ease the transition from research lab to commercialisation of nanostructured surfaces. It was showed that it is possible to fabricate sub 1000 nm nanostructured surface with one of the dimensions is less than 100 nm using non-conventional hot embossing machine. Here, a simple heat plated machine with hydraulic pressure system was utilised. This was made possible by coating a thin layer of anti sticking agent on the master template where the surface contact angle must be in between the range of 90-110°. The anodisation protocol was also revised to be more practical and efficient where the total time to fabricate a highly ordered nanopores template is just 6 h as opposed to 22 h using the standard 2-step anodisation protocol. No

significant difference in terms of the size and regularity of the nanopores were observed between 4h and 20h anodisation time. The versatility of this nanofabrication protocol have been successfully tested on two thermoplastic materials; PET and PMMA but require further optimisation for high performance polymer like PEEK.

The designs of the nanopillared surfaces used in this study were chosen based on three theoretical models on bactericidal mechanism of nanostructured surfaces. In this study, the nanotopography of the nanopillars i.e. the base diameter ( $D_B$ ), tip width ( $D_T$ ), interpillar distance/pitch ( $D_P$ ), height ( $h$ ), aspect ratio ( $AR$ ) and RMS ( $R_q$ ) quantified using SEM and AFM. The contact angle and surface energy were also quantified while the Cassie-Baxter and Wenzel model were compared to describe the wetting behaviour of the PET nanopillared surfaces. It was found that Wenzel model best describes the wetting behaviour of the tested surfaces. Comparative analysis showed that RMS increases linearly with increase in height while surface energy decreases linearly with the increase in pitch distance. XPS analysis showed that there were no significant changes were found on the hot embossed PET substrate when compared to the as received PET substrate. This suggests that the wetting behaviour of the nanotextured surface was not influenced by the contamination of the silane but rather the contribution of nanotopography.

## CHAPTER 4 NANOTRIBOLOGICAL AND NANOMECHANICAL PROPERTIES OF POLYMERIC NANOPILLARED SURFACES

### 4.1 Introduction

Over the past decades, nanostructured surfaces have been considered as an attractive technology with potential to revolutionise the medical field [112]. Most of these nanostructured surfaces were inspired by the ingenious functionality in many naturally occurring surfaces that bear nanostructures like lotus leaves [122], gecko feet [70], shark skin [123], moth eyes [22] and cicada wings [21]. Protruding nanostructures like nanospikes, nanotubes, nanowires and nanopillars are known for their unique wetting properties and were found recently to be able to kill bacteria by rupturing the bacterial cell envelope [21]. However, the precise bactericidal mechanism of action of these nanostructures is still uncertain [56]. To fully understand such bacteria-substratum interactions, it is important to investigate the contact mechanics between the surfaces.

Nanotribology and nanomechanics studies are utilised to help understand the interfacial interactions of nanostructured surfaces with another surface e.g. bacterial cell wall. In general, nanotribology and nanomechanics study friction and adhesion to understand interfacial phenomena in micro/nano structured surface applications [124]. To better exploit protruding nanostructured surfaces like nanowires, nanospikes and nanopillars as antimicrobial surfaces, comprehensive understanding of the mechanisms and dynamics of two contacting surfaces during relative motion are needed. When bacteria land on nanostructured surfaces, contact will occur at multiple asperities. Depending on the hydrodynamics of the environment and the motility of the bacteria, the interactions of nanostructured surfaces and bacteria will be different. Investigating the relative motion between the two surfaces is therefore needed to develop fundamental understanding of the adhesion, friction, and possible deformation of the bacterial cell wall.

Friction and adhesion are two related phenomena that occur when two surfaces are in contact with one another. Wearing of surfaces is due to friction and adhesion, and this effect has been observed in the history of humankind and natural science. The concept of friction was first introduced by Leonardo da Vinci where he concluded that “friction produces double the amount

of effort if the weight be doubled" and "the friction made by the same weight will be of equal resistance at the beginning of the movement, although the contact may be of different breadths or lengths". These principles govern the fundamental laws of friction, whereby the friction force,  $f_f$ , is proportional to the load force,  $L$ , and does not depend on the area of contact between the sliding body and the surface [9] [10]. The laws of friction were then further developed by Amonton, who confirmed da Vinci's observations and devised Amonton's law of friction:

Equation 4.1: Amonton's Law

$$f_f = \mu L$$

where  $f_f$  is the friction force,  $\mu$  is friction coefficient and  $L$  is load force.

Systematic tribological experiments from Bowden and Tabor showed that contact between two macroscopic surfaces is influenced by small asperities that exist on the surfaces. In the Bowden-Tabor model, friction force is proportional to the actual contact area, which takes into account the apparent contact area of the asperities that will be involved in the contact [127]. The Bowden-Tabor model has been previously used to describe the frictional behaviour of nanostructured surfaces [12] [13].

Biotribology is a relatively new field which deals with aspects of tribology within biological systems. It has been applied to various biological systems, including joint tribology, skin tribology and oral tribology [130]. Recently, two studies have demonstrated the effects of surface tribology on bacterial adhesion [131,132]. Both studies found that surfaces with a high friction coefficient promoted bacterial adhesion. Swartjes *et al.* in particular reported that friction forces were involved in immobilising bacteria to a polymer brush surface [131], while Sharma and colleagues found a correlation between shear stress and initial bacterial adhesion to a surface with subnanoscale roughness [132].

The aim of this study was to determine if there was any correlation between the nanotribological aspect of the nanostructured surfaces and the antimicrobial properties of the nanopillars. This understanding could provide further insight into the factors influencing bacterial adhesion to nanostructured surfaces, and the potential importance of surface nanotribology in antimicrobial applications.

## 4.2 Results

### 4.2.1 Friction force measurement

Three interrelated nanostructured surfaces: BWN, BDN and SDN, along with a flat surface as a control, were used in this study. Trace and retrace data were collected by recording the lateral deflection of the cantilever on a scan area of  $1 \times 10 \mu\text{m}$  (512 points per line of 16 lines), with the scanning direction set to be perpendicular to the long axis of the cantilever. The scan speed was chosen to be at  $10 \mu\text{m} \cdot \text{s}^{-1}$ , which is identical to the average speed of swimming bacteria utilising flagella for motion [133].

#### 4.2.1.1 Understanding shear traces

It has been reported that bacteria respond to shear forces differently than to the normal forces. Conventionally, researchers have studied the effects of shear force on bacteria by using microfluidic devices and varying the shear flow rate of the devices. This is fundamentally different from the direct friction force measurement using AFM, where the shear force is dependent on the normal force. In these studies, the friction and adhesion measurements were performed using a silica probe, silica is chemically inert and thus served as a good frictional model for comparison of the nanotribological data with the microbiology data.

The general characteristics of the measured shear traces showed sharp, recurring and irregular peaks for all nanopillared surfaces, while the flat surface showed a smoother sliding profile (Figure 4.1). All surfaces showed stick-slip oscillation characteristics that were more pronounced at higher load forces, where there were noticeable shifts in the y-axis of the whole spectrum in both scan directions (trace and retrace). The flat PET surface showed a small but obvious shift in the y-axis and had a smoother sliding profile compared to the nanopillared surfaces and showed low intensity and low frequency random noise of the stick-slip oscillation, even at higher load forces. The dependency between load force and stick-slip oscillation indicated that there was a stronger interaction between the silica probe and the flat PET surfaces as the applied normal force was increased. When the silica probe was sheared against the nanopillared surfaces, the friction loop showed significantly larger stick-slip oscillation. The random noise oscillation tended to be stronger at higher density nanopillared surfaces (SDN and BDN) compared to the low density nanopillared surface (BWN). Of note, the SDN surface showed pronounced stick-slip oscillation with larger peaks at higher load forces without significant shift of the whole spectrum in the y-axis when compared to the other surfaces.

Previous studies on nanostructured surfaces using silica AFM probe had shown that the raw shear traces can be analysed semi quantitatively by performing fast Fourier transform (FFT), which could show correlations between spatial frequency with the nanotopography [134,135]. Figure 4.2 shows the FFT data from these studies. The friction loop between silica probe and the nanopillared surfaces did not show any distinct peak on the FFT that could be related to the topography of the nanopillared surfaces. However, the FFT revealed that each nanopillared surface had a different level of magnitude for the same range of spatial frequency. The SDN had the highest magnitude at around 50, followed by BDN at 30, BWN at 20 and flat control at 10.

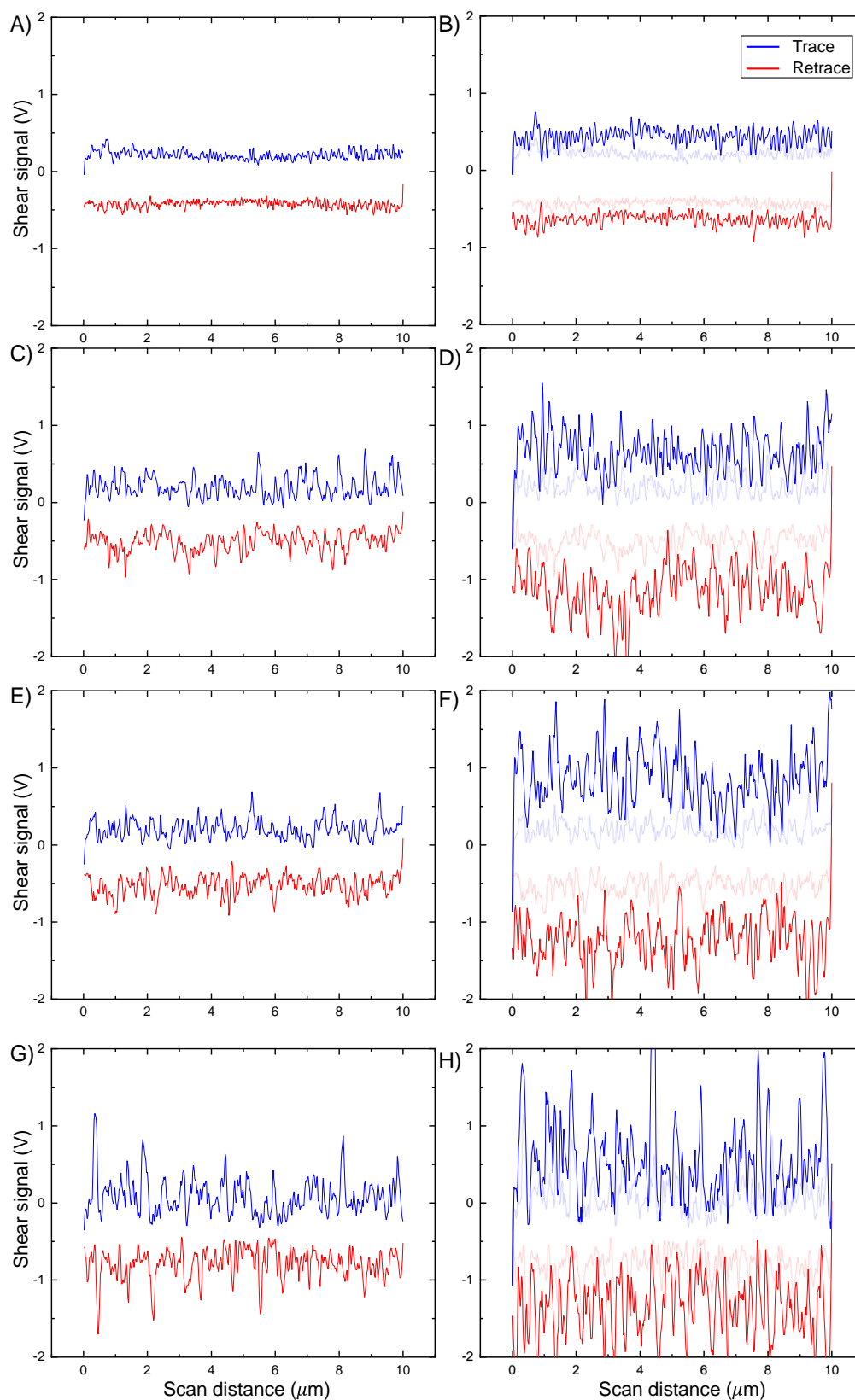


Figure 4.1 Comparison between 0 V shear traces and 2 V shear traces. Raw shear traces were obtained from AFM friction measurements of (a) flat control, (b) BWN, (c) BDN and (d) SDN surfaces at load force of 0 nN. On the left panels and on the right side is load force = 170 nN, both sheared at 10  $\mu\text{m/s}$ . The faded traces on the right panels are the shear traces at load force = 0 nN for comparison purposes.



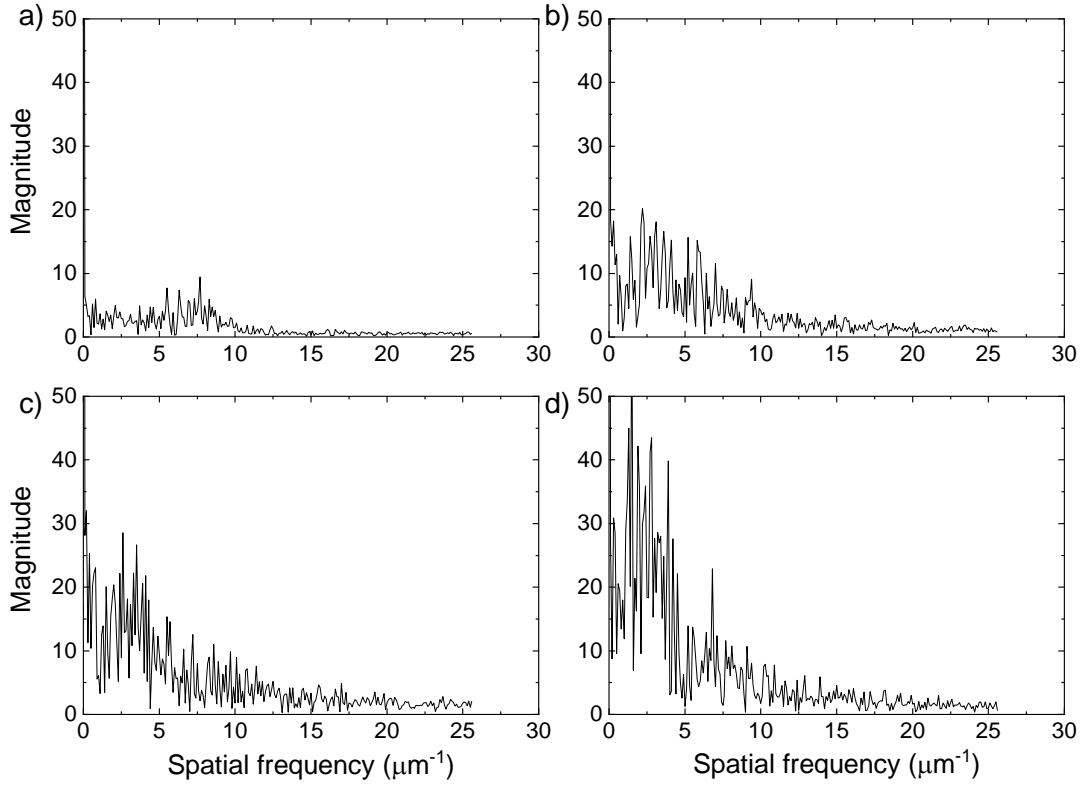


Figure 4.2 Fast Fourier transform (FFT) of the shear traces (from Figure 4.1) at a load force,  $f_L$ , of 170 nN. (a) Flat control, (b) BWN, (c) BDN and (d) SDN surfaces.

#### 4.2.1.2 Friction-load relationship

Friction force was calculated by taking the average of shear forces between the trace and retrace experienced by the silica probe. Figure 4.3 shows the friction against load force when the silica probe was sheared against the flat PET surface (Figure 4.3a) and the nanopillared surfaces (Figure 4.3b-c) at a speed of  $10 \mu\text{m s}^{-1}$  with ( $\blacktriangle$ ) for increasing load and ( $\nabla$ ) for decreasing load (unloading). A linear relationship was found on the friction vs. load force plots for all samples, which is in accordance with Amonton's first law of friction [136]. There was a significant difference in friction coefficient between the flat PET surface and nanopillared PET surfaces but there was no significant difference between the nanopillared surfaces (Table 4.1). The friction coefficient for flat PET substrate was  $\mu = 0.26$ , which is within the range of the reported friction coefficient for polyethylene substrate against a steel or silica [137]. The introduction of the nanostructured surface increased the  $\mu$  to 0.35-0.36, which is comparable to the frictional behaviour between brass and steel [138].

There was a small hysteresis observed on all test surfaces upon loading and unloading, and this was more pronounced with the nanopillared surfaces, especially with the high aspect ratio surfaces SDN and BWN. In general, the friction coefficient was increased upon unloading after

reaching the maximum loading force of 170 nN for all test surfaces including the flat surface. The flat and BDN surfaces showed about 0.01 difference between  $\mu_{UL}$  and  $\mu_L$  while BWN and SDN surfaces had about 0.06 difference between  $\mu_{UL}$  and  $\mu_L$  (Table 4.1).

A finite friction force  $f_o$  at zero load force can be identified from the friction-load plot, which is known as a contribution from intermolecular adhesive forces. Derjaguin showed that the friction force,  $f_f$ , is a sum of finite friction force ( $f_o$ ) and effective load force  $\mu L$ :

Equation 4.2: Relationship between friction force, finite friction force and load force

$$f_f = f_o + \mu L$$

The loading finite friction force,  $f_{oL}$ , for all the test surfaces varied, ranging from 51 nN to 65.3 nN. Of note, the unloading finite friction force,  $f_{oUL}$ , was found to be consistent between each sample at 48 nN, which was lower than the  $f_{oL}$ .

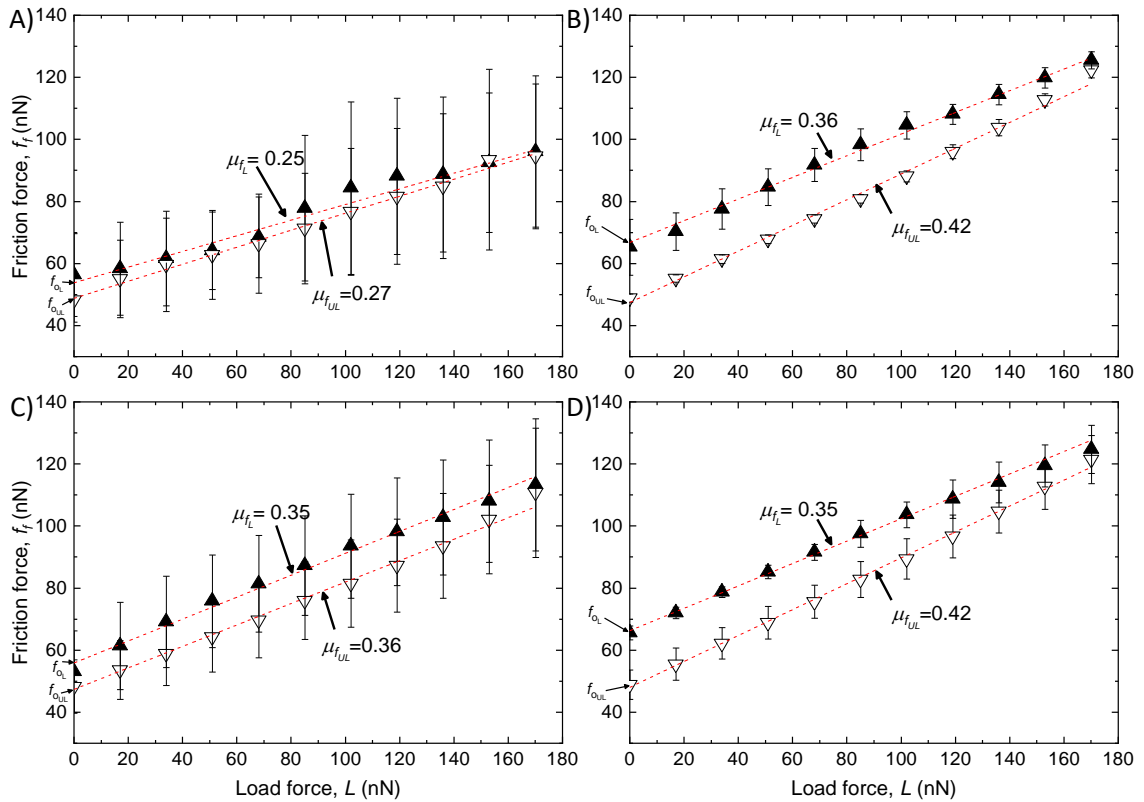


Figure 4.3 Friction force,  $f_f$  against load force,  $L$  plots.  $f_f$  vs.  $L$  plots are shown at a shear velocity  $10 \mu\text{m s}^{-1}$  for (a) flat control, (b) BWN, (c) BDN and (d) SDN surfaces. The gradient for the best fit gives a friction coefficient when loading ( $\mu_L$ ) and unloading, ( $\mu_{UL}$ ). Finite friction forces during load,  $f_{oL}$ , and unload  $f_{oUL}$ , when the applied load equalled 0 nN are marked by the arrows.  $f_{oUL} > f_{oL}$  suggested that all the samples underwent elastic deformation during the friction measurements.

Table 4.1 Adhesion and friction properties of the flat and PET nanopillared surfaces.

Surface	$f_p$ (nN)	$f_{0L}$ (nN)	$f_{0UL}$ (nN)	$\mu_L$	$\mu_{UL}$	$\varepsilon$ (nm)
Flat	76.6 $\pm$ 1.1	56.4 $\pm$ 13.3	48.2 $\pm$ 7.1	0.26 $\pm$ 0.08	0.27 $\pm$ 0.07	81.8 $\pm$ 15.2
BWN	38.4 $\pm$ 1.6	65.3 $\pm$ 9.0	48.9 $\pm$ 1.3	0.36 $\pm$ 0.03	0.43 $\pm$ 0.01	128.5 $\pm$ 13.2
BDN	72.2 $\pm$ 2.5	53.1 $\pm$ 13.1	48.3 $\pm$ 8.6	0.35 $\pm$ 0.06	0.36 $\pm$ 0.07	102.0 $\pm$ 12.8
SDN	78.9 $\pm$ 4.1	62.6 $\pm$ 2.3	48.9 $\pm$ 4.7	0.35 $\pm$ 0.05	0.42 $\pm$ 0.03	101.1 $\pm$ 12.2

Measured pull-off force ( $f_p$ ), finite friction force during load ( $f_{0L}$ ) and unload ( $f_{0UL}$ ), friction coefficient during load ( $\mu_L$ ) and unload ( $\mu_{UL}$ ), and peak-to-peak distance ( $\varepsilon$ ) were measured from the friction loop for each test sample. Data indicate mean values  $\pm$  standard deviation; N = 3.

#### 4.2.2 Normal force measurement

Force vs. separation curves were recorded over an area of  $4 \times 4 \mu\text{m}$ , and more than 5 measurements were performed on each sample, with the experiment repeated for three replicates of each sample type. The recorded curves were reproducible, so only a representative curve is presented (Figure 4.4). All of the force distance curves for the PET substrates were characteristic of a deformable material. As the silica probe approached the PET surface, the probe will have been attracted to the surface due to long-range interaction forces like van der Waals forces. The gradient of the attraction may have exceeded the spring constant of the silica probe, drawing the silica probe to jump onto the surface. After contact was established, adhesion forces will have anchored the silica probe more strongly to the surface. The force needed to separate the silica probe from the control, BWN, BDN and SDN surfaces was 76.56 nN, 38.44 nN, 72.23 nN and 78.91 nN, respectively.

The BWN surface had a significantly lower adhesion force when compared to the flat PET surface, which could have been due to the reduction in total effective contact area between the BWN nanopillars and the probe. Highly dense nanopillar surfaces with a spacing of 100 nm (BDN and SDN) had a higher adhesion force compared to the sparse BWN nanopillars and showed no significant difference in pull-off force compared to the flat surface. The force vs. separation curves can also estimate the vertical deformation of a single nanopillar,  $d'$ , which was measured from the force-separation curve at the maximum separation distance between the approach and retract curve at load force = 0 nN. The flat PET surface was deformed by 1.1 nm, whereas greater deformation was measured for the BWN, BDN and SDN nanopillared PET surfaces of 3.9 nm, 2.3 nm and 2.8 nm, respectively.

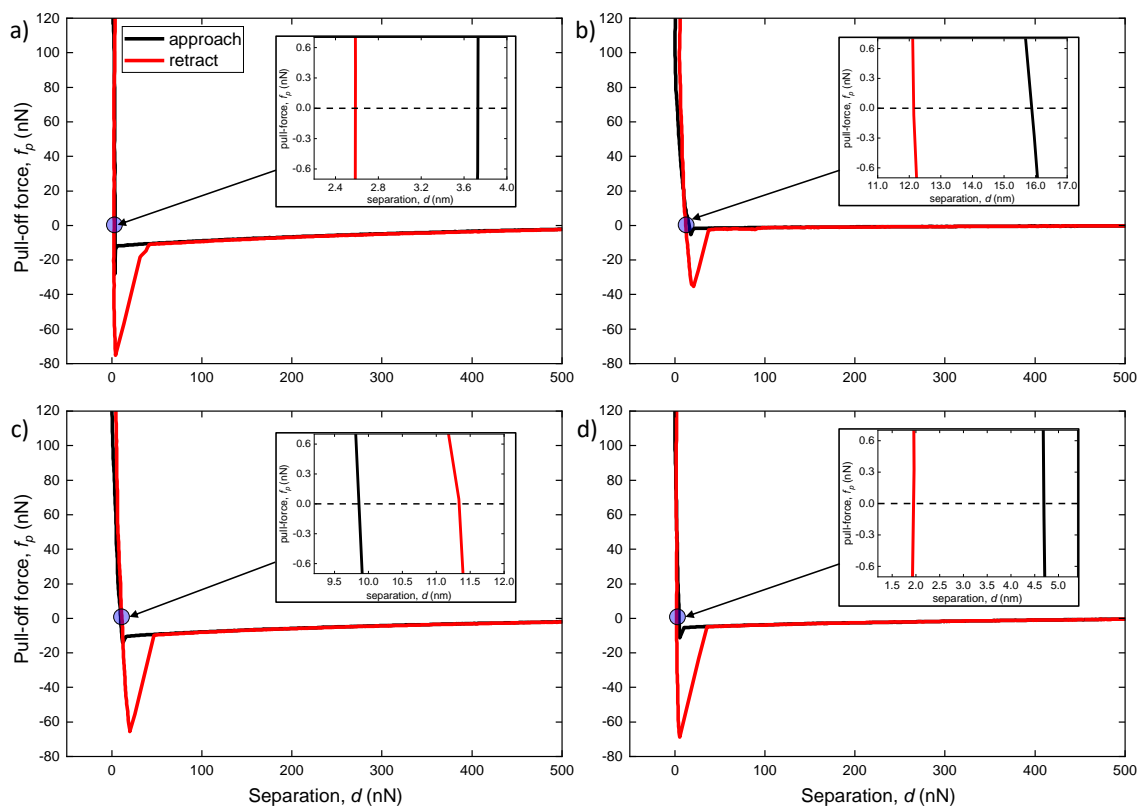


Figure 4.4 Representative force vs. distance curves for control and nanopillared surfaces. (a) Control, (b) BWN, (c) BDN and (d) SDN. The inset on each diagram shows the deformation,  $d'$ , experienced by the nanopillars, which was estimated at the maximum separation distance between the approach and retract curve at load force = 0 nN. The  $d'$  for control, BWN, BDN and SDN surfaces was 1.11 nm, 3.90 nm, 2.32 nm and 2.84 nm, respectively.

#### 4.2.3 Stick-slip amplitude coefficient (SSAC) analysis

The friction loop was further analysed to quantify the significant oscillations in the shear traces, which were induced by the interaction of the silica probe and the nanostructured surfaces. The interaction was mainly attributable to the multiple collisions between the silica probe and the nanopillars, which caused an unstable motion of the silica probe when it slid across the sample.

To quantify the instabilities of the CP-AFM probe with the nanopillared surfaces, the average peak-to-peak amplitudes were calculated for both trace and retrace at each load. The batch processing routine to find the standard deviation of shear signal was set up using OriginPro2018b and the shear trace was corrected by using the “Peak Analyzer” tool. First, the raw shear traces were normalised by subtracting the shear signal from the baseline to ensure consistency between different test surfaces. The baseline was found by calculating the anchor points of the shear signal, which were determined by finding the second derivative of the peaks in the plots. The amplitude parameter,  $\sigma_f$ , of the shear traces was calculated at each load by taking the average of the standard deviation of the peaks for both trace and retrace (Figure 4.5).

$\sigma_f$  was plotted against the load force,  $L$ , for all samples (Figure 4.6). Since the relationship between the signal instabilities and the load force is linear, the gradient of the plot can be defined as the stick-slip amplitude coefficient (SSAC). The control surface had the lowest value of SSAC, which was significantly different from all of the nanostructured surfaces. Unlike the friction coefficient, there were differences in SSAC between different nanopillared surfaces. It was found that the SDN surface had the highest SSAC at 0.040, followed by the BDN surface at 0.034 and the BWN surface with the lowest SSAC of 0.026.

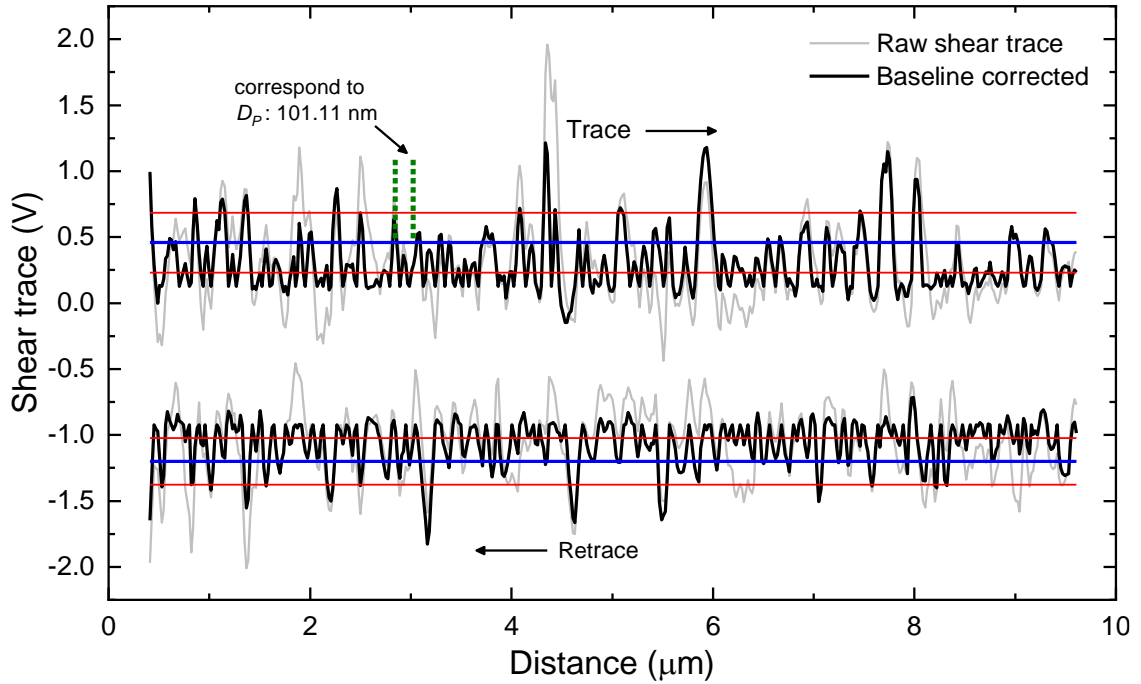


Figure 4.5 Raw shear trace (grey line) and baseline corrected trace (black line) for SDN surface with sliding velocity,  $v = 10 \mu\text{m s}^{-1}$  at load force 20 nN. The blue lines represent the averages of the trace and retrace while the red lines represent the standard deviation for the trace and retrace in the friction loop. The peak-to-peak distance between two adjacent stick slip peaks represents the interpillar distance of the nanopillars (green dotted lines).

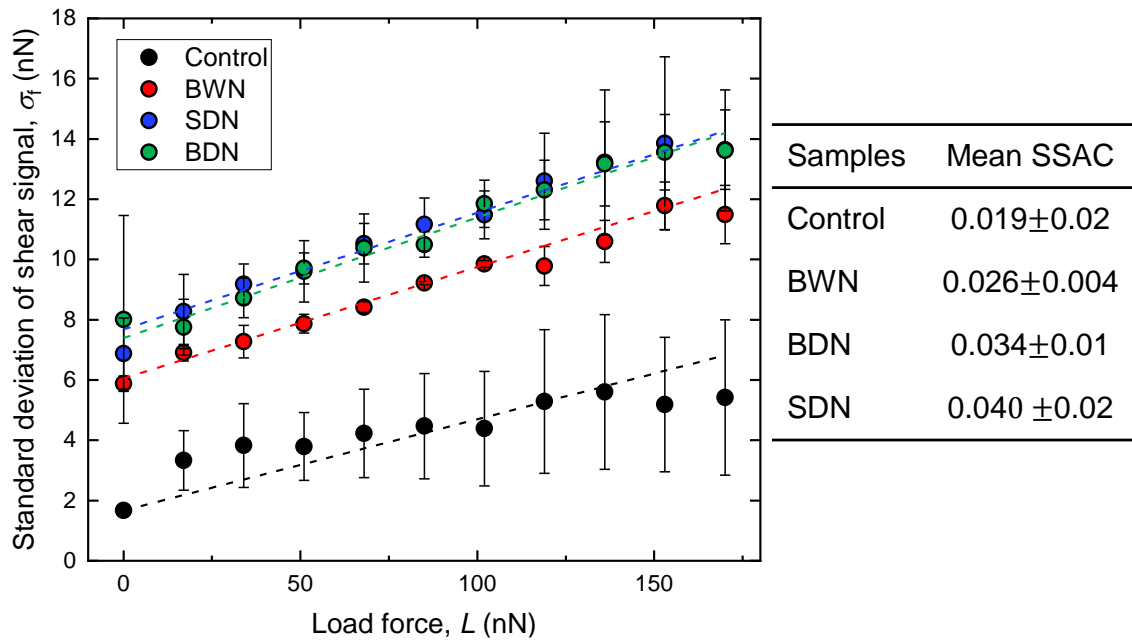


Figure 4.6 The standard deviation of the shear signal plotted against applied load force for flat PET, SDN, BDN and BWN surfaces.  $N=3$  and the error bars are the standard error of the mean values. The best-fit line of the plot is defined as the stick-slip amplitude coefficient (SSAC) and the mean SSAC is shown in the table.

## 4.3 Discussion

### 4.3.1 Adhesion force of nanopillared surfaces

Depending on the direction of the force, two interacting surfaces will experience a normal force and friction force that often results in wearing and damage to the surface. This applies to bacteria adhering to any substratum. The normal force comes from the adhesive forces between the bacterial cell and the surface, while friction force can be due to the hydrodynamic and liquid flow or the lateral movement of bacteria on the surface. Depending on the physicochemical properties, surface roughness and surface tribology, it is likely that the bactericidal effect of nanostructured surfaces is due to the wear and tear effect from the normal and shear forces. The studies presented in this chapter aimed to quantify all of the nanotribological properties of the three nanostructured surfaces, so that this information could subsequently be used to find any relationship with the antibacterial properties of the surfaces. A silica colloidal probe AFM was used as a generic model, as this allowed quantification of interactions between multiple asperities instead of single asperities when using the conventional sharp tip AFM. Established contact mechanics models like JKR could then be used to quantitatively assess the interaction between the colloidal probe and the nanostructured surfaces.

When retracting a colloidal probe from a nanopillared surface, the probe stays in contact with the surface until the cantilever forces overcome the adhesive probe-sample interaction. Generally, the adhesion force or the pull-off force,  $f_p$ , is a combination of other forces available on the surface like the electrostatic force,  $f_{el}$ , the van der Waals force,  $f_{vdW}$ , chemical bonds force,  $f_{cm}$ , and the meniscus or capillary force,  $f_{cap}$  [139]. Similarly, bacteria utilise the surface forces of their capsule or other cell surface determinants to establish strong adhesion before proliferating on a surface. In general, surfaces with a high adhesion force will have higher cell attachment compared to surfaces with a low adhesion force. However, this is not always the case, since the actual mechanisms of bacterium-substratum interactions are more complex than the colloidal particle-substratum interaction due to the complex properties of the bacterial cell membrane [47].

Commonly, the adhesion force of bacteria to a solid surface is measured by using a cell-probe AFM technique. In this technique, a calibrated tipless cantilever is functionalised with a bacterial cell. Then, the force-distance curves of the bacterium interacting with the surface are recorded. The approaching curve allows direct interpretation of distance-dependent cell-surface interactions, while the retracting curve provides the apparent adhesion force of a single

bacterium. Since different strains of bacteria can exhibit totally different interactions with the same surface, data from this technique are highly specific to the measured bacterial strain [140]. For this reason, quantifying the adhesion and friction properties of the nanostructured surfaces with a model surface like silica, as used in this project, has the advantage of allowing direct comparison with the antibacterial performance data to enable correlation of general bacterial responses to surfaces with different tribological properties. Here, this information then served as the basis from which a theoretical model of bacteria interacting with the nanostructured surfaces could be derived.

Adhesive force is governed by two important factors: contact interfacial forces and non-contact forces. Mainly, the adhesive force is related to the intrinsic contact area between the colloidal probe and the surface, where a larger area leads to a bigger adhesive force. In the case of nanostructured surfaces, the nanotopography will result in a decrease in contact area, hence reducing the adhesive force. However, if the effects of surface wetting are considered, a meniscus by the adsorbed water molecule would easily form on the nanostructured surfaces, thus increasing the adhesion force [121]. In this study, full penetration of the probe into the nanopillars was unlikely to occur but the nanopillars were expected to bend and deform upon the interaction with the applied load. This was evident from the characteristic elastic surface force-distance curves found for all tested surfaces, where there was a sudden jump into the surface (Figure 4.4). The observed adhesive force was dependent on the contact angle,  $\theta$ , surface energy,  $\gamma^{TOT}$ , and the interpillar distance,  $D_p$ , of the nanostructured surfaces (Figure 4.7). The  $\theta$  and  $D_p$  showed an inverse relationship, whereby the pull-off force,  $f_p$ , decreased as the  $\theta$  and  $D_p$  got larger. The dependencies of the interpillar distance,  $D_p$ , were also confirmed by previous studies on nanoparticle density and nanostructured surfaces [141]. The pull-off force showed a linear dependency with the surface energy, whereby the pull-off force got stronger as the surface energy increased. This relationship between surface energy and pull-off force has been reported previously with thin film [142] and nanotextured surfaces [121].



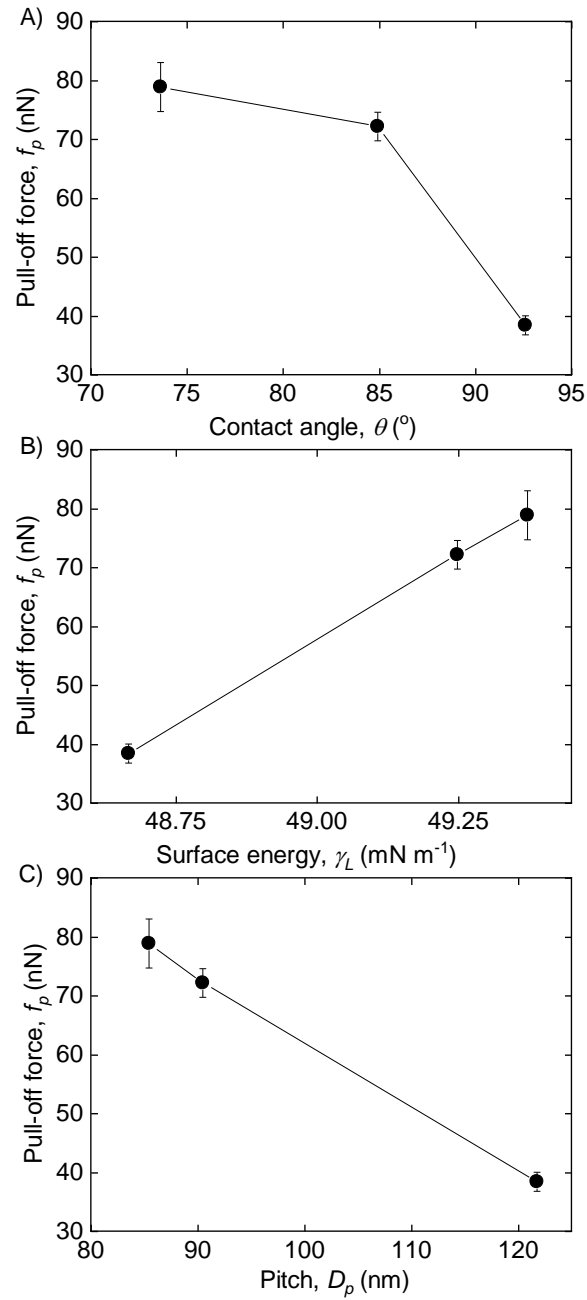


Figure 4.7 Relationship between pull-off force ( $f_p$ ) of the nanostructured surfaces and surface properties.  $f_p$  showed a linear relationship with (A) contact angle ( $\theta$ ), (B) surface energy ( $\gamma_L$ ) and (C) the interpillar distance (pitch) ( $D_p$ ). Data indicate mean values  $\pm$  standard deviation; N=5

#### 4.3.2 Young's modulus (YM) of the PET nanopillars

Although the impact of surface mechanical properties on bacterial attachment is still unclear, there is increasing evidence suggesting that material mechanical properties have an important role in bacterial surface sensing and adhesion [143]. For example, Lichter *et al.* reported that an increase in polyelectrolyte multilayer (PEM) stiffness promoted the adhesion of *S. epidermidis*, and this interaction was found to be independent of the physicochemical properties of the surface and the surface roughness [144]. To explore the relationship between surface mechanical properties and bacterial interactions in this project, the Young's modulus of the PET nanopillars was estimated by using geometric assumption and JKR theory.

As previously discussed in section 3.4, the work of adhesion values for all test surfaces were calculated using the Fowkes method. Data for flat PET surface corroborated with previous study using surface force apparatus (SFA) technique [145]. Contact mechanic models like the Hertz, Johnson, Kendall and Roberts (JKR) and Derjaguin, Muller, and Toporov (DMT) models could then be used to correlate adhesion properties with a pull-off force and so estimate the apparent contact area of the two interacting surfaces. According to the Hertzian model, the effective contact diameter in the absence of adhesion between an elastic sphere and flat surface is given by:

Equation 4.3: Hertzian model

$$a_{Hertz} = \left( \frac{LR}{K} \right)^{1/3}$$

where  $L$  is the applied load,  $R$  is the radius of the colloidal particle and  $K$  is the reduce modulus, which is defined as:

Equation 4.4: Reduce modulus

$$K = \frac{4}{3} \left( \frac{1 - \nu_1^2}{E_1} + \frac{1 - \nu_2^2}{E_2} \right)^{-1}$$

where  $E_1$ ,  $E_2$ , and  $\nu_1$ ,  $\nu_2$  are the Young's moduli and Poisson's ratios of the particle and the surface, respectively.

In the presence of adhesion, JKR and DMT models consider the effects of surface energy and work of adhesion, and give the effective contact diameter as:

Equation 4.5: JKR model

$$a_{JKR} = \left( \frac{R}{K} \left( L + 3\pi R W_{adh} + \sqrt{6\pi R W_{adh} L + (3\pi R W_{adh})^2} \right) \right)^{\frac{1}{3}}$$

Equation 4.6: DMT model

$$a_{DMT} = \left( \frac{R}{K} (L + 2\pi R W_{adh}) \right)^{\frac{1}{3}}$$

where the work of adhesion,  $W_{adh}$  is defined as  $W_{adh} = \gamma_L \cos \theta$ , and was measured and calculated in sub-section 3.4.2.

According to the JKR model, the contacting materials will undergo elastic deformation ( $d_{JKR}$ ) at some applied force, which can be calculated using the following equation:

Equation 4.7: JKR elastic deformation equation

$$d_{JKR} = \frac{a_{JKR}^2}{R} - \frac{2}{3} \sqrt{\frac{6\pi\gamma a_{JKR}}{K}}$$

The deformation of a single nanopillar,  $d'$ , was estimated from the force-separation curves at the maximum separation distance between the approach and retract curve at load force = 0 nN. For these calculations (Table 4.2), it was assumed that  $d' = d_{JKR}$  and all the nanopillars will exhibit the maximum deformation at any  $L$  (during the pull-off force measurement), since the force will be distributed equally across the contacting nanopillars. Since the mechanical properties of a single nanopillar were unknown,  $a_{JKR}$  of a single nanopillar interacting with the colloidal particle could not be calculated using Equation 4.5. However, by rearranging Equation 4.5 and Equation 4.7 for  $K$ , and then solving the equations for  $a_{JKR}$ , the intrinsic contact radius could be calculated without information on the mechanical properties of a single nanopillar (i.e. reduce modulus,  $K$ ):

Equation 4.8: Rearranging Equation 4.5 for  $K$

$$K = \left( \frac{R}{a_{JKR}^3} \left( L + 3\pi R \gamma + \sqrt{6\pi R W_{adh} L + (3\pi R W_{adh})^2} \right) \right)$$

Equation 4.9: Rearranging Equation 4.7 for  $K$

$$K = \frac{8}{3} \left( \frac{\pi W_{adh} a_{JKR}}{\left( \frac{a_{JKR}^2}{R} - d_{JKR} \right)^2} \right)$$

Let Equation 4.8 = Equation 4.9, then  $a_{JKR}$  can be expressed as:

Equation 4.10:  $a_{JKR}$  in terms of  $d_{JKR}$

$$a_{JKR} = \left( \frac{d_{JKR} R \left( L + 3\pi R W_{adh} + \sqrt{6\pi R W_{adh} L + (3\pi R W_{adh})^2} \right)^{1/2}}{\left( L + 3\pi R W_{adh} + \sqrt{6\pi R W_{adh} L + (3\pi R W_{adh})^2} \right)^{1/2} - \left( \frac{8}{3} \pi W_{adh} R \right)^{1/2}} \right)^{\frac{1}{2}}$$

To calculate the intrinsic contact area of a single nanopillar ( $a'_{JKR}$ ), the forces distributed per pillar ( $L'$ ) and nanopillar tip diameter ( $D_T$ ) were used instead of  $L$  and  $R$  in Equation 4.10.

$L'$  could be estimated by finding the total number of nanopillars ( $N$ ) that were in contact with the colloidal probe, which could be calculated using the geometric model. The intrinsic contact radius,  $R_i$ , between the colloidal probe and the nanopillared surface under a known applied load,  $L$ , is given by:

Equation 4.11: Intrinsic contact radius  $R_i$  equation

$$R_i^2 = 2R\delta - \delta^2$$

where  $\delta$  is the penetration depth of the colloidal particle for a known  $L$  due to bending, and could be estimated from the separation vs. load force curves.

As seen in Figure 4.8, the approach curve of the nanopillared surfaces had two regions with different slopes. It was assumed that the first slope was due to the deflection of the cantilever and the second slope was due to the penetration of the probe onto the nanopillars,  $\delta$ , where  $\delta$  is the sum of vertical nanopillar deformation,  $d'$ , and the bending of the nanopillars,  $b$ . When the colloidal probe first jumped to contact at  $p_1$ , the cantilever started to deflect. Then,  $p_2$  marked the start of the second region where  $\delta=0$ . After this point, the colloidal probe was penetrating the bed of nanopillars, causing the nanopillars to experience deformation and bending. As  $L$  increases due to the interaction forces between the colloidal particle and the nanopillared surface,  $R_i$  will increase and the number of nanopillars that are in contact with the colloidal probe will change (Figure 4.9). The total number of nanopillars in contact with the probe,  $N$ , could be calculated using the following equation:

Equation 4.12: Total in contact nanopillars equation

$$N = A_i \cdot \phi$$

where  $A_i$  is the intrinsic contact area ( $A_i = \pi R_i^2$ ) and  $\phi$  is the density of the nanopillars per  $\mu\text{m}^2$ .

For a periodic nanostructured surface with a known interpillar distance,  $D_p$ , density is defined

$$\text{as } \phi = \left(\frac{1000}{D_p}\right)^2.$$

Then,  $L'$  is given by:

Equation 4.13: Intrinsic force per pillars equation

$$L' = \frac{L}{N}$$

Then, the pressure exerted on a single nanopillar,  $\rho$  can be calculated  $\rho = L' / \pi \alpha_{JKR}^2$ . The

Young's modulus of a single nanopillar,  $E'$ , can be calculated using the following equation:

Equation 4.14: Young's modulus of single nanopillar

$$E' = \frac{L'h}{d'\pi D_T^2}$$

Figure 4.9c highlights the differences between  $h$ ,  $\Delta h$ ,  $\delta$  and  $d'$ .

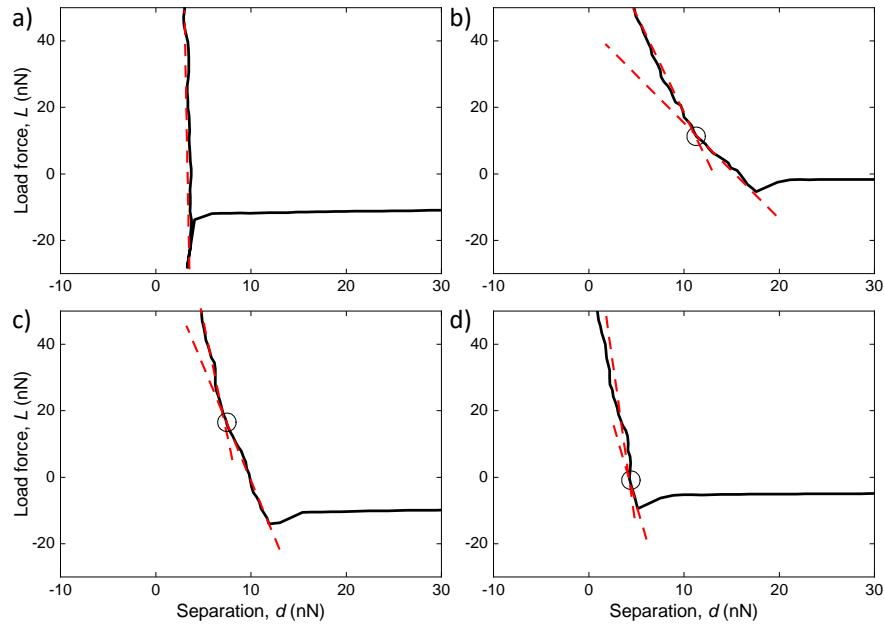


Figure 4.8 Interpreting the force vs. separation curves. Representative approach curves of (a) flat, (b) BWN, (c) BDN, and (d) SDN surfaces measured using a  $15 \mu\text{m}$  colloidal probe are shown. The flat surface showed one clear straight line, which was due to deformation of the cantilever. The nanopillared surfaces showed two regions with different slopes (marked in red for easier visualisation) and the circles are where the lines intersect.

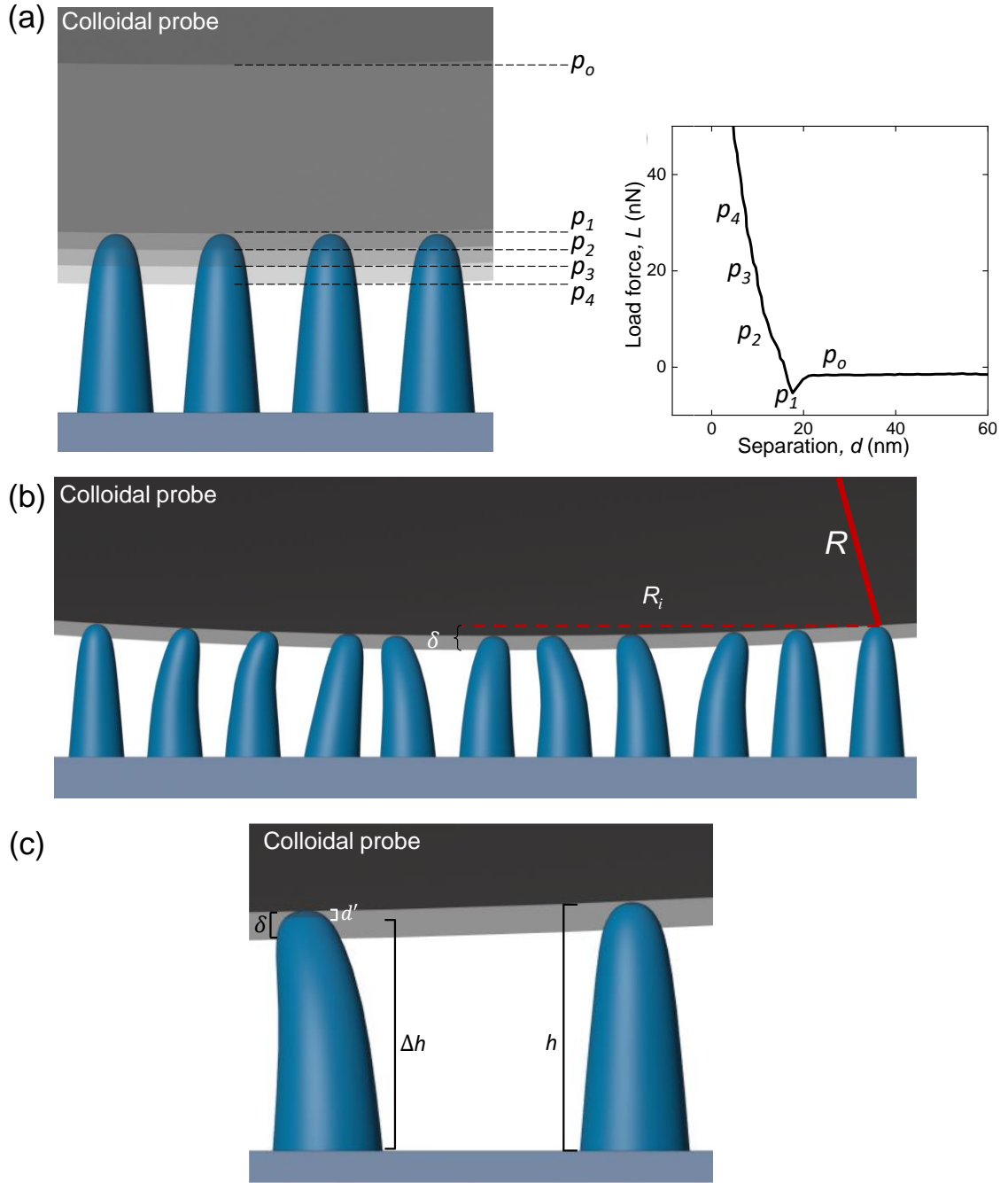


Figure 4.9 Geometric assumption of the intrinsic contact between the colloidal particle and periodic nanopillars based on the pull-off force data. (a) The inset shows the approach pull-off force data of BWN.  $p_o$  is the position of the colloidal probe when not in contact with the surface,  $p_1$  is the position of the colloidal probe when it is in contact with the nanopillars for the first time where the cantilever deflected upon contact with the surface.  $p_2$ ,  $p_3$  and  $p_4$  are the position of the colloidal probe as the  $L$  and  $\delta$  increase. (b) Schematic of the contact between the colloidal probe and the nanopillars.  $R$  is the radius of the colloidal probe,  $R_i$  is the intrinsic contact radius between the colloidal probe and the nanopillars, and  $\delta$  is the penetration depth of the colloidal probe for a known applied load,  $L$ . (c) Schematic indicating the difference between  $\delta$ ,  $d'$ ,  $h$  and  $\Delta h$ .

From the geometric and JKR analyses, it was found that the BWN surface had the highest intrinsic contact radius of the colloidal probe,  $R_i$ , number of nanopillars in contact with the probe,  $N$ , and contact radius of a single nanopillar,  $a'_{JKR}$ , compared to the other surfaces (Table 4.2). It is possible that the BWN surface had the highest  $R_i$  because its nanopillars experienced greater bending than for the BDN and SDN surfaces, which allowed the colloidal probe to penetrate further into the nanopillars. Figure 4.10 shows the changes in the number of contacted nanopillars with the colloidal particle,  $N$ , as a function of penetration depth,  $\delta$ , and the applied load,  $L$ .  $\delta$  and  $N$  show a linear relationship, whereby more nanopillars are in contact with the colloidal particle as the penetration of the probe increases.

SDN had the least amount of maximum penetration ( $\delta = 5.5$  nm) and hence had fewer nanopillars interacting with the probe. By contrast, the BDN and BWN surfaces had a maximum  $\delta$  of 8 nm and 11 nm, respectively, suggesting that there were more nanopillars that were in contact with the probe for these two surfaces. The lack of changes in the number of in contact nanopillars for SDN as a function of depth and load force suggested that the nanopillars exhibited higher stiffness compared to the BWN and BDN surfaces (Figure 4.10). Indeed, this was further supported by the average Young's modulus of a single nanopillar,  $E'$ , calculated using Equation 4.14.  $E'$  for the SDN surface was significantly higher at 60.7 MPa than 13.8 MPa for BDN and 9.3 MPa for BWN. Table 4.2 shows that  $E'$  decreased as the diameter of the nanopillars increased. A similar observation was reported by Chen *et al.*, where the mechanical elasticity of GaN nanowires decreased with increasing diameter [146]. Shin *et al.* also reported that the elastic modulus of a polymer fibre decreased with increasing size in diameter [147]. Despite studies that have shown that  $E'$  can also increase with an increase in nanostructure diameter [148–151] or remain constant [34][35], the changes of  $E'$  observed in this study match those reported by most studies previously [28][32][34][36].

Elasticity of a macroscopic structure is independent of size, and so the Young's modulus of a material does not depend on size and structure and follows Hooke's law and the Euler-Bernoulli theory [155]. However, data from this and other studies show that the mechanical behaviour of micro-nanostructures cannot be explained using the classical elastic theory. Hence, other theories have been developed to explain nanoscopic elasticity behaviour by including other parameters for consideration. Currently, five theories have been proposed to explain the size effects seen in nano/microstructures: residual stress theory, couple stress theory, grain boundaries theory, surface elasticity theory and surface stress theory [155]. The residual stress theory is the most widely used model to explain the change in mechanical properties of

nanostructures that are fabricated from a substrate e.g. hot embossing. According to the theory, the residual stress from the fabrication process remains in the structures so that the total elastic energy of the material when it is deformed is the contribution from both structure bending and residual stress. Figure 4.11 shows the change in  $E'$  as a function of  $D_T$ , where, as the  $D_T$  increases,  $E'$  gets smaller.

Table 4.2 Calculated interactions between the colloidal probe and surfaces.

	$R_i$ (nm)	$N$	$a'_{JKR}$ (nm)	$A_{TOT}$ (nm <sup>2</sup> )	$\rho$ (MPa)	$E'$ (MPa)
Control	149.4 $\pm$ 21.6	N/A	N/A	7.0 $\times$ 10 <sup>4</sup>	N/A	N/A
BWN	306.5 $\pm$ 87.5	38 $\pm$ 8	12.7 $\pm$ 1.6	1.1 $\times$ 10 <sup>4</sup>	3.8 $\pm$ 0.7	9.3 $\pm$ 3.7
BDN	250.8 $\pm$ 54.4	35 $\pm$ 5	9.7 $\pm$ 1.4	6.5 $\times$ 10 <sup>4</sup>	9.9 $\pm$ 2.3	13.8 $\pm$ 4
SDN	207.4 $\pm$ 57.2	23 $\pm$ 5	7.6 $\pm$ 0.9	2.7 $\times$ 10 <sup>4</sup>	26.4 $\pm$ 4.7	60.7 $\pm$ 19

Contact radius between colloidal probe and test surfaces  $R_i$ , maximum number of in contact nanopillars  $N$ , intrinsic contact radius of a single nanopillar interacting with the colloidal probe  $a'_{JKR}$ , total contact area  $A_{TOT}$ , average pressure exerted on a single pillar due to adhesion  $\rho$ , average Young's modulus of a single nanopillar  $E'$ .

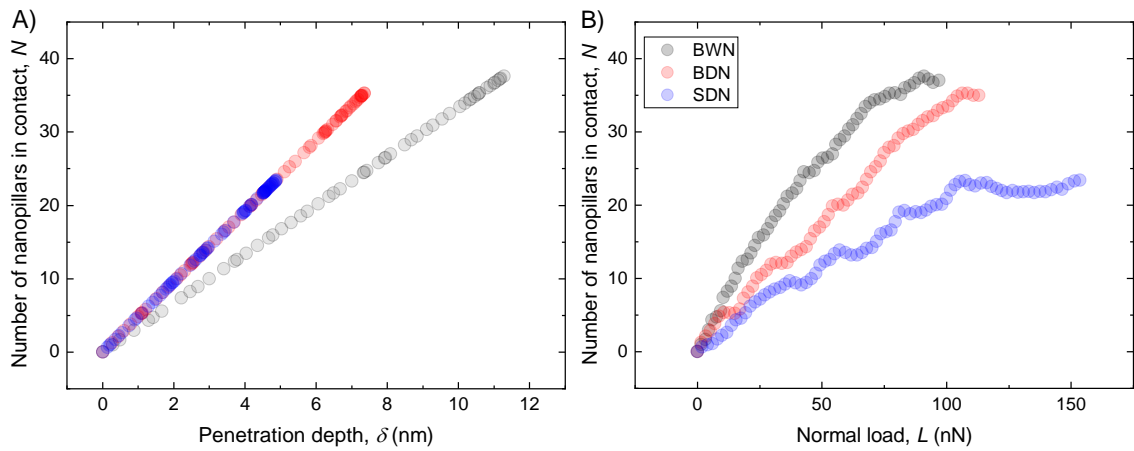


Figure 4.10 Probe interaction with the nanostructured surfaces. The number of nanopillars in contact with the colloidal probe,  $N$ , as a function of (A) penetration depth,  $\delta$ , and (B) the normal load,  $L$ , is shown for BWN (black dots), BDN (red dots) and SDN (blue dots) surfaces.



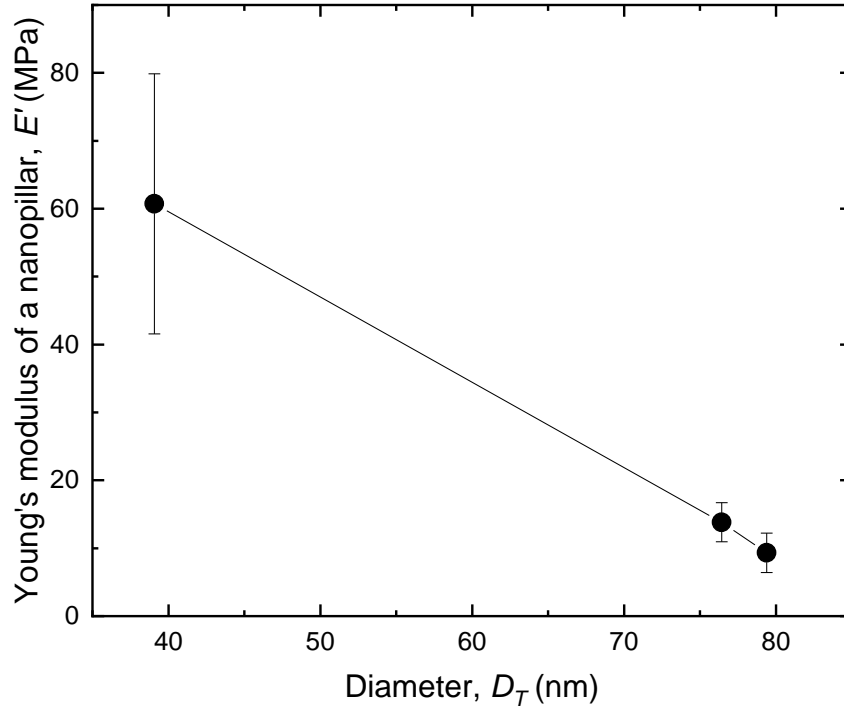


Figure 4.11 Young's modulus of a nanopillar as a function of the diameter,  $D_T$ . Data indicate mean values  $\pm$  standard deviation;  $N=50$

It was found that the total apparent contact area,  $A_{TOT}$ , between the colloidal particle and the test surfaces was largest for the flat surface, followed by BWN, BDN and SDN surfaces. This is interesting, because while the reduction in  $f_p$  found for the BWN surface compared to the flat surface is due to the reduction in  $A_{TOT}$ , this relationship between  $f_p$  and  $A_{TOT}$  collapses as the density ( $N$ ) and diameter of the nanopillars ( $D_T$ ) changes. Pilkington *et al.* also found no correlation between the features of various nanostructured surfaces with the  $f_p$ . For example, ZnO nanograin with a diameter of 40 nm was reported to have a  $f_p$  of 2.77 nN while a nanograin with a diameter of 80 nm had a  $f_p$  of 0.02 nN.

As previously shown in Chapter 3, PET nanopillared surfaces followed the Wenzel model, which describes a wetting state that displaces the gas phase trapped between the nanostructures. Recently, Bartosik *et al.* and Kwon *et al.* both showed that a nanoscale water bridge can form between a sharp AFM tip and flat surface at different relative humidities. In this study, the AFM experiment was performed at 40% relative humidity which, according to the study by Bartosik *et al.*, would mean that a nanoscale water bridge was likely to have formed between the nanopillars and the silica colloidal probe. It is possible that the higher adhesion found on the more densely compacted nanopillared surfaces (BDN and SDN) were due to the effects of water

bridges (Figure 4.12). Bhushan *et al.* also reported similar findings when studying the adhesion and friction properties of dried and fresh leaves using a  $15\text{ }\mu\text{m}$  colloidal particle. It was found that the dried leaves had a lower adhesion force compared to fresh leaves, which they proposed was due to the presence of a thin liquid film on the surface that caused meniscus bridges to build up around and near the contacting bumps.

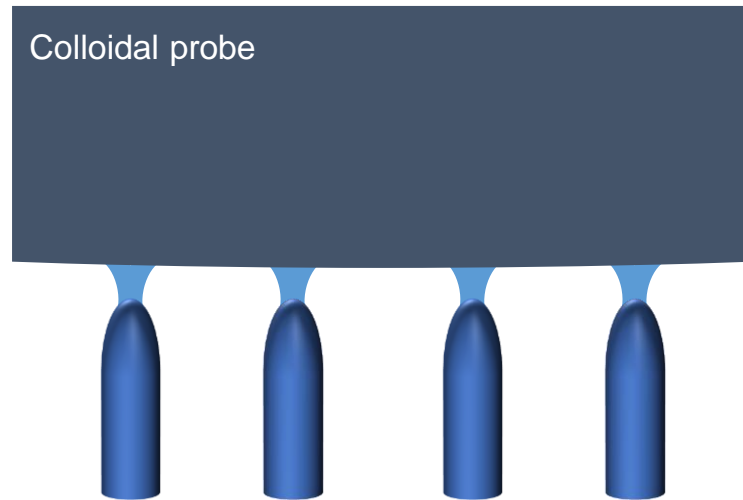


Figure 4.12 Nanoscale water bridges form on individual nanopillars.

#### 4.3.3 Frictional properties of PET nanopillared surfaces

Two surfaces that are in contact can experience two types of directional force: 1) adhesion force, which is normal to the surface, and 2) frictional force, which is parallel or at some angle to the surface. These forces not only affect macroscopic materials, but also micro/nanoscale biotic and abiotic surfaces. Due to challenges in measuring accurate tribological responses of bacteria to a surface, there is currently no conclusive evidence as to how nanostructured surfaces with different tribological properties affect bacterial responses. For this project, the frictional properties of PET nanopillared surfaces were therefore used to provide insight into potential correlations between bacterial responses to a surface and the surface nanotribological properties.

The distinct shear traces observed on the nanopillared surfaces are consistent with previous studies on textured surfaces such as zinc oxide (ZnO) nanograins [128], flexible microstructured silicon surfaces [135], pyrolytic graphite steps [156], nanorods with a gelatinous layer [157], silicon with nanopits and nanogrooves [158], and aluminium oxide (Al<sub>2</sub>O<sub>3</sub>) nanodomes [129]. These different surfaces bearing different nanotopographies showed distinct but qualitatively similar pronounced stick-slip profiles in their shear traces. The distinct stick-slip profile on the PET nanopillared surfaces reported here was likely related to more pronounced elastic bending by the nanopillars compared to the more rigid nanostructures made from ZnO and Al<sub>2</sub>O<sub>3</sub> [12][13]. It has also been reported that a polymer surface could form molecular bonds with another surface (including silica) owing to the energy instabilities at the contact interface. Such a strongly adhesive contact could further contribute to the stick-slip profile of the PET nanopillared surfaces investigated here [159].

The friction measurements performed on the different nanopillared PET surfaces with a smooth silica colloidal particle showed interesting dependencies between the surface topography, wettability and surface energy with the frictional properties. It has been reported previously that textured surfaces show quantitative nanoscale instabilities [13][42][43]. The hysteresis between  $\mu_{oL}$  and  $\mu_{oUL}$  in these studies highlighted the apparent discrepancies of the PET nanopillared surfaces used. The hysteresis in friction coefficient during load and unload could be attributed to higher elastic bending for the higher aspect ratio nanopillars compared to the flat control surface and short, blunt nanopillars. As the elastic nanopillars were subjected to an increase in load force from 0 nN to 170 nN, the nanopillars may have experienced significant bending, which will have increased the effective contact area with the silica particle. The finite friction force during load and unload also showed hysteresis. This may have been caused by

temporary bonding between the polymeric surface and the silica particle as the surface was subjected to an increase in load force from 0 nN to 170 nN before the unloading process took place.

When studying an array of microneedles with a small silica colloidal probe, Thormann *et al.* found that the Fourier transform of the shear traces revealed the relationship between the spatial frequency and the spacing between microneedles [135]. Interestingly, when using a larger silica probe, the stick-slip oscillation increased in randomness and did not show any systematic patterns of distinct peaks, as previously observed when using a small silica probe i.e. no correlation was found between the peaks identified from FFT data and the nanotopography. Similarly, in this study, there were no significant peaks that could be identified from the spatial frequency that corresponded to topographic contribution of the surface, even at high load force. Instead, the distance between the adjacent peaks on the shear traces was found to correspond to the periodicity of the nanopillars (for BWN, BDN and SDN surfaces  $D_p$  was  $\sim 128$  nm, 101.98 nm, and 101.11 nm, respectively). These values were in agreement with the pitch distance measured using SEM and AFM analysis. Similarly, Sundararajan *et al.* reported that there were direct topographic contributions found on the trace and retrace signals when analysing a microscopic silicon grid consisting of 5 and 10  $\mu\text{m}$  square pits with a silicon nitride cantilever [158].

In this work, the friction force,  $f_f$  of the nanopillared surfaces showed a linear increase with the applied force,  $L$ , which was consistent with previous work studying nanopatterned surfaces [12][13]. Pilkington *et al.* used a sharp AFM tip to study the tribological properties of nanostructured surfaces bearing nanoseeds, nanodiamonds, nanodomes and nanorods. They found that, at the microscale, the linear nature of the friction-load relationship could be explained using the Bowden and Tabor model, which states that the model holds if the surfaces are plastically deformed [127]. However, at the atomic scale, the Tomlinson model [45][46] and the Cobblestone model [164] are preferred, since these models consider the energy dissipation as a result of climbing the asperities. It is important to note that Amonton's law is known for explaining macroscopic friction behaviour instead of describing the nanoscopic frictional behaviour, where the linear relationship between  $f_s$  and  $L$  is not typical, especially with nanostructured surfaces. For example, a previous AFM study showed a non-linear relationship between  $f_f$  and  $L$  for the interaction between Ni nanoporous membrane and 0.93-2.28  $\mu\text{m}$  silica beads [165].

The interactions between the silica probe and the nanopillars in this study were dominated by the multiple collisions between the silica probe and the nanopillars instead of the short-range and long-range surface forces. Due to large variation in the data, there was no conclusive correlation found between  $\mu$  and the  $h$  or the  $R_q$  of the nanopillared surfaces (Figure 4.13). Previous studies have reported conflicting results on the dependencies between vertical dimensions of nanostructures and the friction coefficient [12][13]. Pilkington *et al.* reported a possible correlation between vertical dimensions and geometric friction coefficient when studying nanotextured surfaces with varying nanotopographies. A study on the tribological behaviour of GeSbTe thin films found a linear correlation between friction coefficient and surface roughness [166]. By contrast, Quignon *et al.* did not find any correlation when studying nanodome structures on an aluminium oxide surface with an AFM nanotip [129]. Instead of measuring the interactions between single asperities, the use of a colloidal probe in this work facilitated measurement of the interactions from multiple asperities over a larger surface area. As discussed earlier, the PET nanopillared surfaces had a higher elastic bending modulus than materials used in prior studies. This could have contributed to the linear dependence found here between friction coefficient and the vertical geometry of the surfaces.

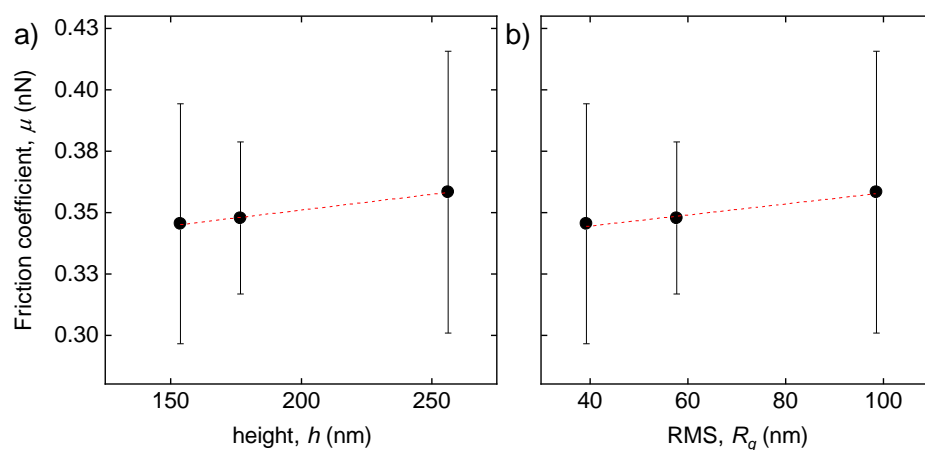


Figure 4.13 Correlation between friction coefficient and vertical geometry of the surface. Correlations between  $\mu$  and (a) average height,  $h$ , or (b) measured RMS roughness,  $R_q$  are shown. Data indicate mean values  $\pm$  standard deviation; N=3

#### 4.3.4 Nanomechanical properties and SSAC

Frictional instabilities have previously been reported at the atomic scale involving polymer brushes; an increase in lateral force was observed due to an increase in dissipative energy barrier i.e. the Schwoebel-Ehrlich barrier at atomic step edges [167]. The Prandtl-Tomlinson model also accounts for tip-sample interactions at the atomic scale, and states that the AFM tip might be stuck in a potential energy minimum that will cause a sudden increase in lateral deflection signal. The tip will remain in this position until enough energy is obtained for the tip to slide again, which causes another sudden change in the lateral deflection signal [168].

Several studies have also reported frictional stabilities at the nanoscale. For example, when studying molybdenum disulphide coatings, the friction data were analysed by decomposing the data into two components, which were a constant value and a fluctuating value. The fluctuating value was to account for the variation found on the local surface slope [169]. Another study found abrupt oscillations when studying microgrooved silicon surfaces, where the peaks and troughs on the surface gave rise to sharp fluctuations found on the friction loop [158]. It was also proposed that the asperities on the surface caused the tip's linear momentum to convert to angular momentum during the interaction between the AFM tip and the asperities, and also led to the sudden lateral jump of the tip to the surface.

In this study, the constant and strong fluctuations observed on the nanostructured surface friction loops suggested that the interactions between the AFM tip and the nanopillars were dominated by the interaction between the silica probe and the nanopillars. As discussed earlier, direct evidence of the interaction was that the distance between two adjacent peaks on the shear traces corresponded to the interpillar distance of the nanopillars, and there was a small dependency of the friction coefficient on the height of the nanopillars and the RMS of the surface. The instabilities of the friction loop suggested that the CP-AFM probe was colliding with the nanopillars, which was in contrast to the smooth sliding friction loop found on the flat PET substratum. As the probe was trying to jump off from the surface, the energy was dissipated, which corresponded to the abrupt increase and decrease in the lateral deflection signal. SSAC was a semiquantitative analysis that measured frictional instabilities of a surface and was not dependent on the measured friction coefficient.

It was found that the SSAC had a direct relationship with the nanopillar density,  $N$ , pull-off force,  $f_p$ , the surface energy,  $\gamma^{TOT}$ , and the Young's modulus of the nanopillars,  $E'$  (Figure 4.14). Higher values of  $N$ ,  $f_p$ ,  $\gamma^{TOT}$ , and  $E'$  resulted in higher SSAC. Stiffer nanopillars will resist bending upon

interaction with the colloidal probe. If the surface has high adhesive energy due to high  $f_p$ , and  $\gamma^{TOT}$ , then the colloidal probe would require more energy to release from the nanopillars. As the fluctuations in energy increase, so the dissipations will result in higher frictional instabilities. This finding also highlighted the possibility that it may be possible to control the wearing properties of polymeric nanostructured surfaces for different applications by manipulating the nanotopography of the polymer substrate.

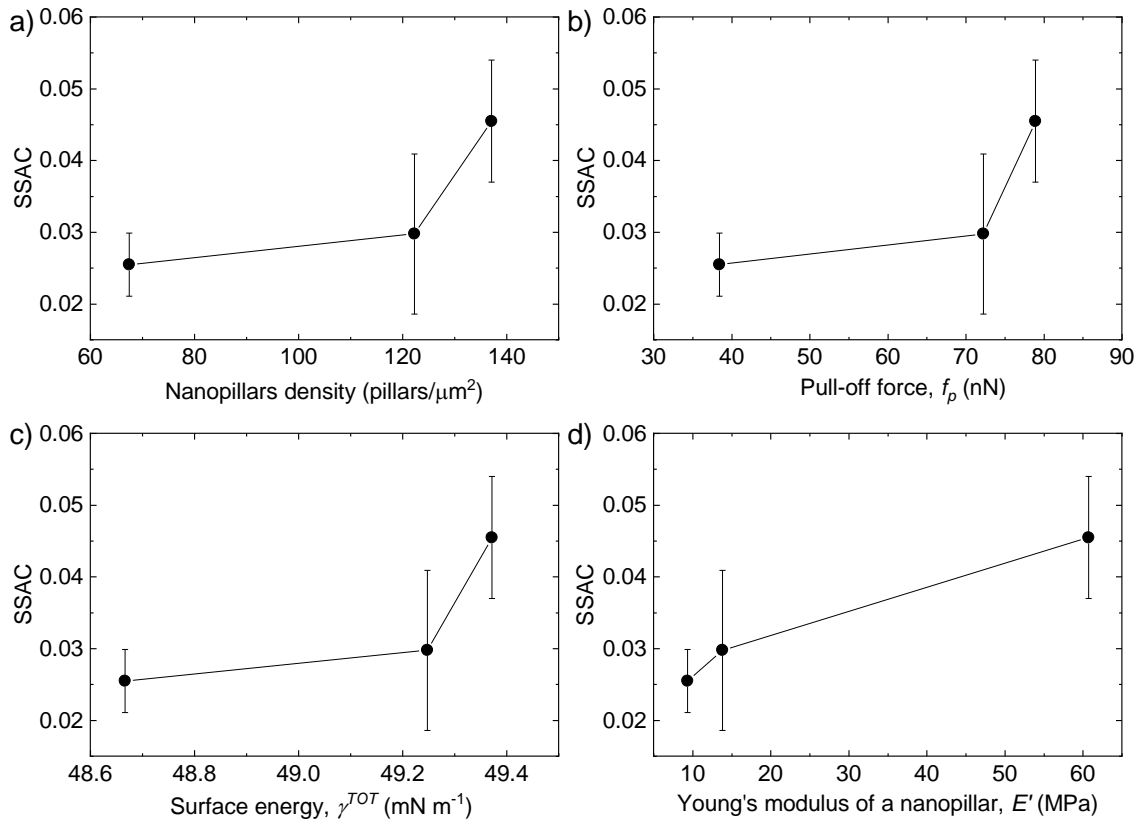


Figure 4.14 Correlation between SSAC and surface properties of nanopillared surfaces. Plot of SSAC against (a) nanopillar density,  $N$  (b) pull-off force,  $f_p$ , (c) surface energy,  $\gamma^{TOT}$ , and (d) Young's modulus of a single nanopillar,  $E'$ . Data indicate mean values  $\pm$  standard error;  $N=3$ .

## CHAPTER 5 UNDERSTANDING THE BACTERIAL RESPONSE TO POLYMERIC NANOPILLARED SURFACES: A PHYSICOCHEMICAL AND NANOTRIBOLOGICAL PERSPECTIVE

### 5.1 Introduction

Bacterial adhesion to an implant can be separated into two time-dependent phases. Phase I occurs during the first 1-2 h post implantation and involves reversible interactions with the surface. During this phase, the bacteria may interact with the surface via long-range and short-range interactions like van der Waals forces, electrostatic forces, hydrogen bonding, dipole-dipole, ionic and hydrophobic interactions [9]. The majority of the bacteria remain in the planktonic state. Phase II occurs 2-3 h post implantation and is characterised by stronger adhesion between the bacterial cell and the surface, in which the interactions are between cell surface determinants of the bacterium, such as polysaccharides and protein adhesins, and the substratum. During this phase, bacteria may also use elongated structures such as pili and flagella to penetrate the energy barrier of the substratum and help to bridge between the cell and the surface [47].

A similar mode of action is expected for bacteria during attachment to a nanostructured surface, whereby the majority of bacteria are in planktonic state during phase I, and then during phase II the bacteria use their surface appendages to promote attachment to the nanostructured surface by establishing a higher adhesion force. On a flat surface, a higher adhesion force is desirable to facilitate attachment to the surface and for subsequent biofilm formation. By contrast, on a nanopillared surface, a high adhesion force may increase the intrinsic pressure within the bacterial cell on and around the nanostructures, which could potentially cause harm to the bacterium. When bacteria establish contact with the nanopillars, it is expected that the bacteria may use their surface appendages to enhance adhesion on the surface. This adhesion will get stronger over time, which will promote stretching of the suspended bacterial cell wall, eventually reaching the stretching limit and leading to rupture (Figure 5.1).



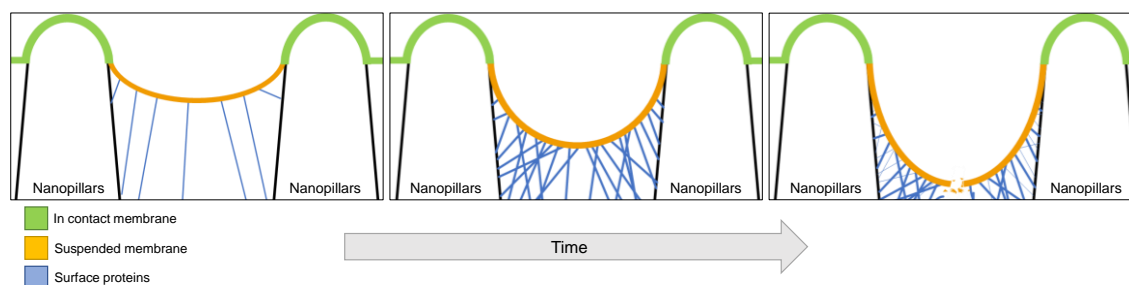


Figure 5.1 Potential mechanism of bacterial attachment to a nanopillared surface using its surface proteins. The driving force for adhesion is likely to be due to higher total interaction forces between the bacterial surface proteins and the nanopillared surface.

## 5.2 Results

### 5.2.1 Bacterial membrane susceptibility on nanostructured surfaces

The current postulated bactericidal mechanism of action for nanostructured surfaces is via a physical process, whereby the nanotopography can cause significant damage to the bacterial cell envelope. Specifically, the nanopillars can deform the bacterial cell wall until the suspended region between the nanopillars ruptures, or the nanopillars may penetrate the cell wall and cause loss of turgor pressure. This physical damage of the cell wall can be quantified using a fluorophore dye that permeates a cell with a compromised membrane. LIVE/DEAD assay is a technique that uses two different fluorescent dyes: SYTO9 and propidium iodide (PI). Upon staining a sample with LIVE/DEAD reagent, the SYTO9 will permeate all cells, causing the cells to fluoresce green when viewed under the fluorescence microscope, while PI can only enter cells with a compromised cell membrane, where it will displace SYTO9 and cause the cells to fluoresce red. Thus, green fluorescent cells can be quantified as viable, while red or orange fluorescent cells can be quantified as cells with a damaged membrane. Using this approach, the BWN, BDN, and SDN were tested against *E. coli*, *K. pneumoniae* and *S. aureus* for 3 hours, as this correlated with the predicted second phase of bacterial adhesion, where stronger adhesion to the surface would be established [47]. *E. coli* was chosen as a model motile Gram-negative bacterium, *K. pneumoniae* as a model non-motile Gram-negative bacterium, and *S. aureus* as a model Gram-positive bacterium. Moreover, *E. coli*, *K. pneumoniae* and *S. aureus* are reported to be amongst the most commonly isolated strains for BAIs, making them clinically relevant [6]. After 3 hours static incubation at 37°C, the nanopillar surfaces were washed gently to remove the non-adherent bacteria, prior to staining with SYTO9 and PI. Five images per surface type at 20× magnification were collected and analysed using ImageJ, enabling quantitation of numbers of viable and compromised bacterial cells (Figure 5.2)(Figure 5.3).

As reported in the literature [53], the BWN surface that resembled the cicada wing topography had some negative effects on the bacteria. Approximately 26% of *E. coli* cells and 8% for *K. pneumoniae* exhibited damage (Figure 5.3). Denser nanopillars with the same diameter as the BWN surface i.e. BDN surface caused more substantial effects, with about 54% of adherent *E. coli* cells and 45% of *K. pneumoniae* cells exhibiting a compromised membrane. At a density of 100 pillars  $\mu\text{m}^{-2}$  with sharper nanopillars (SDN surface), 71% of *E. coli* cells and 80% of *K. pneumoniae* cells displayed a compromised membrane. The *S. aureus* cell membrane was not affected to the same degree as for the Gram-negative bacteria. Adherent *S. aureus* exhibited 9%, 8% and 6% membrane permeability, respectively, on BDN, BWN and flat surfaces. Only SDN showed significant increases in membrane permeability for the adherent bacteria, which reached about 15%.

The total number of cells per area for each test surface was also calculated and compared (Figure 5.2). There were no significant differences between different surfaces for each bacterial strain. However, there were significantly more *K. pneumoniae* cells ( $7\text{--}12 \times 10^6$  cells  $\text{cm}^{-2}$ ) adhered to the test surfaces compared to *E. coli* at  $1.2\text{--}2.2 \times 10^6$  cells  $\text{cm}^{-2}$  or *S. aureus*  $3.7\text{--}5 \times 10^6$  cells  $\text{cm}^{-2}$ . Although the average values for numbers of adherent *E. coli* cells were reduced on the nanopillared surfaces when compared to the flat surface, the data were too scattered for the differences to reach statistical significance. A trend was less obvious for *K. pneumoniae* and *S. aureus*; BWN showed an increase in the average number of adhered cells compared to the control whereas this number was lower than control for BDN and SDN. Again, the data were too variable to reach statistical significance. Together, these data suggested that different bacterial strains had different mechanisms of adhesion and susceptibility to the same nanotopography. Sharper and denser nanopillared surfaces were seemingly the most effective at causing significant damage to the cell wall of Gram-negative bacteria, while there was a small indication that these surfaces could also mediate potential damage to the cell wall of Gram-positive bacteria.

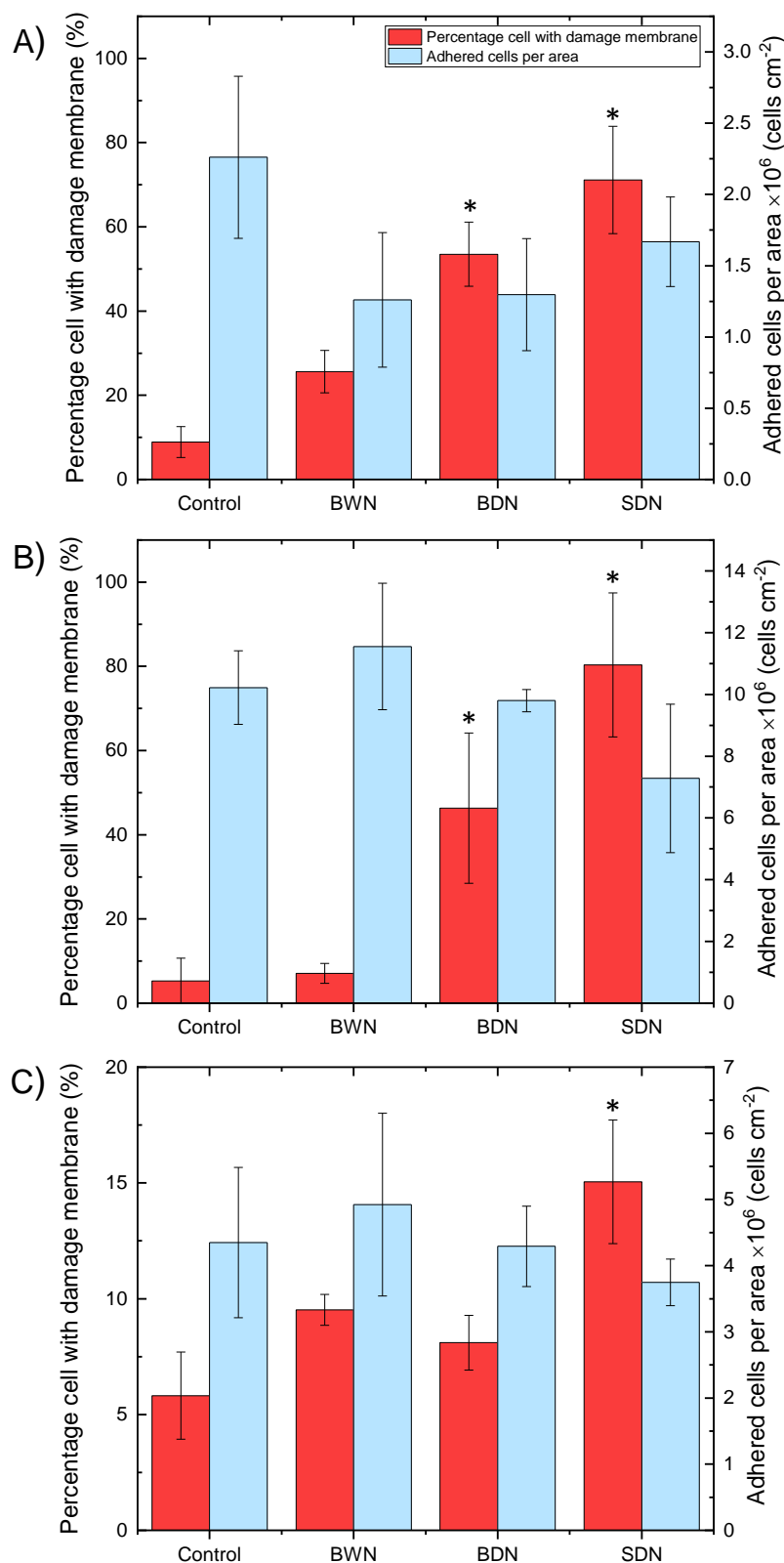


Figure 5.2 Quantitation of viable and compromised bacteria on nanostructured surfaces. (A) *E. coli*, (B) *K. pneumoniae*, and (C) *S. aureus* were incubated on nanostructured surfaces for 3 h. Percentage of adherent cells with a damaged membrane (red) and the total number of adherent cells per area (blue) were then determined following LIVE/DEAD staining. Data indicate mean values  $\pm$  SD. \* $P < 0.05$  compared to the control, as determined by one-way ANOVA with Tukey HSD post-hoc test;  $N=3$ .

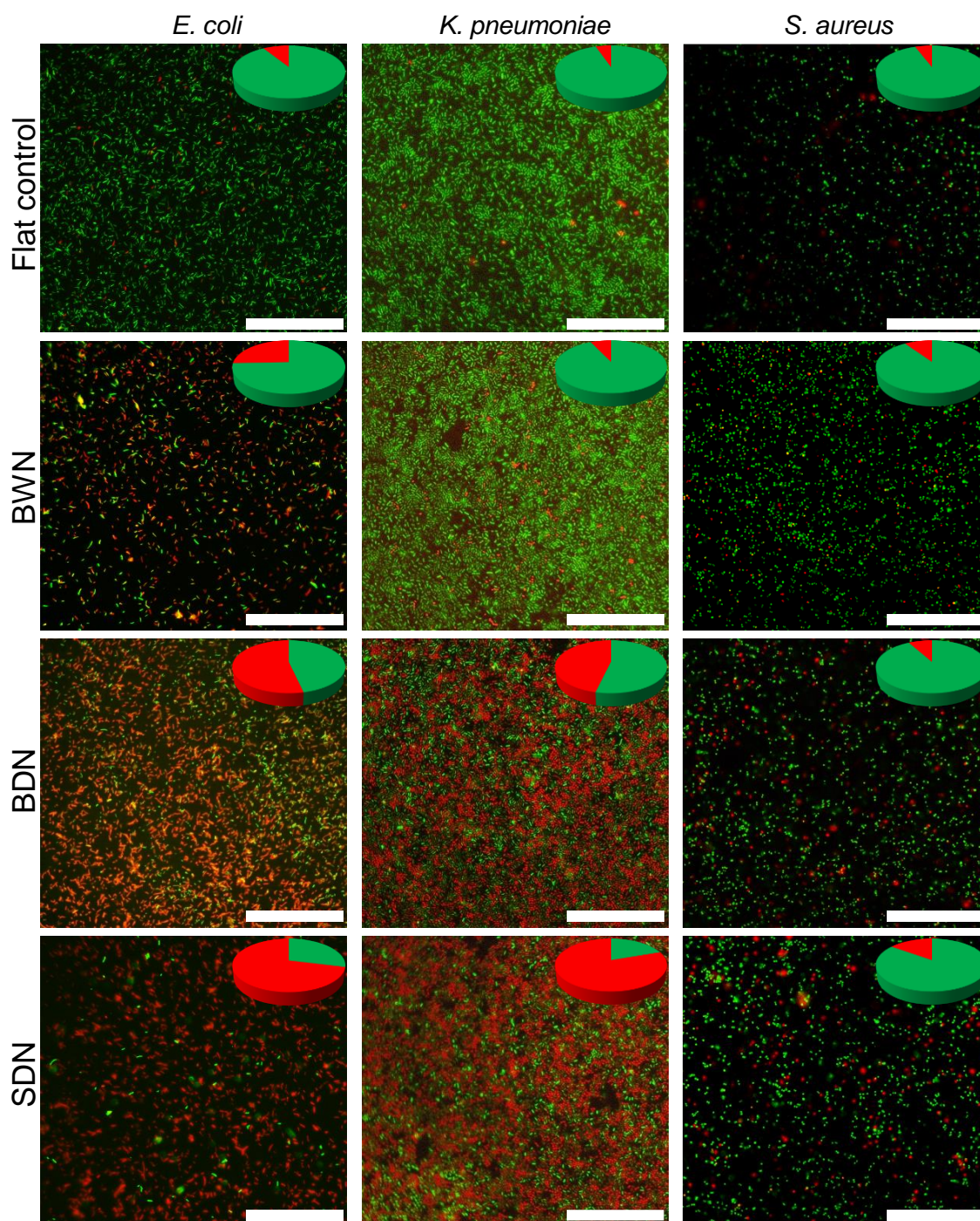


Figure 5.3 Representative fluorescence micrographs of bacteria on the test surfaces. *E. coli*, *K. pneumoniae* and *S. aureus* were incubated on flat PET control, BWN, BDN and SDN surfaces for 3 hours. Green coloured cells were considered to be viable, while red coloured cells were considered to be bacteria with a damaged membrane. Inset on each image is a pie chart indicating the relative proportions of intact cells (green) and damaged cells (red). Scale bar is 40  $\mu\text{m}$ .

### 5.2.2 Metabolic activity of bacteria on different nanotopographies

LIVE/DEAD staining and bacterial viable counts are the most common techniques used to quantify the antibacterial performance of nanostructured surfaces, with both methods determining the viability of the cell population. However, as evidenced from the literature, the vitality of adhered cells on a nanostructured surface may be impaired even without significant physical damage to the bacteria. To fully understand the bacterial response to the nanopillared surfaces, it was therefore important to quantify both the viability and vitality of the cells. Thus, the BacTiter-Glo (BTG) assay was used to assess the vitality of both the adherent cells and those in the surrounding suspension. This assay quantifies the concentration of ATP by using oxidative enzymes that produce bioluminescence as the by-product of the reaction. This bioluminescence correlates directly with ATP levels and consequently levels of bacterial vitality. The relative luminescence units (RLU) were then converted to colony forming units (CFU) using standard curve information that had been generated for each bacterium by a former PhD student (J. Jenkins, University of Bristol).

There were no significant differences seen between numbers of metabolically active cells on the BWN surface and the flat control for any of the three bacterial strains (Figure 5.4). The SDN surface had the largest effects, with fewer metabolically active bacteria found on the surface for *E. coli* ( $4.1 \times 10^5$  CFU) and *K. pneumoniae* ( $2.6 \times 10^6$  CFU) when compared to the BDN surface (*E. coli* ( $8.5 \times 10^5$  CFU) and *K. pneumoniae* ( $3.8 \times 10^6$  CFU)) or BWN surface (*E. coli* ( $1.2 \times 10^6$  CFU) and *K. pneumoniae* ( $6.2 \times 10^6$  CFU)). For *S. aureus*, there were significantly lower metabolically active cell numbers on the SDN surface ( $3.9 \times 10^6$  CFU) compared to the flat control ( $6.2 \times 10^6$  CFU) or BWN ( $5.6 \times 10^6$  CFU), but not compared to the BDN surface ( $5.0 \times 10^6$  CFU). No significant differences were found when comparing the numbers of metabolically active cells in the suspensions between all of the test surfaces for each bacterium (Figure 5.4).

Total numbers of metabolically active cells (CFU surface + suspension) after 3 hours increased for all three bacterial strains when compared to the starting inoculum of  $5 \times 10^5$  CFU: *E. coli*,  $1.4$ - $2.4 \times 10^6$  CFU; *K. pneumoniae* and *S. aureus*,  $6.8$ - $10.0 \times 10^6$ . This indicated that bacterial replication was occurring over the 3-hour period. For *E. coli*, the flat control and BWN surfaces had more viable cells adherent to the surface than in the suspension, while the opposite was seen for the BDN and SDN surfaces. The same trend was seen with *K. pneumoniae*. *S. aureus* had more adherent bacteria than in the planktonic phase for all of the test surfaces. Taken together, these results suggested that sharper and denser nanopillared PET surfaces could significantly

impair the metabolic activity of adhered cells after 3-hour static incubation, and possibly also impair bacterial attachment of at least the two Gram-negative species tested.

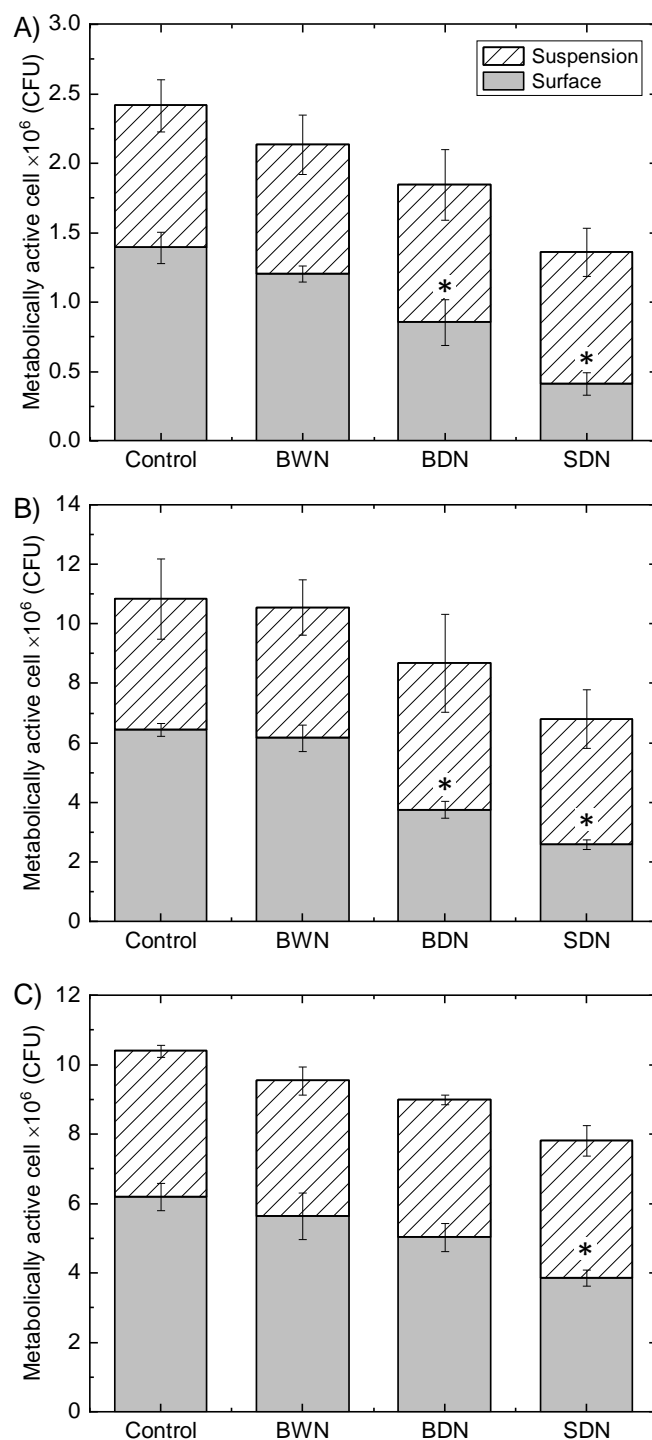


Figure 5.4 Quantitation of bacterial vitality on nanostructured surfaces using Bactiter-Glo™. CFU of metabolically active cells adhered on the surface (grey coloured) and remain in planktonic state (lines pattern) for (A) *E. coli* K12, (B) *K. pneumoniae*, (C) *S. aureus*. Data indicate mean values  $\pm$  standard deviation. \* $P < 0.05$  compared to the control, as determined by one-way ANOVA with Tukey HSD post-hoc test; N=3



### 5.2.3 Nanomechanical properties of the bacterial cell wall

Before the advancement in scanning probe microscopy, it was very challenging to measure the mechanical properties of biological samples. This was especially true for bacterial cells due to their fragile microstructures in comparison to the crude methods used to measure mechanical properties of a material in the past. Knowledge of the stiffness or rigidity of the bacterial cell wall is necessary in order to better understand bacterial responses to nanostructured surfaces. If the cell wall of the adhered cells is stretched and deformed by the nanopillars, there should be changes to the stiffness of the cell wall when compared to the bacteria adhered on the flat control. Stiffness is a measurement of the resistance of a material in response to an applied force, which in mathematical terms is the ratio between stress i.e. force per unit area ( $\sigma = F/A$ ), and strain i.e. fractional change in length ( $\varepsilon = \Delta L/L_0$ ) in a material [56]. Stiffness is also known as Young's modulus or elastic modulus ( $E$ ) and is measured in a unit of Pascal (Pa) or  $\text{N}\cdot\text{m}^{-2}$ , where a soft material will have a low  $E$  value while harder and stiffer materials will have larger  $E$  values. The general formula to calculate Young's modulus is given as:

Equation 5.1: General Young's modulus formula

$$E = \frac{\sigma}{\varepsilon} = \frac{F/A}{\Delta L/L_0} = \frac{FL_0}{A\Delta L}$$

where  $F$  is the applied force,  $A$  is the affected area,  $L_0$  is the initial length and  $\Delta L$  the change in length.

The Young's modulus of *E. coli* adsorbed onto the nanopillared surfaces was measured using the PeakForce system on a quantitative nanomechanical mapping AFM (QNM AFM) with a sharp AFM tip (radius of 5 nm). The Young's modulus of a single bacterium,  $E_B$ , was quantified by scanning 3 small areas ( $50\times 50\text{ nm}^2$ ) of the top side of the cell to represent the  $E_B$  of the whole cell. Three bacterial cells were scanned per surface type and the data are presented in Table 5.1.  $E_B$  of bacteria on the flat control was 7.4 MPa, which correlated with previous studies [42]. The  $E_B$  increased to 7.8 MPa on the BWN and BDN surfaces. The SDN surface showed the highest  $E_B$  at 8.86 MPa. This general increase in stiffness of the bacteria on the nanopillared surfaces relative to control suggested that the bacterial cell walls may have sustained deformation and/or stretching on the sharp and dense nanopillars. The morphology of the cells was also measured using the QNM AFM, and there were no significant changes observed in the morphology of the measured bacteria. Thus these data showed that the bacterial cell wall became stiffer when adhered to the nanopillars, with the sharp and dense surface showing the most significant

effects, but there was no evidence that the tested bacterial cells had undergone any changes in turgor pressure in response to the nanopillars.

Table 5.1 Young's modulus of the top side of *E. coli* cells when adhered to flat control or nanostructured surfaces.

Sample	Young's modulus, $E_b$ (MPa)
control	$7.40 \pm 1.74$
BWN	$7.78 \pm 1.44$
BDN	$7.76 \pm 1.30$
SDN	$8.86 \pm 1.38$

#### 5.2.4 Effects of trypsinisation on bacterial adhesion

Trypsin is a serine protease and is recognised as an important enzyme for protein digestion in animals. It is a globular protein, composed of 13 beta strands and four regions of alpha helix. Trypsin is highly active towards the positive side-chains of basic amino acid residues like lysine (Lys) and arginine (Arg), and cleaves at the carboxyl side of these residues during the hydrolytic reaction (Lee and Manoil, 1997). The affected proteins will have a negatively charge carboxylate group at the end of the chain after the tryptic attack. Trypsin is commonly used in mammalian cell culture to remove adherent cells. In this project, trypsin was used to cleave the surface proteins of *E. coli* to better understand their potential role in modulating bacterial attachment to the nanostructured surfaces. *E. coli* was chosen as the test bacterium in these studies because the effects of trypsin on *E. coli* are well established, and it is generally accepted that *E. coli* uses its surface proteins to establish strong adhesion to abiotic surfaces [170,171]. The SDN surface was used instead of other nanopillared surfaces since SDN had shown the best antibacterial performance.

##### 5.2.4.1 Effects on *E. coli* adhesion to an abiotic surface

An adhesion assay was first performed to confirm the success of trypsinisation on *E. coli* in pH 7.0 PBS buffer solution. In this assay, the ability of *E. coli* to adhere to a polycarbonate 96-well plate  $\pm$  trypsinisation was quantified after 3 hours of static incubation by crystal violet staining of total biomass. Significantly fewer bacteria adhered to the wells following trypsinisation relative to untreated control bacteria (Figure 5.5A). Furthermore, a dose response was seen with increasing duration of trypsinisation. Bacteria exposed to trypsin for 5 min or 10 min exhibited a 25% and 55% reduction in the biomass, respectively. This effect then seemed to plateau, with



no further reduction seen in biomass following 15 minutes trypsinisation, potentially indicating that 10 min was sufficient for trypsin to cleave all available proteins. LIVE/DEAD staining was used to confirm that trypsinisation did not negatively impact the viability of the cells (Figure 5.5B). From these data, 15 min of trypsinisation was chosen as the preferred treatment period for subsequent studies.

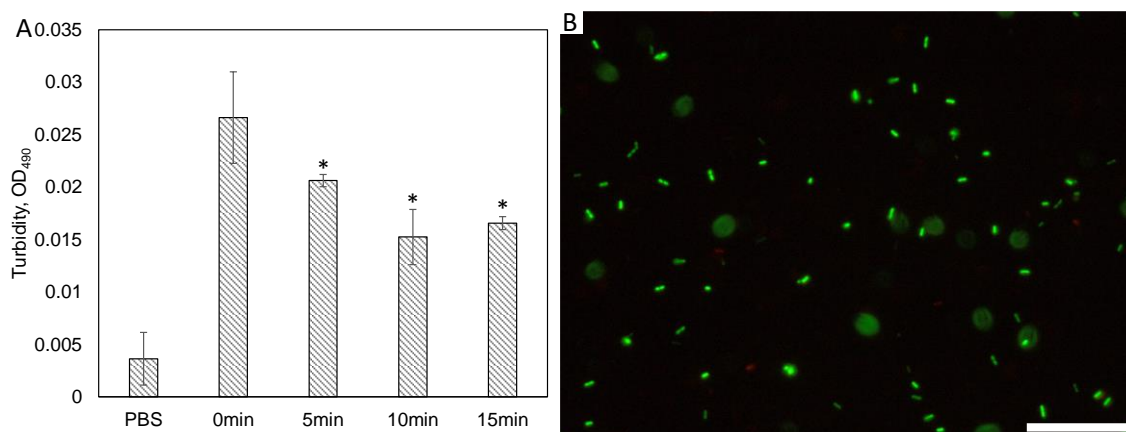


Figure 5.5 Quantitation of *E. coli* adhesion following a time-course of trypsin treatment. (A) Biomass at A490 of adhered *E. coli* K12 that had been treated with 0.5% trypsin in EDTA for 0 min, 5 min, 10 min, or 15 min to a polycarbonate surface (96 well plate). Data indicate mean values  $\pm$  SD. \* $P < 0.05$  compared to the control, as determined by one-way ANOVA with Tukey HSD post-hoc test;  $N=4$ . (B) Representative fluorescence micrograph of trypsinised *E. coli* treated for 15 min in 0.5% trypsin and stained using LIVE/DEAD. Scale bar is 20  $\mu\text{m}$ .

#### 5.2.4.2 Effects on hydrophobicity

When considering bacterial adhesion to a solid surface, hydrophobic interactions are generally the strongest amongst all of the long range, non-covalent interactions. A hydrophobic interaction is defined as the attraction between apolar moieties, such as particulates or cells in water [172]. Hydrophobic groups on the bacterial cell surface play a major role in removing water films between interacting surfaces to allow adhesion. To check whether the trypsinisation treatment affected the *E. coli* surface proteins with hydrophobic groups, the relative hydrophobicity of the treated cells was compared to the untreated cells. Bacterial cell surface hydrophobicity was assessed using a hydrocarbon assay. Bacteria were suspended in hexadecane, which causes hydrophobic cells to adhere to the hydrophobic hydrocarbon phase, while hydrophilic cells remain in the aqueous phase. These effects could then be measured by monitoring changes in the absorbance of the aqueous phase. After 30 min incubation in

hexadecane, untreated *E. coli* showed a significantly higher hydrophobicity of 92% compared to 99% for the trypsinised cells (Figure 5.6). This indicated that the hydrophobicity of the *E. coli* cells changed after trypsin treatment.

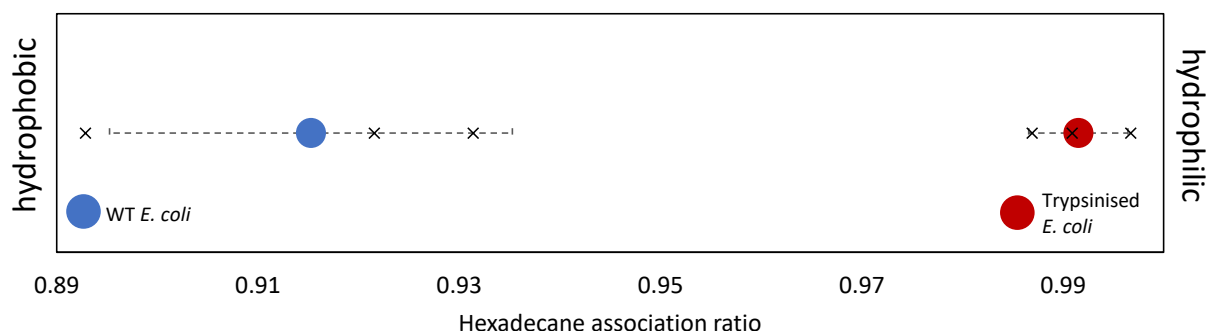


Figure 5.6 Hydrophobicity of non-treated (blue) and trypsinised *E. coli* (red). Data indicate mean values  $\pm$  SD.  $P < 0.05$  compared to the control, as determined by one-way ANOVA with Tukey HSD post-hoc test;  $N = 3$ .

#### 5.2.4.3 Effects on cell surface charge

Since the *E. coli* proteins that are affected by the tryptic attack will expose a negatively charged carboxylate group, it was anticipated that trypsinisation may change the surface charge of the cells. Surface charge was therefore quantified using dynamic light scattering (DLS), which measures the zeta potential of the cells. Zeta potential is the electrical potential of a charged particle (in this experiment, a single bacterium) at the shearing plane, where the motion of the charged particle is caused by an electrical field. Zeta potential,  $\zeta$ , is determined using the Helmholtz-Smoluchowski equation:

Equation 5.2: Helmholtz-Smoluchowski equation

$$\zeta = \frac{v}{E} = \frac{\eta}{\varepsilon \cdot \varepsilon_0}$$

Where  $v$  is particle velocity,  $E$  electrical intensity,  $\eta$  is viscosity, and  $\varepsilon \cdot \varepsilon_0$  is the dielectric constant.

The zeta potential of untreated wild-type (WT) and trypsinised (TRY) *E. coli* was used as an indicator of the electrical charge of the cell surface. A diluted bacterial suspension in PBS buffer was transferred into a specifically designed cuvette for the zeta potential measurement. Both

WT and TRY *E. coli* were both in mid-exponential phase during the measurement and the test was repeated in triplicate on three independent occasions. It was found that WT *E. coli* at mid-exponential phase had a significantly ( $P < 0.05$ ) higher electrophoretic mobility at  $-16.0 \pm 1.4$  mV than TRY *E. coli*, which had a total electrophoretic mobility of  $-11.1 \pm 0.7$  mV (Table 5.2). This correlates with previous studies [173,174]. As seen in Figure 5.7, TRY *E. coli* cells had a broader zeta potential distribution than untreated WT cells. This suggested that the trypsinisation may have altered the bacterial surface proteins in a way that affected the overall surface charge and ultrastructure of *E. coli*, making the cells less negatively charged.

Table 5.2 DLS data for untreated or trypsinised *E. coli* in PBS buffer (pH 7.4).

	WT* <i>E. coli</i> (mV)	TRY° <i>E. coli</i> (mV)
AVG <sup>§</sup>	-16.0	-11.1
STDEV	1.4	0.7

\* WT, untreated cells

° TRY, trypsinised cells

§ n = 3

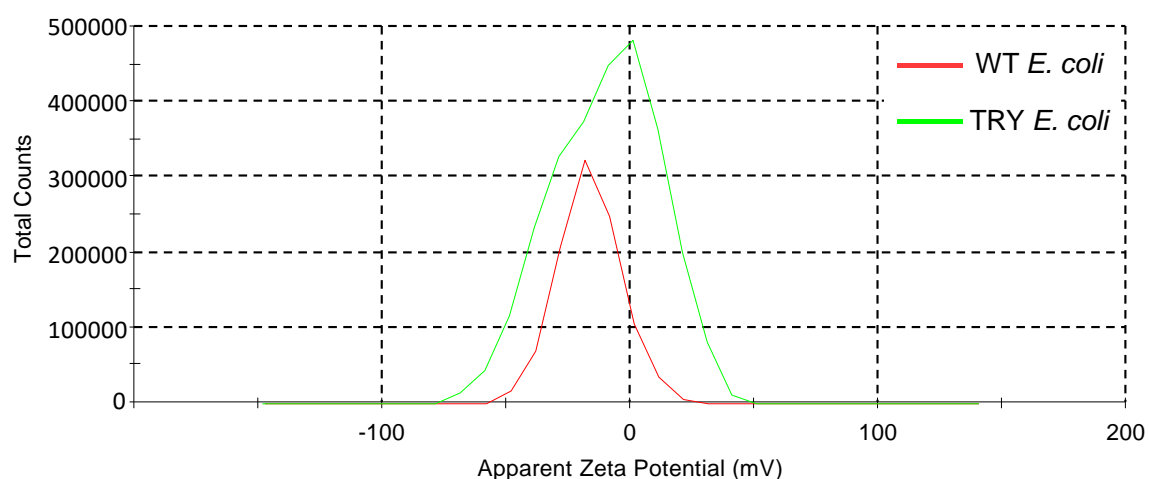


Figure 5.7 Zeta potential distribution for untreated (red line) and trypsinised *E. coli* (green line) in PBS buffer at pH 7.4.

#### 5.2.4.4 Effects on bacterial interactions with nanopillared surfaces

The interactions between *E. coli* ± trypsinisation and the substrata were measured by i) quantifying the viability of the *E. coli* cells using BacTiter Glo (BTG), and ii) quantifying the total

adherent biomass by SYTO9 staining. Untreated WT and TRY *E. coli* cells were incubated at 37°C with the flat control or SDN surface for 3 h in a static incubator. Then, the surfaces were washed gently, and the viability and biomass of the adhered cells were quantified using BTG and SYTO9 staining, respectively. It should be noted that RLU from these BTG assays could not be converted to CFU because the standard curve used previously was for *E. coli* grown in growth medium rather than the PBS used here.

Levels of metabolically active *E. coli* cells were comparable across the control surfaces, regardless of trypsinisation, and for TRY cells on the SDN surface. By contrast, levels of metabolic activity were significantly reduced for untreated WT *E. coli* cells on the SDN surface (Figure 5.8). The SYTO9 data also indicated some reduction in biomass on the SDN surface for untreated WT cells, but this was not significant, and overall levels of biomass were comparable for all test samples.

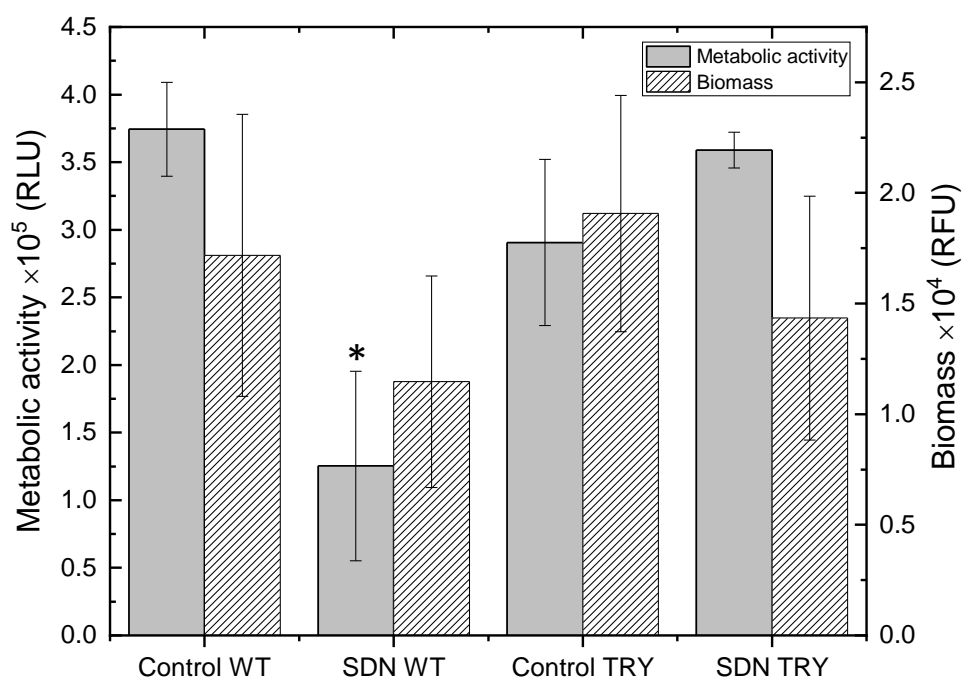


Figure 5.8 Effects of trypsinisation on *E. coli* attachment on flat control and SDN surfaces. Metabolic activity (filled) and total biomass (striped) of untreated, wild type (WT) and trypsinised (TRY) *E. coli* are shown. Data indicate mean values  $\pm$  standard deviation. \* $P < 0.05$  compared to the control, as determined by one-way ANOVA with Tukey HSD post-hoc test; N=3

SEM images of untreated WT and TRY *E. coli* on the flat and SDN surfaces confirmed that there were no obvious differences in cell morphology caused either by the trypsinisation or the nanopillars (Figure 5.9). In all instances, *E. coli* cells appeared healthy and had maintained their turgor pressure (Figure 5.9). However, the SEM images were not able to show changes to the surface proteins due to trypsinisation.

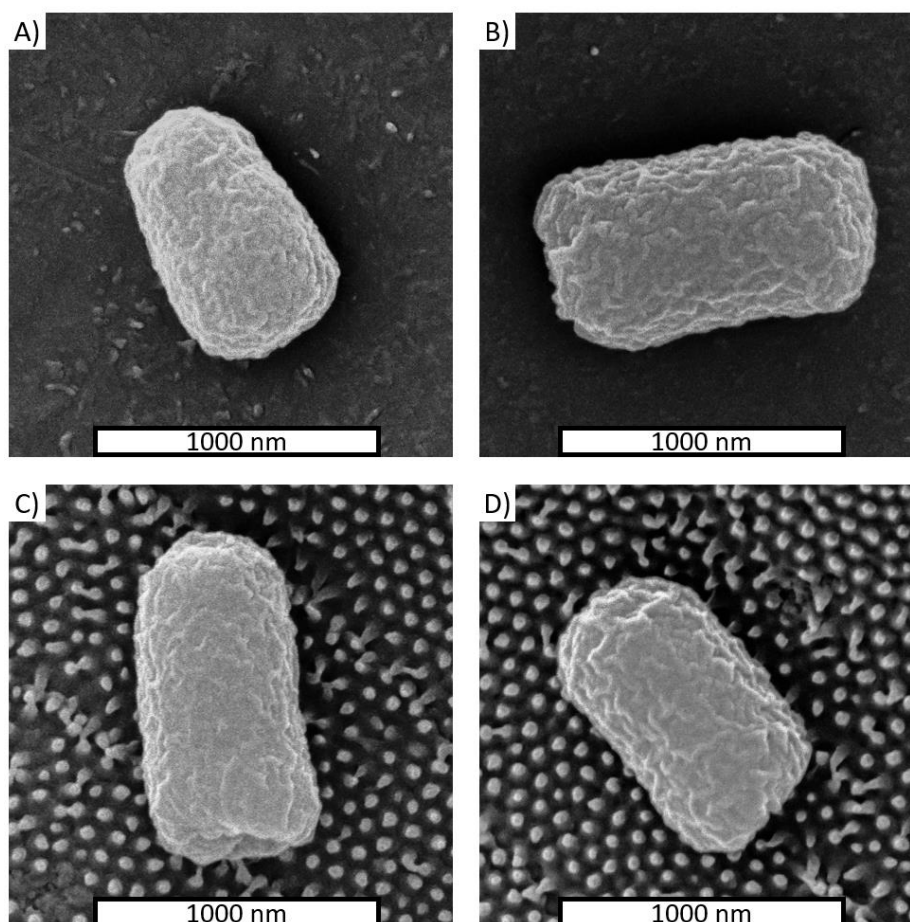


Figure 5.9 Representative SEM images of *E. coli*  $\pm$  trypsinisation on flat or SDN surfaces.

(A) and (C) are SEM images of untreated WT *E. coli* on flat and SDN surface, respectively; (B) and (D) are SEM images of TRY *E. coli* on flat surface and SDN surface, respectively.

### 5.2.5 Assessment of bacterial interactions with nanostructured surfaces using high resolution microscopy

The LIVE/DEAD and BTG assays both suggested that the adhered bacteria, particularly Gram-negative species, may experience membrane damage upon contact with nanostructured surfaces that, in turn, leads to loss of viability. To further test this hypothesis, SEM and FIB-SEM were utilised to assess bacterial interactions with the flat control, BWN, BDN and SDN surfaces.

#### 5.2.5.1 SEM analysis

SEM has been extensively used to investigate bacteria-surface interactions, as it can provide qualitative evidence of any changes in cell morphology when adhered to a surface. Visualising bacteria from the top was insufficient, as direct bacterial cell wall-nanostructure interactions occurred beneath the cell (i.e. potential penetration or membrane rupturing of cell wall). However, by tilting the SEM stage at a large angle ( $TA > 50^\circ$ ), it was possible to observe bacterial interactions with the solid surface. On the flat surface, *E. coli* could clearly be seen to anchor itself to the substratum via surface appendages, particularly when viewed using the backscattered electron (BSE) detector (Figure 5.10A, B). Similar anchoring was also seen for *E. coli* on the SDN surface, but this was less obvious (Figure 5.10C, D). SEM also confirmed that *E. coli* cells bound to the flat surface displayed the typical bacillus shape. This is in keeping with the data from LIVE/DEAD and BTG assays, which implied that the majority of bacteria on the flat control had an intact cell wall and were metabolically active. The majority of bacteria attached to the SDN surface also had the expected cell morphology. Nevertheless, a small fraction of the adherent cells showed changes in their morphology. Figure 5.11 shows that an *E. coli* cell that was fully adsorbed onto the SDN surface and had a noticeable deformation in cell structure. There was evidence of the nanopillars bending towards the cell, which indicates potential penetration of the nanopillars inside the cell. Thus, the deformation may have been due to partial loss of turgor pressure. There was also evidence that bacteria may have interacted with the surface in a manner that minimised contact with the nanopillars, either by not fully adsorbing to the surface along the plane of the cell or by targeting defective areas that lacked the nanostructures (Figure 5.12).

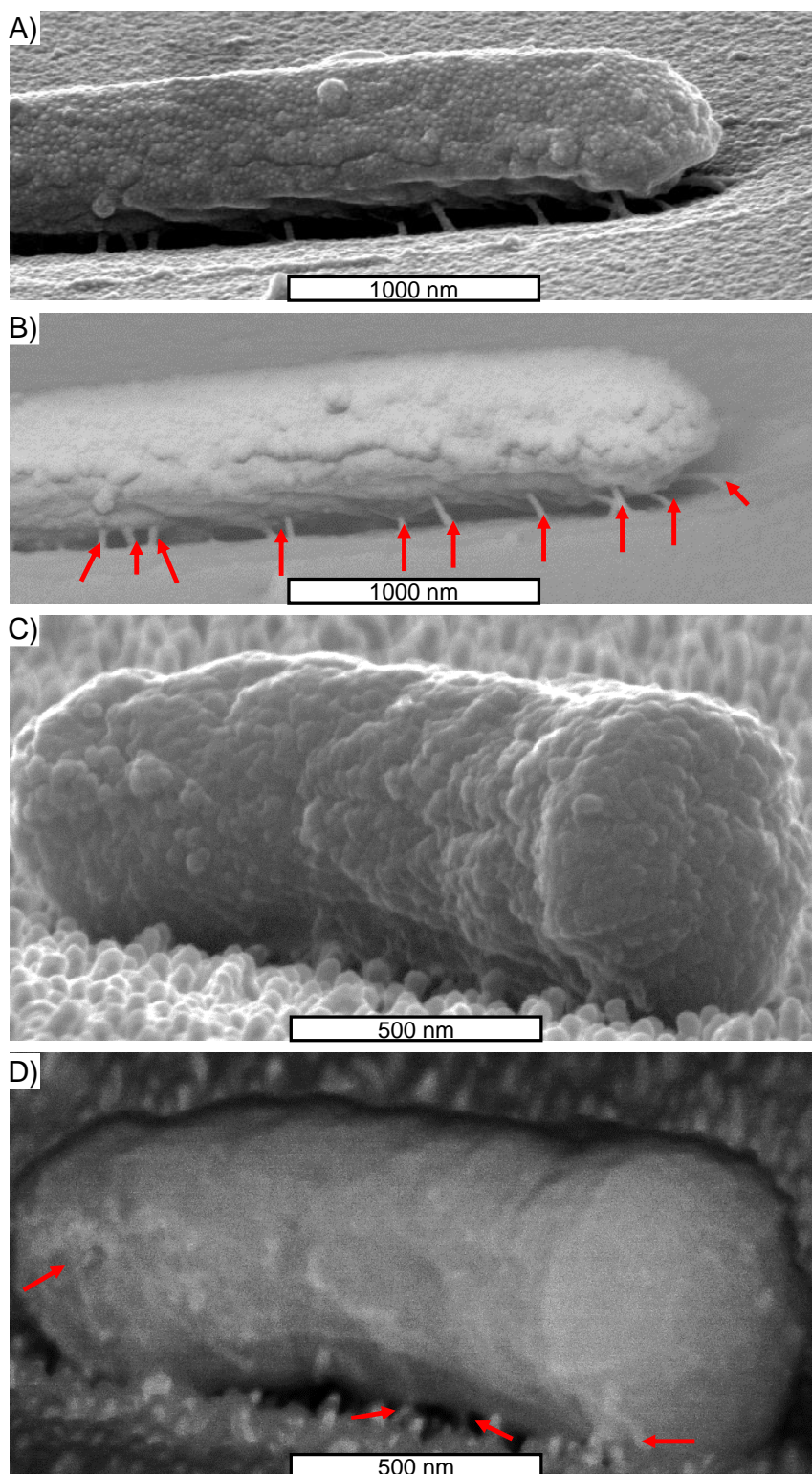


Figure 5.10 High tilted angle SEM images of *E. coli* bound to flat or SDN surfaces. (TA = 80°) of *E. coli* reveal the interaction between the bacterial surface proteins and solid surfaces. *E. coli* cells were incubated for 3 hours at 37°C in static incubator on (A,B) flat PET surface and (C,D) SDN surface. A and C were recorded using secondary electron detector (SE) while B and D were recorded using back scattered electron (BSE) detector. The red lines show the anchoring surface appendages from the cells onto the surface.



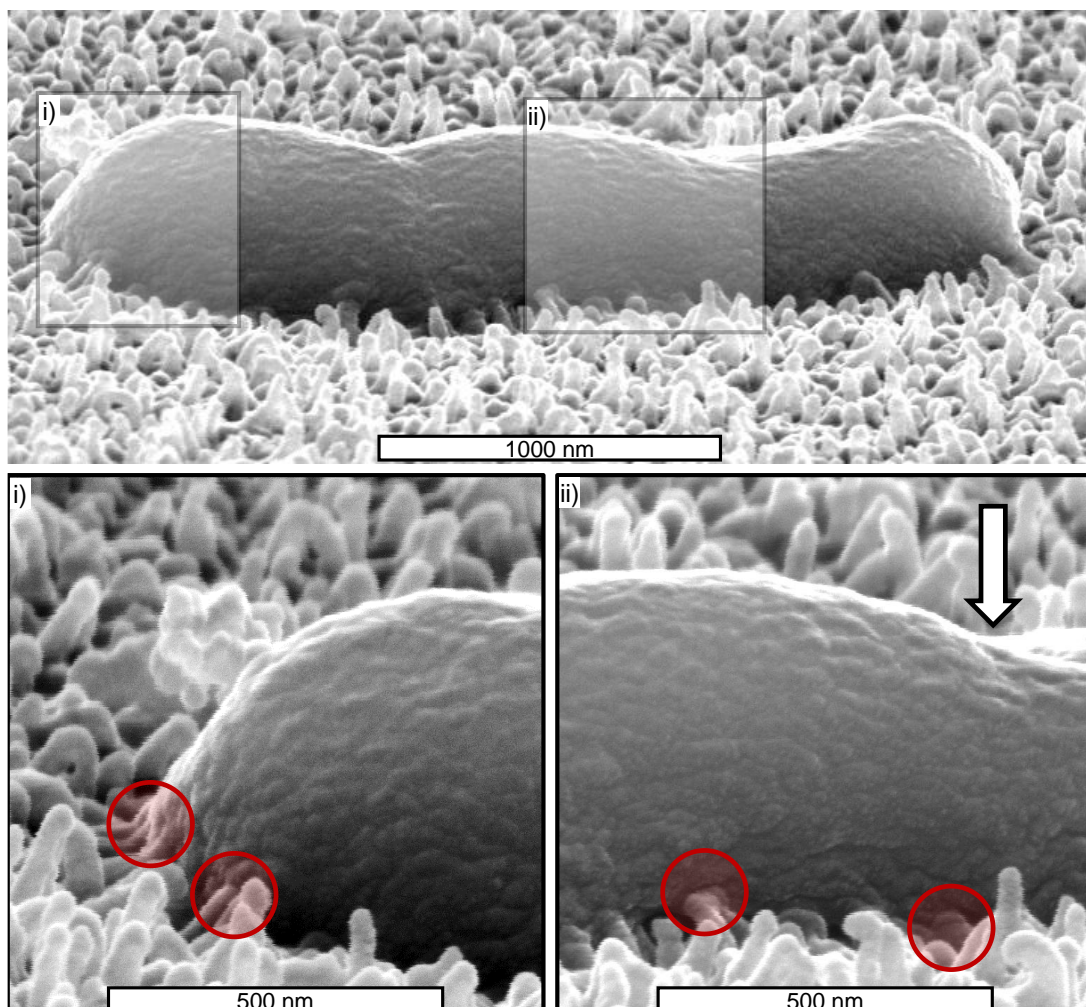


Figure 5.11 SEM image of fully adsorbed *E. coli* cell on the SDN surface. *E. coli* cells were incubated for 3 hours on the SDN surface at 37°C. The adsorbed *E. coli* appears to display a modified cell morphology due to potential cell wall damage. Two areas of interest (i and ii) have been magnified to show nanopillars that appear to have penetrated the cell (red circles). Arrow indicates deflated region of the cell, which may indicate a reduction in volume due to loss of turgor pressure.



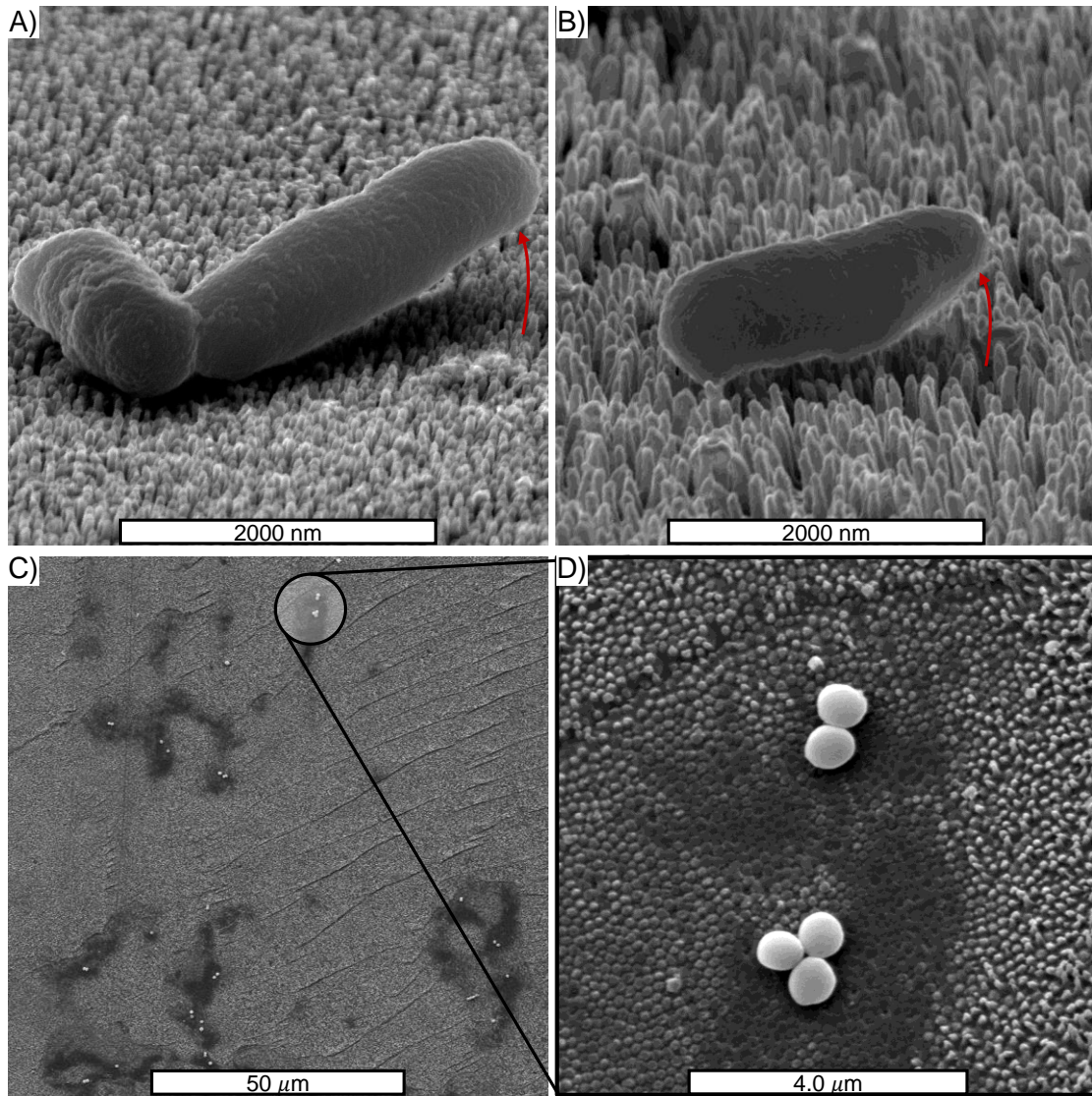


Figure 5.12 Potential bacterial evasion of nanopillar contact. Bacterial cells were incubated on the nanostructured surfaces for 3 hours at 37°C. It was noted that *E. coli* cells were not always in full contact with the (A) SDN or (B) BWN nanostructured surfaces. (C, D) *S. aureus* cells were often found bound to defective areas that lacked nanopillars. (D) Higher magnification image of the highlighted area in (C).

## 5.2.5.2 FIB-SEM analysis

SEM images provided some indication of bacterial cell-surface interactions, but observations of the direct interactions occurring at the underside of the bacterium were limited. Consequently FIB-SEM was utilised to further investigate such interactions. Two FIB-SEM techniques were employed during these experiments, which were performed in DESY Hamburg: (1) taking the cross section of the bacterial cell by cutting the sample in half, and (2) milling the bacterial cell to collect slice and view data that could then be used to generate a detailed 3D volume model of the bacterial cell using Avizo software.

FIB-SEM cross section was used to investigate the ultrastructure of bacteria following a 3-hour incubation on the SDN surface. The cross-section of an *E. coli* cell revealed that one nanopillar had potentially penetrated through the bacterial envelope by about 10 nm (Figure 5.13). These images also showed that the bacterial cells were suspended on top of the nanopillars, with the cell wall covering the entire top section of the nanopillars rather than just the very tip, as is seen when a solid particle interacts with the nanopillars.

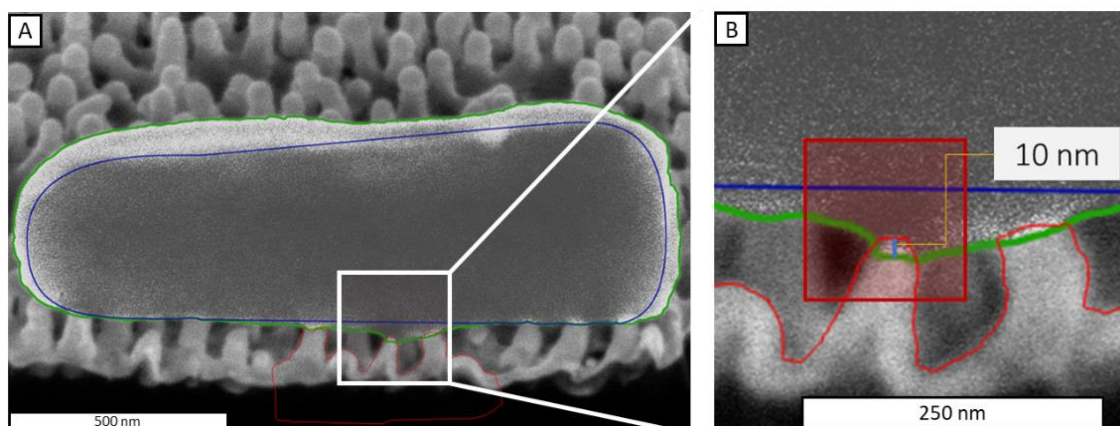


Figure 5.13 FIB-SEM cross-section of an *E. coli* cell adhered to the SDN surface after a 3 hour incubation. A) is the cross-section of the whole bacterium, while B) shows an enlarged image of the cell membrane with a 10 nm penetration from a nanopillar. Green line, trace line for the whole bacterium; blue line, outline of the inner part of the bacterium; red line, tracing the nanopillars.

The cross-sections of the bacteria also implied that strong adhesion forces from the nanopillars were pulling on the bacterial cell wall, causing its deformation (Figure 5.14). This effect was seen not only for Gram-negative bacteria but also Gram-positive bacteria. These observations were

not in agreement with prior studies that proposed that the suspended region of the bacterial cell membrane between nanostructures will move closer to the substrate rather than away from the substrate. However, there was a possibility that the inward movement of the cell wall seen here was due to shrinkage of the cells due to the sample preparation. Section 5.3.2 will discuss the possibility of the response of the cell wall to the nanostructured surfaces further.

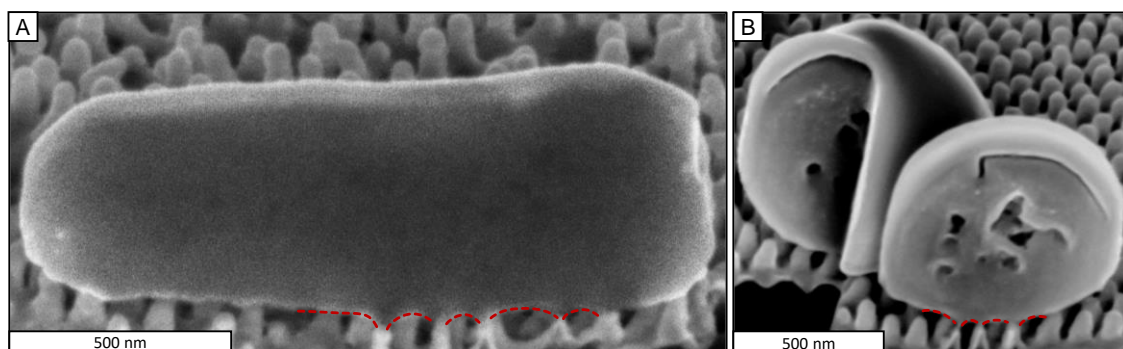


Figure 5.14 Underside cell wall deformation of adhered bacterial cells. FIB-SEM cross section of (A) *E. coli* and (B) *S. aureus* on the SDN surface. The curved lines indicate how the cell wall of the bacteria is interacting with the nanopillars.

#### 5.2.5.3 FIB-SEM 3D reconstruction

A major advantage of the FIB-SEM over the SEM technique is that the 3D volume of an entire bacterial cell can be reconstructed when using the milling method of FIB-SEM. A 500 nm protective platinum layer was deposited onto the samples to reduce the curtaining and drifting effects. The samples were then sequentially sliced with a thickness of 30 nm using the ion beam. The FIB milling data were then used to generate a 3D mesh using Avizo 9.4 software, which was exported in a .OBJ format so that the models could be coloured in Microsoft Paint 3D and used with other programmes. The 3D volume analysis allowed the visualisation of every interaction of the bacterial cell and the nanopillars. Figure 5.15A shows the tilted SEM image of two *E. coli* cells adhered to the SDN surface, while Figure 5.15B is the 3D model of the bacteria generated with Avizo and false coloured using Microsoft Paint 3D. This model allowed careful observation of individual bacterium, as the cell could be viewed in 360 degrees. Bacterium (i) showed changes in morphology when viewed using SEM, which suggested possible damage to the cell membrane and loss of turgor pressure. The orthoslice data from the FIB milling experiment revealed that there were at least two nanopillars that were interacting with this bacterium in a way that was causing significant deformation of the cell wall (Figure 5.16A-C). Bacterium (ii) did

not show any changes in morphology from the top view image. However, FIB-SEM revealed that there were significant changes to the morphology of the cell wall that was interacting with the nanopillars, but there was no clear evidence of cell penetration by the nanopillars.

FIB milling analysis also confirmed the pulling of the bacterial cell wall when in contact with nanopillars, as seen in Figure 5.14. In fact, three different outcomes were observed (Figure 5.16E-F). First, the suspended bacterial cell wall did not show any significant changes when in contact with nanopillars. Second, the cell wall of the suspended bacterial cell had an inward deformation away from the surface. Third, the cell wall of the suspended bacterial cell showed outward deformation, where it had sunk in between the nanopillars. The reason for these different states is currently unknown.



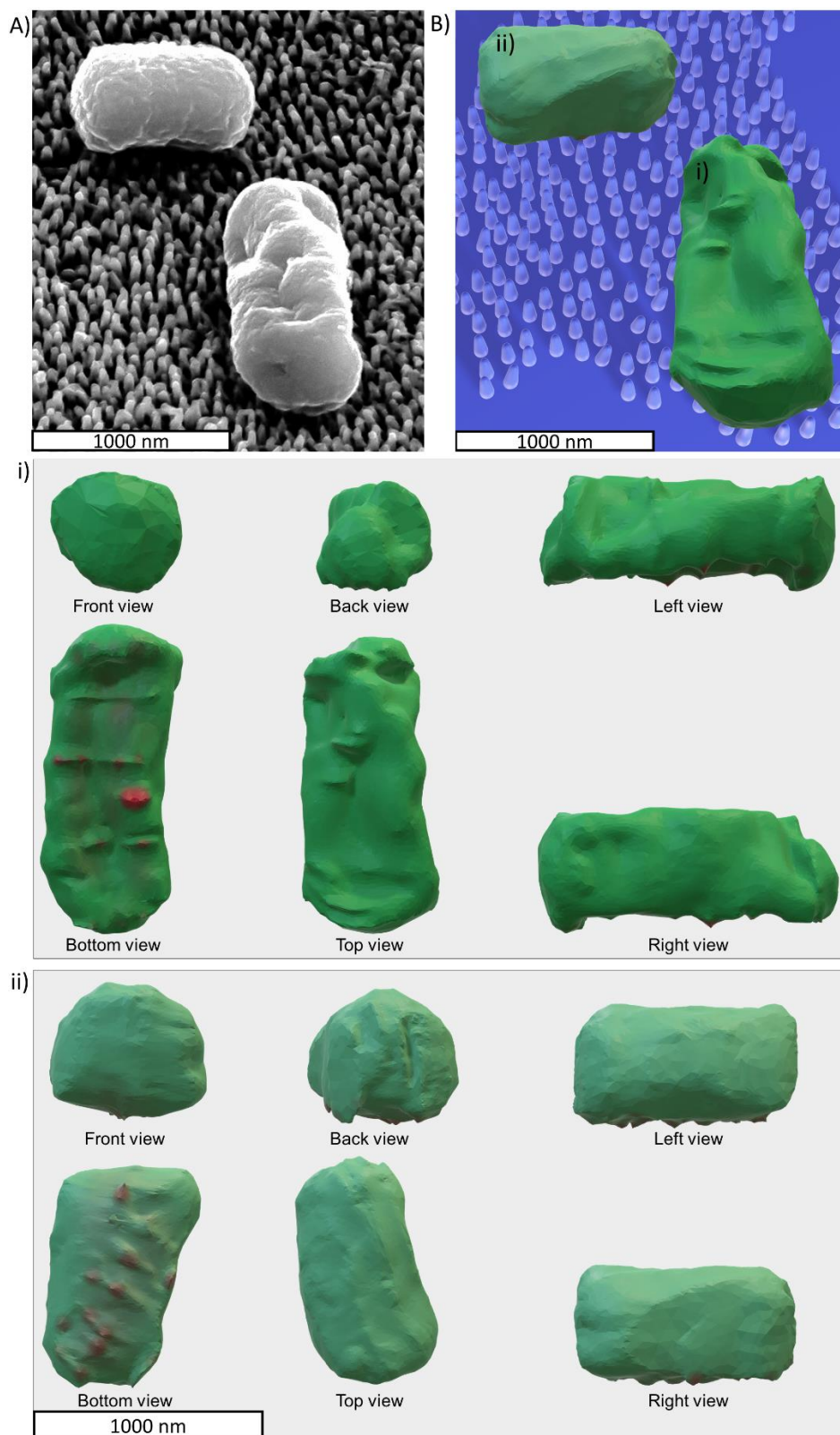


Figure 5.15 3D reconstruction of *E. coli* adhered to the SDN surface. SEM image of 2 *E. coli* cells on SDN surface. (B) 3D reconstruction of the 95 orthoslices from FIB milling data using Avizo 9.4 software. The 3D model meshes were imported into Microsoft 3D Paint software for colouring purposes. Front, back, sides, top and bottom view of bacteria (i) and bacteria (ii) are shown in detail. The red colour on the underside of the cell indicates the contact point with the nanopillars.

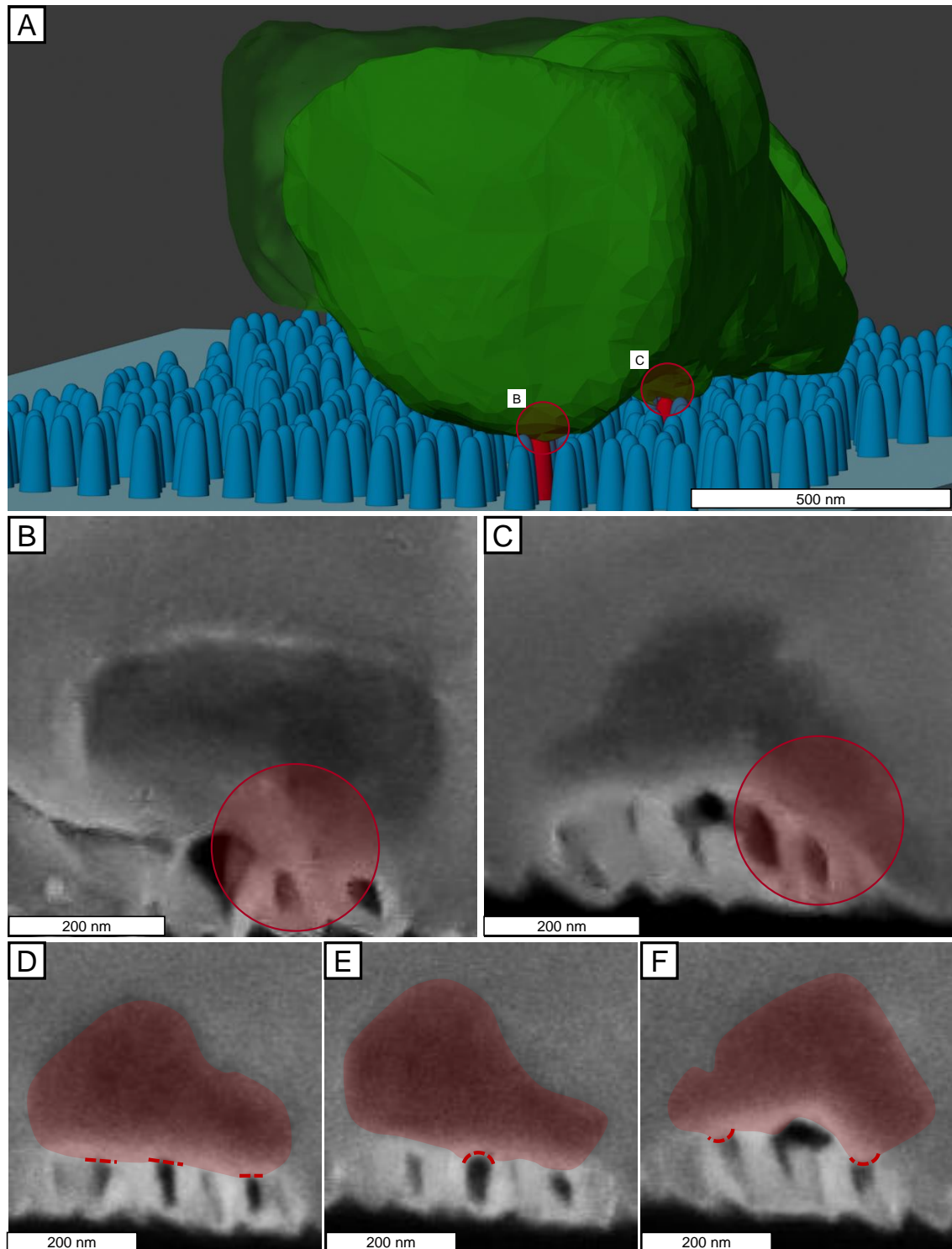


Figure 5.16 FIB-SEM analysis on an *E. coli* cell on the SDN surface. (A) 3D volume rendering in Blender 3.8 shows potential regions of the cell wall that were affected by the nanopillars (red circle). Red nanopillars indicate those that seemed to penetrate the cell wall. (B) and (C) are the orthoslices FIB milling data of the affected cell wall. (D-F) shows three possible ways in which the bacterial cell wall may deform in response to the nanopillars: flat, inward, outward.

The occurrence of deformed *S. aureus* cells on a nanopillared surface was rare and, in most cases, the cells appeared to be suspended on top of the nanopillars, with no changes in morphology. However, as evidenced from LIVE/DEAD and BTG results, the SDN surface could induce *S. aureus* cell damage. Figure 5.17 shows two cells that had a deformed morphology on the SDN surface in amongst other cells with no apparent deformation. FIB-SEM sections revealed that the deformed cells were in direct contact with the nanopillars and that the nanopillars were fully adsorbed by the cells, seemingly causing the partial loss of turgor pressure (Figure 5.17D). Of the 9 cells that were sectioned, 4 were deformed and showed signs of losing some turgor pressure due to potential rupturing of the cell membrane by the nanopillars. Interestingly, there were four *S. aureus* cells that were not in direct contact with the nanopillars but rather were using other bacterial cells as the substratum or represented daughter cells in a growing chain. SA4 was adhering to the dead cell SA3, while SA7 was replicated from SA6. Similarly, SA8 and SA9 were replicated from SA7 (Figure 5.18). The cell designated SA6 appeared to be interacting directly with the nanopillars but showed no significant changes in morphology.

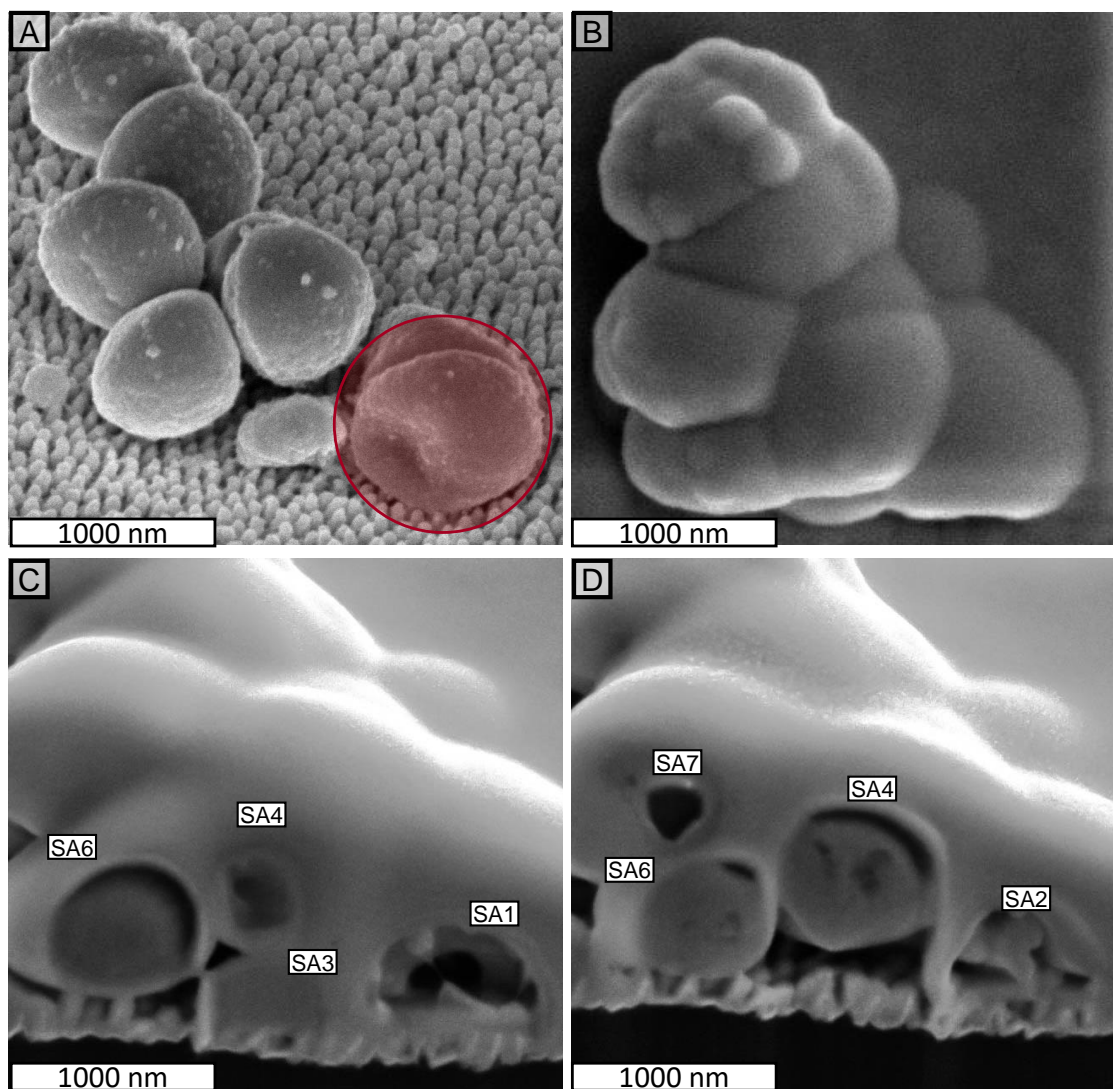


Figure 5.17 FIB-SEM analysis on *S. aureus* cells bound to the SDN surface. (A) SEM image of *S. aureus* cells adhered on the SDN surface after a 3 h incubation. Two cells show significant deformation (highlighted in red), while the other cells appear intact. (B) The cells were coated with 500 nm thickness of platinum prior to ion beam milling. (C) and (D) show different sections of the milling interface. The visible bacteria at each section are marked as SA1 to SA7.



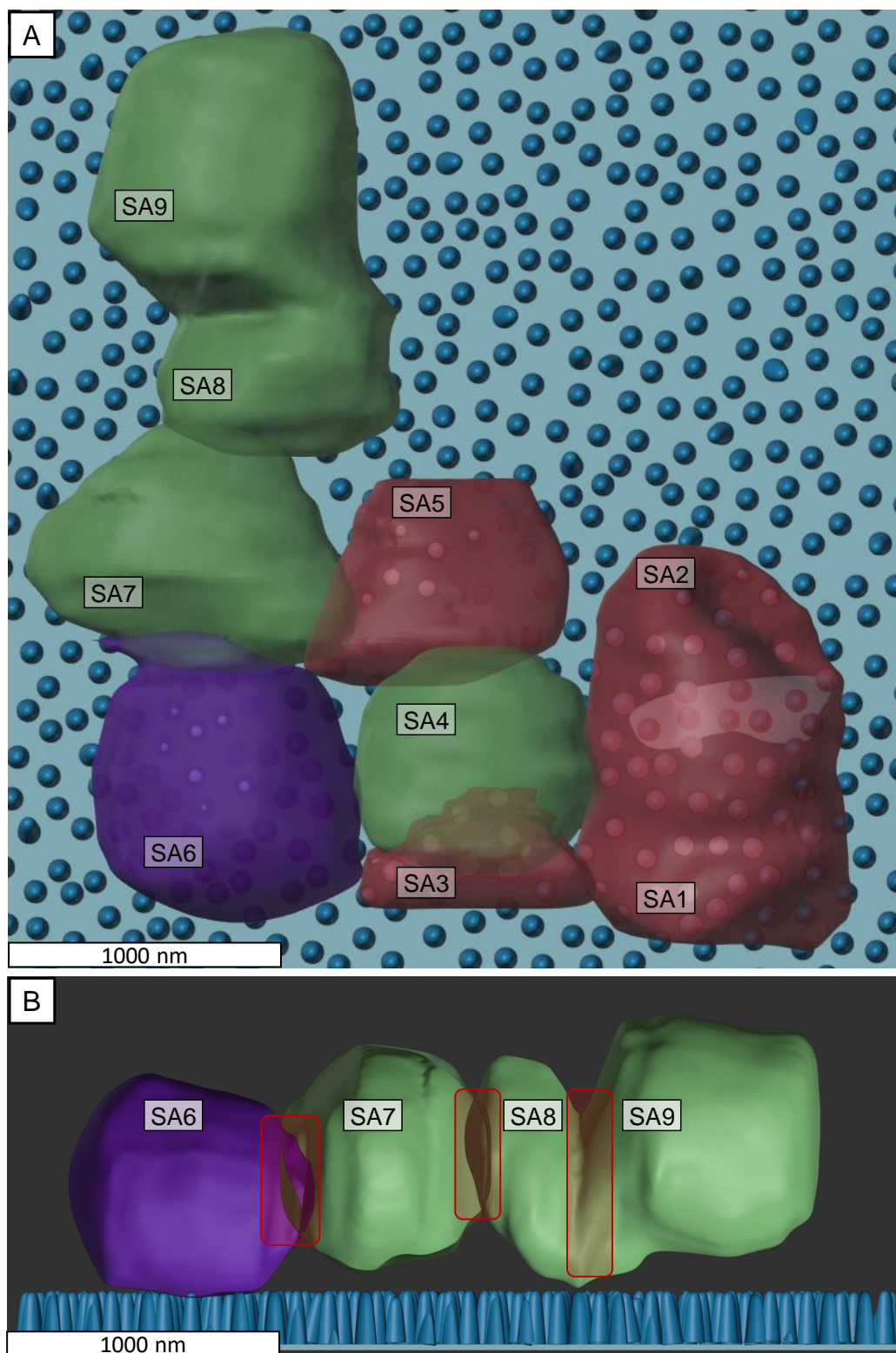


Figure 5.18 3D volume rendering of *S. aureus* cells bound to the SDN surface using Blender 2.8. (A) Top view of all nine *S. aureus* cells adhered to the SDN surface. Careful analysis showed that at least 4 cells were fully adsorbed onto the nanopillars: SA1, SA2, SA3, and SA5 (marked in red). (B) Clipping mask on 3D rendering of the samples revealed that SA6 was suspended (purple) on the top of nanopillars while SA7, SA8 and SA9 cells were the sister cells from SA6 and not in direct contact with the nanopillars. Septa are marked in the red box.

## 5.3 Discussion

### 5.3.1 Bacterial response to the polymeric nanopillared surfaces

Bacterial attachment to a substratum is a sophisticated multistep process that includes positioning, approaching, and sensing the surface. At each step, bacterial cells continuously scan for physicochemical and biological signals from their surroundings and react accordingly. In this project, the topological information, surface chemistry, nanotribology, bacterial viability, bacterial mechanical and surface chemistry, and changes to bacterial morphology were quantified and assessed using multiple techniques in order to comprehensively determine the bacterial interactions with the nanostructured surfaces. Such an understanding is important to provide potential solutions to biomaterial associated infections and bacterial attachment to abiotic surfaces in general.

#### 5.3.1.1 Effects of surface topography

During bacterial interactions with nanopillared surfaces, membrane rigidity is a key factor that influences the biological response and viability of the bacteria. It is generally accepted that Gram-negative bacteria like *E. coli* are more susceptible to cell wall rupturing when adsorbing to nanostructured surfaces like nanopillars, nanospikes or nanowires than Gram-positive bacteria. This is due to the generally thicker peptidoglycan layer of the Gram-positive cell wall compared to Gram-negative bacteria. Theoretical modelling from Pogodin *et al.*, Xue *et al.*, and Li *et al.*, reinforce the importance of cell rigidity in determining the bactericidal properties of nanostructured surfaces [32,52,54].

In this study, the BWN surface, which is the one that most closely resembles the cicada wing surface, showed a similar bactericidal performance against Gram-negative bacteria to the surfaces reported by Dickson *et al.* and Hazell *et al.* Dickson *et al.* studied the bactericidal performance of cicada wing replicas on PMMA substrate and reported that nanotopography with a diameter = 70 nm, spacing = 170 nm and height = 210 nm killed 22% of the adhered *E. coli* cells. They also reported that other nanopillared surfaces with greater spacing and a wider diameter had a lower bactericidal performance. Hazell *et al.* reported a similar bactericidal performance using *E. coli* and *K. pneumoniae* on PET nanocones fabricated using colloidal mask lithography. They found that dense nanocones with 200 nm spacing and 22 nm tip width had a greater bactericidal performance than nanocones spaced at 500 nm. Around 30% of the adhered *E. coli* and *K. pneumoniae* cells were dead after 1 hour of incubation on the dense nanocone surface. By contrast, the BWN surface was found to be unable to cause any significant damage

to the cell wall or impair the viability of *S. aureus*. This result is in line with the study by Pogodin *et al.*, which reported that *S. aureus* was resistant to the actions of the nanopillars on cicada wings, but became susceptible after the rigidity of the cell wall was tempered using microwave radiation. [52]. Together, these data support the hypothesis that the thicker peptidoglycan layer and stiffer cell wall affords greater protection to Gram-positive bacteria than Gram-negative bacteria against damage from nanostructures.

The nanopillars on the BDN surface had the same diameter as those on the BWN surface, but were more densely compacted, with an interpillar distance of 100 nm. The increase in nanopillar density,  $N$ , meant that the bacteria interacted with more nanopillars compared to the BWN surface. It was therefore anticipated that the BDN surface would show a greater decrease in bacterial viability and an increase in cell wall susceptibility compared to the BWN surface. Indeed, this was the case, and the number of *E. coli* cells that were negatively affected (in terms of the cell wall susceptibility and cell viability) by the BDN surface were significantly higher when compared to the BWN surface. However, the increase in  $N$  did not improve the antibacterial performance against Gram-positive bacteria, for which the average number of cells with a compromised cell wall on the BDN surface was slightly lower than on the BWN surface. Nevertheless, the average number of metabolically active *S. aureus* cells on the BDN surface was lower than on the BWN surface. This suggested that while the increase in  $N$  was not effective at causing damage to the cell wall of Gram-positive cells, the increased number of bacterial interactions with the nanopillars did impair the metabolic activity of bacteria. To the best of the author's knowledge, for a periodic nanostructured surface, the nanopillar density of BDN and SDN is by far the highest, as opposed to the cicada wing that has a density of 35 nanopillars/ $\mu\text{m}^2$ , or other biomimetic surfaces that have been reported on PMMA or PET [53,77].

Previous studies that tested the antibacterial performance of different nanostructured surfaces reported a correlation between increased number of susceptible cells with increased number of nanopillars density ( $N$  of up to 60 nanopillars/ $\mu\text{m}^2$ ). However, it is important to note that most studies used nanostructured surfaces that had different  $N$  and different  $D_T$ . This makes it difficult to distinguish whether the improvement in antibacterial performance was due to the increase in  $N$  or the reduction/increment of  $D_T$ . To distinguish this effect in this project, a surface with a similar density to the BDN surface but with a much smaller  $D_T$  was designed and tested. This SDN surface had a  $D_T$  of 40 nm, which is about 2 times smaller than the one on cicada wings, and an  $N$  of 100 nanopillars/ $\mu\text{m}^2$ , which is about 2 times more than the  $N$  on cicada wings. The SDN surface showed the best antibacterial performance against Gram-negative bacteria and also

promising results against Gram-positive cells. Again, the reduced efficiency against Gram-positive bacteria was expected due to the much thicker peptidoglycan layer making the cells more rigid compared to Gram-negative bacteria, thereby minimising potential cell wall deformation that could lead to nanopillar penetration or cell wall rupturing. The SDN surface was comparable to the nanostructures found on dragonfly wings, which have a  $D_T$  of 48 nm and  $N$  of 74 nanopillars/ $\mu\text{m}^2$  [175]. Furthermore, the reported antibacterial performance of the dragonfly wing against Gram-negative bacteria (*P. aeruginosa*) was comparable to that seen here for the SDN surface, where up to 87% of the adhered cells were compromised by the nanopikes after 3 hours incubation. However, the dragonfly wing has also been reported to kill up to 97% of adhered *S. aureus* cells [175], which is significantly higher than the effects seen with the SDN surface, for which only 23% of *S. aureus* cells were compromised. This discrepancy could be due to the higher aspect ratio of the nanopike and also the experimental variance. Of note, the negative effects of the SDN surface on metabolic activity of *S. aureus* cells were more prevalent than the damage to the cell wall, and comparable to the reduction in metabolic activity of Gram-negative cells.

#### 5.3.1.2 The stretching of the cell wall

Bacteria adhered on nanostructured surfaces are predicted to have a stretched cell wall as they attempt to enhance adhesion in response to the reduced contact area relative to a flat surface. This bacteria-nanopillars interaction will cause stretching and deformation, which in turn will change the nanomechanical properties of the cell wall. Two regions of the cell wall are expected to experience stretching: the unbound cell wall and bound cell wall regions, with the latter experiencing greater stretching [32,52,54]. In this study, the measured  $E_B$  was representative of the mechanical properties of the unbound cell wall (Figure 5.19). It was found that the average value of  $E_B$  for *E. coli* cells that adhered on BWN and BDN was higher than the cells adhered on the flat surface, which supports the hypothesis that the cell wall is stretched by the nanopillars. There was no difference in the  $E_B$  of cells adhered on the BWN and BDN surfaces, potentially because the nanopillar diameter was the same, and suggests that the stretching mechanism of the unbound cell wall regions was identical on both nanostructured surfaces. Since the  $D_T$  of both surfaces was almost identical, the contact area will have been the same, making the pressure from the nanopillars identical, and hence the stretching and deformation of the cell wall around the nanopillars similar (N.B. this is only true for the nanopillars that were close to the unbound cell wall region). This is interesting because, from the LIVE/DEAD assay, the BDN surface showed a significantly greater number of *E. coli* cells with a susceptible cell wall than the

BWN surface, which in theory should mean that the BDN surface had a higher  $E_B$  than the BWN surface, but this was not the case. It is possible, therefore, that the cell wall of bacteria in the bound region on the BDN surface experienced significantly greater stretching and deformation than on the BWN surface, thereby allowing PI to permeate the cells to a greater level and displace SYTO9. Bacteria adhered on the SDN surface showed the highest  $E_B$  of the nanostructured surfaces, potentially due to the much lower total contact area when compared to the BDN surface, resulting in higher pressure and higher stretching and deformation of the unbound and bound cell wall regions.

It is important to understand that the differences in  $E_B$  reported here cannot give any indication of the viability of the cell, mainly because the measurements were performed in the dry state, meaning that the bacteria were already dead. Thus, this measurement is purely looking at the potential changes in the stiffness of the cell wall when interacting with the nanopillared surfaces. Bacterial morphology was assessed by scanning the cell with imaging mode and no significant changes to the top side of the cell were measured across the different surfaces. It can therefore be assumed that the changes in cell wall stiffness were not affected by a change in turgor pressure of the cell but rather physical perturbation of the materials. Results from cross-sectioning FIB-SEM confirmed that while the unbound regions of the bacterial cell wall showed minimal perturbation, the bound regions often showed significant changes. This was especially true for the SDN surface compared to the BWN surface (Figure 5.20).

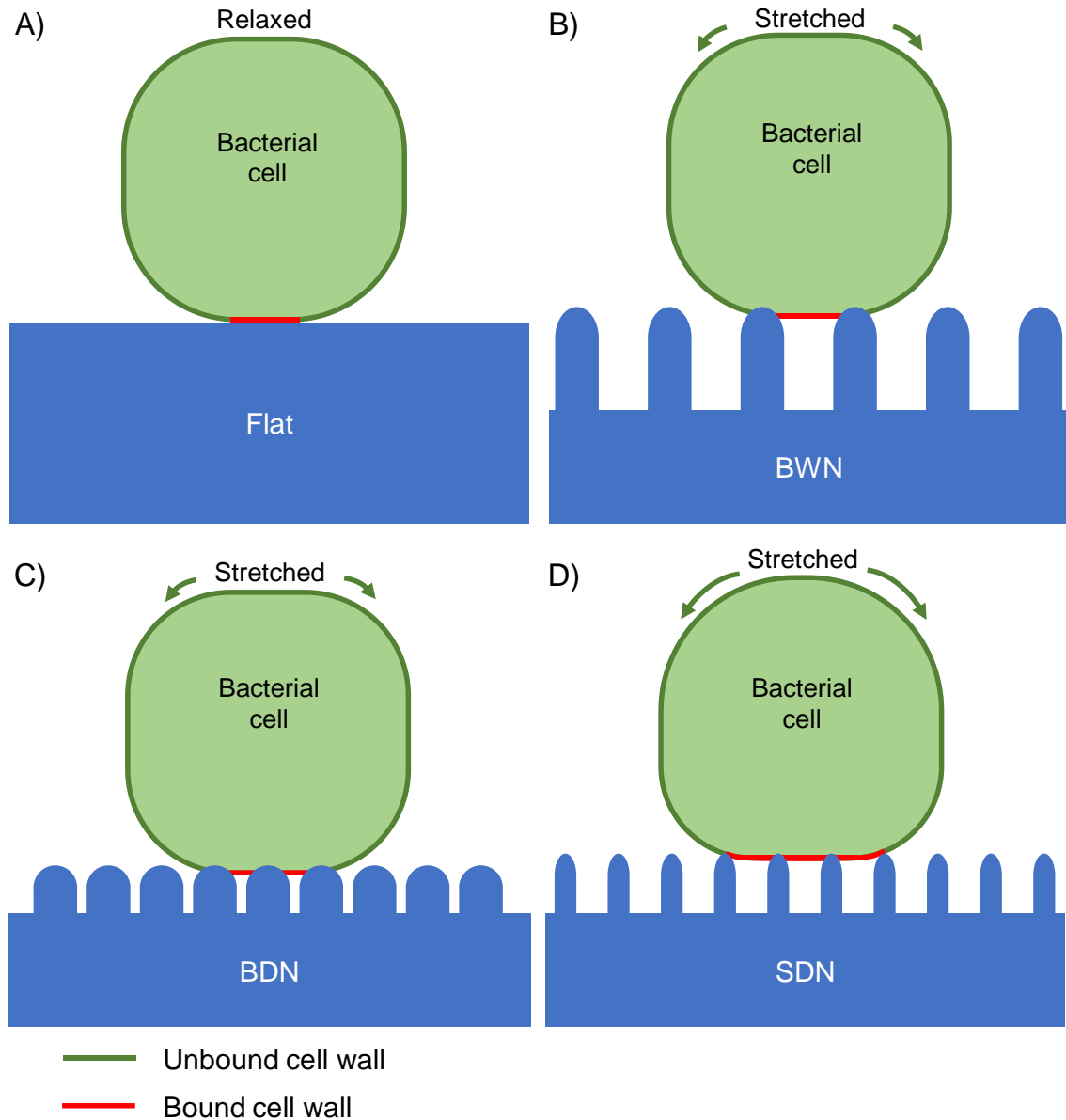


Figure 5.19 Comparison of bacterial attachment to a flat or nanostructured surface and its effects on the cell wall. (A) A bacterial cell that is bound to a flat surface will have a relaxed cell wall, resulting in a low  $E_B$  value. A bacterial cell that is bound to (B) BWN or (C) BDN surfaces will have a stretched cell wall in the unbound region (green line) due to lower intrinsic contact area compared to the flat control. A stretched cell wall will have a higher stiffness, resulting in a high  $E_B$  value. (D) The unbound region of the cell wall will be more stretched on the SDN surface due to the smaller intrinsic contact area compared to BWN and BDN surfaces.

The interaction between the bacterial cell wall and the nanopillar is one of the most important parameters when modelling bacterial attachment to nanostructured surfaces. Pogodin *et al.* and Xue *et al.* included a specific equation to calculate the suspended region  $\alpha_B$ . Li *et al.* also

included an identical equation in their model, despite using a thermodynamic approach rather than the geometric approach used by Pogodin *et al.* and Xue *et al.*

Equation 5.3: Pogodin's  $\alpha_B$  equation

$$S_B = D_p^2 - \pi R_t^2 \sin^2 \theta$$

Equation 5.4: Xue's  $\alpha_B$  equation

$$S_B = 2(1 - \cos \theta) \left( \frac{D_p - \pi R_t^2}{\sin^2 \theta} \right)$$

Equation 5.5: Li's  $S_{ad}$  equation

$$S_{ad} = \frac{\pi L^2}{2} + N[\pi R_t^2 + 2\pi R_t(h - R_t)]$$

All three equations contain the topological information of the nanostructures, which are the radius of the tip ( $R_t$ ) and the interpillar spacing ( $D_p$ ). Li's equation includes other parameters like the height of the nanopillar ( $h$ ), the length of the bacterium ( $L$ ), and the total number of interacting nanopillars ( $N$ ). Thus, it is crucial to properly understand the behaviour of the suspended cell wall to explain the bactericidal mechanism of nanostructured surfaces. Figure 5.20 shows the predicted deformation of  $\alpha_B$  by Pogodin *et al.* and Xue *et al.*, as well as the actual deformation observed from FIB-SEM cross section of an *E. coli* cell adhered on SDN or BWN surfaces. Results from FIB-SEM suggested that *E. coli* adhered on the SDN surface would have significant changes to the  $\alpha_B$  compared to when adhered on the BWN surface. This finding was supported with the LIVE/DEAD and BacTiter-Glo studies, which showed that the SDN surface caused greater membrane damage and lower metabolic activity of the adhered cells compared to the BWN surface. This study also confirmed that the cell wall of the unbound region behaved differently to the bound region. It is well known that bacterial cells show a specific response upon contact with a solid object e.g. surfaces, nanoparticles, AFM tip, and it has been proposed that bacteria can localise adhesins to the area of contact to increase adhesion [176,177]. As evidenced from the change in  $E_b$  and viability results, increased adhesive forces on the bound region of the cell wall may have caused the significant stretching and deformation of the cell wall, which renders adherent bacteria non-viable. This increase in adhesive force could be due to the bacteria expressing surface appendages that anchor the cell wall more strongly to the surface, as evident from Figure 5.10.



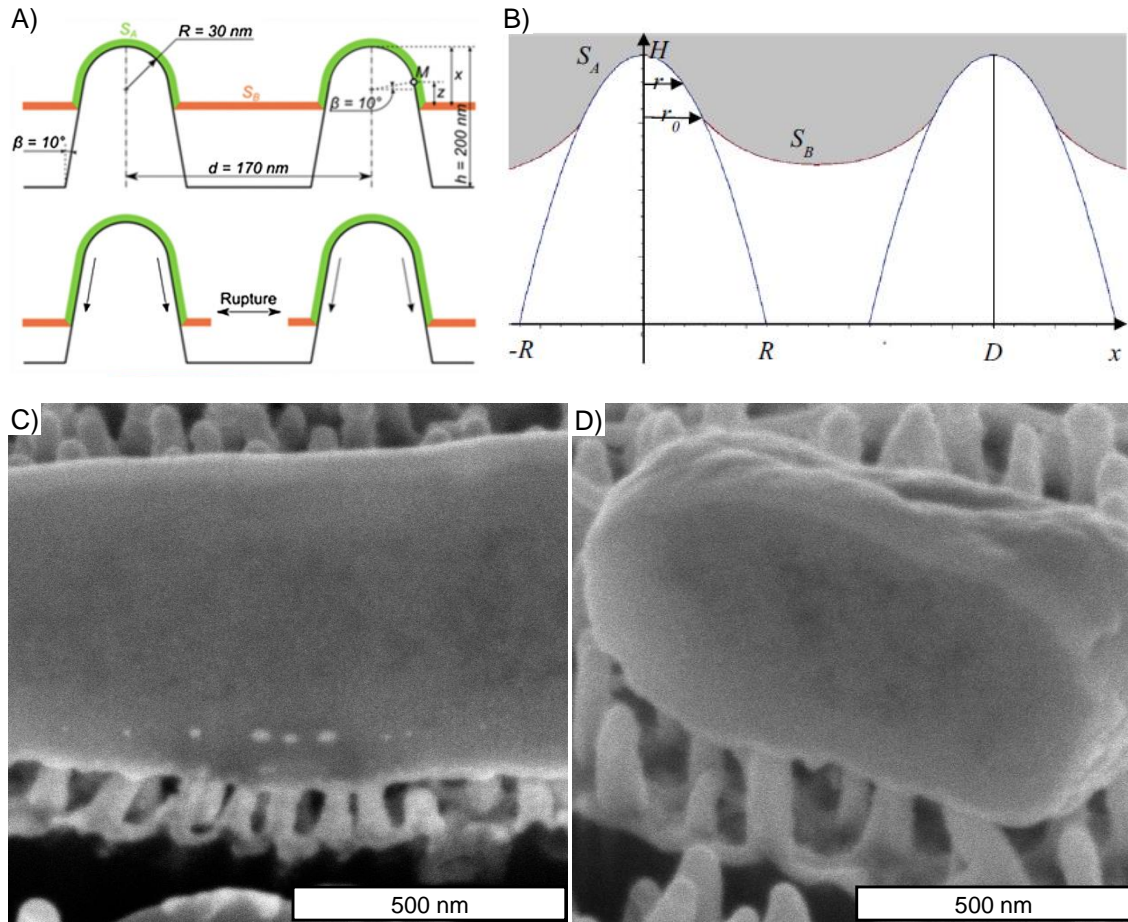


Figure 5.20 Deformation of the suspended cell wall of an adhered bacterium. (A) and (B) are the predicted deformation of the suspended cell wall by Pogodin *et al.* and Xue *et al.*, respectively. The list of parameters used by both models are the following; where  $\beta$  is the pillar angle,  $d$  is the distance between pillars,  $h$  and  $H$  are the height of the pillar for panel (A) and (B), respectively,  $r$  and  $R$  are the radius of the nanopillar for panel (A) and (B), respectively,  $r_0$  is the distance from centre of the pillar to the edge of the suspended membrane,  $S_A$  is the surface of the absorbed membrane,  $S_B$  is the suspended membrane,  $x$  is the vertical distance from  $S_B$  to the tip of the nanopillar and  $z$  is the vertical distance between  $S_B$  and junction point  $M$ . (C) shows the deformation of the suspended cell wall of an adhered *E. coli* cell on SDN surface while (D) is on the BWN surface. *E. coli* was incubated statically on both surfaces for 3 hours at  $37^\circ\text{C}$ , followed by processing as outlined in Chapter 2.

### 5.3.1.3 Importance of surface proteins in *E. coli* interactions with nanopillared surfaces

To study the importance of surface proteins in mediating bacterial attachment to nanopillared surfaces, trypsinisation of *E. coli* was used. Trypsinisation was used instead of using a specific adhesin knockout mutant strain(s), because the aim was to investigate the global effects of disrupting surface proteins rather than focus on an individual target. Trypsin has been shown to digest around 40% of the total surface proteins of *E. coli* without affecting its phospholipid



content or causing cell lysis [178]. Here, trypsinisation was found to change the surface charge and hydrophobicity of *E. coli*, indicative of the anticipated physical “trimming” of the outer surface proteins (Figure 5.21). Moreover, trypsinisation changed the physicochemical properties of the bacterial cells, making them less negatively charged and less hydrophobic. However, the physicochemical changes caused by trypsinisation is minimal and it has been shown that wettability and surface charge alone were insufficient as predictive parameters for bacterial adhesion [179].

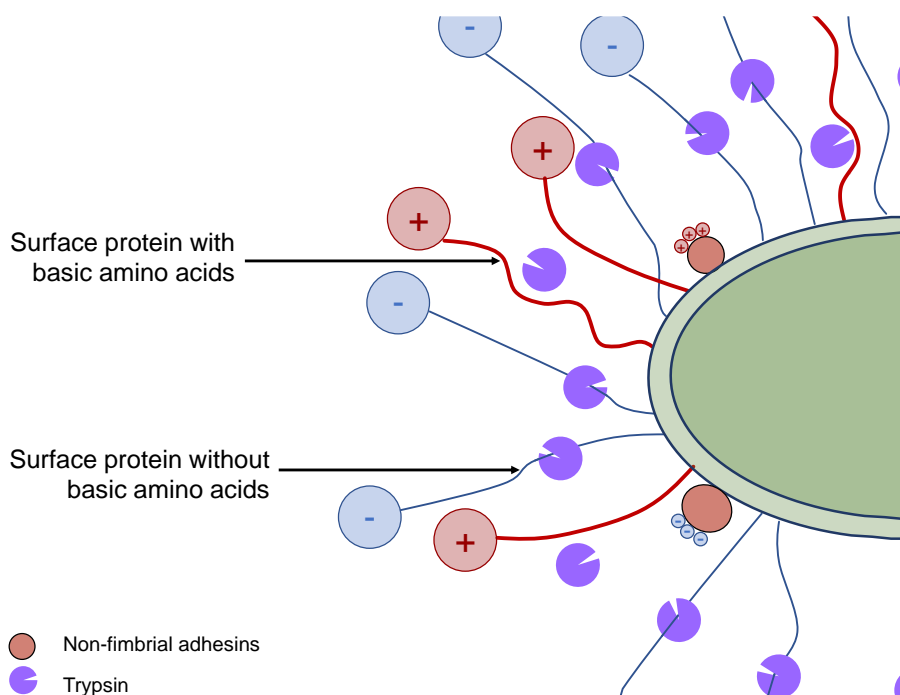


Figure 5.21 Predicted effects of trypsinisation on *E. coli* surface proteins. Surface proteins without any basic amino acid like arginine or lysine will not be susceptible to enzymatic cleavage by trypsin, while surface proteins that have arginine or lysine will be cleaved at the C-terminus of the basic residues.

It is well established that *E. coli* uses surface proteins to mediate attachment to a variety of substrata. These include flagella, which are used to breach the repulsive force on solid surfaces [170], and two fimbrial types, type I fimbriae and curli, which have been shown to promote adhesion to abiotic surfaces [180–182]. It was therefore anticipated that trypsinisation may impair the ability of *E. coli* to adhere to the surfaces, particularly since type I fimbriae have been shown to be susceptible to trypsin [183]. However, this was not the case. Nonetheless, while untreated *E. coli* cells exhibited reduced viability on the SDN surface relative to the flat surface, trypsinised *E. coli* was not affected by the nanopillars, with comparable numbers of metabolically active cells on the flat and SDN surface. As discussed earlier, due to the importance

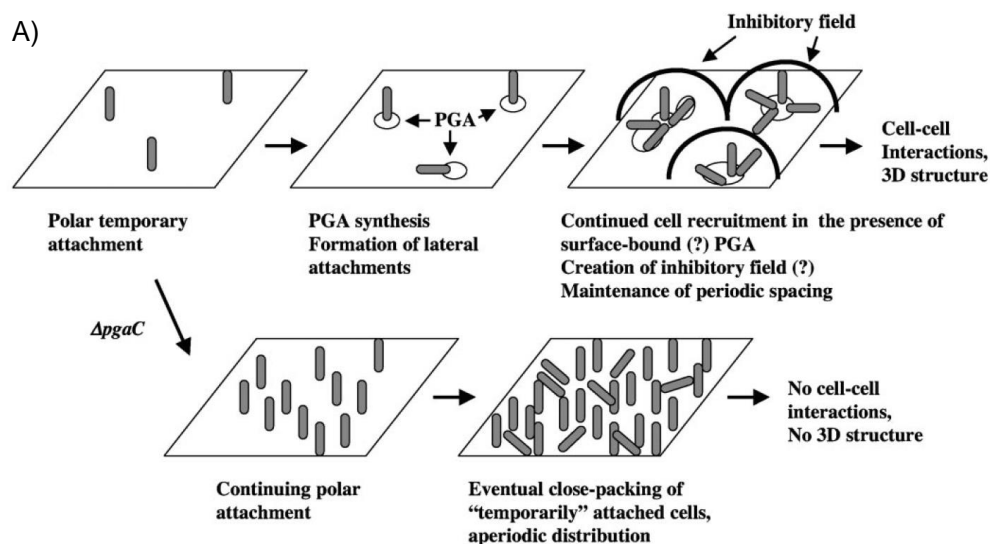
of surface proteins in mediating bacterial attachment to solid surfaces, the disruption of surface proteins due to trypsinisation may have reduced the ability of *E. coli* cells to anchor themselves to the surface. As the consequence, the total attractive force towards the surface will have been reduced, meaning that the negative effects (i.e. cell wall deformation, stretching, and rupturing) of the nanopillars could have also been reduced.

### 5.3.2 Potential bacterial evasion of nanopillars

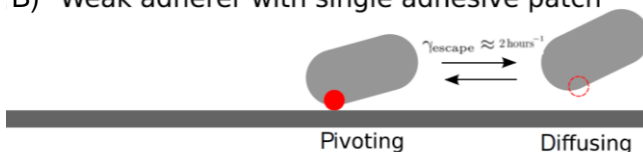
For bacteria incubated with the nanopillared surfaces, there were indications that the cells may have tried to minimise contact with the nanopillars. These observations were most obvious with *E. coli* and *K. pneumoniae* on BWN and SDN nanopillars (Figure 5.12 & Figure 5.22D,E), with cells exhibiting a polar orientation of attachment. This type of bacterial attachment is proposed to be a reversible attachment, whereby the cells are loosely attached at a single pole and can easily detach to return to the planktonic phase. During this phase, bacteria can be spinning, vibrating or exploring the nearby surface [184]. Localisation of adhesins has been previously observed in studies involving different strains of bacillus-shaped bacteria attached to abiotic surfaces [176]. For instance, Agladze *et al.* reported the importance of poly- $\beta$ -1,6-N-acetyl-D-glucosamine (PGA) binding protein for *E. coli* K12 in mediating temporary attachment to an abiotic surface, and proposed that the attachment was mediated by the preferential localisation of adhesins at the bacterial cell poles. They also found that the adhesive strength of polar/vertical attachment was weaker compared to lateral attachment, which could be due to the smaller contact area in polar attachment (Figure 5.22A). More recently, Vissers *et al.* reported polydispersity of individual adhesion behaviour within a clonal population of *E. coli* on a glass surface [177]. Vissers *et al.* determined the positions, orientations, and projected lengths of a tracked bacterium by using an algorithm that had been specifically developed for rod-shaped colloids and proposed a model to explain the adhesion dynamics of their data. They reported two types of bacterial adherers: (a) freely pivoted temporary adherers and (b) strong adherers that can switch between pivoting state and rotationally wobbling motion and are firmly bound to the surface (Figure 5.22B,C).

There were also similar observations for *S. aureus*, for which cells were found attached to defective areas of the surfaces with no or damaged nanopillars. For these samples, the cells had been incubated with the SDN surfaces for 3 h prior to fixation with glutaraldehyde, allowing sufficient time for cells to strongly adhere across the surface, as observed on the flat surface. Results from FIB milling also showed that *S. aureus* could avoid contact with the nanopillars by adhering to already bound cells, and evidence of replication did show the chain of cells extending

away from the surface. While further investigation is undoubtedly required, these observations may indicate potential strategies by bacteria to avoid contact with damaging nanostructured surfaces.



B) Weak adherer with single adhesive patch



Strong adherer with multiple adhesive patches

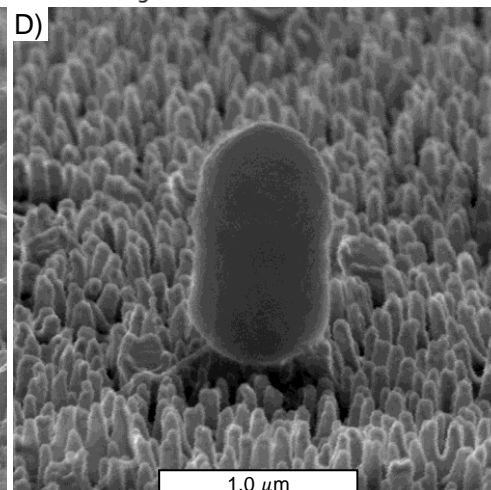
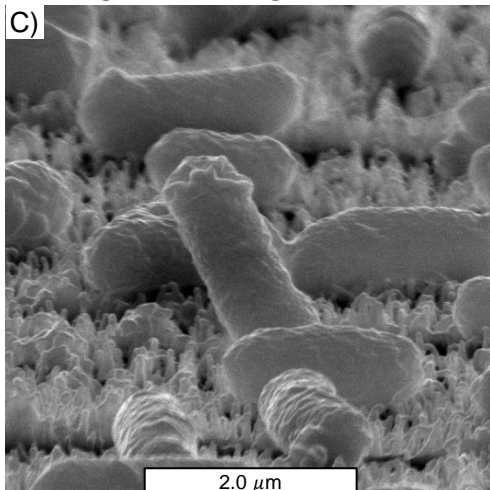
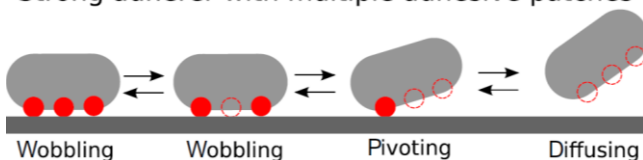


Figure 5.22 Vertical or polar attachment of bacterial cells to a surface. (A) Proposed model for the initial polar temporary attachment of *E. coli* to an abiotic surface from [176]. (B) Proposed patchy colloid model for *E. coli* adhesion to an abiotic surface from [177]. (C) Tilted ( $\text{TA}=80^\circ$ ) SEM image of vertically oriented *K. pneumoniae* on BWN surface. (D) Tilted ( $\text{TA}=70^\circ$ ) SEM image of vertically oriented *E. coli* on BWN surface.

### 5.3.3 Modulation of the bacterial cell wall

The cell wall of adherent bacterial cells was seen to adopt one of three different states when in contact with the nanopillars. In some instances, the cell wall was suspended flat between the nanopillars, or was deformed outward to increase adhesion to the surface. These states have been observed in other studies that have utilised FIB-SEM [24,185], and have been used in different models to explain the bactericidal mechanism of action of nanostructures [32,52,54]. In the third state, the bacterial cell wall was deformed inward, away from the surface. This deformation have been observed previously with *E. coli* adhered on gold nanoparticle but was not discussed in detail [186]. There are a few reasons that could explain this scenario. First, it is possible that the cell wall was deforming inward due to shrinkage of the cell from the sample processing procedure. For example, Wollweber *et al.* reported that the combination of glutaraldehyde, tannic acid, and uranyl acetate showed 5% shrinkage, while other techniques could cause up to 40% shrinkage [187]. If it is assumed that the bacteria had established non-reversible contact with the tip of the nanopillars, then the inward deformation of the cell wall could be due to the cell shrinkage. By comparing the total volume of the bacterium shown in Figure 5.23 before and after shrinkage, a volume reduction of 18% had occurred, which is higher than the values reported by Wollweber and colleagues. A second possibility is that the deformation represents further evidence of the bacterium actively trying to minimise contact with the nanopillars.

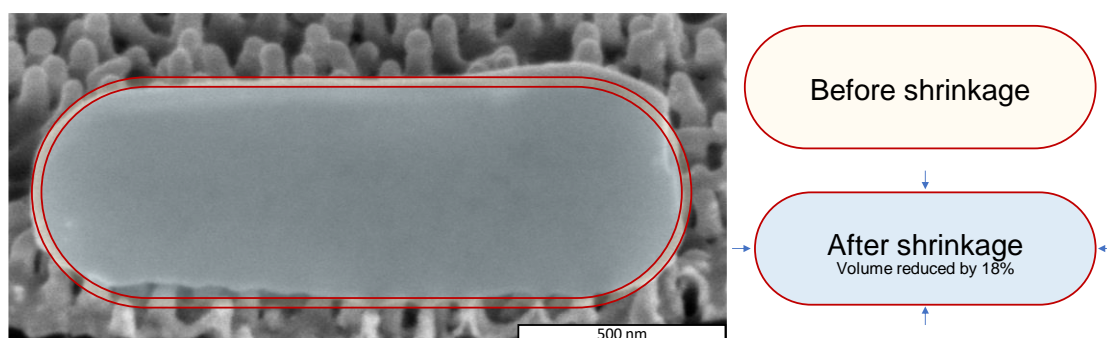


Figure 5.23 Volume shrinkage estimation. The cell showed in this image was assumed to be the cell after shrinkage and to measure the size of the cell before shrinkage, it was assumed that the cell wall attached to the nanopillars does not affected by the shrinkage due to firm attachment to the nanopillars. The numerical values used to calculate the volume reduction can be referred in the Appendix B.

### 5.3.4 Effects of nanotopography, surface wetting and surface energy on bactericidal performance

Chapter 3 summarised the nanotopographic features of the BWN, BDN and SDN surfaces, including contact angle, surface energy and work of adhesion, while Chapter 4 discussed the findings from nanotribological studies using the geometric assumption and contact mechanics model: the JKR theory. These quantifications have allowed an in-depth comparative analysis between different features of the nanopillared surface with the microbiology assay results i.e. the susceptibility of the cell membrane to damage and the vitality of the cells when adhered to the nanopillared surfaces.

Figure 5.24 shows the relationship between the nanotopographic features of tip diameter  $D_T$ , pitch distance  $D_p$  and roughness  $R_q$  of the nanopillars and the outcome of the LIVE/DEAD and BTG assays. These three features have been proposed in the literature to be some of the most important parameters to consider when designing antibacterial surfaces. The data from this study suggest that nanopillars with a small diameter (i.e. sharp nanopillars) are very effective at causing significant damage to the cell wall of Gram-negative bacteria. Despite differences in the absolute CFU count for *E. coli*, *K. pneumoniae*, and *S. aureus*, all strains showed a similar trend, whereby nanopillars with the smallest  $D_T$  resulted in the lowest levels of bacterial viability. A similar trend was observed for the interpillar distance,  $D_p$ , with closely packed nanopillars tending to be the most effective at causing damage to the bacterial cell wall and negatively affecting the vitality of the cells. However, no clear trend was found between the roughness of the surface and the resulting antibacterial properties of the surfaces.

It was also found that the nanostructured surfaces with the highest surface energy  $\gamma^{\text{TOT}}$ , work of adhesion  $W_{\text{adh}}$ , and pull-off force  $f_p$  were associated with the highest degree of membrane damage to Gram-negative bacteria and loss of vitality. By contrast, no obvious trend was seen for *S. aureus* with regards to membrane damage, although there was evidence that *S. aureus* vitality could be affected negatively with nanostructured surfaces that have a high  $\gamma^{\text{TOT}}$ ,  $W_{\text{adh}}$ , and  $f_p$ . (Figure 5.25).

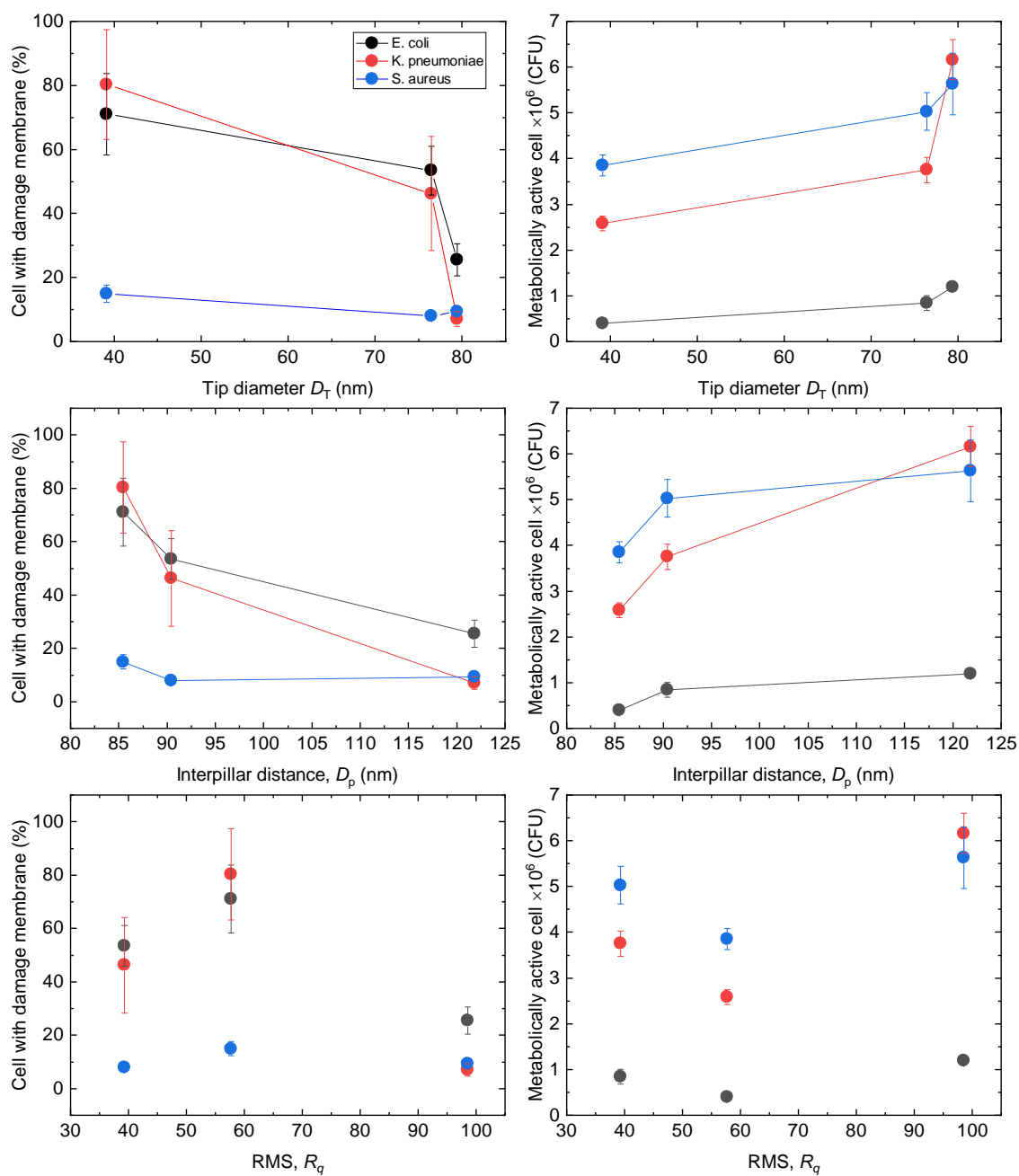


Figure 5.24 Correlation between nanotopography tip diameter  $D_T$ , interpillar distance  $D_p$ , and roughness  $R_q$ , and the antibacterial effects of the surface. Data indicate mean values  $\pm$  standard deviation; N=3.

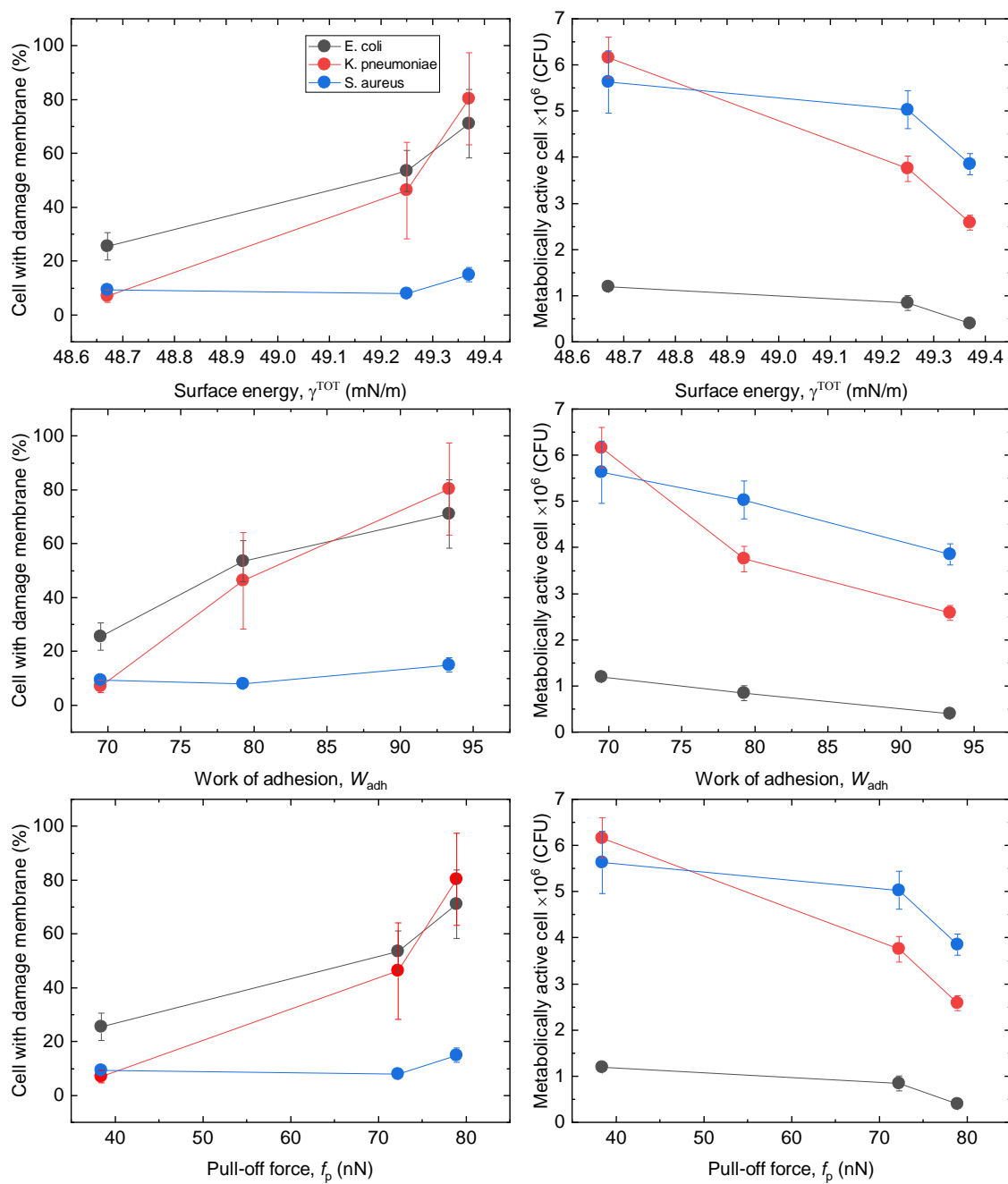


Figure 5.25 Correlation between the surface energy  $\gamma^{\text{TOT}}$ , work of adhesion  $W_{\text{adh}}$  and pull-off force  $f_p$  of a nanopillared surface and its antibacterial effects. Data indicate mean values  $\pm$  standard deviation; N=3.

### 5.3.5 Correlation between nanotribology and antibacterial activity of PET substrates

Nanotribological aspects of nanostructured surfaces like nanospikes, nanotubes, and nanopillars have been known to affect the surface forces that are proportional to area like adhesion, friction, meniscus forces, viscous drag forces and surface tension, compared to forces that are proportional to volume like inertial and electromagnetic forces [188]. There have been a few studies that correlate nanotribological aspects of nanostructured surfaces with adhesive properties of a surface for lubrication applications. However, to the best of the author's knowledge, there is no publication that investigates the correlation between nanotribology and the antibacterial properties of nanostructured surfaces. Chapter CHAPTER 4 highlighted the nano-tribological properties of the BWN, BDN, and SDN surfaces such as pull-off force, friction coefficient  $\mu$ , and stick-slip amplitude coefficient (SSAC). Figure 5.26 shows the correlation between these parameters, along with the maximum pressure exerted on a single nanopillar  $p$ , with the antibacterial effects of the surfaces. Changes in  $\mu$  did not show any clear trend with the microbiology results. However, the bacterial cell wall of Gram-negative bacteria appeared to be more susceptible to damage at higher SSAC compared to lower values, and there were less metabolically active cells on a surface with a higher SSAC (Figure 5.26C-D).

Applying geometric assumptions and by using the JKR theory, the maximum pressure that can be exerted by a single nanopillar due to adhesion force of the surface was calculated and the results discussed in Chapter 4. Figure 5.26E-F shows that surfaces with a high  $p$  are associated with causing more damage to the bacterial cell wall and reducing the overall metabolic activity of the cells. The percentage of cells with membrane damage increased significantly from 13% (*K. pneumoniae*) and 23% (*E. coli*) to around 50% for both *K. pneumoniae* and *E. coli* as the pressure was increased from 3 MPa to 10 MPa. However, the percentage of damaged cells only increased by a further 20% as the pressure on a pillar was increased from 10 MPa to around 26 MPa, highlighting the flexibility and adaptability of the bacterial cell wall. Although the evidence was less obvious for Gram-positive bacterium *S. aureus*, the data did suggest that more damage could be inflicted on the cell wall, with increasing pressure on the single nanopillars (Figure 5.26E-F).

Bacterial cells bound to a solid surface can experience two types of shear force. First, the shear force arising between a cell and the substratum when initial contact is established by a bacterium approaching the surface at an angle, and second, the shear adhesion force, which is dependent on the strength of the bond between the adhered cell and a surface, and which breaks when the bacterium moves along the surface following attachment [140].



The comparative analysis performed here between nanotribological properties and antibacterial performance of the nanostructured surfaces shows that there are dependencies between the frictional instabilities of the surface (SSAC) and the incidence of bacterial cell membrane disruption and impaired metabolic activity. SSAC relates to the amount of energy dissipated between oscillation of the applied force. To explain the SSAC-bacterial activity relationship, it is also important to consider the nanoscopic vibration of bacteria when adhering to a solid surface. Song *et al.* observed that when bacteria adhered to a substratum, the cells showed nanoscopic and random vibration around their equilibrium position [189]. They also reported that under shear forces, the bacterial bonds with a solid surface were stretched by the fluid shear force, yielding stiffening of the bacterial cell wall. It was proposed that Brownian motion and accompanying vibration can either stimulate attachment or detachment. In Chapter 4, it was found that the Young's modulus of a single sharp nanopillar (SDN) was much higher than the blunt nanopillars (BDN). The high stiffness of nanopillars could induce instabilities to the adhering cell which, if Brownian motion and random vibration of the bacterium are considered, could enhance the nanoscopic vibration of the adherent bacterium. Studies with an AFM tip cantilever also support that a stiffer cantilever results in higher flexural vibration [190,191]. Potentially, high instabilities of the nanopillared surfaces, and local nanoscopic vibration of the adhered bacterium, could mean that the suspended cell wall is more prone to stretching, eventually leading to membrane rupturing and cell lysis. Indeed, these effects were observed when comparing the Young's modulus of a single nanopillar,  $E'$ , with the antimicrobial properties (Figure 5.26G,H). As the  $E'$  increases, the antimicrobial properties of the nanostructured surfaces increase, which corroborate with the initial assumption that high stiffness can induce greater vibration and could lead to higher bactericidal properties. This effect would be more pronounced in the later stages of surface colonisation, where the bacteria start to spread across the surface, as this would involve lateral movement that could generate shear forces on the cell wall interacting with the nanopillars. Additionally, the damage to the cell membrane and reduction in metabolic activity was further enhanced by the high intrinsic pressure exerted by the nanopillars on the adhering bacteria.

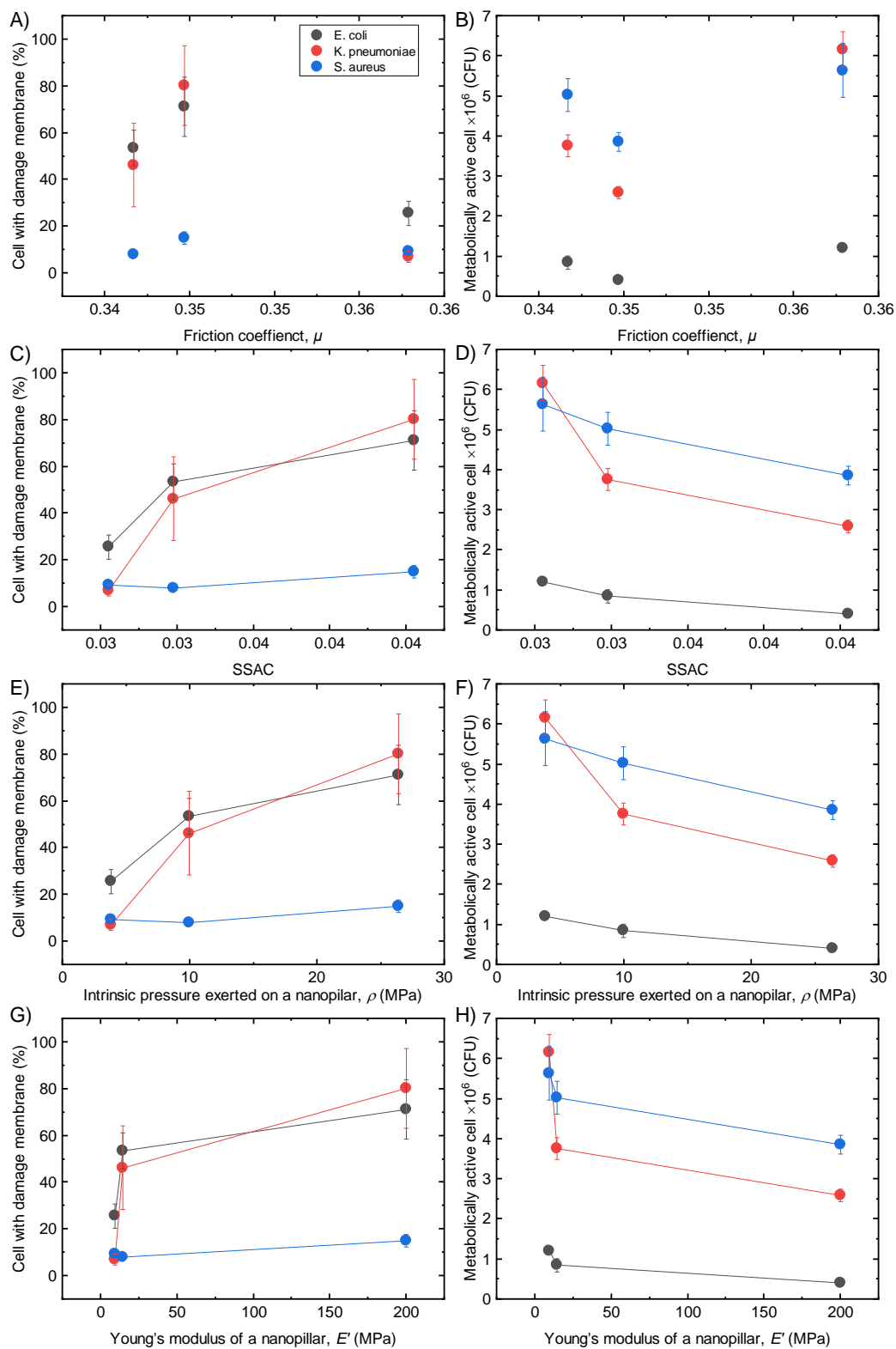


Figure 5.26 Correlation between the friction coefficient  $\mu$ , stick-slip amplitude coefficient SSAC, intrinsic pressure exerted on a nanopillar  $\rho$ , and Young's modulus of a single pillar of a nanopillared surface,  $E'$  and its antibacterial properties. Data indicate mean values  $\pm$  standard deviation; N=3.

Putting all of these data together, six properties of the nanopillars were found that showed the most obvious correlations with antibacterial performance. These are presented in a performance profile radar chart for easier comparison between the different nanostructured surfaces (Figure 5.27). Of note, these are the first studies to identify a relationship between the frictional instabilities of the nanostructured surfaces and their antibacterial performance. This figure also serves to clearly highlight that the sharp and dense nanopillars (SDN) exhibited the greatest antibacterial activity of the nanostructures tested.

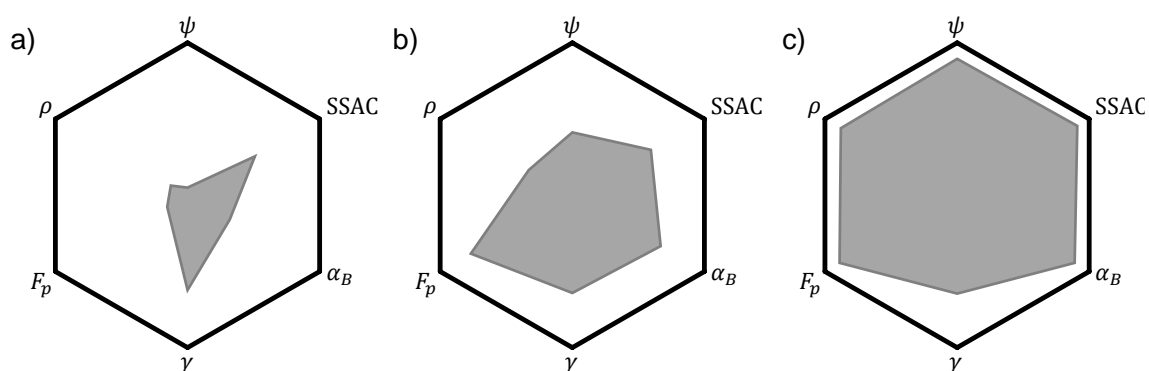


Figure 5.27 Performance profile of the nanopillared surfaces. The performance profile showed six properties for the (a) BWN, (b) BDN and (c) SDN surfaces that were crucial for their antibacterial properties: i) ability to reduce vitality of the adhered cells,  $\psi$ ; ii) degree of cell wall damage,  $\alpha_B$ ; iii) surface energy,  $\gamma$ ; iv) surface adhesion force,  $F_p$ ; v) frictional instabilities, SSAC; and vi) intrinsic nanopillar pressure,  $\rho$ . The antimicrobial properties used in this figure were from *E. coli* cells and the data were normalised to set the scale of all parameters between 0 – 1 for easier visualisation.

## CHAPTER 6 CONCLUSIONS AND FUTURE WORK

Biomaterial-associated infections affect both permanent implants and temporary devices. Despite promising avenues from frontier research on strategies for combatting BAIs, there are only a few new technologies that have been clinically proven to be effective in reducing the incidence of BAIs in the past decades. This is particularly true for polymeric medical devices, for which the progress in device design represents only a small development in polymer chemistry. Currently, there is tremendous effort being made to accelerate the translation of breakthrough discoveries in the laboratory setting to functional and marketable products. This is particularly important for polymeric medical devices, for which there are immediate demands from the clinic due to an increasing use of medical devices globally, with a concomitant increase in BAIs. The urgent need to find an immediate solution to the problem of BAIs is exacerbated by the rise in numbers of antibiotic resistant bacteria.

Recent studies have shown promising results for the use of nanostructured surfaces in combatting BAIs. Protruded nanostructures can be found on natural surfaces like cicada wings, dragonfly wings, shark skin, etc. These have been successfully mimicked on a variety of biomaterials such as titanium, stainless steel, PMMA and PET, and shown to possess antimicrobial activity against Gram-negative and Gram-positive bacteria and yeast, making them desirable candidates for future anti-infective medical device materials. Better understanding of the interactions between bacteria and such nanostructured surfaces will provide clearer direction for the functional design of these materials, thereby accelerating the potential translation of this technology to the clinic.

### 6.1 Scalability of nanofabrication

Anodisation is a versatile technique with great potential as a mass fabrication process to make nanopore master moulds for the generation of reproducible nanopillared surfaces. The nanofabrication process to make the nanopillared surfaces was optimised in this project so as to carefully maximise output with reduced overall fabrication costs and increased efficiency. To increase efficiency, the two-step anodisation process was revised by (a) reducing the overall fabrication time for a nanopore mould from 22 hours to just 4 hours and (b) coating the master stamp with an anti-stick layer to ease the demoulding process and to allow the re-use of the mould. XPS results confirmed that the embossing process did not cause any significant chemical

changes to the PET substrate, and the PET nanopillars generated were not contaminated significantly from the silane film deposited onto the AAO mould.

The nanopillared surfaces used in this study were not fabricated using a sophisticated hot embossing machine but rather a simple hot-press machine. The versatility of the hot-press machine was tested by fabricating 3 clinically relevant polymer substrates that had 3 different  $T_g$  including PET, PMMA and PEEK. Nanopillars were successfully fabricated on PET and PMMA substrates that mimic those found on cicada wings. Due to the high  $T_g$  and viscoelasticity of the PEEK substrate, the resulting nanostructures were short and not fully optimised.

While not tested here, it would be possible to scale up the nanofabrication process in the laboratory by performing anodisation in a bigger container with a large aluminium sheet. Instead of using a magnetic stirrer to agitate the electrolyte, a powerful mechanical pump could be used to circulate the electrolyte in the container. Some modifications would be needed to properly control the dissolution of the oxide layer during anodisation to produce uniform nanopores. The scale up of the hot embossing procedure could be achieved by using other variations of hot embossing like thermal roll embossing, where a large polymer sheet is wrapped around a roller to reproduce nanopatterns on the polymer sheet in a continuous manner [192].

To further reduce the production costs of the nanopore stamps, alloyed or lower purity aluminium sheets could be used. The price for an ultrapure aluminium sheet is very expensive compared to the alloy or lower purity sheets. Zaraska *et al.* reported that anodisation with alloyed and low purity aluminium sheets resulted in no significant difference in pattern uniformity when compared to the nanopore pattern produced on an ultrapure aluminium sheet [93]. Alloyed and low purity aluminium sheets do, however, have an increased number of grain boundaries, which may result in different orientations of the hexagonal unit pattern between different grain areas. The use of a different stamp material to generate soft and reusable elastomeric moulds could allow pattern transfer onto non-planar substrates.

## 6.2 Surface design

Three different but interrelated nanopillared designs were chosen carefully based on the analysis of three different bactericidal mechanism models proposed by Pogodin *et al.*, Xue *et al.*, and Li *et al.*: blunt and wide nanopillars (BWN), blunt and dense nanopillars (BDN) and sharp and dense nanopillars (SDN). The topography and the wettability of these three nanopillared surfaces were characterised using a contact angle analyser, AFM and SEM. It was found that the surface roughness,  $R_q$ , of the PET nanopillared surfaces increased linearly with nanopillar height,

$h$ , while the surface energy,  $\gamma^{TOT}$ , decreased linearly with  $D_p$ . The wetting of nanopillared surfaces fit the Wenzel model, whereby a water droplet partially or completely wetted the surface.

For future work, it could be beneficial to investigate additional nanotopography designs like sharp and wide nanopillared surfaces, tapered nanostructures (e.g. nanocones), or novel shapes (e.g. domed shape, “raspberry” shape, or branched shape) [115]. Since the interaction between bacteria and nanostructures are still not fully understood, investigating other novel nanostructured surface may provide further information that could inform design of the ideal (most effective) antimicrobial surface. Due to the versatility of anodisation and hot-embossing lithography, it would be possible to fabricate such nanostructures on different types of clinically relevant polymer substrates like polyurethane, which is the most commonly used in catheter tubing, polyvinyl chloride (PVC), which is widely used in blood bags and other non-breakable containers, or high performance polymers like PEEK, which is used in dental and orthopaedic implants [1]. Recommendations for further optimisation of the hot embossing process for such polymers, especially the highly viscoelastic PEEK, include using a longer holding time or introducing mechanical vibrations during embossing to improve the filling of the polymer into the nanopores.

### 6.3 Nanotribological properties of PET nanopillared surfaces

One of the main objectives of this project was to find correlations between the nanotribological properties and the antibacterial performance of the nanostructured surfaces. Firstly, the nanotribology was quantified using the colloidal probe AFM to measure the adhesion and friction forces. It was found that the friction force was directly proportional to load force, which correlated with Amonton’s first law of dry friction. The adhesive force of the nanopillared surfaces was dependent on the contact angle,  $\theta$ , surface energy,  $\gamma^{TOT}$ , and the interpillar distance,  $D_p$ . The Young’s modulus of the PET nanopillars was estimated by using geometric assumption and the application of JKR theory. Careful analysis of the approach curve of the force-distance plot revealed that the total penetration of the colloidal probe onto the bed of nanopillars was due to vertical deformation and bending of the nanopillars. It was found that smaller diameter nanopillars (SDN) had a higher intrinsic Young’s modulus,  $E'$ , hence, there was less bending of the nanopillars upon interaction with the colloidal probe. This resulted in a low intrinsic contact radius for the colloidal probe,  $R_i$ , and total apparent contact area,  $A_{TOT}$ , for the SDN surface compared to surfaces bearing larger nanopillars (BDN, BWN). The  $D_p$  showed a

direct correlation with the  $E'$ , whereby larger nanopillars had a smaller  $E'$ . Of note, the adhesion force was not due to an increase in total contact area but rather the potential formation of nanoscale water bridges between the nanopillars and the colloidal probe. Since the surface energy of the SDN surface was larger than other nanopillared surfaces, more water droplets may have formed on top of the SDN nanopillars, hence increasing the adhesive force of the surface. The shear loops of the nanostructured surfaces showed constant and strong fluctuations, which were due to interactions between the silica probe and the nanopillars. The frictional instabilities were quantified by measuring the SSAC and it was found that SSAC had a direct relationship with nanopillar density,  $N$ , pull-off force,  $f_p$ , the surface energy,  $\gamma^{TOT}$ , and the Young's modulus of the nanopillars,  $E'$ .

For future work, colloidal probe AFM studies could be performed with a “soft” colloidal particle probe that has a comparable Young's modulus to that of bacterial cells, such as polystyrene (PS) or PMMA. Ultimately, frictional experiments should ideally be performed with a single bacterial cell attached to the tipless cantilever instead of an artificial colloidal particle. Other improvements that could be made include running the experiment in a liquid cell with the bacterial growth medium, shearing the surface at different speeds and comparing the nanotribological properties recorded using the sharp tip AFM, colloidal probe AFM and bacterial cell probe AFM. In this way, the quantitative data from these measurements could be used to derive a more accurate model for the antibacterial mechanism of action of the nanostructured surfaces.

## 6.4 Correlation between surface topography, wettability, nanotribology and bacterial response

The antibacterial performance of the nanostructured surfaces was quantified using two different assays: LIVE/DEAD assay and BTG assay. The LIVE/DEAD assay allowed assessment of the capacity for the nanopillars to compromise bacterial cell walls, while the BTG assay quantified the vitality of the cells upon exposure to the nanopillars. It was found that the SDN surface had the best overall antibacterial performance followed by the BDN and BWN surfaces, and this trend was consistent using both assays and between different bacterial strains. The viability data indicated that the diameter and interpillar distance of the nanopillars were the most important parameters to consider in the design of the antibacterial surfaces, and it is possible that the  $D_T$  and  $D_p$  worked synergistically to give the best antibacterial performance. The data from the assays were further supported by visualisation of the bacteria adhering to the

nanopillared surfaces by SEM. High tilted SEM images and FIB-SEM revealed that as bacteria adhered to the nanopillars, two regions of the cell wall were affected: the adhered region and the suspended region. The initial contact area of the adhered region was dependent on the size and shape of the nanopillar tip diameter, while the suspended region was affected by the interpillar distance. FIB-SEM revealed that the suspended region did not deform at all during the interaction, deformed outward to increase adhesion to the nearby solid surface, or deformed inward away from the surface, although the latter situation could have been due to bacterial shrinkage during sample fixation. The deformation of the bacterial cell wall was also found to stiffen the outer structure of the bacterium and this effect was most evident for the SDN surface compared to the BWN and BDN surfaces. The evidence of physical deformation of the bacterial cell wall and the change in cell wall stiffness suggested that deformation of the unbound cell wall region was different from that of the bound region, with the former expected to experience less stretching. Since the effects of gravity were expected to be minimal in this scenario, it is likely that interaction forces such as hydrodynamic force, Brownian motion, and direct bacterium-substratum interactions were responsible for the deformation effects. There was also qualitative evidence from the microscopy studies that bacteria may mitigate the antibacterial effects of the nanopillars by reducing their contact area. Potential strategies included (1) adhering to defective areas of the surface that lacked nanopillars or to already bound bacteria; (2) bacillus-shaped bacteria adhering in a vertical rather than horizontal orientation; or (3) coccoid-shaped bacteria replicating away from the surface.

To study the effects of surface proteins in facilitating the attachment of bacteria to the nanopillared surfaces, trypsinisation was employed. Trypsin treatment of *E. coli* reduced the hydrophobicity and negative charge of the cells compared to untreated *E. coli*. Changes in these important physicochemical properties, together with the cleavage of trypsin-susceptible surface proteins, reduced the antibacterial effects of the SDN surface. These data were in agreement with the XDLVO theory, for which hydrophobic interactions are indicated as the predominant forces in facilitating bacterial attachment to a surface.

Correlative analysis between bacterial responses to the nanopillars and nanotribology revealed some important associations. All of the tested bacterial strains showed a non-linear relationship between cell wall permeability or metabolic activity with the nanopillar tip diameter, interpillar distance, surface energy, work of adhesion, pull-off force and the SSAC. This suggested that the antibacterial performance of the nanostructured surfaces was not due to one specific property, such as nanotopography, surface roughness, contact angle, adhesion force, friction coefficient,



or frictional instabilities, but rather reflected a synergistic effect from a combination of different surface properties. It is also important to consider that non-specific mechanical responses of the bacteria, such as their nanoscopic vibration on the nanopillars, could have potentially helped to induce damage to the cell wall or reduce the metabolic activity of the cell. This analysis also showed the importance of nanotribology in modulating bacterial attachment and thus potentially biofilm development. Due to greater frictional instabilities on the nanostructured surfaces compared to a flat surface, bacterial adhesion was negatively affected. As previously reported, despite common trends seen in the responses of different bacterial species, the precise susceptibility of bacterial cells to the nanostructured surfaces was strain-dependent, reflecting differences in parameters such as their physicochemical properties, surface appendage profiles, turgor pressure and mechanical properties of the cell wall [21,24,31,56,95]. The data in this project were consistent with the conventional XDLVO theory of bacterial adhesion, and partially in agreement with bactericidal mechanism theories that have been proposed to date for nanostructured surfaces. For instance, the cell walls of bacteria did deform and stretch when in contact with nanopillars. However, not all bacteria fully adsorbed onto the nanopillars. Gram-negative bacteria were also more susceptible to the sharper and denser nanopillared surfaces, which mimicked the nanotopography found on cicada wings, than Gram-positive bacteria.

Further studies could include an investigation of other bacterial strains such as *Pseudomonas* and *Streptococcus*, yeast strains like *Candida* and moulds like *Aspergillus* and *Fusarium* to test the spectrum of the antimicrobial activity of nanostructured surfaces. By developing a surface that had a broad spectrum of antimicrobial activity, the surface could then be applied to a number of different clinical environments. Longer incubation times should also be investigated to determine the effectiveness of the nanopillared surfaces at reducing biofilm formation. As evidence in the literature, influence of nanostructured surfaces on bacterial attachment becomes more dominant after 3 hours [186]. To better understand shearing effects on bacterial attachment, a flow cell or microfluidic device could be utilised, and this would also provide better understanding of the swimming and landing dynamics of bacteria on nanostructured surfaces, particularly for motile species. To more precisely investigate the role of surface proteins in contributing to nanostructure-mediated cell wall damage, specific knockout mutant strains could be used, such as those lacking expression of fibrillar surface appendages. The nanomechanical measurements of the bacterial cell wall could also be improved if these studies were performed in liquid while the bacteria are still viable. To quantitatively measure the

interactive forces between bacteria and the surfaces using XDLVO theory, the surface wetting and surface energy of bacterial cell must be quantified.

While not an area that was able to be considered in this project, it will be important for future studies to also test the biocompatibility of the nanopillared surfaces with mammalian cells. Biocompatibility testing is an important requirement to get regulatory approval for medical devices prior to clinical study. A previous biocompatibility study has shown that nanopillars on cicada wings are biocompatible with eukaryotic cells [193]. However, since the nanostructures used in this work are much sharper, denser and showed higher antibacterial activity, there is a need for their biocompatibility to be evaluated. Ideally, to be an effective novel medical device material, a nanostructured surface should be biocompatible while maintaining a high level of antimicrobial activity.

## REFERENCES

1. Grand View Research. Medical Polymers Market Analysis By Product, Application, and Segment Forecasts To 2020. 2017.
2. Yin J, Luan S. Opportunities and challenges for the development of polymer-based biomaterials and medical devices. *Regen Biomater*. 2016;3(2):129–35.
3. Harding JL, Reynolds MM. Combating medical device fouling. *Trends Biotechnol*. 2014;32(3):140–6.
4. Darouiche ROO, Weinstein RA. Device-associated infections: a macroproblem that starts with microadherence. *Clin Infect Dis*. 2001;33(9):1567–72.
5. Busscher HJ, Van Der Mei HC, Subbiahdoss G, Jutte PC, Van Den Dungen JJAM, Zaat SAJ, et al. Biomaterial-associated infection: Locating the finish line in the race for the surface. *Sci Transl Med*. 2012;4(153).
6. Broekhuizen CAN, De Boer L, Schipper K, Jones CD, Quadir S, Feldman RG, et al. Peri-implant tissue is an important niche for *Staphylococcus epidermidis* in experimental biomaterial-associated infection in mice. *Infect Immun*. 2006;75(3):1129–36.
7. T.F. Moriarty, S.A.J. Zaat HJB. Biomaterials associated infection: Immunological aspects and antimicrobial strategies. Springer Science & Business Media. 2012.
8. Campoccia D, Montanaro L, Arciola CR. A review of the biomaterials technologies for infection-resistant surfaces. *Biomaterials*. 2013;34(34):8533–54.
9. Hetrick EM, Schoenfisch MH. Reducing implant-related infections: Active release strategies. *Chem Soc Rev*. 2006;35(9):780–9.
10. Rai M, Yadav A, Gade A. Silver nanoparticles as a new generation of antimicrobials. *Biotechnol Adv*. 2009;27(1):76–83.
11. Price JS, Tencer AF, Arm DM, Bohach GA. Controlled release of antibiotics from coated orthopedic implants. *J Biomed Mater Res*. 1996;30(3):281–6.
12. Stigter M, Bezemer J, De Groot K, Layrolle P. Incorporation of different antibiotics into carbonated hydroxyapatite coatings on titanium implants, release and antibiotic efficacy. *J Control Release*. 2004;99(1):127–37.

13. Pisani E. Antimicrobial resistance: What does medicine quality have to do with it? *Rev Antimicrob Resist*. 2015;11(1):3–39.
14. Notification FDAP. Submissions for Medical Devices that include antimicrobial agents. Draft Guid Ind FDA Staff US Dep Heal Hum Serv Food Drug Adm Cent Devices Radiol Heal Off Device Eval Issued July. 2007;19.
15. Kirschner CM, Brennan AB. Bio-Inspired Antifouling Strategies. *Annu Rev Mater Res*. 2012;42(1):211–29.
16. Carman ML, Estes TG, Feinberg AW, Schumacher JF, Wilkerson W, Wilson LH, et al. Engineered antifouling microtopographies - Correlating wettability with cell attachment. *Biofouling*. 2006;22(1):11–21.
17. Scardino A, De Nys R, Ison O, O'Connor W, Steinberg P. Microtopography and antifouling properties of the shell surface of the bivalve molluscs *Mytilus galloprovincialis* and *Pinctada imbricata*. *Biofouling*. 2003;19(S1):221–30.
18. Bers AV, Wahl M. The influence of natural surface microtopographies on fouling. *Biofouling*. 2004;20(1):43–51.
19. Iijima S. Helical microtubules of graphitic carbon. *Nature*. 1991;354(6348):56–8.
20. Chou SY, Krauss PR, Renstrom PJ. Nanoimprint lithography. *J Vac Sci Technol B Microelectron Nanom Struct Process Meas Phenom*. 1996;14(6):4129–33.
21. Ivanova EP, Hasan J, Webb HK, Truong VK, Watson GS, Watson JA, et al. Natural bactericidal surfaces: mechanical rupture of *Pseudomonas aeruginosa* cells by cicada wings. *Small*. 2012;8(16):2489–94.
22. Minoura K, Yamada M, Mizoguchi T, Kaneko T, Nishiyama K, Ozminskyj M, et al. Antibacterial effects of the artificial surface of nanoimprinted moth-eye film. *PLoS One*. 2017;12(9):1–19.
23. Kelleher SM, Habimana O, Lawler J, O'reilly B, Daniels S, Casey E, et al. Cicada Wing Surface Topography: An Investigation into the Bactericidal Properties of Nanostructural Features. *ACS Appl Mater Interfaces*. 2016;8(24):14966–74.
24. Bandara CD, Singh S, Afara IO, Wolff A, Tesfamichael T, Ostrikov K, et al. Bactericidal Effects of Natural Nanotopography of Dragonfly Wing on *Escherichia coli*. *ACS Appl Mater*

- Interfaces. 2017;9(8):6746–60.
25. Mainwaring DE, Nguyen SH, Webb H, Jakubov T, Tobin M, Lamb RN, et al. The nature of inherent bactericidal activity: Insights from the nanotopology of three species of dragonfly. *Nanoscale*. 2016;8(12):6527–34.
  26. Tuson HH, Auer GK, Renner LD, Hasebe M, Tropini C, Salick M, et al. Measuring the stiffness of bacterial cells from growth rates in hydrogels of tunable elasticity. *Mol Microbiol*. 2012;84(5):874–91.
  27. Vadillo-Rodríguez V, Dutcher JR. Viscoelasticity of the bacterial cell envelope. *Soft Matter*. 2011;7(9):4101–10.
  28. Thwaites JJ, Mendelson NH. Biomechanics of bacterial walls: studies of bacterial thread made from *Bacillus subtilis*. *Proc Natl Acad Sci*. 2006;82(7):2163–7.
  29. Cabeen MT, Jacobs-Wagner C. Bacterial cell shape. *Nat Rev Microbiol*. 2005;3(8):601.
  30. Salton MRJ, Owen P. Bacterial membrane structure. *Annu Rev Microbiol*. 1976;30(1):451–82.
  31. Tripathy A, Sen P, Su B, Briscoe WH. Natural and bioinspired nanostructured bactericidal surfaces. *Adv Colloid Interface Sci*. 2017;248(1):85–104.
  32. Xue F, Liu J, Guo L, Zhang L, Li Q. Theoretical study on the bactericidal nature of nanopatterned surfaces. *J Theor Biol*. 2015;385:1–7.
  33. Suo Z, Avci R, Deliorman M, Yang X, Pascual DW. Bacteria survive multiple puncturings of their cell walls. *Langmuir*. 2009;25(8):4588–94.
  34. Thwaites JJ, Mendelson NH. Mechanical Behaviour of Bacterial Cell Walls. *Adv Microb Physiol*. 1991;32(C):173–222.
  35. Koch AL, Woeste S. Elasticity of the sacculus of *Escherichia coli*. *J Bacteriol*. 1992;174(14):4811–9.
  36. Koch AL. Shrinkage of growing *Escherichia coli* cells by osmotic challenge. *J Bacteriol*. 1984;159(3):919–24.
  37. Thwaites JJ, Mendelson NH. Biomechanics of bacterial walls: studies of bacterial thread made from *Bacillus subtilis*. *Proc Natl Acad Sci*. 1985;82(7):2163–7.

38. Deng Y, Sun M, Shaevitz JW. Direct measurement of cell wall stress stiffening and turgor pressure in live bacterial cells. *Phys Rev Lett*. 2011;107(15):158101.
39. Cayley DS, Guttman HJ, Record Jr MT. Biophysical characterization of changes in amounts and activity of *Escherichia coli* cell and compartment water and turgor pressure in response to osmotic stress. *Biophys J*. 2000;78(4):1748–64.
40. Whatmore AM, Reed RH. Determination of turgor pressure in *Bacillus subtilis*: a possible role for K<sup>+</sup> in turgor regulation. *Microbiology*. 1990;136(12):2521–6.
41. Osawa M, Erickson HP. Turgor pressure and possible constriction mechanisms in bacterial division. *Front Microbiol*. 2018;9(1):111.
42. Tuson HH, Weibel DB. Bacteria-surface interactions. *Soft Matter*. 2013;9(17):4368–80.
43. Vadillo-Rodriguez V, Beveridge TJ, Dutcher JR. Surface viscoelasticity of individual gram-negative bacterial cells measured using atomic force microscopy. *J Bacteriol*. 2008;190(12):4225–32.
44. O'Toole GA, Wong GCL. Sensational biofilms: surface sensing in bacteria. *Curr Opin Microbiol*. 2016;30(1):139–46.
45. Cusick K, Lee YY, Youchak B, Belas R. Perturbation of flil interferes with *proteus mirabilis* swarmer cell gene expression and differentiation. *J Bacteriol*. 2012;194(2):437–47.
46. Qi M, Gong X, Wu B, Zhang G. Landing Dynamics of Swimming Bacteria on a Polymeric Surface: Effect of Surface Properties. *Langmuir*. 2017;33(14):3525–33.
47. Hori K, Matsumoto S. Bacterial adhesion: From mechanism to control. *Biochem Eng J*. 2010;48(3):424–34.
48. Simoni SF, Harms H, Bosma TNP, Zehnder AJB. Population heterogeneity affects transport of bacteria through sand columns at low flow rates. *Environ Sci Technol*. 1998;32(14):2100–5.
49. Marshall KC, Cruickshank RH. Cell surface hydrophobicity and the orientation of certain bacteria at interfaces. *Arch Mikrobiol*. 1973;91(1):29–40.
50. Morisaki H, Nagai S, Ohshima H, Ikemoto E, Kogure K. The effect of motility and cell-surface polymers on bacterial attachment. *Microbiology*. 1999;145(10):2797–802.
51. Atabek A, Camesano TA. Atomic force microscopy study of the effect of

- lipopolysaccharides and extracellular polymers on adhesion of *Pseudomonas aeruginosa*. *J Bacteriol.* 2007;189(23):8503–9.
52. Pogodin S, Hasan J, Baulin VA, Webb HK, Truong VK, Nguyen THP, et al. Biophysical model of bacterial cell interactions with nanopatterned cicada wing surfaces. *Biophys J.* 2013;104(4):835–40.
  53. Dickson MN, Liang EI, Rodriguez LA, Vollereaux N, Yee AF. Nanopatterned polymer surfaces with bactericidal properties. *Biointerphases.* 2015;10(2):021010.
  54. Li X. Bactericidal mechanism of nanopatterned surfaces. *Phys Chem Chem Phys.* 2015;18(2):1311–6.
  55. Ivanova EP, Hasan J, Webb HK, Gervinskas G, Juodkasis S, Truong VK, et al. Bactericidal activity of black silicon. *Nat Commun.* 2013;4(1):1–7.
  56. Elbourne A, Chapman J, Gelmi A, Cozzolino D, Crawford RJ, Truong VK. Bacterial-nanostructure interactions: The role of cell elasticity and adhesion forces. *J Colloid Interface Sci.* 2019;546(1):192–210.
  57. Pimpin A, Srituravanich W. Reviews on micro- and nanolithography techniques and their applications. *Eng J.* 2012;16(1):37–55.
  58. Kawai S, Foster AS, Canova FF, Onodera H, Kitamura SI, Meyer E. Atom manipulation on an insulating surface at room temperature. *Nat Commun.* 2014;5(1):1–7.
  59. Tseng AA, Notargiacomo A, Chen TP. Nanofabrication by scanning probe microscope lithography: A review. *J Vac Sci Technol B Microelectron Nanom Struct.* 2005;23(3):877–94.
  60. Asano T, Sakai K, Yamamoto K, Hiura H, Nakayama T, Hayashi T, et al. The advantages of nanoimprint lithography for semiconductor device manufacturing. In: International Society for Optics and Photonics. International Society for Optics and Photonics; 2019. p. 1109580G.
  61. Chou SY, Krauss PR, Renstrom PJ. Imprint of sub-25 nm vias and trenches in polymers. *Appl Phys Lett.* 1995;67(1995):3114.
  62. Schiff H, Kristensen A. Nanoimprint Lithography – Patterning of Resists Using Molding. In: Bushan B, editor. *Springer Handbook of Nanotechnology*. 3rd ed. Springer; 2010. p.

- 271–312.
63. Costner EA, Lin MW, Jen W-L, Willson CG. Nanoimprint Lithography Materials Development for Semiconductor Device Fabrication. *Annu Rev Mater Res.* 2009;39(1):155–80.
  64. Meyer AD, Aten K, Krause AJ, Metzger ML, Holloway SS. Creating a university technology commercialisation programme: Confronting conflicts between learning, discovery and commercialisation goals. *Int J Entrep Innov Manag.* 2011;13(2):179–97.
  65. Esawi AMK, Morsi K, Sayed A, Taher M, Lanka S. Effect of carbon nanotube (CNT) content on the mechanical properties of CNT-reinforced aluminium composites. *Compos Sci Technol.* 2010;70(16):2237–41.
  66. Zhang R, Zhang Y, Zhang Q, Xie H, Qian W, Wei F. Growth of half-meter long carbon nanotubes based on Schulz-Flory distribution. *ACS Nano.* 2013;7(7):6156–61.
  67. Oliveira CP, Freitas RG, Mattoso LHC, Pereira EC. Nanostructured Materials in Electrochemistry. 1st ed. Eftekhari A, editor. *Nanostructured Materials in Electrochemistry.* Wiley Online Library; 2008. 117–186 p.
  68. Ahn J, Son SJ, Min J. The control of cell adhesion on a PMMA polymer surface consisting of nanopillar arrays. *J Biotechnol.* 2013;164(4):543–8.
  69. Chen G, Soper SA, McCarley RL. Free-standing, erect ultrahigh-aspect-ratio polymer nanopillar and nanotube ensembles. *Langmuir.* 2007;23(23):11777–81.
  70. Kim DS, Lee HS, Lee J, Kim S, Lee KH, Moon W, et al. Replication of high-aspect-ratio nanopillar array for biomimetic gecko foot-hair prototype by UV nano embossing with anodic aluminum oxide mold. *Microsyst Technol.* 2007;13(5–6):601–6.
  71. Kim DS, Lee HU, Kim NH, Lee KH, Cho DW, Kwon TH. Fabrication of microchannel containing nanopillar arrays using micromachined AAO (anodic aluminum oxide) mold. *Microelectron Eng.* 2007;84(5–8):1532–5.
  72. Alumet. Avant-garde in anodizing [Internet]. 2016 [cited 2019 Aug 6]. p. About Us. Available from: <https://alumet.nl/en/about-us/>
  73. Lee W, Ji R, Gösele U, Nielsch K. Fast fabrication of long-range ordered porous alumina membranes by hard anodization. *Nat Mater.* 2006;5(9):741–7.



74. Masuda H, Fukuda K. Ordered metal nanohole arrays made by a two-step replication of honeycomb structures of anodic alumina. *Science* (80- ). 1995;268(June):1466–8.
75. Nielsch K, Choi J, Schwirn K, Wehrspohn RB, Gösele U. Self-ordering Regimes of Porous Alumina: The 10 Porosity Rule. *Nano Lett.* 2002;2(7):677–80.
76. Choi J. Fabrication of monodomain porous alumina using nanoimprint lithography and its applications. Max Planck Institute-Halle; 2004.
77. Hazell G, Fisher LE, Murray WA, Nobbs AH, Su B. Bioinspired bactericidal surfaces with polymer nanocone arrays. *J Colloid Interface Sci.* 2018;528(1):389–99.
78. Viela F, Navarro-Baena I, Hernández JJ, Osorio MR, Rodríguez I. Moth-eye mimetic cytocompatible bactericidal nanotopography: a convergent design. *Bioinspir Biomim.* 2018;13(2):26011.
79. Wu S, Zuber F, Maniura-Weber K, Brugger J, Ren Q. Nanostructured surface topographies have an effect on bactericidal activity. *J Nanobiotechnology.* 2018;16(1):20.
80. Valle J, Burgui S, Langheinrich D, Gil C, Solano C, Toledo-Arana A, et al. Evaluation of surface microtopography engineered by direct laser interference for bacterial anti-biofouling. *Macromol Biosci.* 2015;15(8):1060–9.
81. Serrano C, García-Fernández L, Fernández-Blázquez JP, Barbeck M, Ghanaati S, Unger R, et al. Nanostructured medical sutures with antibacterial properties. *Biomaterials.* 2015;52(1):291–300.
82. Kim S, Jung UT, Kim SK, Lee JH, Choi HS, Kim CS, et al. Nanostructured multifunctional surface with antireflective and antimicrobial characteristics. *ACS Appl Mater Interfaces.* 2015;7(1):326–31.
83. Barry AL. Methods for determining bactericidal activity of antimicrobial agents: approved guideline. Vol. 19. National Committee for Clinical Laboratory Standards Wayne, PA; 1999.
84. Lenard JG. Primer on flat rolling. Newnes; 2013.
85. Goodfellow. Polymethylmethacrylate Sheet ME303017 [Internet]. Goodfellow catalogue. 2020 [cited 2019 Oct 23]. Available from: [https://www.goodfellow.com/catalogue/GFCat4l.php?ewd\\_token=8Nt4BxQ3y7N5raU](https://www.goodfellow.com/catalogue/GFCat4l.php?ewd_token=8Nt4BxQ3y7N5raU)

HdmJnKA8YgCdkKJ&n=qXGeEG5zv9LK8odYUk5luHNG9eAu68

86. Alvarez-Asencio R, Thormann E, Rutland MW. Note: Determination of torsional spring constant of atomic force microscopy cantilevers: Combining normal spring constant and classical beam theory. *Rev Sci Instrum.* 2013;84(9):96102.
87. Zhao W, Wang L, Xue Q. Fabrication of low and high adhesion hydrophobic au surfaces with micro/nano-biomimetic structures. *J Phys Chem C.* 2010;114(26):11509–14.
88. Ma D, Li S, Liang C. Electropolishing of high-purity aluminium in perchloric acid and ethanol solutions. *Corros Sci.* 2009;51(4):713–8.
89. Neufeld P, Southall DM. The electropolishing of aluminum. *Electrodepos Surf Treat.* 1975;3(3):159–68.
90. Muse LA. Safe handling of the perchloric acid in the laboratory. *J Chem Educ.* 1972;49(9):A463.
91. Schilt AA, McBride L, Long JR. Perchloric Acid and Perchlorate. GF Smith Chemical Company Columbus, OH; 1979. 100–102 p.
92. Choi J, Sauer G, Nielsch K, Wehrspohn RB, Gösele U. Hexagonally arranged monodisperse silver nanowires with adjustable diameter and high aspect ratio. *Chem Mater.* 2003;15(3):776–9.
93. Zaraska L, Sulka GD, Szeremeta J, Jaskuła M. Porous anodic alumina formed by anodization of aluminum alloy (AA1050) and high purity aluminum. *Electrochim Acta.* 2010;55(14):4377–86.
94. Alumeco. Risk of condensation [Internet]. 2015 [cited 2019 Sep 22]. Available from: <https://www.alumeco.com/knowledge-technique/storage-handling/risk-of-condensation>
95. Kelleher SM, Habimana O, Lawler J, O'Reilly B, Daniels S, Casey E, et al. Cicada wing surface topography: an investigation into the bactericidal properties of nanostructural features. *ACS Appl Mater Interfaces.* 2015;8(24):14966–74.
96. Li X, Chen T. Enhancement and suppression effects of a nanopatterned surface on bacterial adhesion. *Phys Rev E.* 2016;93(5):52419.
97. Rodford RA, Braden M, Clarke RL. Variation of Young's modulus with the test specimen's

- aspect ratio. *Biomaterials*. 1993;14(10):781–6.
98. David C, Schweizer T, Gobrecht J, Schiff H, Heyderman L. Flow behaviour of thin polymer films used for hot embossing lithography. *Microelectron Eng*. 2002;54(3–4):229–45.
  99. Jaszewski RW, Schiff H, Gobrecht J, Smith P. Hot embossing in polymers as a direct way to pattern resist. *Microelectron Eng*. 1998;41:575–8.
  100. Caño-García M, Geday MA, Gil-Valverde M, Megías Zarco A, Otón JM, Quintana X. A 3D-printed device for polymer nanoimprint lithography. *Rev Sci Instrum*. 2018;89(2):025106.
  101. Schiff H, Heyderman LJ, Auf der Maur M, Gobrecht J. Pattern formation in hot embossing of thin polymer films. *Nanotechnology*. 2001;12(2):173–7.
  102. Saito M, Kitamura A, Murahashi M, Yamanaka K, Hoa LQ, Yamaguchi Y, et al. Novel gold-capped nanopillars imprinted on a polymer film for highly sensitive plasmonic biosensing. *Anal Chem*. 2012;84(13):5494–500.
  103. Cecchini M, Signori F, Pingue P, Bronco S, Ciardelli F, Beltram F. High-Resolution Poly(ethylene terephthalate) (PET) Hot Embossing at Low Temperature: Thermal, Mechanical, and Optical Analysis of Nanopatterned Films. *Langmuir*. 2008;24(21):12581–6.
  104. Rosenzweig R, Perinbam K, Ly VK, Ahrar S, Siryaporn A, Yee AF. Nanopillared Surfaces Disrupt *Pseudomonas aeruginosa* Mechanoresponsive Upstream Motility. *ACS Appl Mater Interfaces*. 2019;11(11):10532–9.
  105. McKeen LW. *Plastics Used in Medical Devices*. 1st ed. Modjarrad K, Ebnesajjad S, editors. *Handbook of Polymer Applications in Medicine and Medical Devices*. Oxford: William Andrew Publishing; 2014. 21–53 p.
  106. Wiesli MG, Özcan M. High-Performance Polymers and Their Potential Application as Medical and Oral Implant Materials: A Review. *Implant Dent*. 2015;24(4):448–57.
  107. Schwitalla A, Müller W-D. PEEK dental implants: a review of the literature. *J Oral Implantol*. 2013;39(6):743–9.
  108. Schulz H, Wissen M, Bogdanski N, Scheer HC, Mattes K, Friedrich C. Impact of molecular weight of polymers and shear rate effects for nanoimprint lithography. *Microelectron Eng*. 2006;83(2):259–80.

109. De Jesus Silva AJ, Berry NG, Da Costa MF. Structural and thermo-mechanical evaluation of two engineering thermoplastic polymers in contact with ethanol fuel from sugarcane. *Mater Res*. 2016;19(1):84–97.
110. Volynskii AL, Bazhenov S, Lebedeva O V., Bakeev NF. Mechanical buckling instability of thin coatings deposited on soft polymer substrates. *J Mater Sci*. 2000;35(3):547–54.
111. Lee W, Lee JK. Non-lithographic approach to the fabrication of polymeric nanostructures with a close-packed 2D hexagonal array. *Adv Mater*. 2002;14(17):1187–90.
112. Wu S, Zuber F, Maniura-Weber K, Brugger J, Ren Q. Nanostructured surface topographies have an effect on bactericidal activity. *J Nanobiotechnology*. 2018;16(1):1–9.
113. Owens DK, Wendt RC. Estimation of the surface free energy of polymers. *J Appl Polym Sci*. 1969;13(8):1741–7.
114. Hu G, Zhang H, Di W, Zhao T. Study on Wet Etching of AAO Template. *Appl Phys Res*. 2014;1(2):78–82.
115. Jo H, Haberkorn N, Pan JA, Vakili M, Nielsch K, Theato P. Fabrication of chemically tunable, hierarchically branched polymeric nanostructures by multi-branched anodic aluminum oxide templates. *Langmuir*. 2016;32(25):6437–44.
116. Škvarla J, Luxbacher T, Nagy M, Sisol M. Relationship of surface hydrophilicity, charge, and roughness of PET foils stimulated by incipient alkaline hydrolysis. *ACS Appl Mater Interfaces*. 2010;2(7):2116–27.
117. Markiewicz P, Goh MC. Simulation of atomic force microscope tip–sample/sample–tip reconstruction. *J Vac Sci Technol B Microelectron Nanom Struct Process Meas Phenom*. 1995;13(3):1115–8.
118. Liu Y, Zhao Q. Influence of surface energy of modified surfaces on bacterial adhesion. *Biophys Chem*. 2005;117(1):39–45.
119. Wasik P, Seddon AM, Wu H, Briscoe WH. Bénard-Marangoni Dendrites upon Evaporation of a Reactive ZnO Nanofluid Droplet: Effect of Substrate Chemistry. *Langmuir*. 2019;35(17):5830–40.
120. Ivanova EP, Truong VK, Wang JY, Bemdt CC, Jones RT, Yusuf II, et al. Impact of nanoscale roughness of titanium thin film surfaces on bacterial Retention. *Langmuir*.

- 2010;26(3):1973–82.
121. Zhao W, Wang L, Xue Q. Design and fabrication of nanopillar patterned au textures for improving nanotribological performance. *ACS Appl Mater Interfaces*. 2010;2(3):788–94.
  122. Cheng YT, Rodak DE. Is the lotus leaf superhydrophobic? *Appl Phys Lett*. 2005;86(14):144101.
  123. Ball P. Shark skin and other solutions. *Nature*. 1999;400(6744):507–9.
  124. Bhushan B. Nanotribology, Nanomechanics, and Materials Characterization. In: Bhushan B, editor. *Springer handbook of nanotechnology*. 4th ed. Springer; 2017. p. 789–856.
  125. Enachescu M. Nanoscale Effects of Friction, Adhesion and Electrical Conduction in AFM Experiments. In: Bellitto V, editor. *Atomic Force Microscopy - Imaging, Measuring and Manipulating Surfaces at the Atomic Scale*. 1st ed. IntechOpen; 2012. p. 99–146.
  126. Wenning L, Müser MH. Friction laws for elastic nanoscale contacts. *Europhys Lett*. 2001;54(5):693–9.
  127. Bowden FP, Tabor D. Friction, lubrication and wear: A survey of work during the last decade. *Br J Appl Phys*. 1966;17(12):1521.
  128. Pilkington GA, Thormann E, Claesson PM, Fuge GM, Fox OJL, Ashfold MNR, et al. Amontonian frictional behaviour of nanostructured surfaces. *Phys Chem Chem Phys*. 2011;13(20):9318–26.
  129. Quignon B, Pilkington GA, Thormann E, Claesson PM, Ashfold MNR, Mattia D, et al. Sustained frictional instabilities on nanodomed surfaces: Stick-slip amplitude coefficient. *ACS Nano*. 2013;7(12):10850–62.
  130. Zhou ZR, Jin ZM. Biotribology: recent progresses and future perspectives. *Biosurface and biotribology*. 2015;1(1):3–24.
  131. Swartjes JJTM, Veeregowda DH. Implications for directionality of nanoscale forces in bacterial attachment. *Biophys reports*. 2015;1(3):120–6.
  132. Sharma S, Jaimes-Lizcano YA, McLay RB, Cirino PC, Conrad JC. Subnanometric roughness affects the deposition and mobile adhesion of *Escherichia coli* on silanized glass surfaces. *Langmuir*. 2016;32(21):5422–33.
  133. Gnecco E, Meyer E. *Fundamentals of Friction and Wear on the Nanoscale*. Springer; 2015.

134. Lomboy G, Sundararajan S, Wang K, Subramaniam S. A test method for determining adhesion forces and Hamaker constants of cementitious materials using atomic force microscopy. *Cem Concr Res*. 2011;41(11):1157–66.
135. Thormann E, Yun SH, Claesson PM, Linnros J. Amontonian friction induced by flexible surface features on microstructured silicon. *ACS Appl Mater Interfaces*. 2011;3(9):3432–9.
136. Amontons M. De la resistance cause'e dans les machines. *Mem l'Academie R des Fr*. 1699;44(4):209.
137. Mens JWM, de Gee AWJ. Friction and wear behaviour of 18 polymers in contact with steel in environments of air and water. *Wear*. 1991;142(1–2):255–68.
138. Engineeringtoolbox. Friction and Friction Coefficients [Internet]. Engineering Toolbox. 2016 [cited 2019 Jun 14]. Available from: [https://www.engineeringtoolbox.com/friction-coefficients-d\\_778.html](https://www.engineeringtoolbox.com/friction-coefficients-d_778.html)
139. Moore NW, Houston JE. The pull-off force and the work of adhesion: new challenges at the nanoscale. *J Adhes Sci Technol*. 2010;24(15–16):2531–44.
140. Swartjes JJTM, Veeregowda DH, Van Der Mei HC, Busscher HJ, Sharma PK. Normally oriented adhesion versus friction forces in bacterial adhesion to polymer-brush functionalized surfaces under fluid flow. *Adv Funct Mater*. 2014;24(28):4435–41.
141. Ramakrishna SN, Nalam PC, Clasohm LY, Spencer ND. Study of adhesion and friction properties on a nanoparticle gradient surface: Transition from JKR to DMT contact mechanics. *Langmuir*. 2013;29(1):175–82.
142. Madeira DMF, Vieira O, Pinheiro LA, de Melo Carvalho B. Correlation between Surface Energy and Adhesion Force of Polyethylene/Paperboard: A Predictive Tool for Quality Control in Laminated Packaging. *Int J Chem Eng*. 2018;2018(1):1–7.
143. Cheng Y, Feng G, Moraru CI. Micro- and Nanotopography Sensitive Bacterial Attachment Mechanisms: A Review. *Front Microbiol*. 2019;10:191.
144. Lichter JA, Thompson MT, Delgadillo M, Nishikawa T, Rubner MF, Van Vliet KJ. Substrata mechanical stiffness can regulate adhesion of viable bacteria. *Biomacromolecules*. 2008;9(6):1571–8.

145. Myshkin N, Kovalev A. Adhesion and surface forces in polymer tribology—A review. *Friction*. 2018;6(2):143–55.
146. Chen Y, Stevenson I, Pouy R, Wang L, McIlroy DN, Pounds T, et al. Mechanical elasticity of vapour–liquid–solid grown GaN nanowires. *Nanotechnology*. 2007;18(13):135708.
147. Shin MK, Kim SI, Kim SJ, Kim S-K, Lee H, Spinks GM. Size-dependent elastic modulus of single electroactive polymer nanofibers. *Appl Phys Lett*. 2006;89(23):231929.
148. Li X, Ono T, Wang Y, Esashi M. Ultrathin single-crystalline-silicon cantilever resonators: fabrication technology and significant specimen size effect on Young's modulus. *Appl Phys Lett*. 2003;83(15):3081–3.
149. Nilsson SG, Borrisse X, Montelius L. Size effect on Young's modulus of thin chromium cantilevers. *Appl Phys Lett*. 2004;85(16):3555–7.
150. Nam C-Y, Jaroenapibal P, Tham D, Luzzi DE, Evoy S, Fischer JE. Diameter-dependent electromechanical properties of GaN nanowires. *Nano Lett*. 2006;6(2):153–8.
151. Babaei Gavan K, Westra HJR, van der Drift EWJM, Venstra WJ, van der Zant HSJ. Size-dependent effective Young's modulus of silicon nitride cantilevers. *Appl Phys Lett*. 2009;94(23):233108.
152. Ni H, Li X, Cheng G, Klie R. Elastic modulus of single-crystal GaN nanowires. *J Mater Res*. 2006;21(11):2882–7.
153. Wong EW, Sheehan PE, Lieber CM. Nanobeam mechanics: elasticity, strength, and toughness of nanorods and nanotubes. *Science* (80- ). 1997;277(5334):1971–5.
154. Stan G, Ciobanu C V, Parthangal PM, Cook RF. Diameter-dependent radial and tangential elastic moduli of ZnO nanowires. *Nano Lett*. 2007;7(12):3691–7.
155. Abazari AM, Safavi SM, Rezazadeh G, Villanueva LG. Modelling the size effects on the mechanical properties of micro/nano structures. *Sensors*. 2015;1508(11):28543–62.
156. Weilandt E, Menck A, Marti O. Friction studies at steps with friction force microscopy. *Surf Interface Anal*. 1995;23(6):428–30.
157. Haugstad G, Gladfelter WL, Weberg EB. Friction force microscopy of silver bromide crystals: Ag<sub>0</sub> rods and adsorbed gelatin films. *Langmuir*. 2005;9(12):3717–21.
158. Sundararajan S, Bhushan B. Topography-induced contributions to friction forces

- measured using an atomic force/friction force microscope. *J Appl Phys.* 2000;88(8):4825–31.
159. Deruelle M, Léger L, Tirrell M. Adhesion at the Solid–Elastomer Interface: Influence of the Interfacial Chains. *Macromolecules.* 1995;28(22):7419–28.
  160. Rota A, Serpini E, Gazzadi GC, Valeri S. AFM-based tribological study of nanopatterned surfaces: The influence of contact area instabilities. *J Phys Condens Matter.* 2016;28(13):134008.
  161. Kaiwen Tian, Nitya N. Gosvami, David L. Goldsby and RWC. Stick–Slip Instabilities for Interfacial Chemical Bond-Induced Friction at the Nanoscale. *J Phys Chem B.* 2018;122(2):991–9.
  162. Socoliuc A, Bennewitz R, Gnecco E, Meyer E. Transition from stick-slip to continuous sliding in atomic friction: Entering a new regime of ultralow friction. *Phys Rev Lett.* 2004;92(13):134301.
  163. Tomlinson GA. CVI. A molecular theory of friction. London, Edinburgh, Dublin *Philos Mag J Sci.* 1929;7(46):905–39.
  164. Israelachvili JN, Chen YL, Yoshizawa H. Relationship between adhesion and friction forces. *J Adhes Sci Technol.* 1994;8(11):1231–49.
  165. Choi D, Lee S, Kim S, Lee P, Lee K, Park H, et al. Dependence of adhesion and friction on porosity in porous anodic alumina films. *Scr Mater.* 2008;58(10):870–3.
  166. Xie G, Ding J, Zheng B, Xue W. Investigation of adhesive and frictional behavior of GeSbTe films with AFM/FFM. *Tribol Int.* 2009;42(1):183–9.
  167. Müller T, Lohrmann M, Kässer T, Marti O, Mlynek J, Krausch G. Frictional force between a sharp asperity and a surface step. *Phys Rev Lett.* 1997;79(25):5066.
  168. Hölscher H, Ebeling D, Schwarz UD. Friction at atomic-scale surface steps: Experiment and theory. *Phys Rev Lett.* 2008;101(24):246105.
  169. Zhang Xiangjun, Yonggang Meng and SW. Micro contact and stick-slip number between AFM probe tip and sample surface. *Sci China Ser E.* 2003;46(5):537–45.
  170. Beloin C, Roux A, Ghigo J-M. *Escherichia coli* biofilms. In: Romeo T, editor. *Bacterial Biofilms.* Springer; 2008. p. 249–89.



171. Francius G, Polyakov P, Merlin J, Abe Y, Ghigo JM, Merlin C, et al. Bacterial surface appendages strongly impact nanomechanical and electrokinetic properties of *Escherichia coli* cells subjected to osmotic stress. *PLoS One*. 2011;6(5):1–18.
172. Harimawan A, Rajasekar A, Ting YP. Bacteria attachment to surfaces - AFM force spectroscopy and physicochemical analyses. *J Colloid Interface Sci*. 2011;364(1):213–8.
173. Zubova S V, Ivanov AY, Prokhorenko IR. The effect of composition of the core region of *Escherichia coli* K-12 lipopolysaccharides on the surface properties of cells. *Microbiology*. 2008;77(3):293–7.
174. Ng W. Zeta potential of *Escherichia coli* DH5 $\alpha$  grown in different growth media. *PeerJ Prepr*. 2018;6:e26697v1.
175. Truong VK, Geeganagamage NM, Baulin VA, Vongsvivut J, Tobin MJ, Luque P, et al. The susceptibility of *Staphylococcus aureus* CIP 65.8 and *Pseudomonas aeruginosa* ATCC 9721 cells to the bactericidal action of nanostructured *Calopteryx haemorrhoidalis* damselfly wing surfaces. *Appl Microbiol Biotechnol*. 2017;101(11):4683–90.
176. Agladze K, Wang X, Romeo T. Spatial periodicity of *Escherichia coli* K-12 biofilm microstructure initiates during a reversible, polar attachment phase of development and requires the polysaccharide adhesin PGA. *J Bacteriol*. 2005;187(24):8237–46.
177. Vissers T, Brown AT, Koumakis N, Dawson A, Hermes M, Schwarz-Linek J, et al. Bacteria as living patchy colloids: Phenotypic heterogeneity in surface adhesion. *Sci Adv*. 2018;4(4):eaao1170.
178. Inouye M, Yee M-L. Specific removal of proteins from the envelope of *Escherichia coli* by protease treatments. *J Bacteriol*. 1972;112(1):585–92.
179. Bruinsma GM, Van der Mei HC, Busscher HJ. Bacterial adhesion to surface hydrophilic and hydrophobic contact lenses. *Biomaterials*. 2001;22(24):3217–24.
180. Ong Y-L, Razatos A, Georgiou G, Sharma MM. Adhesion Forces between *E. coli* bacteria and biomaterial surfaces. *Langmuir*. 1999;15(8):2719–25.
181. Pratt LA, Kolter R. Genetic analysis of *Escherichia coli* biofilm formation: roles of flagella, motility, chemotaxis and type I pili. *Mol Microbiol*. 1998;30(2):285–93.
182. Harris SL, Elliott DA, Blake MC, Must LM, Messenger M, Orndorff PE. Isolation and

- characterization of mutants with lesions affecting pellicle formation and erythrocyte agglutination by type 1 piliated *Escherichia coli*. *J Bacteriol.* 1990;172(11):6411–8.
183. Munera D, Palomino C, Fernández LÁ. Specific residues in the N-terminal domain of FimH stimulate type 1 fimbriae assembly in *Escherichia coli* following the initial binding of the adhesin to FimD usher. *Mol Microbiol.* 2008;69(4):911–25.
  184. Petrova OE, Sauer K. Sticky situations: key components that control bacterial surface attachment. *J Bacteriol.* 2012;194(10):2413–25.
  185. Linklater DP, Nguyen HKD, Bhadra CM, Juodkakis S, Ivanova EP. Influence of nanoscale topology on bactericidal efficiency of black silicon surfaces. *Nanotechnology.* 2017;28(24):245301.
  186. Dewald C, Lüdecke C, Firkowska-Boden I, Roth M, Bossert J, Jandt KD. Gold nanoparticle contact point density controls microbial adhesion on gold surfaces. *Colloids Surfaces B Biointerfaces.* 2018;163(1):201–8.
  187. Wollweber L, Stracke R, Gothe U. The use of a simple method to avoid cell shrinkage during SEM preparation. *J Microsc.* 1981;121(2):185–9.
  188. Nosonovsky M, Bhushan B. Multiscale friction mechanisms and hierarchical surfaces in nano- and bio-tribology. *Mater Sci Eng R Reports.* 2007;58(3–5):162–93.
  189. Song L, Sjollem J, Sharma PK, Kaper HJ, van der Mei HC, Busscher HJ. Nanoscopic vibrations of bacteria with different cell-wall properties adhering to surfaces under flow and static conditions. *ACS Nano.* 2014;8(8):8457–67.
  190. Espinoza-Beltrán FJ, Geng K, Saldaña JM, Rabe U, Hirsekorn S, Arnold W. Simulation of vibrational resonances of stiff AFM cantilevers by finite element methods. *New J Phys.* 2009;11(8):83034.
  191. Wu T-S, Chang W-J, Hsu J-C. Effect of tip length and normal and lateral contact stiffness on the flexural vibration responses of atomic force microscope cantilevers. *Microelectron Eng.* 2004;71(1):15–20.
  192. Peng L, Deng Y, Yi P, Lai X. Micro hot embossing of thermoplastic polymers: a review. *J Micromechanics Microengineering.* 2013;24(1):13001.
  193. Watson GS, Green DW, Cribb BW, Brown CL, Meritt CR, Tobin MJ, et al. Insect Analogue

to the Lotus Leaf: A Planthopper Wing Membrane Incorporating a Low-Adhesion, Nonwetting, Superhydrophobic, Bactericidal, and Biocompatible Surface. *ACS Appl Mater Interfaces*. 2017;9(28):24381–92.

## APPENDICES

### Appendix A: Batch processing to count cells or particles (FIJI)

```

dir=getDirectory("Choose a Directory");
print(dir);
path2= dir + "/batch process/"; //
print(path2);
File.makeDirectory(path2);
list = getFileList(dir);

for (i=0; i<list.length; i++) {
    if (endsWith(list[i], ".jpg")){
        print(i + ": " + dir+list[i]);
        open(dir+list[i]);

        //adjust level
        //run("Window/Level...");
        //title = "WaitForUserLevel";
        //msg = "If necessary, use the \"Threshold\" tool
to\nadjust the threshold, then click \"OK\".";
        //waitForUser(title, msg);
        //selectImage(ID);

        run("8-bit");
        //adjust threshold
        run("Threshold..."); // open Threshold tool
        title = "WaitForUserDemo";
        msg = "If necessary, use the \"Threshold\" tool
to\nadjust the threshold, then click \"OK\".";
        waitForUser(title, msg);
        //selectImage(ID);
        getThreshold(lower, upper);
        if (lower==-1)
            exit("Threshold was not set");

        setOption("BlackBackground", true);
        run("Convert to Mask");
        run("Watershed Irregular Features", "erosion=6
convexity_threshold=0 separator_size=0-Infinity");
        run("Analyze Particles...", "size=50-Infinity
display include");
        selectWindow("Results");
        saveAs("Results", path2 + list[i] + ".txt");
        run("Close All");
        selectWindow("Results");
        run("Close");
    }
}

```

## Appendix B: Volume shrinkage calculation

Table A1. Parameters to calculate volume shrinkage of adhered bacteria

Cell condition	Cell average radius (nm), $r_b$	Cell length (nm), $L_b$	Radius shrinkage %	Cell volume (nm <sup>3</sup> ), $V_b$	Volume shrinkage %
Before shrinkage	249.33±2.98	1560.00		3.70×10 <sup>8</sup>	
After shrinkage	233.34±3.78	1459.90	6.42%	3.03×10 <sup>8</sup>	18.04%

Volume of a bacteria was assumed to be a cylindrical shape with hemispherical cap at both ends.

Then, the cell volume,  $V_b$  is given by:

Equation A1: Volume of the cell

$$V_b = \frac{4}{3}\pi r_b^3 + \pi r_b^2 L_b$$

where  $r_b$  and  $L_b$  are the radius and the length of the bacterium